ABSTRACT

Title of dissertation: IR Hall Angle Measurements
On Single Crystal
$Bi_2Sr_2CaCu_2O_{8+x}$
Gregory S. Jenkins, Doctor of Physics, 2003

Dissertation directed by: Professor H. D. Drew
Department of Physics

The far-infrared complex ac- Hall angle was studied in thin optimally doped single crystal $Bi_2Sr_2CaCu_2O_{8+x}$ as a continuous function of temperature in both the normal and superconducting states. The temperature was varied from 25 to 300 K at a discrete set of frequencies in the range of 25 cm^{-1} to 175 cm^{-1}.

Much of this dissertation focuses on the design and construction of an instrument that is capable of measuring the FIR ac-Hall angle in BSCCO as a continuous function of temperature with high sensitivity. The heterodyne system is capable of measuring the real and imaginary part of the Hall angle to an accuracy of $\sim \pm 0.1$ mrad over a temperature range of 20 to 320 K, and a frequency range of 20 cm^{-1} to 240 cm^{-1}.

The normal state properties are measured from T_c up to room temperature at four discrete frequencies, demonstrating clear non-Drude frequency dependence. Further-

more, a recently proposed square- Lorentzian model does not reasonably describe the present data, although previous relatively noisy FIR Hall angle measurements which the model appeared to describe are consistent with the present measurements.

Specifically, the real part of the inverse Hall angle obeys a temperature power law, T^{α}, where $\alpha = 1.65 \pm 0.1$ which is consistent with the dc- value of 1.75 ± 0.05. The values show a decrease with increasing frequency, clearly displaying non-Drude behavior.

For the three frequencies below 90 cm^{-1}, the Hall frequency is a constant in temperature and frequency to within 20% from T_c up to room temperature. The Hall frequency is 0.38 ± 0.03 cm^{-1}/T which corresponds to an effective mass of (2.5 ± 0.21) m_e in reasonable agreement with the values found in FIR optical measurements (3.0 ± 0.4), ARPES dispersion results along the (π, π) nodal direction (2.9 m_e), and near-IR ac- Hall measurements (2.8 m_e) where m_e is the bare electron mass.

The salient features of the superconducting state are qualitatively consistent with a simple model of the conductivity which contains a quasi-particle cyclotron resonance, a zero frequency (London) superfluid resonance, and a finite frequency chiral oscillator at ~ 35 cm^{-1}. The high frequency (175 cm^{-1}) data is consistent with one collective mode cyclotron resonance. A frequency dependent feature in the imaginary part of the Hall angle is observed 10 K above T_c, suggestive of precursive superconducting state behavior.

IR HALL ANGLE MEASUREMENTS ON SINGLE CRYSTAL $Bi_2Sr_2CaCu_2O_{8+x}$

by Gregory S. Jenkins

Dissertation submitted to the Faculty of the Graduate School of the
University of Maryland, College Park in partial fulfillment
of the requirements for the degree of
Doctor of Physics
2003

Advisory Committee:
Professor H. Dennis Drew, Chair/Advisor
Professor Richard A. Webb
Professor Frederick C. Wellstead
Professor Victor M. Yakovenko
Professor Lourdes G. Salamanca-Riba

To Barbara

whose love and support
compels me to grow beyond what I am.
She compassionately consoles,
never complains or interferes,
asks nothing and endures all,
and writes my dedications.

Behind every successful man there is a surprised woman.
- Maryon Pearson

ACKNOWLEDGEMENTS

I could not have endured the trials of graduate school without the emotional support of my closest friends and family. My mother and father have always been proud of my accomplishments whether big or small and supportive regardless of seemingly incomprehensible endeavors. To classify as my friend and wife the person who has witnessed my best and worst moments, and intimately shared our mutually intertwined lives is ostensibly a gross underrepresentation. To her, I want to express my profound gratitude.

The work presented in this volume is collaborative. Jeff Simpson is not only a coworker but a friend who has, in conjunction with his own research, diligently repaired, maintained, and in many cases improved various laboratory equipment which we share. Directly pertinent examples include the Bomem spectrometer, pump stations, computers, and bolometers. Friend and colleague Andrei Sushkov endured the sleep depravity in the experimental trenches for a duration of 3 months offering much needed and appreciated help and advice. Don Schmadel, whose conversations run the gamut of topics, set-up various components of the laboratory prior to my tenure including the pump manifold, the design of the laboratory floor plan, and the design of the FIR laser. My advisor, Dennis Drew, was instrumental in solving apparent insurmountable problems. The BSCCO samples were grown by Gendu Gu (Brookhaven National Laboratories) and peeled by Don Schmadel. Geoff Evans measured the index of refraction of epoxy and wrote a new control program for the SPECAC spectrometer. I enjoyed the informative conversations with Matt Grayson and appreciate his donation of the GaAs 2-DEG samples used in calibrating the system.

I wish to thank the defense committee (Professor H. Dennis Drew, Professor Richard A. Webb, Professor Frederick C. Wellstead, Professor Victor M. Yakovenko, and Professor Lourdes G. Salamanca-Riba) as well as the friends and colleagues who joined us for their attentiveness and insightful questions. I especially appreciate the generosity of Professor F. C. Wellstead who returned my thesis scrupulously edited having heroically corrected content as well as the more mundane grammar mistakes resulting in a much more readable document.

TABLE OF CONTENTS

LIST OF TABLES

LIST OF FIGURES

Chapter 1

Introduction

After the discovery of high temperature superconductivity,[1] it was soon realized the new class of cuprate perovskites exhibited unique behavior both in the normal and superconducting states. Presently, there is no clear consensus as to the mechanism causing superconductivity in the high-T_c materials although it is generally believed that the key lies in understanding the precursive normal state properties. It is currently known that a one-band Hubbard model with d-wave symmetry arising from the wavefunction hybridization of the 3d copper orbitals together with oxygen $p\sigma$ orbitals result in a quasi-2D Fermi surface. However, simple Fermi-liquid models do not describe the observed phenomenology of the normal state. Indeed, as stated by Millis and Orenstein,"The last 5 years of high-T_c research have provided ample evidence that the excitations in [the cuprate high-T_c superconductors] are not electron quasi-particles."[2] Phillip Anderson believes that the "non-Fermi liquid normal state" can be explained in terms of a Luttinger liquid spin-charge separation theory.[3] Other prominent theories have focused on modification of Fermi liquid theory incorporating a quasi-2D d-wave symmetric gap with highly anisotropic momentum dependent

scattering. Of central importance is whether the quasi-particle excitations of the system are naturally describable in terms of Fermi liquid theory, or a more exotic theory necessary.

1.1 Normal state

Angular resolved photo-emission experiments became prominent in the discussion of high-T_c materials with the recent improvements in both energy (2 meV) and angular (0.2°) resolution incorporating the Scienta SES2000 electron analyzer.[4] A complete 2-D $\vec{k}$-space map at the Fermi-level of optimally doped $Bi_2Sr_2CaCu_2O_{8+x}$ (BSCCO) reveals a well defined Fermi surface (it should be noted that the presence of a sharp structure that is *interpreted* as a Fermi surface does not necessarily imply well defined one-electron states[5]). Measurements in the superconducting state show a clear $d_{x^2-y^2}$ symmetric (d-wave) order parameter.[6] The quasi-particle lifetimes have two distinct characteristic behaviors. Along the (π,π) (nodal) direction, a 1/T ($\omega < 2.5k_bT$) or a $1/\omega$ ($\omega > 2.5k_bT$) Marginal Fermi liquid-like[7] scattering rate is observed from room temperature down to 48 K with no defining structure separating the normal and superconducting states. Along the (π,0) (gapped) direction, a sharp quasi-particle peak (the mean-free path is substantially less than the Fermi wavelength) is observed in the superconducting state and disappears in the normal state. An interpretation is that the normal state properties are well described by the electronic properties along the nodal direction, and the superconducting state is primarily governed by the properties along the gapped direction.[4]

Transport measurements demonstrate distinctly non-Fermi liquid-like behavior in

the normal state. dc- resistivity measurements reveal a linear temperature dependence well above the Debye temperature ($\sim$ 250 K)[8,9] whereas Boltzman theory predicts that the resistivity should remain constant above $\sim 0.4\ T_D$. Furthermore, the resistivity, which is ~ 1000 times larger than that of copper, continues to increase linearly even when the mean-free path becomes shorter than the interatomic lattice spacing (known as the Mott-Ioffe-Regel limit) which suggests, in the context of Boltzmann transport theory, the Fermi surface is ill-defined.

Spectroscopic measurements reveal that the longitudinal conductivity, σ_{xx}, behaves as $1/\sqrt{\omega}$ at high frequencies (above, say, the gap energy), a much more gradual change than the $1/\omega^2$ predicted by a simple Drude model.[10,11] In the FIR, the scattering rate found from an extended-Drude analysis is proportional to temperature, and the plasma frequency is temperature independent, consistent with both ARPES and dc- resistivity measurements. At higher frequencies, the scattering rate shows a linear dependence on frequency reminiscent of the marginal Fermi-liquid behavior found from ARPES.

dc- measurements of the cotangent of the Hall angle in optimally doped BSCCO reveal a scattering rate that obeys a $T^{1.78}$ temperature power law[12] distinctly different from the linear-T dependence found in dc- resistivity measurements. Since the dc- Hall effect measures the ratio of the Hall scattering rate and the effective mass, it is unclear as to whether the discrepancy in the two temperature power laws is due to fundamentally different scattering rates, or one characteristic scattering rate with a frequency dependent effective mass, or possibly a combination of both.

My ac- Hall effect experiment as well as others[13,14] are largely motivated to resolve this particular question. By extending the Hall measurements into the frequency

domain, one can independently obtain the temperature dependence of the Hall mass and scattering rate. This can be illustrated by extending the $\cot\theta_H$ measurements from dc- into the frequency domain via the transformation $1/\tau \rightarrow 1/\tau - i\omega$ giving the result:

$$\cot\theta_H = \frac{1/\tau - i\omega}{\omega_H}$$

where $\omega_H = \frac{q\,B}{m^*\,c}$ is the Hall frequency, q is the charge of the carrier, B is the applied magnetic field, m^* is the effective Hall mass, and ω is the frequency of the incident electric field.

The above Drude model result arises from considering exponential relaxation of electric currents which yields a Lorentzian Hall angle response function. Grayson *et al.*[14] found that their FIR ac- Hall angle data in YBCO, when parameterized in terms of a Drude model, resulted in an unphysical scattering rate which decreases with increasing frequency. However, Grayson *et al.* were better able to describe their spectral FIR Hall angle data with a *squared* Lorentzian response function over the temperature range 95 to 190 K. A model by Abrahams and Varma which ascribes an anisotropic $\vec{k}$-dependent marginal Fermi liquid scattering rate predicts this form of the Hall angle.[15,16] However, Hlubina[17] argues that one of the major underlying assumptions in this model is erroneous (namely, that the squared-scattering term cannot be greater than the presumed negligible linear-scattering term). This form of the Hall angle leads to a sum which, when integrated over all frequencies, yields a vanishing Hall frequency, contradicting ARPES measurements and band theory.[14]

While the square-Lorentzian model is largely a phenomenological one, the description of Grayson's data within this model is impressive. He finds that his data is naturally described by one scattering rate that is linear in temperature and frequency

and a renormalized Hall frequency that is temperature and frequency independent. The scattering rate increases with frequency in accord with FIR spectroscopic measurements[10] and recent ARPES measurements.[4]

The higher frequency behavior is markedly different. Schmadel[13] and Cerné[18] both found that the near-IR ($\sim 900 - 1110\ cm^{-1}$) Hall scattering rate has virtually no frequency dependence and increases linearly with temperature. The Hall frequency was found to be frequency independent with a slight temperature dependence. Both data sets appear to be well described by a simple Drude model.

The broadband FTIR-spectroscopic ac- Hall data acquired by Grayson *et al.*[14] on optimally doped YBCO exhibits low signal-to-noise and was taken over a narrow temperature range (95 to 190 K) with few points (95, 120, 150, and 190 K), impeding the determination of a precise functional form for the temperature dependence of the complex ac- Hall angle. Another impediment is the unknown contribution to the Hall angle from the YBCO copper-oxygen chains although presumed negligible. Furthermore, ARPES measurements are primarily performed on BSCCO making direct comparisons difficult.

The majority of this thesis focuses on the design and performance of an instrument that measures the complex FIR Hall angle as a continuous function of temperature to greater precision than previous measurements. Furthermore, the experiment is performed on single crystal BSCCO which embodies no copper-oxygen chains. The purpose is to precisely measure the temperature dependence of the Hall scattering rate and Hall frequency. In particular, can the longstanding mystery of the different temperature power laws observed between the dc- Hall scattering rate ($T^{1.78}$ as measured by Konstantinovic[12]) and the longitudinal scattering rate (linear in temperature

as measured by Quijada[11]) be resolved? Is the complex ac- Hall angle in the FIR described by the Drude model, the square- Lorentzian model, or neither? How do the results compare with the higher frequency NIR ac- Hall angle results acquired by D. Schmadel[13] and L. Rigal[19] as well as the zero frequency dc- Hall angle measurements? The answer to these questions are gradations in comprehending the electronic properties of the normal state in the hopes of significantly contributing to the understanding of the mechanism in which the high-T_c materials become superconducting.

Chapter 2 gives an overview of the experimental technique, physical hardware, and general design considerations. Chapter 3 develops the mathematical tools necessary to extract the Hall angle from the raw data. For the expressed purpose of transferring the experiment to new personnel with minimal loss of time, Chapter 4 painstakingly details the experimental steps required to acquire data. Several appendices are incorporated into the thesis for the same purpose. Chapter 5 describes characterizations of the single crystal BSCCO sample and system calibrations. Hall angle measurements of BSCCO are discussed in Chapter 6.

1.2 Superconducting state

BCS theory[20] with a d-wave symmetric order parameter[6] predicts the number of allowed low lying excitations is proportional to temperature due to the linear increase of the density of states with temperature along the nodal directions. Bonn and Hardy[21] performed microwave surface impedance measurements that directly verified that the density of the superconducting fluid is related to the number of excited quasi-particles by $\rho_s(T) = \rho_s(0) - \alpha T$ at temperatures below 30 K. This

suggests that the basic electronic excitation of the superconducting state can be conventionally understood in terms of a d-wave BCS theory whose excitation are typical Landau quasi-particles.[2]

However, there co-exists collective excitations of the superconducting system. A perpendicularly applied magnetic field ($H_{c1} < H_{applied} < H_{c2}$) causes vortices to form. A vortex, in simple models, is usually thought of as a cylindrical normal-state core of radius ξ (the order parameter coherence length) that contains one fluxoid ($\Phi_0 = h/2e$) created by a circulating supercurrent that extends out from the core a distance of the London penetration length. Since vortices are trapped by various types of sample inhomogeneities and repel one another, they tend to form a (Abrikosov) lattice below a "vortex freezing temperature". Typically, this is $\sim$ 70 K, but depends strongly on the strength and number of pinning sites, which, in turn, depends upon sample purity and the characteristics of grain boundaries.[22] Vortices respond to electric fields and manifest a variety of transport phenomena which include the presence of a Hall effect, resistivity (dissipation), and optical resonances. A consensus as to the equations that govern vortex dynamics has not been reached and is currently an active research topic. However, useful models have been developed. A rich history of experiments that probe the FIR vortex response[22–25] have been performed over the past decade. H. D. Drew, S. Lihn, and S. Wu[22,24] have developed a phenomenological model heavily based upon T. C. Hsu's model[26] of vortices that describe the measured excitations as a function of frequency at low temperatures. In this model, the conductivity is viewed as arising from three parts: the massless supercurrent coupled to a vortex core which is assumed to have a finite mass, confined quasi-particle excitations within the core, and the nodal quasi-particle cyclotron response. The model gives rise to a

zero frequency London resonance and three Lorentzian resonances centered at various finite frequencies. Above $\sim 100\ cm^{-1}$, Karai *et al.* observed that the magneto-optical dichroic response of the system was well described by a single collective cyclotron resonance. Multiple resonant features become increasingly important as the frequency is decreased.

The above models are deficient in understanding my complex Hall data. Since I have acquired the complex Hall angle in the superconducting state as a continuous function of temperature, the phenomenological model developed by Drew *et al.* at low temperatures is presumed to be only qualitatively useful since many of the parameters have unknown temperature dependencies. Furthermore, the experimentally acquired values associated with the resonant frequencies and oscillator strengths of YBCO do not necessarily apply to BSCCO. For these reasons, my main aim is to qualitatively understand the behavior and point out interesting features. The results are presented and discussed in Chapter 6.

Chapter 2

Description of the Experiment

2.1 Experimental overview

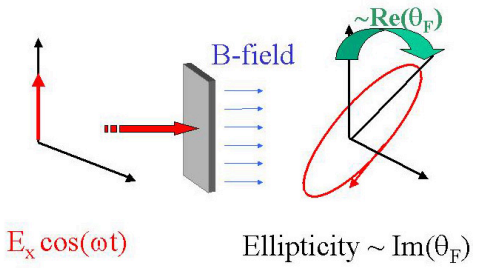

Figure 2.1: A linearly polarized electric field after passing through a sample in magnetic field is elliptically polarized with the major axis at some angle with respect to the initial polarization.

The ac- Hall effect is, in general, represented in figure 2.1. A linearly polarized electric field impinges on a material in a uniform magnetic field. In general, the transmitted electric field will be elliptically polarized with the major axis at an angle with respect to the initial polarization. The resultant complex Faraday angle is defined as follows:

$$\tan\tilde{\theta}_F = \frac{\tilde{t}_{xy}}{\tilde{t}_{xx}} \qquad (2.1)$$

where $\tilde{t}_{xy}$ and $\tilde{t}_{xx}$ in a linearly polarized basis is the off-diagonal and diagonal complex Fresnel coefficients, respectively.

The angle of the major axis of the ellipse with respect to the initial polarization is the real part of the Faraday angle, and the ellipticity is proportional to the imaginary part of the Faraday angle.

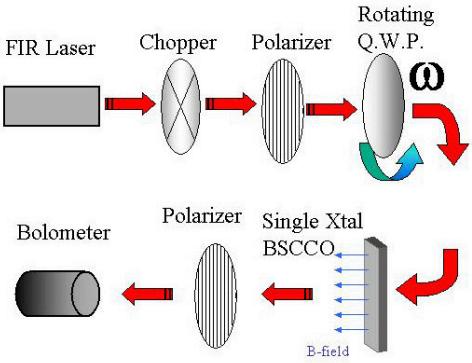

Figure 2.2: A linearly polarized electric field is modulated by a rotating quarter waveplate, passes through an optically active sample, and is then analyzed with a polarizer before entering the detector

The Hall angle is defined as the following:

$$\tan\tilde{\theta}_H = \frac{\tilde{\sigma}_{xy}}{\tilde{\sigma}_{xx}} \tag{2.2}$$

where $\tilde{\sigma}_{xy}$ and $\tilde{\sigma}_{xx}$ in a linearly polarized basis is the off-diagonal and diagonal complex conductivity, respectively.

Converting from the complex Faraday angle to the complex Hall angle involves a simple conversion factor that contains the complex conductivity, σ_{xx}. This conversion factor, although temperature and frequency dependent, is typically much less than 10% for BSCCO (see equation 3.39).

The polarization modulation technique illustrated in figure 2.2 is used to directly measure the complex Faraday angle. Radiation from a FIR laser is initially chopped, linearly polarized, and then polarization modulated by a quarter waveplate rotating at frequency ω. This modulated beam then serially propagates through a magneto-optically active sample and an analyzing polarizer. The intensity is ultimately measured by a bolometer detector.

A lock-in amplifier is used to measure the in- and out- of phase components of the

second and fourth harmonic of the rotational frequency of the rotator. Deferring all the mathematical details to Chapter 3, the complex Faraday angle is related to the measured harmonics in the following way:

$$Re(\tilde{\theta}_F) \propto \frac{\sin(4\omega t)}{\cos(4\omega t)} \tag{2.3}$$

$$Im(\tilde{\theta}_F) \propto \frac{\sin(2\omega t)}{\cos(4\omega t)} \tag{2.4}$$

The temperature of the sample can be continuously varied in magnetic field. Simultaneously, the transmission of the sample as a continuous function of temperature is acquired and used in the analysis of σ_{xx}.

2.2 Optical description

A detailed layout of the optical system is illustrated in figure 2.3. Notice that two distinct optical set-ups are drawn on the same figure, one with mirrors Ma and Mb, the other without mirrors Ma and Mb. Ignoring mirrors Ma and Mb for the time being, the beam, represented in blue, emanates from the FIR laser which is columnated by off-axis parabolic (AOP) mirror M1 and steered to the optics table by the flat mirror M2. A horizontal flat mirror periscope composed of the two flat mirrors M3 and M4 steer the beam into AOP mirror M5 which focuses the beam to the position of the chopper. The beam is again columnated by AOP mirror M6 and focused by AOP mirror M7 through mylar beam splitter BS, through a wire polarizer on a mylar substrate, and onto a rotating quarter waveplate. The resulting beam is

focused onto the sample that resides in vacuum between an 8T split coil magnet and two 1 mil thick kapton vacuum windows of the cryostat. After exiting the cryostat, the beam is focused through an analyzing wire polarizer. An aperture is placed at the image of the sample so that stray scattered beams can be eliminated. A polished brass waveguide is placed directly behind the aperture that guides the beam into a bolometer detector.

If we insert flat mirrors Ma and Mb into the optical path, the beam may be steered into a step-scan FT-FIR wire polarizer spectrometer. In this configuration, the FIR laser output spectrum may be measured to ensure the presence of one lasing frequency.

2.2.1 Off-axis parabolic mirrors and mounts

Mirrors M1, M5, M6, and M11 are all large 4" diameter aluminum off-axis parabolic mirrors (see appendix A for a comprehensive parts list). Due to the large size, mounts for these mirrors were entirely custom made, with the exception of the modified aluminum kinematic mounts made by Newport.

All mounts are constructed and/or modified so a minimum of magnetic material is present. Stainless steal 304 screws and nuts as well as aluminum pressed inserts replaced all springs, hardened steel inserts, and hardened ball bearings.

Mirrors M7, M8, M9, and M10 were originally ordered by Dr. John Cerné in the mid 1990's, a former member of the laboratory. The mirrors are 3.5" in diameter, 1/8" thick Cu mirror substrates with an evaporated Al surface. A few of the mirrors were previously very noticeably damaged. The most severely damaged mirrors were not placed on the table at all, and the most damaged of the remaining 4 mirrors were

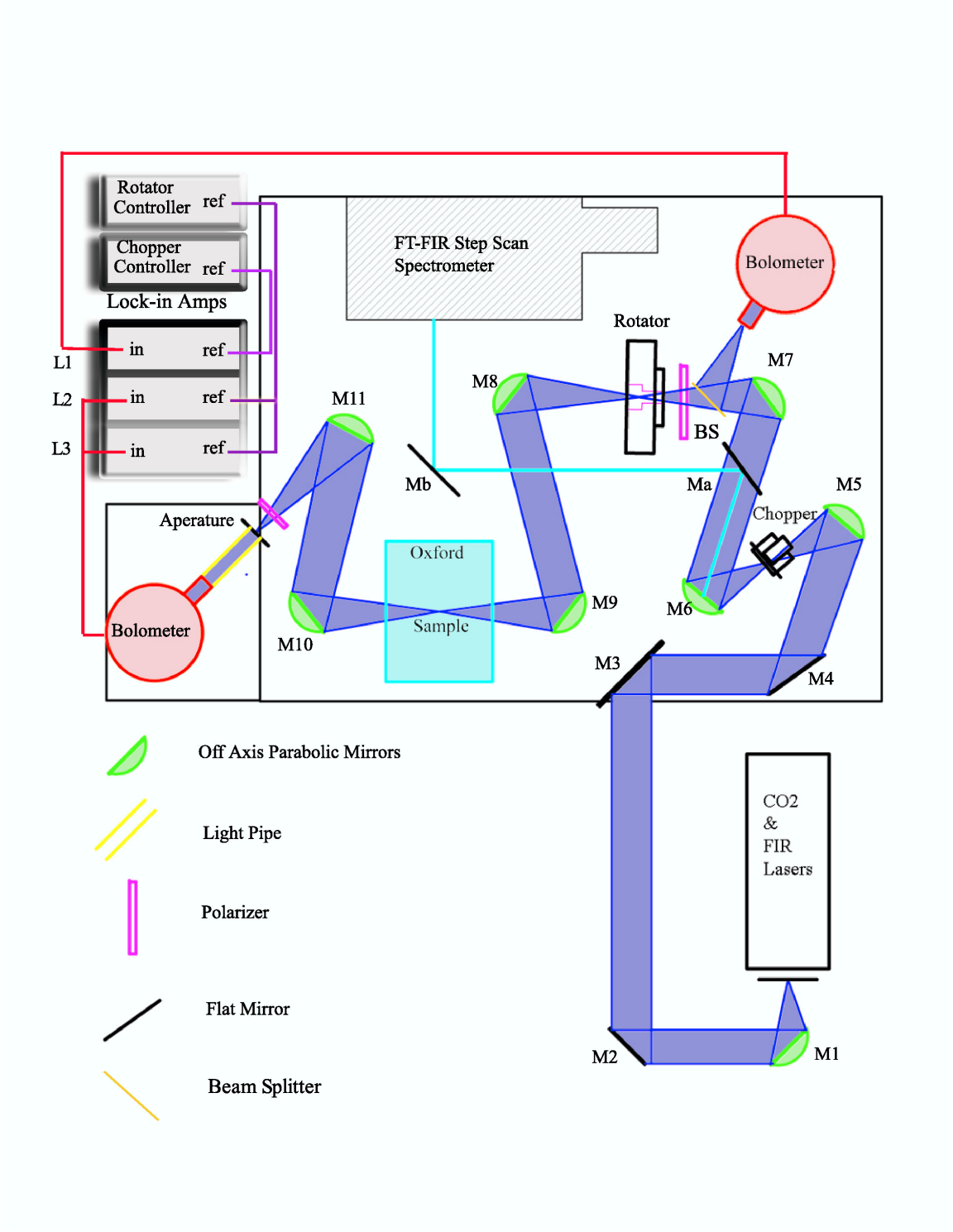

Figure 2.3: The optical table lay-out schematic is a scaled CAD drawing. A block diagram of all pertinent electronics is included.

placed at position M8 and M9.

A periscope was designed at the output of the FIR laser to columnate and steer the beam to the optics table. Mirror M1 and M2 are mounted on modified kinematic optical mounts that attach to a Newport Model 75 style post. The aluminum base is mounted to an x-y stage that has 2" of travel in both directions.

2.2.2 Beam splitter

The beam splitter is a 0.00048" thick sheet of mylar that is tautly sandwiched between 2 flanges with o-rings. The reflectance is slightly frequency dependent, but is $\sim$10% at 84 cm^{-1}.

2.2.3 Polarizers

All polarizers were ordered from ScienceTech (appendix A). They are Au lines evaporated onto a $\sim$0.001" thick mylar sheet. The material is cut into circles of the right diameter and mounted. All polarizer mounts are designed so that the mylar is stretched tautly as 2 flanges are tightened.

2.2.4 Waveplates

All waveplates are x-cut quartz. The thickness is chosen for maximum modulation depth (details in section 2.4). An anti-reflection coating of NiCr is evaporated onto each waveplate to a resistance of 338 $\frac{\Omega}{\square}$ (see section 4.1).

2.2.5 Magnet

A split coil superconducting magnet generates a maximum field of 8T with a current of 100 amps. The magnet is maintained at 4 K in a liquid helium bath. The vacuum windows are 0.001" thick kapton. The entire dewar rests on four 1/4-20 screws to allow height and tilt alignment with respect to the optical beam.

2.2.6 Sample and sample stick

Single crystal optimally doped BSCCO samples were grown by Genda Gu at Brookhaven National Laboratories[27] using the floating zone method. Due to the micaceous nature of BSCCO, Don Schmadel, extending the work of Danillo Romero, was able to peel thin $\sim$ 100 nm thick large area ($\sim$2.5 mm effective diameter) single crystal BSCCO samples. As part of the procedure, these thin crystals were mounted to quartz using a clear epoxy (see section 4.2 for sample preparation procedure).

The sample stick was designed and produced by Oxford Instruments (see figure 2.9 for a picture of the end of the sample stick). The sample rests on a 1/8" thick copper plane which has a graphite aperture of diameter 2.5 mm and a 400 Ω, 1/4 W resistor inserted into a slot and epoxied into place using Stycast. The temperature can be continuously varied between 20 and 320 K. The sample is held in place with a spring clip on one end and silver epoxy on the other, which minimizes thermal stress on the sample. The rotational and horizontal translational degrees of freedom of the sample stick allow for sample alignment.

2.2.7 Detectors

All of the bolometer elements and dewars were purchased from Infrared Laboratories (appendix A). These dewars have been modified from their original configurations by multiple users (filters changed, pre-amps rewired, bolometer elements replaced, etc.). These bolometers are semi-conducting elements whose resistance is a function of temperature (see reference 24 for a discussion of the principles of operation). The elements are mounted to FIR radiation absorbing material. These elements are kept at liquid helium temperatures in order to minimize shot noise. The noise-equivalent-power of these detectors are on the order of 10^{-13} W/$\sqrt{Hz}$. Load curves are given in appendix C.

2.2.8 Lasers

A CO_2 laser is used to optically pump a homemade FIR laser cavity. The CO_2 laser, commercially produced by Edinburgh Instruments Ltd., is continuous wave and tunable from 9 to 11 μm, and has a maximum output of 50W on the strongest lasing lines. The output is focused by a ZnSe lens into the FIR resonator cavity.

The FIR laser is a home-built dielectric waveguide laser[28,29] with 2 adjustable flat mirrors on either end. The input and output radiation is coupled to the cavity through holes in these mirrors whose size is optimized (typically between 1 to 3 mm) for a particular wavelength. Different diameter dielectric Vycor waveguides may be used to define the cavity (typically 1 to 3 inches). The power output depends strongly on the chosen FIR frequency, but is typically between 1 and 100uW. The output window is quartz which absorbs the CO_2 radiation but allows radiation $\lesssim 240\ cm^{-1}$ to pass.

2.2.9 Spectrometer

The FIR laser lines are scanned for the presence of multiple resonances using a SPECAC fourier transform step scan polarizing spectrometer (appendix A). Flat mirrors Ma and Mb are used to steer the optical beam into the spectrometer. These mirrors are mounted on magnetic mounts so that they may be easily inserted and removed from the system. A 4 K bolometer is mounted on a platform (see picture 2.7) with a short light pipe and a homemade 90 degree brass reflector which guides the focused beam from the SPECAC into the bolometer.

2.3 Electronics description

The electronic block diagram is shown in figure 2.3.

The bolometer detectors are equipped with pre-amplifiers that allow a high impedance ($\gg 50\ \Omega$) output at gain settings of 1, 200, or 1000.

There are two digital EG&G 7260 lock-in amplifiers and one EG&G 7265 lock-in amplifier. These lock-in amplifiers are nearly identical in appearance, functionality, and performance. The 7265 is used in dual harmonic mode so that the second and fourth harmonic in- and out- of phase signals from the rotating waveplate may be simultaneously acquired.

A chopper amplitude- modulates the beam which allows both the reference and transmission ac- coupled bolometer detector signals to be measured by two EG&G 7260 lock-in amplifiers. The optical beam is typically chopped at $\sim$ 300Hz. The TTL output signal from the chopper controller is fed into the TTL reference input of the two lock-in amplifiers.

A rotating waveplate polarization-modulates the optical beam. The output signal of the transmission bolometer detector is fed into an EG&G 5113 low-noise pre-amplifier (gain 1 to 750, band-pass filter of 6db/octave at 3Hz and 3kHz) which is then fed into the 7265 EG&G lock-in amplifier. The rotator motor controller supplies a TTL signal which is fed to the 'TTL reference' input of the lock-in amplifier. The 7265 decomposes the signal into in- and out- of phase components of the second and fourth harmonics.

A Lakeshore 340 temperature controller monitors and regulates the temperature of the sample and simultaneously monitors the temperature of the sample-stick.

An Oxford PS120-10 power supply controls the superconducting magnet current.

An in-house Labview program controls and acquires all data (section 4.5.6). A National Instruments GPIB card controls and acquires data from the three EG&G lock-in amplifiers and the Lakeshore temperature controller. The magnet power supply and the EG&G 5113 pre-amp are controlled via two separate serial ports.

An HP spectrum analyzer is used to determine optimal, low-noise operating conditions. The noise spectrum from the detectors are analyzed to choose operating frequencies of the chopper and rotator so that no interfering signals compete with the bonified signals.

A separate Windows- based PC computer and in-house Labview program is used to control the SPECAC step scan FT spectrometer. The motor is controlled through the serial port. A National Instruments GPIB card is used to acquire data from a 7260 lock-in amplifier that is connected to a detector and the chopper reference TTL signals.

2.4 Design considerations

2.4.1 System etalons

Due to the coherent nature of the radiation, standing waves ('etalons') can occur between any pair of partially reflecting optical elements. It is necessary to minimize these effects in order to acquire useful data.

The chopper, rotator, beam splitter, polarizers, and sample were all set at an angle (as much as the geometry would allow) with respect to the beam direction. In addition, the chopper, rotator, and polarizers were not placed directly at the foci, but rather were placed at points near the foci so as not to magnify any standing waves that may occur in the system. The exception to this rule was the sample itself, where it is important to minimize the spot size.

Etalon can also occur between the parallel surfaces of the quartz waveplate. To reduce these internal standing waves, anti-reflecting coatings of NiCr were deposited to a specific sheet resistance to impedance match the quartz substrates to air (see section 4.1 for the coating procedure).

The vacuum windows of the magnet cryostat were specifically chosen to be thin sheets of kapton (5 μm thick) in order to minimize etalon effects within the windows. The index of refraction is ~ 2 so that the first etalon maximum would occur at a frequency of $1/(2 \times 2 \times 5 \times 10^{-4})\ cm^{-1} = 500\ cm^{-1}$. The highest theoretical frequency achievable with the current system is the optical cut-off frequency of quartz, which is $\sim 240\ cm^{-1}$.

2.4.2 Sample considerations

All of the BSCCO samples were made by peeling thin sections off of a single srystal. It is critical during the peeling process to visibly look through the BSCCO crystal to gauge the homogeneity of the sample. Therefore, the epoxy and the substrate both need to be transparent in the visible spectrum. Suitable substrates that have a large FIR transparent window include diamond, quartz, and sapphire. Diamond would be the best in this regard, but is prohibitively expensive. In the FIR, the quartz cut-off frequency is slightly higher than sapphire near room temperature, and both are roughly the same at low temperature.[30] We chose as our substrate the same material, quartz, that is prevalent elsewhere in our system (waveplates, cold filters in the bolometers, sample substrate, and a filter for CO_2 radiation).

Since we are measuring the transmission of BSCCO in the normal and superconducting state, the crystal is required to be thin. The transmitted radiant power can be estimated using equation F.9 and published values of the conductivity. In our system, the transmission with respect to AR-quartz was directly measured to be $\sim$3% at room temperature, $\sim$1% at 100 K, and $\sim$.01% in the superconducting state.

Since the experiment is sensitive to electric fields, an aperture can cause the E-field near the edges to significantly suffer spurious circular dichroic effects. In principle, this is not a problem if the beam and sample do not move, in which case the spurious signal may be mathematically eliminated. However, thermal expansion of the sample stick, spacial mode fluctuations, and/or beam movement are always present to some extent. To minimize edge effects, the sample is made as large as possible to maximize the distance between the spot and the aperture. The aperture itself is constructed of absorbing graphite which eliminates a metallic boundary condition on the electric

field.

Since our BSCCO sample is highly reflective and marginally transmissive, the effects of leakage light can cause serious repercussions in the experiment. If, for example, there existed a hole in the crystal itself, the part of the beam transmitting through the hole (in a simple minded picture) would not exhibit a Faraday rotation which would tend to decrease the total measured Faraday angle. A .1% leakage signal would completely dominate our Faraday signal in the superconducting state.

Metallic surfaces are pragmatically perfect reflectors in the FIR. To reduce stray scattered radiation from re-entering the beam path, FIR absorbing material is placed on the sample stick (see picture 2.9) as well as on surfaces near the sample inside the magnet bore.

In order to minimize the movement of the sample due to temperature induced length changes, the sample stick is clamped at one point near the sample. In additin, the sample is mounted to a copper plate that rests on thermally insulating plastic spacers. A heater is mounted directly to the same copper plate. A wire is used as a thermal link between the plate and the sample stick. The link is chosen such that the change in sample temperature from room temperature to 30 K occurs on a reasonable time scale ($\sim$ 15 minutes). The thermal link should be sufficiently weak to allow the 2.5 W heater to warm the sample to room temperature while negligibly warming the sample stick.

Thermal lag between the thermometer and the sample is minimized by gluing the thermometer directly to the sample substrate using silver-epoxy.

Schmadel and Rigal reported observing stress induced rotations in their experiment at 1000 cm^{-1}. In order to minimize thermal stress induced rotations, the sample

is mounted using a spring clip on one side and silver-epoxy on the opposite side (see picture 2.9).

Multiple reflections between the back of the quartz substrate and the BSCCO side of the substrate can cause erroneous Faraday rotation signals. It is difficult to model multiple reflections in the substrate since the amount of rotation is sensitively dependent upon angle of incidence (which in reality is a cone of incidence with f/ $\# \sim 3$) as well as the substrate thickness and index of refraction. An anti-reflection coating is deposited on the back side of the quartz substrate (section 4.1) so that all calculations may assume a single-pass through the BSCCO-quartz-AR coated sample. Multiple reflections are considered error signals.

2.4.3 Warming the magnet vacuum windows

The kapton vacuum windows are permeable to helium gas allowing ambient helium gas to diffuse into the magnet vacuum jacket. This exchange gas chills the windows eventually allowing water and ice to condense onto the windows which drastically reduces transmission. The best technique to prevent water and ice from condensing is to continuously blow room temperature air directly across the windows. Large diameter green tubes direct air from a blower motor to the windows which are visible in figure 2.5.

2.4.4 Beam movement and spacial fluctuations

Beam movement in the system will register as a spurious Faraday rotation. For example, if the spot were to move slightly at the location of the chopper, the signal could appear phase-shifted in time. This would manifest as a phase shift at the lock-

in amplifier and would be equivalent to the effect of a real Faraday rotation. Similar spurious phase shifted signals would occur due to beam motion associated with the rotating waveplate.

To minimize phase noise from beam movement, all optical mounts and mirrors are made of non-magnetic materials. Also, the distance between the magnet and the chopper and rotator (which contain electrical motors with magnets) is maximized, and the distance between the magnet and the magnetic invar of the CO_2 laser is sufficiently distanced.

The magnet itself tends to pull itself towards the ferrous material located in the walls, floor, and/or ceiling of the laboratory. The force the magnet bears on the optics table varies as a function of magnetic field. The optics table then flexes causing all the optical components on the table to move with respect to the incoming beam. This is minimized in practice by inserting a 2.5" diameter PVC bracing pipe between the ceiling and the top of the magnet cryostat as well as a floor brace inserted beneath the optics table, thus clamping the entire dewar between the floor and the ceiling. The down bearing force is adjusted by a crude z-stage placed on top of the cryostat beneath the PVC pipe.

If the output of the FIR laser were multi-mode, then the fluctuation of power between the spatially separated modes would register as phase fluctuations. The FIR laser is designed with a dielectric waveguide which, together with other geometrical considerations such as the size of the input and output coupler, strongly favors a single mode.[28,29,31,32] Polarization drift is minimized by inserting a polarizer in the system between the chopper (which alters the polarization due to the presence of a metallic edge) and rotating waveplate.

Thermal drift associated with the CO_2 and FIR laser cavities also causes the alignment of the beam to change slowly over time. The power as a function of time decreases away from optimal tuning. It is not *a priori* apparent how thermal drift would manifest as phase noise. However, in practice, changing the CO_2 cavity piezoelectric, diffraction grating, output coupler alignment, the FIR laser mirror alignment, or cavity length all cause varying amounts of phase change. After running the system for several hours so that the 2-laser system is in a thermal equilibrated state, I find that the CO_2 piezo (cavity length adjustment) is the main culprit for short term drift of the phase. The lasers are aligned by trial and error to a configuration where varying the CO_2 piezo by small amounts has no effect on the phase so that it may be adjusted during scans with no significant repercussions.

To minimize thermal drift of the FIR cavity, the dielectric waveguide of the FIR laser is chosen to be VYCOR, a doped amorphous quartz tube which has an extremely small thermal expansion coefficient of $7.5 \times 10^{-7}/K$.

2.4.5 Diffraction and spot size

The f-number of a system is defined as

$$f/\# = \frac{1}{2\sin\theta} \approx f/D \tag{2.5}$$

where f is the focal length, D is the diameter of the collecting optic, and θ is half the cone angle. As will be shown below, it is an important parameter since it determines the smallest spot at the sample location.

The f-number of the system is limited by the magnet bore diameter and the

distance between the vacuum window and the location of the sample. The off-axis parabolic mirror just outside the cryostat has a diameter of 3.25" and a focal length of 10.7". The resulting limiting f-number of the system is 3.5.

Diffraction plays a large role in determining beam diameter and spot size. The diffraction limit of the focused spot diameter in the longest wavelength used in our experiment ($\sim$20 cm^{-1}) is calculated in the following way:

$$\begin{aligned} D &= 2f \sin\frac{\Delta\theta}{2} \\ &\text{where } \Delta\theta = 1.22\lambda/d = \text{diffraction angle, } \lambda \text{ is the wavelength,} \\ &\text{D is the mirror diameter, and d is the spot diameter} \\ \Rightarrow d &\approx 1.22\lambda\frac{f}{D} \approx .22\ mm \end{aligned} \tag{2.6}$$

This is quite small compared to the effective sample diameter of $\sim$ 2.5mm. However, since we are sensitive to electric field effects, the full-width-half-max (FWHM) value is not an appropriate measure of our spot size. For errors to necessarily be negligible from aperture edge effects, the E-field must be less than $\sim$ 1% at the edge of the aperture (which is .01% in intensity!). Since the FWHM value represents one standard deviation, a better estimate of our spot size is to consider $\sim$ 5 standard deviations, resulting in a diffraction limited spot size on the order of 1 mm which is still substantially smaller than our sample size.

As can be seen from equation 2.6, if we are under-filling the mirrors, then D is effectively reduced increasing our spot size. To estimate the collimated beam diameter, it is necessary to analyze the output of the FIR laser. The size of the beam when

it strikes the first columnating mirror is:

$$\text{Beam Size} = 2\ f \sin\frac{\Delta\theta}{2}\ \approx\ 1.22\ f\ \lambda/d = \\ 1.22\ (7.6\ cm)(20\ cm^{-1})^{-1}/(.3\ cm) = 1.5\ cm \tag{2.7}$$

The beam is then columnated but will diverge up to the first focusing mirror roughly 3m away:

$$\text{Beam Size} \approx 1.5\ cm + 1.22\ d'\ \lambda/D' = \\ 1.5\ cm + 1.22 \times (300cm) \times (20\ cm^{-1})^{-1}/(1.5\ cm) \approx 14\ cm \tag{2.8}$$

This is much larger than the 3.5" optics. However, the columnating lens may be adjusted to slightly focus the beam somewhat compensating for the diffraction effects. In this way, no significant radiant power is lost from over-filling the optics, but a detailed analysis of the spot size becomes rather difficult.

Aberrations from misaligned or damaged off-axis parabolic mirrors contribute to larger spot sizes compared to the diffraction limit. In practice, the actual measured spot size at the sample location is a factor of two larger than the diffraction limited minimum.

2.4.6 Detector noise/laser power limits on the signal

The measured Faraday angle can be represented as $\theta_F \approx \frac{\Delta Y}{X}$ where ΔY is the change in the out- of phase component of the rotator signal (as represented by equation 2.3, and in more detail in equation 3.10) between zero and the maximum magnetic field ($\pm 8T$). The in- phase component, X, will not change appreciably as a function of magnetic field and will, to a very good approximation, equal the magnitude of the modulated beam. The signals are generally small, meaning $Y \ll X$.

The bolometer noise and responsivity are measured independently using methods outlined in section D.7.1, and are tabulated in appendix C for all bolometer detectors.

Given the bolometer responsivity, the minimum power output of the FIR laser can be estimated given the desired minimum achievable noise level of the Faraday angle.

$$\theta_{Fmin} \approx \frac{\Delta Y}{X} \approx \frac{N}{R_{sig}}$$

where N is the bolometer dark noise under operating conditions

$$\approx 75nV/\sqrt{Hz},$$

and R_{sig} is the modulated signal magnitude, $\sqrt{X^2 + Y^2} \approx X$

$$R_{sig} = P \times R \times L$$

where P is the total laser power output,

R is the responsivity of the bolometer, and

L is the total attenuation between the laser and bolometer

$$\Rightarrow \; P_{min} = \frac{N}{\theta_{Fmin} \times R \times L}$$

The attenuation factors are measured for each optical component:

$L_{sample} = 5 \times 10^{-3}$ $\quad$ $L_{chop} = \frac{1}{2}$

$L_{waveplate} = 0.25$ $\quad$ $L_{beam-splitter} = 0.9$

$L_{kapton} = 2 \times 0.9$ $\quad$ $L_{lightPipe} = 0.9$

$L_{mylarPolarizers} = 0.9$ $\quad$ $L_{aperature} = 0.75$

$L_{air} = variable$

$$L_{modulation} = \begin{cases} \frac{1}{2} & \text{for } Re(\theta_F) \\ \frac{1}{4}\frac{1-\cos(\Delta\beta)}{\sin(\Delta\beta)} & \text{for } Im(\theta_F) \text{ where } \Delta\beta \sim \pi/4 \end{cases}$$

$$\Rightarrow \; L \approx 3 \times 10^{-4}$$

Most of the attenuation factors are obviously labelled. L_{air} is the attenuation of the beam propagating through air along the entire optical path. Water resonances absorb some output FIR laser frequencies catastrophically while not significantly effecting others. In calculating L_{total}, I assume $L_{air} \sim 1$. From equations 3.10, it is apparent that proportionality constants scale the total signal. I combine these scaling factors into $L_{modulation}$. Quartz has a strong frequency and temperature dependent absorption above $\sim 100 cm^{-1}$ (see the graph in figure 5.2), so the attenuation factors $L_{waveplate}$ and L_{sample} will subsequently vary. The attenuation suffered in BSCCO is frequency and temperature dependent as well. However, the above values represent reasonable values at 84 cm^{-1} and a temperature of ~ 100 K.

If we require $\lesssim 0.5$ mrad of detector noise in the measured Faraday angle, then

the minimum output laser power is:

$$P_{min} = \frac{N}{\theta_{Fmin} \times R} = \frac{75nV/\sqrt{Hz}}{.5 \times 10^{-3} \ \times \ 3.5 \times 10^{5} V/W \ \times \ 3 \times 10^{-4}} \approx 4\mu W \qquad (2.9)$$

2.4.7 Waveplates

The largest polarization-modulation depth occurs at the quarter- waveplate condition: the intensity ranges from a maximum (the optical axis of the waveplate is aligned with the polarization) to half of the maximum value (the optical axis is at an angle of $\pi/4$ with respect to the polarization).

The phase shift between the extraordinary (e) and ordinary (o) axis of a waveplate depends upon the differential index of refraction, $\Delta n = n_e - n_o$. This differential index of refraction is a function of frequency. The differential phase shift associated with a waveplate of thickness d is given by:

$$\Delta\beta = 2\pi \ \nu \ d \ \Delta n(\nu) \text{ where } \nu = 1/\lambda_0, \ \lambda_0 \text{ is the free-space wavelength} \qquad (2.10)$$

Using published $\Delta n(\nu)$ data[30] and solving equation 2.10 for $\Delta\beta = \pi/4$ for a discreet set of frequencies yields a set of optimal thicknesses. The modulation efficiency ϵ is given by the relation $\epsilon = 1 - |1 - \frac{\sin\Delta\beta}{\sin\pi/4}|$ and is plotted in figure 2.4 for all waveplate thicknesse which I purchased. The 2ω and 4ω signals directly scale with the modulation depth efficiency.

The waveplates are used as first-order quarter waveplates. As will be seen in equation 3.10, it is desirable to minimize the differential absorption, $\Delta\Gamma$, to prevent mixing of the real and imaginary parts of the Faraday angle.

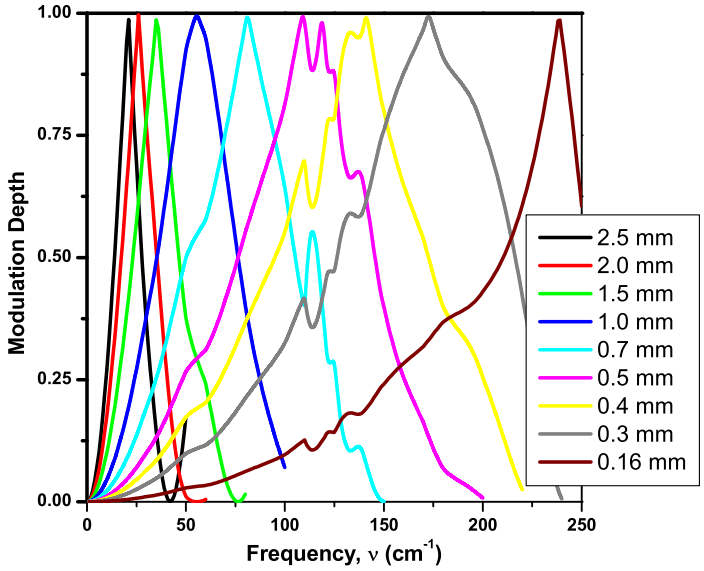

Figure 2.4: The polarization modulation depth frequency dependence for various waveplate thicknesses

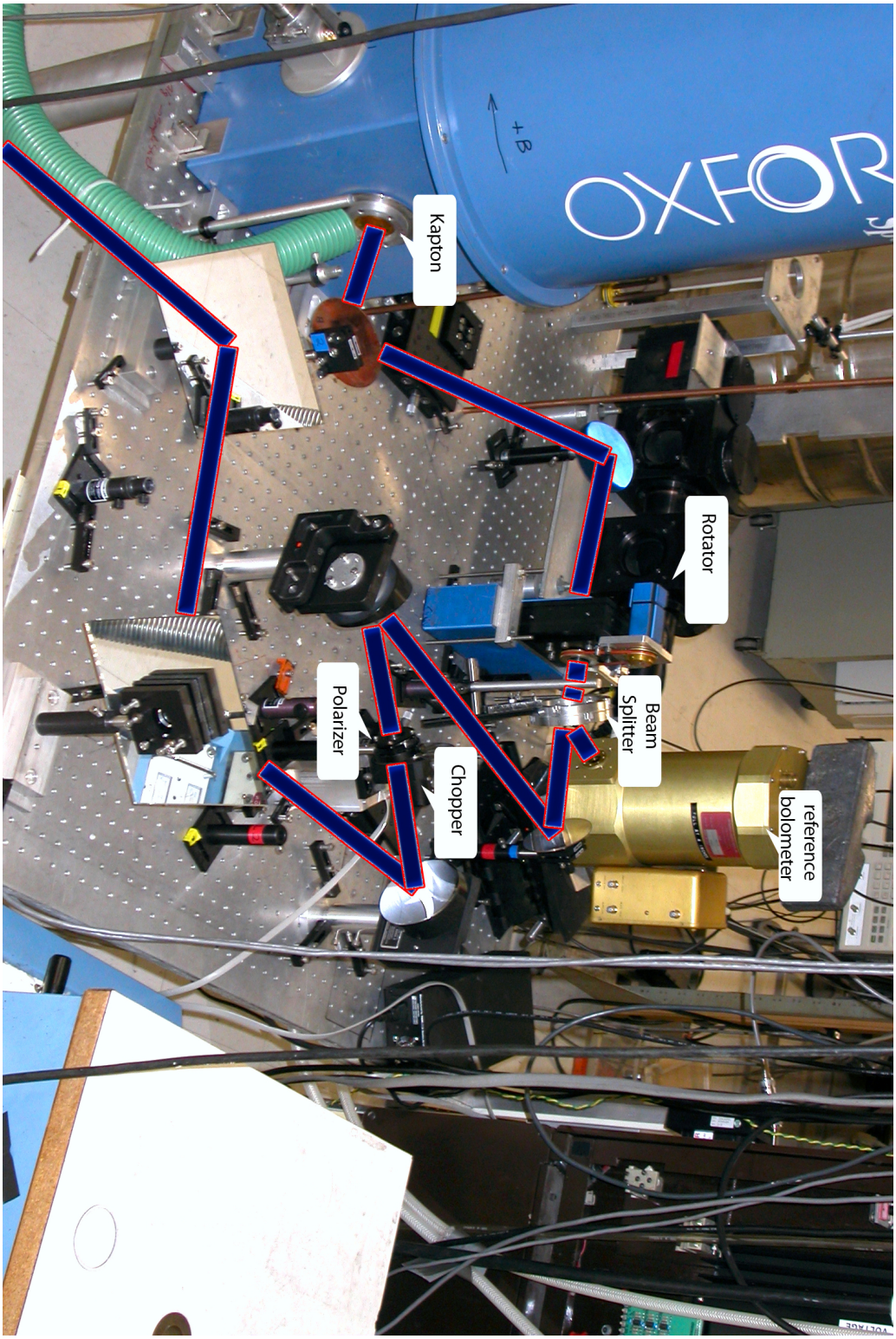

Figure 2.5: Picture of the optics table - from the laser table to the sample

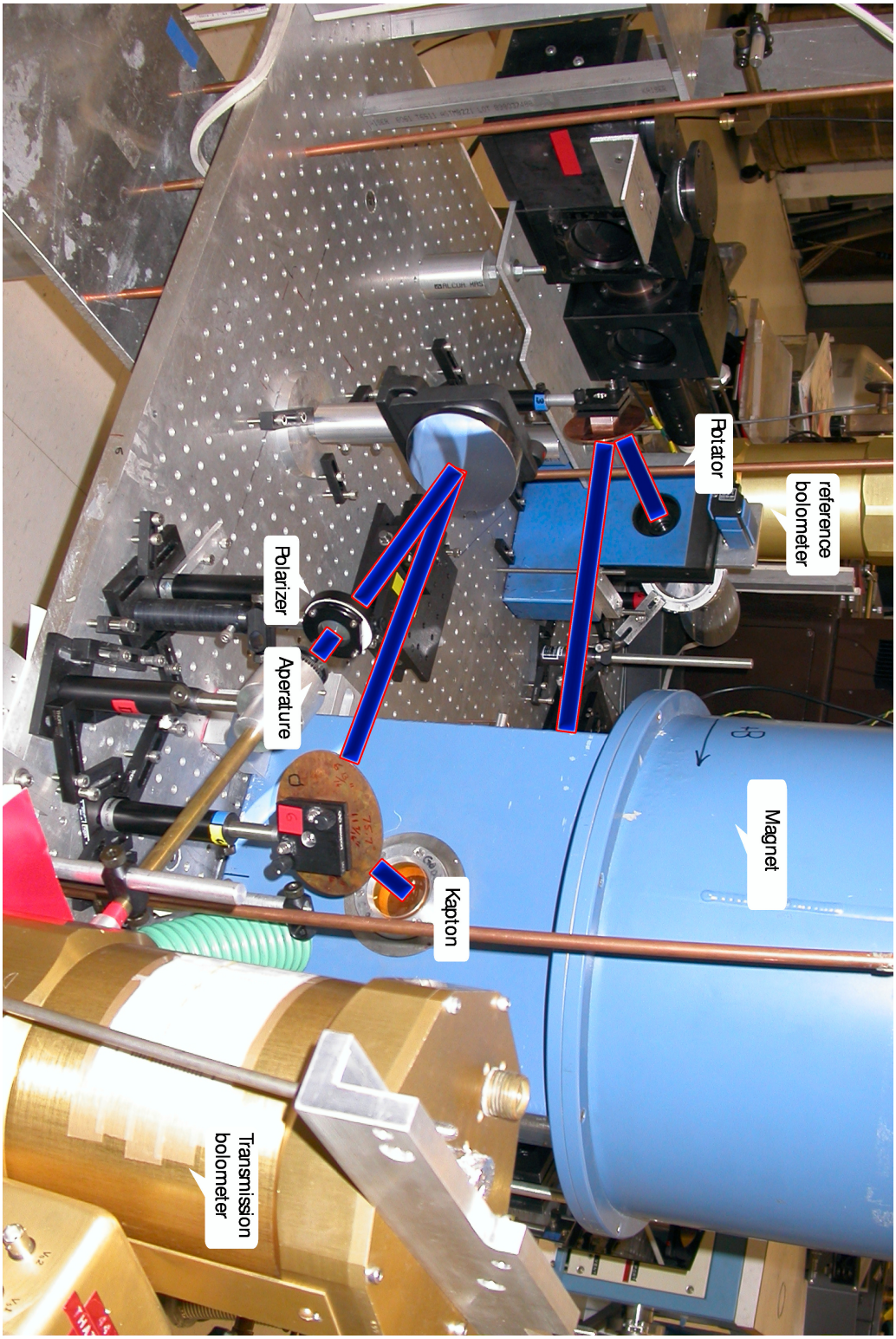

Figure 2.6: Picture of the optics table - from the sample to the bolometer

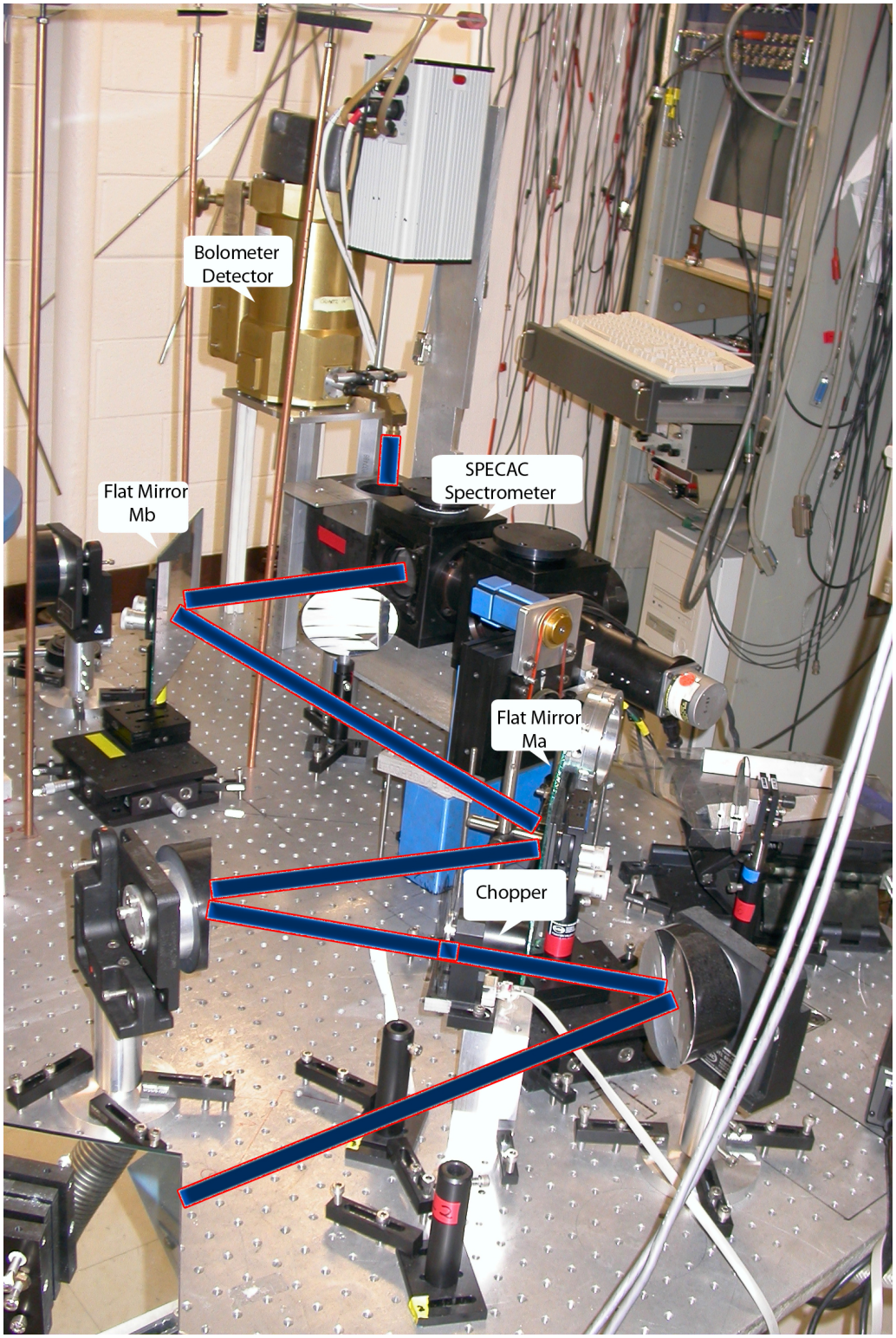

Figure 2.7: Optics table - from the FIR laser, through the SPECAC spectrometer, and into a detector

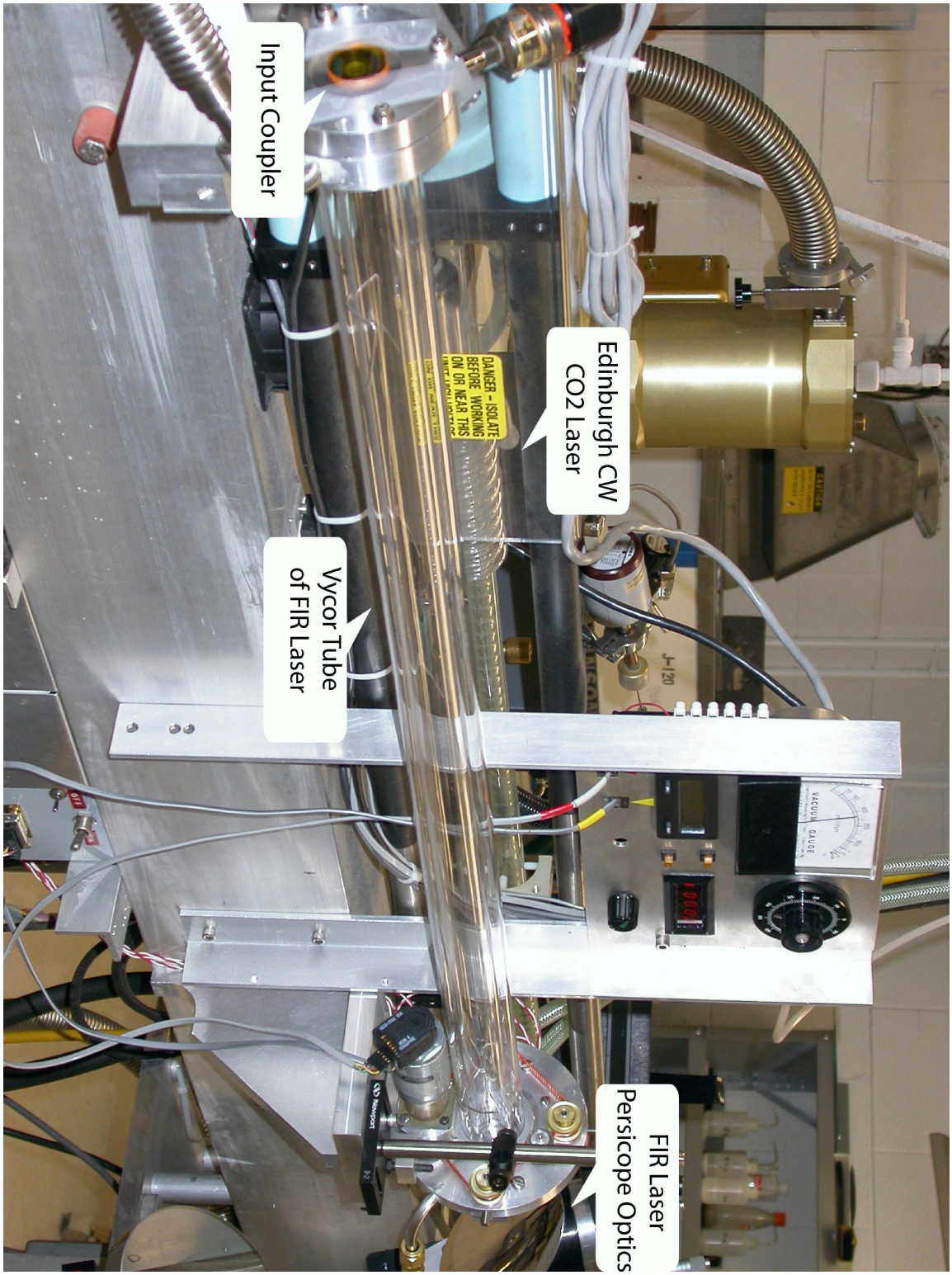

Figure 2.8: CO_2 and FIR laser

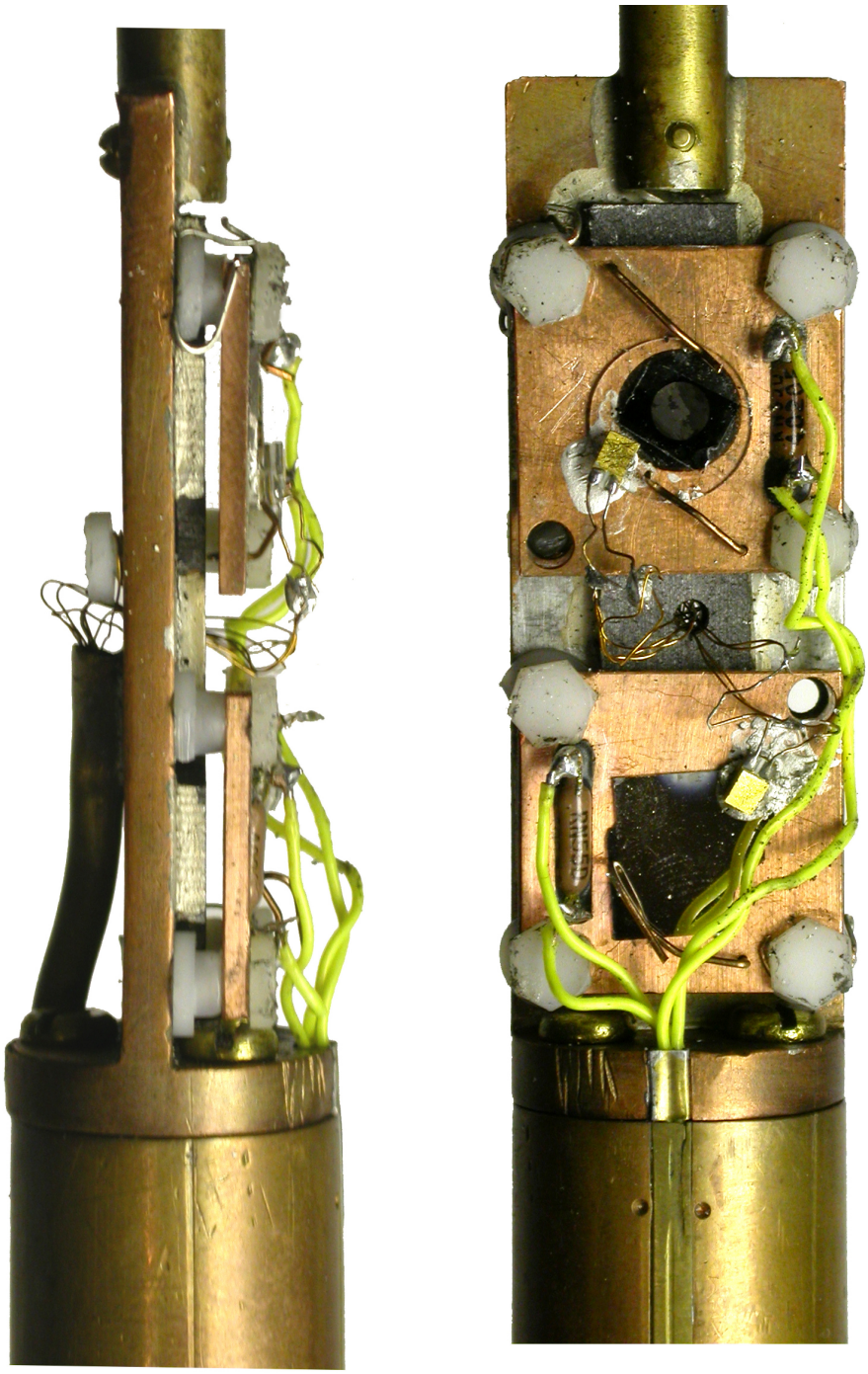

Figure 2.9: Picture of end of sample-stick - top and side view. Total length shown is 2.5 inches. The top sample is peeled single crystal BSCCO on a quartz substrate with an AR- coating,the bottom sample is a NiCr coated GaAs-2DEG with an AR-coating.

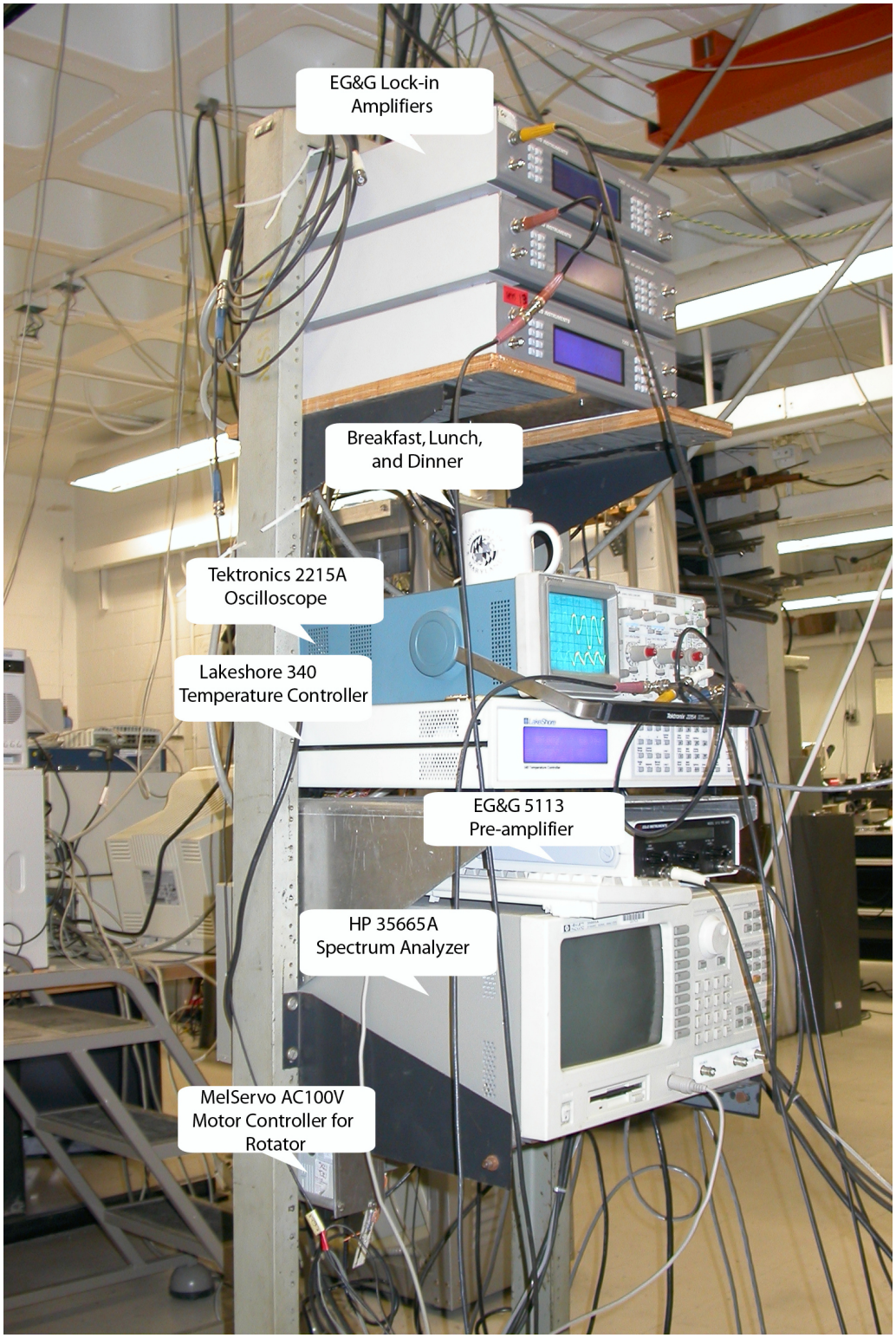

Figure 2.10: Main electronics rack

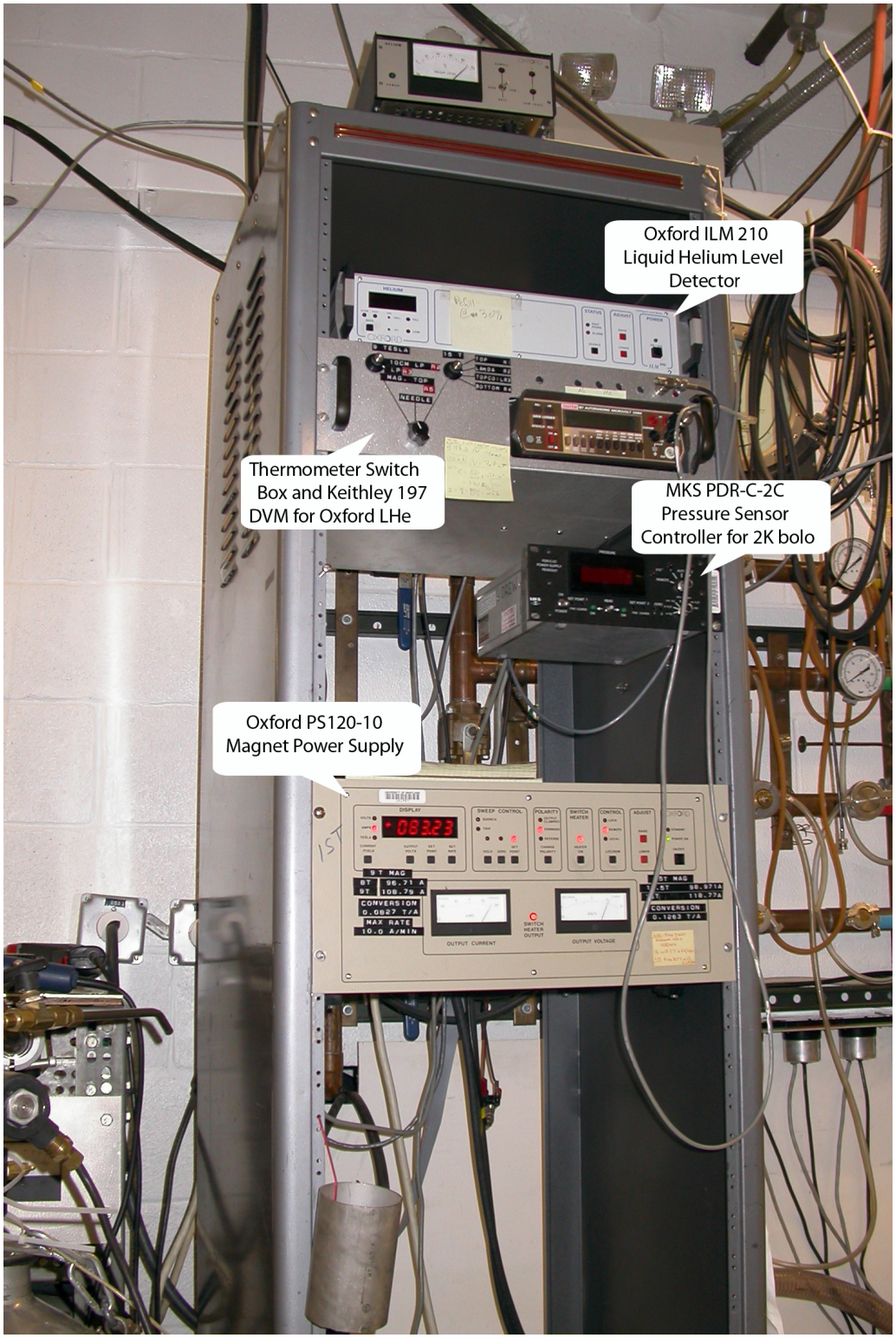

Figure 2.11: Oxford magnet electronics rack

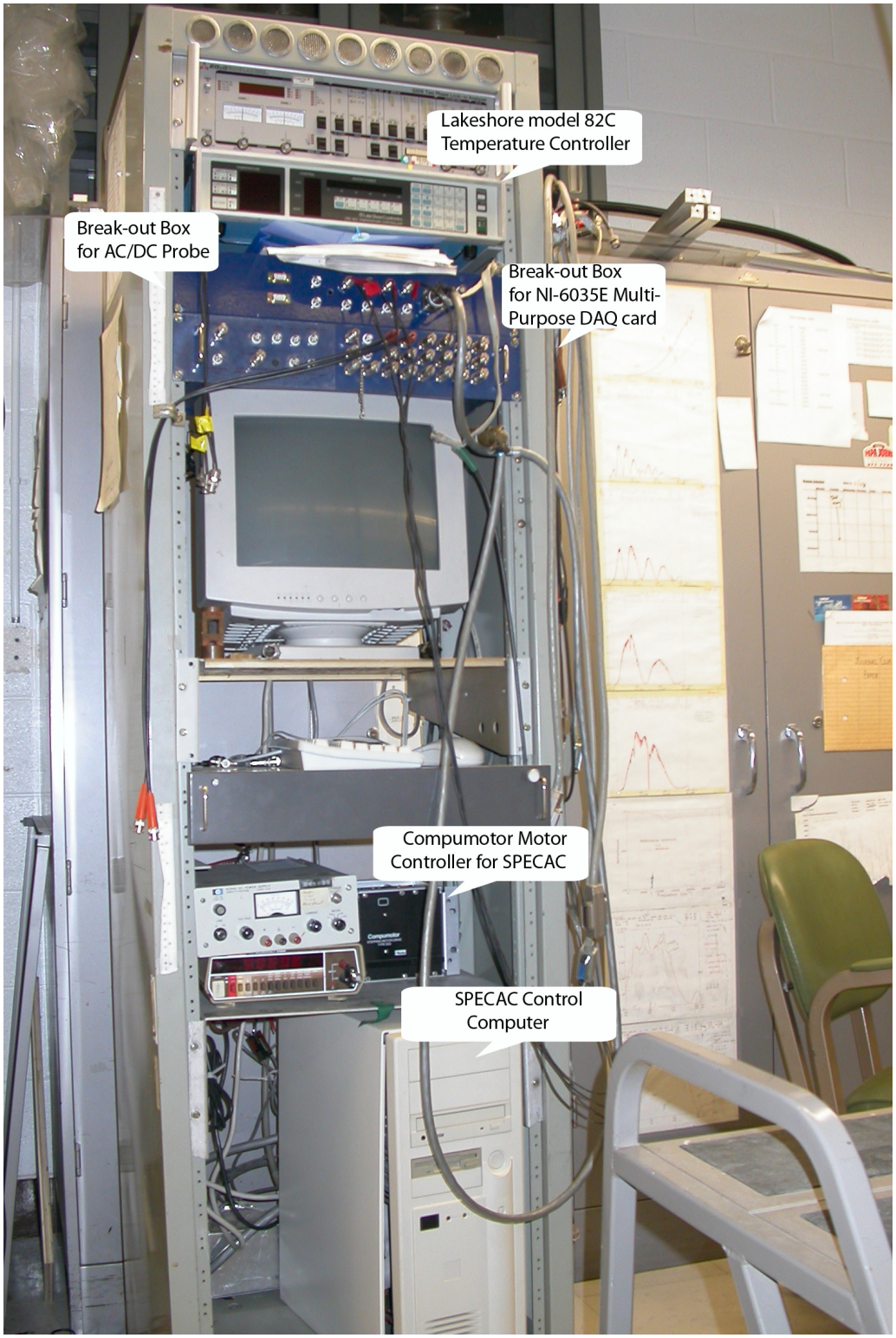

Figure 2.12: SPECAC spectrometer electronics rack

Chapter 3

Mathematical description

3.1 Background mathematical development

The entire optical system can be described as a series of transfer functions which operate on the initial state of an incident electro-magnetic plane wave. For example, an initial electro-magnetic plane wave propagating in the $\hat{z}$-direction can be represented in vector form as $\begin{pmatrix} E_x \\ E_y \end{pmatrix}$. A polarizer oriented along the $\hat{x}$-direction can be represented in matrix form as $\begin{pmatrix} 1 & 0 \\ 0 & 0 \end{pmatrix}$. The final state for an arbitrary plane wave passing through a polarizer is obtained by applying the transfer function to the initial state.

The above operator and state are written in a linear polarization basis. We could have just as easily constructed these operators in a circular polarization basis, $\begin{pmatrix} E_+ \\ E_- \end{pmatrix}$ where $\vec{E}_\pm = E_x e^{i\omega t}\hat{x} \pm iE_y e^{i\omega t}\hat{y}$. To help us efficiently keep track of the transfer functions in the two separate basis, I will invoke bra-ket notation commonly used in

quantum mechanics:[13]

$$\text{Linear Polarization Basis} \quad \langle L|E\rangle = \begin{pmatrix} E_x \\ E_y \end{pmatrix}$$

$$\text{Circular Polarization Basis} \quad \langle C|E\rangle = \begin{pmatrix} E_+ \\ E_- \end{pmatrix}$$

The components of our system may be represented as follows:

$$\text{Polarizer:} \quad \langle L|Pol|L\rangle = \begin{pmatrix} 1 & 0 \\ 0 & 0 \end{pmatrix}$$

$$\text{Waveplate:} \quad \langle L|WP|L\rangle = \begin{pmatrix} e^{i\Delta\beta-\Delta\Gamma} & 0 \\ 0 & 1 \end{pmatrix}$$

$$\text{General Sample:} \quad \langle L|S|L\rangle = \begin{pmatrix} t_{xx} & t_{xy} \\ t_{yx} & t_{yy} \end{pmatrix}$$

$\Delta\beta$ and $\Delta\Gamma$ are the differential phase shift and absorption between linearly polarized light along the ordinary and extra-ordinary optical axis of the waveplate. The waveplates used in this experiment are ideally quarter-waveplates. However, the $\Delta\beta$ and $\Delta\Gamma$ of each waveplate are experimentally determined and are known to deviate from the ideal values, $\Delta\beta = \frac{\pi}{4}$ and $\Delta\Gamma = 0$ (see section 5.2.3 for the waveplate calibration methods).

t_{xx}, t_{xy}, t_{yx}, and t_{yy} are the complex Fresnel transmission coefficients for an arbitrary sample. Most of the measured samples are homogeneous meaning that $t_{xx} = t_{yy}$ and $t_{xy} = -t_{yx}$. In this case, it is convenient to define the following:

$$\text{Homogeneous Sample:} \qquad \langle L|HomoS|L\rangle \quad = \quad \begin{pmatrix} t_{xx} & t_{xy} \\ -t_{xy} & t_{xx} \end{pmatrix} \tag{3.1}$$

For converting between the linear and circular basis, we need the following relations:

$$\langle L|C\rangle = \frac{1}{\sqrt{2}} \begin{pmatrix} i & -i \\ 1 & 1 \end{pmatrix} \tag{3.2}$$

$$\langle C|L\rangle = \frac{1}{\sqrt{2}} \begin{pmatrix} -i & 1 \\ i & 1 \end{pmatrix} \tag{3.3}$$

A linear coordinate system is rotated by an arbitrary angle ϕ clockwise about $\hat{z}$ by the following operator:

$$\langle L|Rotation(\phi)|L\rangle = \begin{pmatrix} \cos(\phi) & \sin(\phi) \\ -\sin(\phi) & \cos(\phi) \end{pmatrix}$$

A rotating quarter-waveplate spinning at an angular frequency ω is represented

by:

$$\langle L|RotWP(\omega)|L\rangle = \langle L|Rotation(-\omega t)|L\rangle\langle L|WP|L\rangle\langle L|Rotation(\omega t)|L\rangle \tag{3.4}$$

3.2 Definition of the Faraday angle

Consider an $\hat{x}$ linearly polarized beam that traverses an optically active medium. In general, the medium will scale and induce a phase shift in the x-component as well as produce a y-component to the field. The general net effect is elliptically polarized light where the ellipse is tilted at some angle with respect to the initial polarization. In this case, the complex Faraday angle is defined as:

$$\tan(\theta_F) \;=\; \frac{E_y}{E_x} \tag{3.5}$$

More generally, the initial polarization is at an arbitrary angle $\tan\theta$ defined by the ratio of the initial $\hat{y}$-component to $\hat{x}$-component of the electric field. The medium will act on this polarization producing a complex angle $\tan\alpha$ defined as the resultant ratio of the $\hat{y}$-component to the $\hat{x}$-component polarization. The complex Faraday angle is defined as the difference between the initial and final angles. Formally, this is written as the following:

$$\langle L|S|L\rangle \begin{pmatrix} \cos\theta \\ \sin\theta \end{pmatrix} = \begin{pmatrix} \cos\theta\, t_{xx} + \sin\theta\, t_{xy} \\ \cos\theta\, t_{yx} + \sin\theta\, t_{yy} \end{pmatrix}$$

$$\text{and } \tan\alpha \equiv \frac{\cos\theta\, t_{yx} + \sin\theta\, t_{yy}}{\cos\theta\, t_{xx} + \sin\theta\, t_{xy}} \equiv \tan(\theta_F + \theta)$$

$$\Rightarrow \tan(\theta_F + \theta) = \frac{\tan\theta_F + \tan\theta}{1 - \tan\theta_F \tan\theta} = \frac{t_{yx} + \tan\theta\, t_{yy}}{t_{xx} + \tan\theta\, t_{xy}}$$

$$\Rightarrow \tan\theta_F = \frac{t_{yx} - t_{xy}\tan^2\theta + t_{yy}\tan\theta - t_{xx}\tan\theta}{t_{xx} + t_{yy}\tan^2\theta + (t_{xy} + t_{yx})\tan\theta} \tag{3.6}$$

Using the condition for a homogeneous samples, $t_{xx} = t_{yy}$ and $t_{yx} = -t_{xy}$, yields:

$$\begin{aligned} \tan\theta_F &= -\frac{t_{xy}}{t_{xx}} \\ &\approx \theta_F \quad \text{for } |t_{xy}| \ll |t_{xx}| \end{aligned} \tag{3.7}$$

3.3 Harmonic analysis of the detector signal

3.3.1 Rotating waveplate system

Referring to figure 2.2, an initial beam from the FIR laser ($|E_0\rangle$) is linearly polarized, modulated by a rotating waveplate, transmitted through the sample, analyzed by a final linear polarizer parallel to the initial polarizer, and the final intensity is measured. The intensity at the detector is given by the following:

$$I_D = \left|\langle L|Pol|L\rangle\langle L|HomoS|L\rangle\langle L|RotWP(\omega)|L\rangle\langle L|Pol|L\rangle\langle L|E_0\rangle\right|^2 \tag{3.8}$$

Performing the above computation results in $\cos(\omega t)$'s and $\sin(\omega t)$'s to the first, second, third, and fourth powers with coefficients that involve the real and imaginary

parts of t_{xx} and t_{xy} and the waveplate parameters $\Delta\beta$ and $\Delta\Gamma$. Using double angle formulae, the various powers of the $\cos(\omega t)$'s and $\sin(\omega t)$'s reduce to $\cos(n\omega t)$'s and $\sin(n\omega t)$'s where n is either 2 or 4, the odd harmonic terms cancelling. The final result of the computation is given by:

$$
\begin{aligned}
&I_D = \\
&\tfrac{e^{-\Gamma}}{4}\Big(\big(|t_{xx}|^2 - |t_{xy}|^2\big)\cos\Delta\beta - \big(3|t_{xx}|^2 - |t_{xy}|^2\big)\cosh\Delta\Gamma\Big) && \text{x} \quad 1 \\
&+\ e^{-\Gamma}\Big(Im(\theta_F)|t_{xx}|^2\sin\Delta\beta + Re(\theta_F)|t_{xx}|^2\sinh\Delta\Gamma\Big) && \text{x} \quad \sin(2\omega t) \\
&-\ e^{-\Gamma}|t_{xx}|^2\sinh\Delta\Gamma && \text{x} \quad \cos(2\omega t) \\
&+\ \tfrac{e^{-\Gamma}}{2}Re(\theta_F)|t_{xx}|^2\big(\cos\Delta\beta - \cosh\Delta\Gamma\big) && \text{x} \quad \sin(4\omega t) \\
&-\ \tfrac{e^{-\Gamma}}{4}\big(|t_{xx}|^2 - |t_{xy}|^2\big)\big(\cos\Delta\beta - \cosh\Delta\Gamma\big) && \text{x} \quad \cos(4\omega t)
\end{aligned}
\tag{3.9}
$$

where $\Delta\Gamma = \Gamma_2$ - Γ_1, $\Gamma = \Gamma_2 + \Gamma_1$, and Γ_1 and Γ_2 are the absorption along the extraordinary and ordinary axis of the waveplate, respectively.

In typical circumstances, t_{xy} is zero in zero magnetic field. Furthermore, $|t_{xy}|^2 \ll |t_{xx}|^2$ for most of our samples even in the maximum applied magnetic field, $\pm$ 8T.

All the waveplates are approximately first order quarter waveplates meaning $\Delta\beta \simeq \pi/4$. The differential absorption between the extraordinary and ordinary axis of the quartz waveplates is very small, especially at lower FIR frequencies below $\sim 100\ cm^{-1}$, so that $\Delta\Gamma \simeq 0$.

Taking various ratios of the in- and out- of phase harmonics given in equation 3.9, we can separately solve for the real and imaginary part of the Faraday angle:

$$\begin{aligned}
Re(\theta_F)_1 &= -\frac{1}{2}\frac{\sin(4\omega t)}{\cos(4\omega t)} \\
Re(\theta_F)_2 &= \frac{1}{2}\frac{\cos\Delta\beta+3\cosh\Delta\Gamma}{\cos\Delta\beta-\cosh\Delta\Gamma}\frac{\sin(4\omega t)}{DC} \\
Im(\theta_F)_1 &= \frac{-Re(\theta_F)\sinh\Delta\Gamma}{\sin\Delta\beta}+\frac{1}{4}\frac{\cos\Delta\beta+3\cosh\Delta\Gamma}{\sin\Delta\beta}\frac{\sin(2\omega t)}{DC} \\
Im(\theta_F)_2 &= \frac{-Re(\theta_F)\sinh\Delta\Gamma}{\sin\Delta\beta}+\frac{1}{4}\frac{\cosh\Delta\Gamma-\cos\Delta\beta}{\sin\Delta\beta}\frac{\sin(2\omega t)}{\cos(4\omega t)}
\end{aligned} \tag{3.10}$$

where DC is the first term in equation 3.8.

It is also interesting to take a couple of other ratios which provide information regarding the performance of the system:

$$\begin{aligned}
Constant_1 &= \frac{\cos(4\omega t)}{DC} = \frac{4\cosh\Delta\Gamma}{\cos\Delta\beta+3\cosh\Delta\Gamma}-1 \\
Constant_2 &= \frac{\cos(2\omega t)}{DC} = \frac{-4\sinh\Delta\Gamma}{\cos\Delta\beta+3\cosh\Delta\Gamma}-1
\end{aligned}$$

3.3.2 Rotating polarizer system

Replacing the rotating waveplate with a rotating polarizer is an alternative method for obtaining the real part of the Faraday angle. The rotating polarizer transfer function is expressed as:

$$\langle L|RotPol(\omega)|L\rangle = \langle L|Rotation(-\omega t)|L\rangle\langle L|Pol|L\rangle\langle L|Rotation(\omega t)|L\rangle \tag{3.11}$$

Proceeding in a similar fashion as in subsection 3.3.1, the intensity at the detector for a rotating polarizer is as follows:

$$I_D = \Big|\langle L|Pol|L\rangle\langle L|HomoS|L\rangle\langle L|Rotpol(\omega)|L\rangle\langle L|Pol|L\rangle\langle L|E_0\rangle\Big|^2$$

The final result is given by:

$$\begin{aligned}
I_D = \quad & \tfrac{1}{8}\big(3|t_{xx}|^2 - |t_{xy}|^2\big) && \text{x} && 1 \\
& + \ \tfrac{1}{2}|t_{xx}|^2 Re(\theta_F) && \text{x} && \sin(2\omega t) \\
& + \ \tfrac{1}{2}|t_{xx}|^2 && \text{x} && \cos(2\omega t) \\
& + \ \tfrac{1}{4}|t_{xx}|^2 Re(\theta_F) && \text{x} && \sin(4\omega t) \\
& + \ \tfrac{1}{8}|t_{xx}|^2 && \text{x} && \cos(4\omega t)
\end{aligned}$$

Taking the ratio of the in- and out- of phase harmonics, we obtain:

$$\begin{aligned}
Re\,(\theta_F)_1 &= \tan(2\omega t) \\
Re\,(\theta_F)_2 &= 2\ \tan(4\omega t)
\end{aligned}$$

3.4 Analysis of various ideal samples

3.4.1 Polarizer as a sample

Within our formalism developed in section 3.3.1, the result of a polarizer in place of the sample at an angle α with respect to the initial polarizer gives the following relation:

$$\langle L|SamplePolarizer(\alpha)|L\rangle = \langle L|Rotation(-\alpha)|L\rangle\langle L|Pol|L\rangle\langle L|Rotation(\alpha)|L\rangle \tag{3.12}$$

The resulting signal at the detector is given by:

$$\begin{aligned}
I_D = & \\
& \tfrac{e^{-\Gamma_{Sum}}}{4}\cos(2\alpha)(\cos\Delta\beta + (2+\cos(2\alpha))\cosh\Delta\Gamma) && \text{x} && 1 \\
+ \ & \tfrac{e^{-\Gamma}}{2}\sin(2\alpha)\sinh\Delta\Gamma && \text{x} && \sin(2\omega t) \\
- \ & \tfrac{e^{-\Gamma}}{2}\cos(2\alpha)\sinh\Delta\Gamma && \text{x} && \cos(2\omega t) \\
+ \ & \tfrac{e^{-\Gamma}}{4}(\cos\Delta\beta - \cosh\Delta\Gamma)\sin(2\alpha) && \text{x} && \sin(4\omega t) \\
- \ & \tfrac{e^{-\Gamma}}{4}(\cos\Delta\beta - \cosh\Delta\Gamma)\cos(2\alpha) && \text{x} && \cos(4\omega t)
\end{aligned} \tag{3.13}$$

The relevant ratio is the out-of phase 4th harmonic to the in-phase 4th harmonic:

$$\tan(4\omega t) = \sin(4\omega t)\text{ coefficient}/\cos(4\omega t)\text{ coefficient} = -\tan(2\alpha) \tag{3.14}$$

3.4.2 Waveplate as a sample

Both the real and imaginary part of the Faraday angle can be tested by inserting a waveplate (with parameters $\Delta\beta'$ and $\Delta\Gamma'$) in place of the sample. This produces a transfer matrix:

$$\begin{aligned}
&\langle L|SampleWP(\alpha)|L\rangle = \langle L|Rotation(-\alpha)|L\rangle\langle L|WP|L\rangle\langle L|Rotation(\alpha)|L\rangle \\
&= \begin{pmatrix} e^{i\Delta\beta'-\Delta\Gamma'}\cos^2(2\pi\alpha)+\sin^2(2\pi\alpha) & (e^{i\Delta\beta'-\Delta\Gamma'}-1)\cos(2\pi\alpha)\sin(2\pi\alpha) \\ (e^{i\Delta\beta'-\Delta\Gamma'}-1)\cos(2\pi\alpha)\sin(2\pi\alpha) & e^{i\Delta\beta'-\Delta\Gamma'}\sin^2(2\pi\alpha)+\cos^2(2\pi\alpha) \end{pmatrix} \\
&\equiv e^{i\Delta\beta'/2}\begin{pmatrix} t'_{xx} & t'_{xy} \\ t'_{xy} & t^*_{xx}{}' \end{pmatrix}
\end{aligned} \tag{3.15}$$

where α is the angle between the incident polarization and the ordinary axis of the waveplate.

Note that $t_{xy} = t_{yx}$, and if $\Delta\Gamma \approx 0$ and we factor out the term $e^{(i\Delta\beta')/2}$, then $t_{xx} = t^*_{yy}$. Inserting these relations into equation 3.6 and substituting the results of equation 3.7, we obtain the following relation:

$$\tan\theta'_F = \frac{-\theta_F(1-\tan^2\theta) - \frac{t_{xx}-t^*_{xx}}{t_{xx}}\tan\theta}{\frac{t_{xx}+t^*_{xx}\tan^2\theta}{t_{xx}} - 2\tan\theta_F\tan\theta} \tag{3.16}$$

If we rotate our basis such that the initial polarization is at $\theta = 0$, then

$$\tan\theta'_F = -\tan\theta_F = \frac{t_{xy}}{t_{xx}} \tag{3.17}$$

In the usual manor, the detector signal is calculated:

$$I_D = \Big|\langle L|Pol|L\rangle\langle L|SampleWP(\alpha)|L\rangle\langle L|RotWP(\omega)|L\rangle\langle L|Pol|L\rangle\langle L|E_0\rangle\Big|^2 \quad (3.18)$$

$$\begin{aligned}
&I_D = \\
&\tfrac{e^{-\Gamma}}{4}\Big(\big(|t_{xx}|^2 - |t_{xy}|^2\big)\cos\Delta\beta - \big(3|t_{xx}|^2 - |t_{xy}|^2\big)\cosh\Delta\Gamma\Big) && \text{x} \quad 1 \\
&- e^{-\Gamma}\Big(Im(\theta_F)|t_{xx}|^2\sin\Delta\beta + Re(\theta_F)|t_{xx}|^2\sinh\Delta\Gamma\Big) && \text{x} \quad \sin(2\omega t) \\
&- e^{-\Gamma}|t_{xx}|^2\sinh\Delta\Gamma) && \text{x} \quad \cos(2\omega t) \\
&- \tfrac{e^{-\Gamma}}{2}Re(\theta_F)|t_{xx}|^2\big(\cos\Delta\beta - \cosh\Delta\Gamma\big) && \text{x} \quad \sin(4\omega t) \\
&- \tfrac{e^{-\Gamma}}{4}\big(|t_{xx}|^2 - |t_{xy}|^2\big)\big(\cos\Delta\beta - \cosh\Delta\Gamma\big) && \text{x} \quad \cos(4\omega t)
\end{aligned}$$

Taking ratios of the coefficients of the separate harmonics results in the following:

$$\begin{aligned}
Re(\theta_F)_1 &= -\tfrac{1}{2}\,(1 - \tfrac{|t_{xy}|^2}{|t_{xx}|^2})\,\tfrac{\sin(4\omega t)}{\cos(4\omega t)}) \\
Re(\theta_F)_2 &= \tfrac{1}{2}\,(1 - \tfrac{|t_{xy}|^2}{|t_{xx}|^2} - \tfrac{\cosh(\Delta\Gamma)}{\cos(\Delta\beta)-\cosh\Delta\Gamma})\,\tfrac{\sin(4\omega t)}{DC}) \\
Im(\theta_F)_1 &= -\tfrac{Re(\theta_F)\sinh\Delta\Gamma}{\sin\Delta\beta} + \tfrac{1}{4}\Big(1 - \tfrac{|t_{xy}|^2}{|t_{xx}|^2})\tfrac{\cos\Delta\beta+3\cosh\Delta\Gamma}{\sin\Delta\beta}\,\tfrac{\sin(2\omega t)}{DC}\Big) \\
Im(\theta_F)_2 &= -\tfrac{Re(\theta_F)\sinh\Delta\Gamma}{\sin\Delta\beta} + \tfrac{1}{4}\Big(1 - \tfrac{|t_{xy}|^2}{|t_{xx}|^2})\tfrac{\cosh\Delta\Gamma-\cos\Delta\beta}{\sin\Delta\beta}\,\tfrac{\sin(2\omega t)}{\cos(4\omega t)}\Big)
\end{aligned} \quad (3.19)$$

From equation 3.15, the ratio of $|t_{xx}|^2$ and $|t_{xy}|^2$ is calculated:

$$\frac{|t_{xy}|^2}{|t_{xx}|^2} = \frac{4\sin^2(2\alpha)\sin^2(\frac{1}{2}\Delta\beta')}{3+\cos(4\alpha)+2\cos(\Delta\beta')\sin^2(2\alpha)} \tag{3.20}$$

3.5 Error analysis formalism

Imperfect optical components will result in deviations from the theoretically calculated Faraday angle in the previous section. In particular, any inhomogeneity in the waveplate including dust, scratches, wobble about the ideal rotation axis, etc., will introduce errors in our ideal waveplate matrix (see equation 3.4). *In situ* calibration of the waveplate measures the effective diagonal components directly. However, any off-diagonal error components are ignored in the analysis leading to equation 3.10.

Also of interest are errors introduced by arbitrary scattering that occurs between the sample and the waveplate. This may be caused by scratches or dust on the sample, mirrors, or kapton window.

3.5.1 Imperfect waveplate

Arbitrary errors introduced by an imperfect waveplate may be generally represented as the following:

$$\langle L|\epsilon WP|L\rangle \equiv \begin{pmatrix} \epsilon_{xx}e^{i\Delta\beta+\Delta\Gamma} & \epsilon_{xy} \\ \epsilon_{yx} & \epsilon_{yy} \end{pmatrix}$$

which can be rewritten as:

$$\epsilon' \begin{pmatrix} e^{i\Delta\beta'+\Delta\Gamma'} & \epsilon_{xy}e^{i\phi_{xy}} \\ \epsilon_{yx}e^{i\phi_{yx}} & 1 \end{pmatrix} \tag{3.21}$$

where ϵ_{yx}, ϵ_{xy}, ϕ_{xy}, and ϕ_{yx} are purely real.

The matrix now has the same form as the original waveplate matrix with an effective $\Delta\beta'$ and $\Delta\Gamma'$ on the diagonal, and additional complex off-diagonal components.

Calculating the intensity at the detector yields the following:

$$I_D = |\epsilon'|^2 \Big| \langle L|Pol|L\rangle \langle L|HomoS|L\rangle \langle L|\epsilon RotWP(\omega)|L\rangle \langle L|Pol|L\rangle \langle L|E_0\rangle \Big|^2 \tag{3.22}$$

The pre-factor, $|\epsilon'|^2$, scales the entire intensity at the detector. Since only the ratios of the harmonics are of interest, we can ignore any overall scaling of the signal.

Performing an immense amount of algebra, ignoring the dc term, dropping the primes on $\Delta\beta'$ and $\Delta\Gamma'$, and keeping only leading terms in ϵ and ϕ give the following:

$I_D =$

$$e^{-\Gamma_{Sum}}|t_{xx}|^2\Big(C1 + Im(\theta_F)\sin\Delta\beta + Re(\theta_F)\sinh\Delta\Gamma\Big) \quad \text{x} \quad \sin(2\omega t)$$

$$- e^{-\Gamma_{Sum}}|t_{xx}|^2(f(B) + Re(\theta_F)\sinh\Delta\Gamma) \quad \text{x} \quad \cos(2\omega t)$$

$$+ e^{-\Gamma_{Sum}}|t_{xx}|^2(C2 + \tfrac{1}{2}Re(\theta_F)\big(\cos\Delta\beta - \cosh\Delta\Gamma\big) \quad \text{x} \quad \sin(4\omega t)$$

$$- \tfrac{e^{-\Gamma_{Sum}}}{4}|t_{xx}|^2(\cos\Delta\beta - \cosh\Delta\Gamma + C3\ Re(\theta_F)) \quad \text{x} \quad \cos(4\omega t)$$

where

$$\text{C1} = \tfrac{1}{2}(\epsilon_{xy} + \epsilon_{yx})(e^{\Delta\Gamma} - \cos\Delta\beta)$$

$$\text{C2} = \tfrac{1}{4}(\epsilon_{xy} + \epsilon_{yx})(\cosh\Delta\Gamma + \sinh\Delta\Gamma - \cos\Delta\beta)$$

$$\text{C3} = -2(\epsilon_{xy} + \epsilon_{yx})(\cos\Delta\beta - \cosh\Delta\Gamma) + 2(\epsilon_{xy} + \epsilon_{yx}\sinh\Delta\Gamma)$$

$$\text{f(B)} = Re(\theta_F)(e^{\Delta\Gamma}\epsilon_{xy} + \epsilon_{yx}\cos\Delta\beta) + Im(\theta_F)\epsilon_{yx}\sin(\Delta\beta)$$

(3.23)

Changing notation in which the in-phase components are represented by 'x' and the out-of-phase components by 'y', and subscripts represent the harmonic number

gives:

$$\begin{aligned} y_2' &= y_2 + C1 \\ x_2' &= x_2 + f(B) \\ y_4' &= y_4 + C2 \\ x_4' &= x_4 + \frac{1}{4} Re(\theta) C3 \end{aligned} \tag{3.24}$$

The primes denote the measured signal, and the unprimed variables (x and y) denote the ideal signals found in section 3.3.1.

3.5.2 Arbitrary scattering error matrix

A general error matrix is inserted between the rotating waveplate and the sample of the form:

$$\langle L|\epsilon|L\rangle \equiv \begin{pmatrix} \epsilon_{xx} & \epsilon_{xy} \\ \epsilon_{yx} & \epsilon_{yy} \end{pmatrix} \tag{3.25}$$

which can be rewritten as:

$$= \epsilon' \begin{pmatrix} \epsilon_{xx} & \epsilon_{xy} \\ \epsilon_{yx} & 1 \end{pmatrix} \tag{3.26}$$

In general, the elements are complex. We will consider the ϵ - elements to be either all purely real or all purely imaginary. When the detector intensity is calculated, the matrix being either purely real or purely imaginary give exactly the same results if we make the transformation $\epsilon \rightarrow i\epsilon$ for all elements.

$$
\begin{aligned}
&I_D = \\
&e^{-\Gamma}|t_{xx}|^2\Big(K1 + (1-\epsilon_{xx})(Im(\theta_F)\sin\Delta\beta + Re(\theta_F)\sinh\Delta\Gamma)\Big) \quad \text{x} \quad \sin(2\omega t) \\
&+\ e^{-\Gamma}|t_{xx}|^2(\sinh\Delta\Gamma - G1(B)) \quad \text{x} \quad \cos(2\omega t) \\
&+\ e^{-\Gamma}|t_{xx}|^2(K2 + \tfrac{1}{2}Re(\theta_F)(\epsilon_{xx}-1)\big(\cos\Delta\beta - \cosh\Delta\Gamma)\big) \quad \text{x} \quad \sin(4\omega t) \\
&+\ e^{-\Gamma}|t_{xx}|^2(\cosh\Delta\Gamma - \cos\Delta\beta - G2(B)) \quad \text{x} \quad \cos(4\omega t)
\end{aligned}
$$

where

$$
\begin{aligned}
&\text{K1} = \epsilon_{xy}\sinh\Delta\Gamma \\
&\text{G1(B)} = (2\epsilon_{xx}-1)\sinh\Delta\Gamma \\
&\text{K2} = -\tfrac{1}{2}\epsilon_{xy}(\cos\Delta\beta - \cosh\Delta\Gamma) \\
&\text{G2(B)} = 2\big(Re(\theta_F)(\epsilon_{xy}-\epsilon_{yx}) - \epsilon_{xx}\big)(\cosh\Delta\Gamma - \cos\Delta\beta)
\end{aligned}
\tag{3.27}
$$

Converting to the same notation as in the previous subsection yields:

$$
\begin{aligned}
y_2' &= (1-\epsilon_{xx})y_2 + K1 \\
x_2' &= x_2 - G1(B) \\
y_4' &= y_4(1-\epsilon_{xx}) + K2 \\
x_4' &= x_4 - G2(B)
\end{aligned}
\tag{3.28}
$$

3.6 Drude model of the Hall angle

The form of the Faraday angle can be derived in the context of a simple Drude model.[33] The 2-dimensional conductivity tensor is required.

An electron in a static magnetic field and a driving electric force will, in general, obey the following classical force equation:

$$q\vec{E} + \frac{q}{c}\vec{v} \times \vec{B} - \frac{m}{\tau}\vec{v} = m\frac{d\vec{v}}{dt}$$

where $\vec{E}$ is the electric field, q is the charge of an electron,

and m is the mass of an electron

The damping force term involving $1/\tau$ is a result of the relaxation time approximation.[33]

Assuming that the applied magnetic field, $\vec{B}$, is directed along the $\hat{z}$ direction, and that $\vec{E}$ and $\vec{v}$ are in the x-y plane, we can solve the above equation assuming that all time dependent quantities behave as $\sim e^{-i\omega t}$:

$$\begin{aligned} qE_x - \frac{q}{c}v_y B - \frac{m}{\tau}v_x &= -i\omega m v_x \\ qE_y - \frac{q}{c}v_x B - \frac{m}{\tau}v_y &= -i\omega m v_y \end{aligned} \tag{3.29}$$

Since

$$\vec{J} = \ nq\vec{v} = \tilde{\sigma}\vec{E}$$

where $\vec{J}$ is the current density, n is the charge density

and $\tilde{\sigma}$ is the conductivity matrix

$$\Rightarrow \vec{E} = \tilde{\sigma}^{-1} nq\vec{v}$$

Solving equation 3.29 yields:

$$\begin{pmatrix} E_x \\ E_y \end{pmatrix} = nq \underbrace{\left[\frac{m}{nq^2} \begin{pmatrix} \frac{1}{\tau} - i\omega & -\omega_c \\ \omega_c & \frac{1}{\tau} - i\omega \end{pmatrix} \right]}_{\tilde{\sigma}^{-1}} \begin{pmatrix} v_x \\ v_y \end{pmatrix} \text{ where } \quad \omega_c = \frac{q\ B}{m\ c}$$

Inverting $\tilde{\sigma}^{-1}$ yields the conductivity tensor:

$$\sigma_{xx} = \sigma_{yy} = \frac{nq^2}{m} \frac{\gamma - i\omega}{(\gamma - i\omega)^2 - \omega_c^2} \tag{3.30}$$

$$\sigma_{xy} = -\sigma_{yx} = -\frac{nq^2}{m} \frac{\omega_c}{(\gamma - i\omega)^2 - \omega_c^2} \tag{3.31}$$

where $\gamma = 1/\tau$

The conductivity tensor is currently represented in the linear polarization basis. Using the formalism developed earlier in the chapter, we convert the above expression

to the circular basis via the following transformation:

$$\begin{aligned}\langle C|\sigma|C\rangle &= \langle C|L\rangle\langle L|\sigma|L\rangle\langle L|C\rangle \\ &= \begin{pmatrix} \frac{nq^2}{m}\frac{1}{\gamma - i(\omega-\omega_c)} & 0 \\ 0 & \frac{nq^2}{m}\frac{1}{\gamma - i(\omega+\omega_c)} \end{pmatrix} \\ &\equiv \begin{pmatrix} \sigma_+ & 0 \\ 0 & \sigma_- \end{pmatrix}\end{aligned} \tag{3.32}$$

The complex Fresnel transmission coefficient for a plane wave at normal incidence (appendix F) from air through a thin film ($\lambda \gg$ film thickness) on a substrate can be written in the circular polarization basis as:

$$t_\pm = \frac{\frac{2n_0}{1+n_0}}{1 + Z\sigma_\pm d}$$

where

$$Z = \frac{Z_0}{n_0 + 1} \tag{3.33}$$

$Z_0 = 377\ \Omega/\square$, the impedance of free space

$d =$ thickness of the film

Converting to the linear basis gives the following relations:

$$\begin{aligned}
\sigma_\pm = \sigma_{xx} \pm i\ \sigma_{xy} \quad &\rightarrow \qquad \sigma_{xx} = \tfrac{1}{2}(\sigma_+ + \sigma_-) \\
&\qquad\quad \sigma_{xy} = -i\ \tfrac{1}{2}(\sigma_+ - \sigma_-) \\
t_\pm = t_{xx} \pm i\ t_{xy} \quad &\rightarrow \qquad t_{xx} = \tfrac{1}{2}(t_+ + t_-) \\
&\qquad\quad t_{xy} = -i\ \tfrac{1}{2}(t_+ - t_-)
\end{aligned} \tag{3.34}$$

Combining equations 3.32, 3.33, and 3.34 gives:

$$\begin{aligned}
\tan\theta_F = -\frac{t_{xy}}{t_{xx}} &= \frac{\kappa\omega_c}{\kappa(\gamma - i\ \omega) + ((\gamma - i\ \omega)^2 + \omega_c^2)} \\
\text{where} \quad \kappa &= \frac{nq^2}{m} Z
\end{aligned} \tag{3.35}$$

Taking the real and imaginary parts give:

$$\begin{aligned}
Re(\tan\theta_F) &= \frac{\kappa\ \omega_c\ (\gamma(\kappa+\gamma) - (\omega^2 - \omega_c^2))}{(\gamma(\kappa+\gamma) - (\omega^2 - \omega_c^2))^2 + (\omega\ (2\gamma+\kappa))^2} \\
Im(\tan\theta_F) &= \frac{\kappa\ \omega_c\ \omega\ (2\gamma+\kappa)}{(\gamma(\kappa+\gamma) - (\omega^2 - \omega_c^2))^2 + (\omega\ (2\gamma+\kappa))^2}
\end{aligned} \tag{3.36}$$

$$\begin{aligned}
\text{where} \quad \kappa &= \frac{nq^2}{m} Z' \\
\omega_c &= \frac{q\ B}{m\ c} \\
Z' &= d\ Z_0/(n_0+1), \qquad Z_0 = 377\ \Omega/\square \\
n_0 &= \text{index of substrate} \\
d &= \text{film thickness}
\end{aligned}$$

Two-dimensional electron gas heterostructures are usually characterized in terms

of the electron mobility and electron density. The mobility can be defined as:

$$\mu \equiv \frac{q}{m}\frac{1}{\gamma} \tag{3.37}$$

Inverting equation 3.37 and substituting γ into equation 3.36 gives the Faraday angle in terms of mobility.

3.7 Converting the Faraday angle to the Hall angle

The Hall angle is defined as:

$$\tan\theta_H \equiv \frac{\sigma_{xy}}{\sigma_{xx}} \tag{3.38}$$

It is possible to derive the complex Hall angle in terms of the complex Faraday angle assuming a homogenous film in the thin-film limit. Converting equation 3.7 to the circular basis and substituting the Fresnel transmission coefficients in the thin-film limit (3.33) gives:

$$\begin{aligned}\tan\theta_F &= i\ \frac{t_+ - t_-}{t_+ + t_-} \\ &= i\ Z'\ \frac{\sigma_- - \sigma_+}{2 + Z'(\sigma_+ + \sigma_-)}\end{aligned}$$

Converting back to the linear polarization basis (equation 3.34) and simplifying

gives:

$$\begin{aligned}\tan\theta_F &= Z' \frac{\sigma_{xy}}{1 + Z'\sigma_{xx}} \\ &= \frac{1}{(Z'\sigma_{xx}d)^{-1} + 1} \frac{\sigma_{xy}}{\sigma_{xx}}\end{aligned}$$

Substituting the definition of the Hall angle (equation 3.38) and rearranging yields the desired result:

$$\tan\theta_H = \left(\frac{n_0 + 1}{Z_0\ \sigma_{xx}\ d} + 1\right) \tan\theta_F \tag{3.39}$$

3.8 Vortex dynamics

3.8.1 Gittleman and Rosenblum, T. C. Hsu models

The behaviors of vortices in superconductors is complex. Many models have been constructed in an attempt to understand vortex dynamics. Here, I briefly review three models.

Gittleman and Rosenblum[34] used a simple phenomenological model to describe their microwave measurements of conventional superconductors. In their model, the

equation of motion for a single vortex is written as:

$$M\dot{\vec{v_L}} + \eta\vec{v_L} + \kappa\vec{r_L} = \vec{J_s} \times \vec{\phi_0}$$

where $\vec{v_L}$ is the core velocity

η is the viscous drag coefficient

κ characterizes the harmonic pinning strength

$\vec{J_s}$ is the superfluid current

$\vec{\phi_0}$ is h/2e, a flux quantum in the applied magnetic field direction

A moving vortex containing a magnetic flux quanta generates an (Josephson) electric field perpendicular to its velocity. Dissipation is generated by current flowing through the normal-state core. The resulting equation describing the velocity of the superfluid flow is:

$$m\dot{\vec{v_s}} = q(\vec{E} + \vec{B} \times \vec{v_L})$$

where $\vec{E}$ ($\vec{B}$) is the applied electric (magnetic) field.

Using the relations $\vec{J_s} = n_s q\vec{v_s}$ and $\vec{J_s} = \tilde{\sigma} \cdot \vec{E}$ and solving for the conductivity tensor yields:

$$\begin{aligned} \sigma_{xx} = \sigma_{xy} &= \frac{nq^2/m}{i\omega} \frac{i\omega + \omega_0}{i\omega + \omega_0(1 + nq^2 B\phi_0/m)} \\ \sigma_{xy} = \sigma_{yx} &= 0 \end{aligned} \tag{3.40}$$

This model, although it does well at describing the microwave data with a narrow absorption band centered at zero frequency, does not give rise to a Hall effect.

In superfluid He3 systems, a Magnus force (lift force) results from a vortex moving through a fluid. The Bernoulli equation for laminar flow relates the pressure difference on opposing sides of a vortex with the difference in the relative velocities of the superfluid (the vector sum of the superfluid current and the current associated with the vortex). The direction of the force is perpendicular to the vortex core velocity.

T. C. Hsu,[26] using the Bogoliubov-DeGennes equations, proposed a model that incorporates the quantized quasi-particle excitations within the core. The relaxation of these excitations are dissipative. The resulting equation of motion of a vortex incorporates a Magnus-like force and is given by:

$$\begin{aligned} &\dot{\vec{v_L}}+(1/\tau_v)\vec{v_L}+\alpha^2\vec{r_L}=\dot{\vec{v_s}}-\Omega(\vec{v_L}-\vec{v_s})\times\hat{z} \\ &\text{where } \Omega=(1-\Phi)=1-\omega_c/\Omega_0 \\ &\Omega_0 \text{ is the core energy level spacing} \\ &\omega_c \text{ is the cyclotron resonance for free electrons} \\ &\Rightarrow \sigma_\pm=\frac{nq^2}{im\omega}\frac{\omega(\omega\mp\Omega)-(1-\Phi)(\alpha^2+i\omega/\tau_v)}{(\omega\pm\omega_c)(\omega\mp\Omega)-(\alpha^2+i\omega/\tau)} \end{aligned} \tag{3.41}$$

This model agrees with FIR YBCO ac- Hall data above $\sim 30\ cm^{-1}$. However, it appears to strongly deviate from lower frequency measurements.[24] The model essentially neglects the low frequency Gittleman-Rosenblum depinning resonance (of width $\omega_0=\eta/\kappa$) in the conductivity which is prevalent in measurements.

3.8.2 Drew, Lihn, and Wu phenomenological model

Previous experiments[22–25] have probed the FIR low temperature magneto-optical response of superconducting YBCO thin films. Shanlu Wu and Steve Lihn found

that the transmission spectrum at low temperature (< 20 K) was phenomenologically well described by a magneto-conductivity that is composed of a sum of Lorentzian oscillators:

$$\sigma_{\pm} = \frac{nq^2}{m^*}\Big[\Big(\frac{f_s}{i\omega} + \frac{f_0}{i(\omega \pm \omega_0) + \Gamma_0} + \frac{f_p}{i(\omega \pm \omega_p) + \Gamma_p}\Big)(1 - fn) + \frac{f_n}{i(\omega \pm \omega_c) + \Gamma_q}\Big] \tag{3.42}$$

where f_n is the nodal quasi-particle fraction and ω_c is the cyclotron resonance.

The last term represents the nodal quasi-particle excitations expected in a d-wave superconductor. Since the number of charge carriers are conserved, the oscillator strengths are assumed to obey $f_s + f_0 + f_p = 1$.

Wu *et al* fit their magneto-transmission data using f_s, f_p, f_0, Γ_0, Γ_P, ω_0, and ω_p as parameters. Below 20 K, the vortex parameters are assumed temperature independent. The best fit parameters reveal an electron-like low frequency oscillator at $\lesssim -3\ cm^{-1}$ of width 10 cm^{-1} with a weight of 0.14, a hole-like high frequency oscillator at $\sim 24\ cm^{-1}$ of width $\sim 17\ cm^{-1}$ with a weight of 0.11, a superfluid oscillator strength of 0.36, and a quasi-particle cyclotron frequency of $\sim 3\ cm^{-1}$ of width $\sim 4\ cm^{-1}$.

Chapter 4

Experimental techniques

This chapter outlines various experimental techniques required in preparation and characterizion of the FIR ac- Hall angle measurements. The first two section discuss sample AR-coatings and BSCCO peeling procedures. The next three section discuss characterizing the individual hardware components of the ac- Hall experiment, optical alignment procedures, and step-by-step operational instructions.

4.1 AR coating procedure

Broadband FIR anti-reflection (AR) coatings are made by evaporating a conductive film of a material which has a high scattering rate.[35] The AR coating condition is derived from the Fresnel reflection coefficient. In the thin-film limit, the AR coating

condition becomes:

$$
\begin{aligned}
& r \propto n_1 - (n_2 + Z_0 \sigma_{xx} d) = 0 \qquad \text{from equation F.8} \\
& R_\square \equiv 1/(\sigma_{xx} d) \\
& \Rightarrow R_\square = \frac{Z_0}{n_1 - n_2} \\
& \qquad \text{where } Z_0 = 377\ \Omega\ /\ \square, \\
& \qquad \text{d = film thickness,} \\
& \qquad \text{n1 = substrate index,} \\
& \qquad \text{n2 = 1 for air or vacuum}
\end{aligned}
\tag{4.1}
$$

For a quartz substrate whose index is $n_1 = 2.12$, the AR-coating condition requires a sheet resistance of 337 $\Omega/\square$.

NiCr is vaporized in a deposition chamber under vacuum by passing a current ($\sim$ 200 amps) through a resistive conductive vessel. The sample is mounted $\sim$14" from the vessel.

A standard microscope glass slide is used to monitor the sheet resistance during the evaporation. Two copper strips are evaporated onto the reference slide across the entire width bounding a perfect square of bare glass. Two copper wires are indium soldered to each copper strip. The glass slide is placed very near the sample location. The wires are then connected to a Keithley DVM in a standard four-probe configuration. During the evaporation, the sheet resistance, $R_\square$, is monitored in real-time.

It is assumed that the glass slide and the sample have the same sheet resistance. In practice, this is true only if the surfaces of both the glass slide and the sample are

very clean. I wipe the glass slide with an acetone soaked Kemwipe, and then use a vapor degreaser with Lenium as a solvent to clean both the sample and glass slide.

Immediately following an AR-coating deposition, the surface resistance increases as the sample cools. The resistance further increases when the sample is exposed to air. These combined increases in resistance are calibrated experimentally. The amount of change depends on the thickness of the coating and deposition rate. For a quartz AR coating, this increase is $\sim 12\ \Omega/\Box$.

The final AR coating is characterized via a FIR transmission measurement in a Bomem DA3 spectrometer. An imperfect AR coated quartz substrate will exhibit an etalon pattern whose spectral peak-to-peak spacing is given by:

$$\Delta\nu = \frac{1}{2\ n_{substrate}\ d_{substrate}}$$

where $n_{substrate}$ is the index of refraction, and

$d_{substrate}$ is the thickness

The spacing for a quartz substrate (n=2.12)[30] of thickness .051 cm is $\Delta\nu = 4.6\ cm^{-1}$. The resolution of the spectromenter must be appreciably better than the etalon spacing in order to accurately measure the amplitude. The sheet resistance of the NiCr AR-coating can be extracted from the amplitude of the etalon pattern. Typical results show etalon amplitudes that are less than 1% over the entire FIR region from 20 to 230 cm^{-1}. Note that the index of refraction changes appreciably at $\gtrsim 180\ cm^{-1}$. However, absorption in the quartz tends to suppress etalon effects at the higher frequencies.

4.2 BSCCO peeling procedure

Gendu Gu at Brookhaven National Laboratories grew various single crystal BSCCO samples using the floating zone method.[27] He diced the samples into various sizes that averaged 2 to 3 mm rectangles which were roughly .5 mm thick. The crystals are inherently micaceous which easily flake into thin sheets. However, it is very difficult to peel sufficiently thin, large area ($\lesssim$ 100 nm thick, and $\gtrsim$ .5 mm $\times$ .5 mm) single crystals.

The method adopted by Danilo Romero[36] was substantially modified by Don Schmadel.[13] Small sections of the crystal are removed until the entire surface is a continuous single crystal sheet using a wooden toothpick coated with a 3M adhesive (roughly the same stickiness as scotch tape). By pressing the tip against the crystal, small sections of the crystal adhere to the tip of the toothpick and are peeled away.

The remaining flat surface is epoxied (see appendix A for pertinent epoxy specifications) face down to a quartz substrate. Once cured, the opposite surface of the crystal is peeled in a similar manor. The final result is somewhat a mozaic of thin single crystal BSCCO flakes. The areas of different thickness vary in size, but are roughly 1 to 2 mm^2 in area. The variation in thickness was never estimated, but sample inhomogeneity does not play much of a role in the measurement of the Faraday angle. Theoretically, the thickness of the film does not enter into the equations for the Hall angle in the thin film limit except for the small correction factor given in equation 3.39. Pragmatically, measuring the Faraday angle at various locations on the sample did not exhibit appreciable changes.

The epoxy and substrate are required to be visibly transparent. Looking at the transmitted light from the back side of the substrate through the thin BSCCO lay-

ers, the grayish contrast from one area of the sample to another can be compared while peeling until the sample is sufficiently uniform. Also, it is easy to accidently completely peel away the BSCCO in places causing holes to appear which are only clearly seen if the epoxy and substrate are transparent.

Some of the parent crystals appear to have inherent defects. As the crystal is peeled down to a thin sheet ($\sim$ 100 nm), these defects manifest as small "pinholes." The sample is mounted to minimize the possibility of leakage light in the Faraday experiment. The aperture location and diameter are specifically chosen such that no pinholes are present.

4.3 Aligning the Faraday system

The alignment procedure of the complete system is cursively outlined in this section. It is intended for those readers interested in aligning this specific system.

4.3.1 Lasers

Alignment of the CO_2 laser with the FIR cavity

The objective is to align the CO_2 laser output with the FIR laser axis.

- Level the CO_2 laser table.
- Remove the FIR laser from table.
- Take off the front flange of FIR laser.

- Hold the flange at arms length and align the beam block concentrically with the entrance aperture.

- Align the CO_2 beam horizontally with respect to the laser table (at the FIR laser location), and align the beam at the correct location of the input and output aperture of the FIR laser.

- Re-attach the front flange of the FIR laser, and remove the rear mirror. Measure very carefully the location of the exit aperture and place heat sensitive paper across the open hole. Adjust the FIR laser table levelling screws to align the entrance and exit apertures with the CO_2 beam.

- Re-attach the rear mirror and pump out the FIR laser cavity.

- Insert a homemade aluminum cylinder (it looks like a 1/4" thick silver dollar) into the front laser flange. Coat the side facing the CO_2 laser with vacuum grease. Press a target onto the face of the aluminum cylinder allowing the vacuum grease to hold it in place (I used perpendicular cross-hairs with concentric circles printed on a transparency slide).

- Allow the CO_2 beam to strike the target and adjust the FIR laser front flange position such that the CO_2 beam hits the center of the target.

Alignment of the FIR cavity

- Evacuate the Vycor laser tube. This seats the mirrors at their operating positions.

- Look down the output coupler while concurrently illuminating the rim of both the input coupler and output coupler flanges as shown in figure 4.1.

- You will see many circles. They must be made to be concentric (see figure 4.1). Note that it is difficult to take a picture through a small aperture aimed at mirrors causing some of the circles to appear blurry when, in fact, they are quite sharp when viewing with the naked eye. Align the many circles concentrically with the input and output coupler apertures by adjusting both input and output coupling mirrors.

- Note that you can also look down the input coupler as well. Make sure that the coarse alignment looks good from both ends.

- Fine alignment is accomplished by turning on the CO_2 and the FIR laser and peaking the FIR power as measured by a bolometer. Variables include CO_2 pressure, FIR laser cavity pressure, CO_2 piezo and grating, and the 2 FIR mirror separation and angle.

4.3.2 Optics table

Off-axis parabolic mirrors

Align all angles involving the off-axis parabolic (OAP) mirrors with respect to their mounts.

- Determine the desired working height of all optical components (determined by height of the sample/magnet).

- Place a pinhole across the room and illuminate. Make sure the pinhole is at the correct height.

- Focus all OAP mirrors such that there is minimum aberrations, and the foci are at the correct height off of the optics table. Ensure that the spot on either side of the foci uniformly collapses as you move toward the foci. Measure the angle and distance to determine the mirror focal length and angle.

Align table optics

- Level the optics table with the levelling screws located on each leg.

- Place the magnet 'tail' piece (the bottom section that houses the vacuum windows) on the table at the desired location. Level the magnet with the 1/4-20 levelling screws.

- Place cross hairs (string or a target printed on a transparency) at the sample location and across the exit port of the magnet tail piece. Standing as far back as possible, align the sample stick such that the sample stick cross hairs and the exit port cross hairs are aligned.

- Place a copper OAP mirror at the output port at the correct. location and angle as carefully as you can. Place the next OAP mirror at roughly the correct location and angle, and place a screen at the focal point (detector location). Illuminate the sample stick. A sharp image of the sample should appear at the detector location.

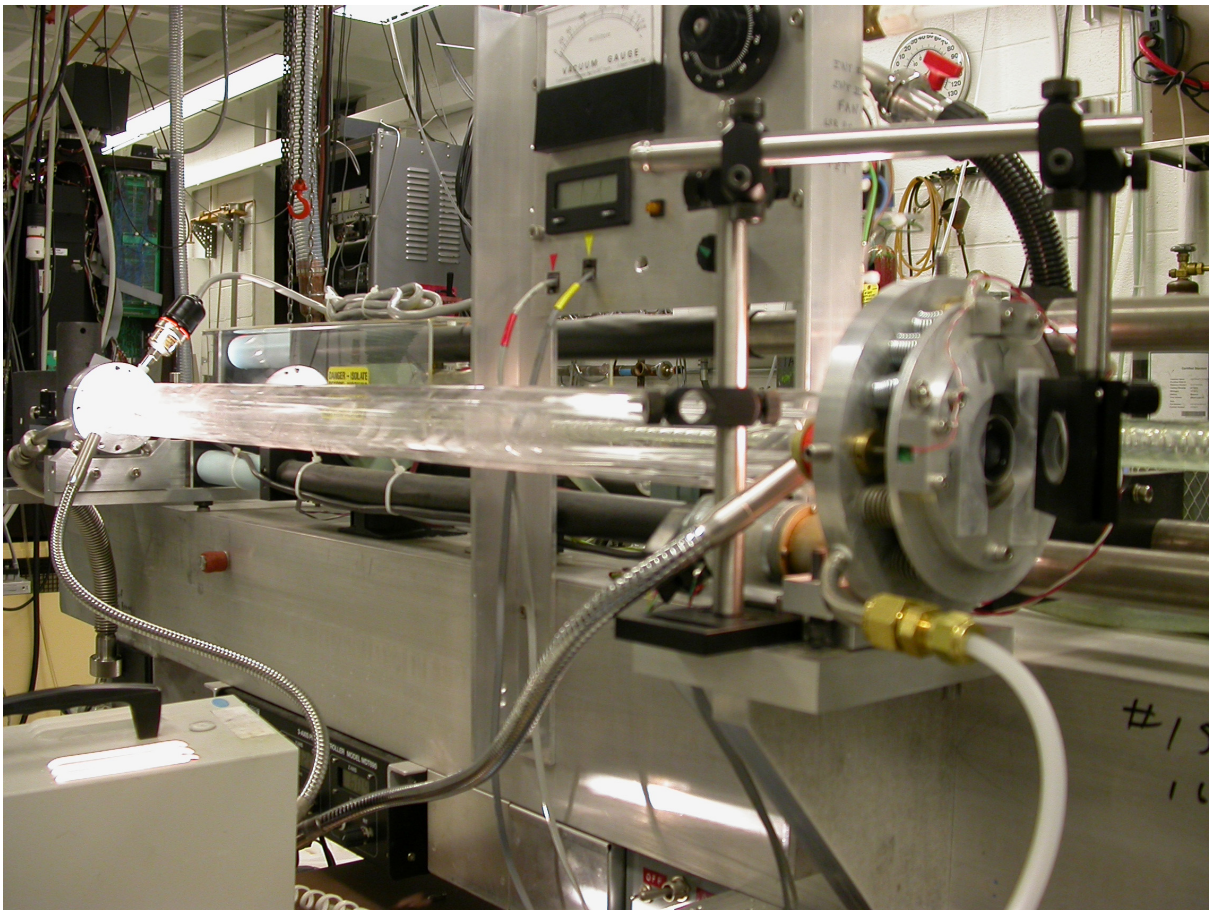

(a) Illumination of the FIR Laser flanges

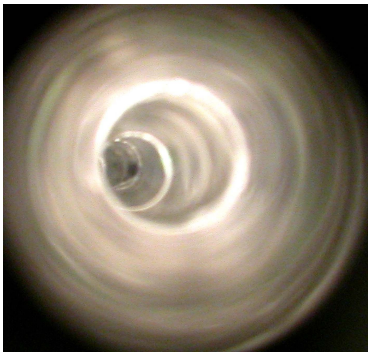

(b) Grossly misaligned

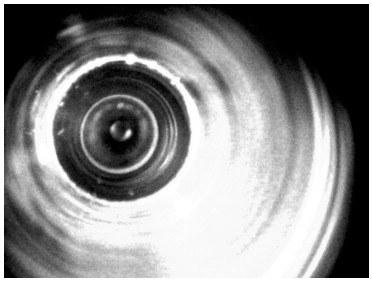

(c) Slightly misaligned

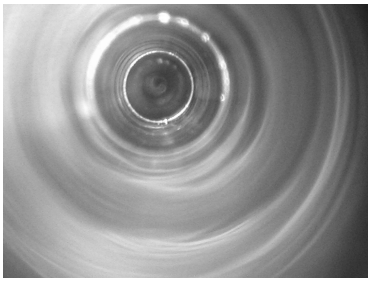

(d) Coarsely aligned

Figure 4.1: Coarse alignment of the FIR laser. The blurry inner circles in the 'Coarsely aligned' figure is an effect produced by the camera and are in actuality very sharp.

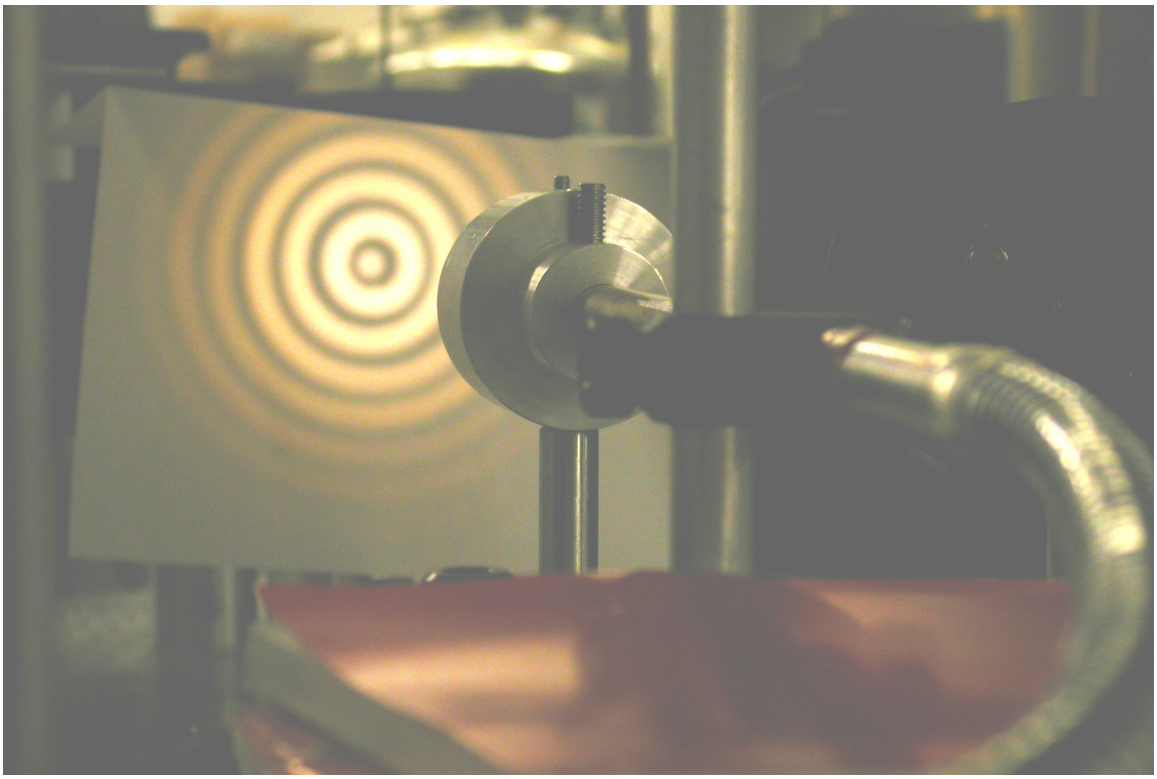

(a) Light from a Cole Parmer 9741-50 illuminator striking a screen in front of mirror M11 after passing through a short brass light pipe and an iris.

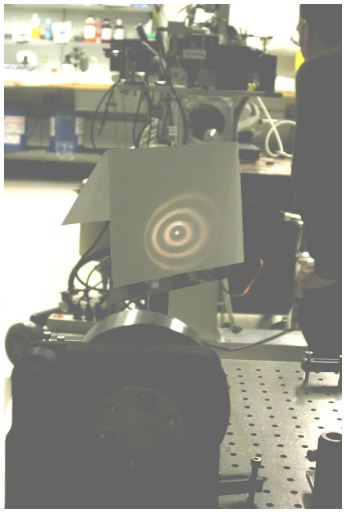

(b) Same beam after propagating backwards through the complete optical table system of mirrors.

Figure 4.2: Coarse aligning the FIR laser. The blurry inner circles in the 'Coarsely aligned' figure is an effect produced by the camera and are in actuality very sharp.

- Place an aperture at the image location of the sample crosshairs, and put a bright light source behind it as in figure 4.2.

- Place a flat mirror in the path of the optical beam after collimation and deflect the beam across the room in order to ensure that the beam stays the same dimensions and is truly collimated. If not, adjust the aperture location and collimating mirror so that the beam is collimated (and measure the distance and angles!). Also, the collimated beam must strike the copper AOP at it's center.

- Adjust the copper OAP mirror such that the cross hairs on the magnet exit port are centrally and circularly illuminated, and that the focus is at the sample location. If not, adjust this mirror.

- Note that this is an iterative process, but outlines the tools necessary to adjust all of the output optics. Repeat until the two OAP mirrors and aperture are in the correct locations to satisfy the above criteria.

- Place a copper OAP mirror at the measured location and angle with respect to the entrance port of the magnet tail piece. Adjust until the beam is collimated (always check collimation by placing a flat mirror in the optical path and beaming across the room onto a screen to check true collimation).

- Place a focusing copper OAP mirror at the next desired location. Adjust the angle such that the focus is free of aberration. Place an iris at this location, turn off the lamp at the aperture, and illuminate the newly placed iris. Ensure that the beam is focused free of aberrations at the sample location, and is focused

well at the detector location. Turn on the detector aperture lamp and verify that the two spots are focused at the same location as the sample.

- Align the next AOP collimating mirror and the next focusing mirror, and place an iris at the focus. Again, illuminate this iris and verify that the spot at the sample is at the same location as that produced by the detector aperture lamp.
- Place and align the next collimating AOP mirror.
- Align the next two flat mirrors such that the beam strikes the FIR laser periscope flat mirror, and a nice aberration free spot is focused onto the diamond window of the FIR laser.
- Check the alignment of the entire optical system by placing a light source at the detector aperture and propagate the beam through all of the table mirrors (see figure 4.2).
- Another check is to illuminate the sample stick and look down the optical path at a collimation point. Ensure that a minimum amount of distortion appears at the sample location, and that all the mirrors are concentrically aligned. During all alignment, always ensure the spot is at the correct height.

Coaxial alignment of the FIR laser output with the optics table

The optics table and the FIR laser are now aligned at a *point* located at the output coupler aperture. This does not ensure that the table optics are coaxially aligned with the output beam of the FIR laser.

- Turn on the light source at the detector aperture.

- Place two irises between the mirrors M3 and M4, and M4 and M5 centered on the beam. Ensure that the beam strikes the FIR laser periscope mirrors concentrically.

- Align a HeNe laser down the axis of the FIR laser from input to output coupler. Carefully measure to ensure the beam strikes at the correct (center) locations on the FIR laser periscope mirrors.

- The objective is to adjust the laser periscope as well as mirror M3 so that both beams are centered on each other, and that the HeNe laser beam is concentric with the two newly placed irises.

- Ensure there are no abberations of the white light beam striking the FIR laser output coupler after the previous alignment. Adjust as necessary and repeat the last 2 steps.

- Keep the two irises in place and turn on the FIR laser with a detector at the transmission detector location. Tweak the FIR laser periscope and the table periscope alignment to maximize the signal. Make sure that the beam strikes all optics in the center.

Other optical components

Use figures 2.6 and 2.5 for reference.

- Place the chopper at the correct location on the optics table and turn it on. With the FIR laser running and the transmission bolometer in position, ensure you have a square signal on the oscilloscope.

- Insert the mylar beam splitter. Place and align the reference bolometer in order to maximize the signal observed on a separate lock-in amplifier referencing the chopping TTL signals.

- Place the polarizer nearest the transmission bolometer onto the table, cross the polarizer with respect to the incoming polarization, and rotate by 90 degrees to align the polarizer with the incoming polarization.

- Repeat for the initial polarizer in the system.

- Choose a correct waveplate (see section 4.4.4) and insert it into the rotator (see section 4.5.5).

- Place the rotator in the beam near the focus. Ensure the beam is moving through the center of the rotator bore on both sides, and angle the rotator as much as possible without clipping the beam.

4.3.3 SPECAC

For reference, a picture of the final setup can be seen in figure 2.7.

- Concentrically place a large iris at the entrance (which is normally the exit) port of the SPECAC.

- Place a small iris at the first focal point between mirrors M5 and M6. Turn on a light source located at this iris.

- Coarsely align the 2 flat mirrors Ma and Mb by measuring with a ruler (height and placement on the table). Center the beam on the SPECAC large iris.

- Adjust the two periscope flats such that the beam impinges at a right angle with respect to the SPECAC entrance port. In order to do this, remove the side panel opposite the entrance port. Remove any beam splitters. Stand as far back as possible and look straight into this port (center your eye such that the two circular ports of the SPECAC are concentric). The source beam and the iris should be concentrically aligned with the ports. If not, adjust the two flats such that everything is concentric.

- Place both mylar beam splitters in the SPECAC (so that you can see the visible beam).

- Stop-down the entrance port using the large iris at the entrance port.

- Look directly at the kinematically adjustable stationary flat mirror through the opposite port. You should ideally see one spot, but you will more than likely observe two. One spot is from direct reflection off of the mylar beam splitter. The other is from the reflection off of the "moving mirror-mylar beam splitter-stationary mirror" combination. Adjust the stationary mirror until the two spots become one. The spot should be in the center of the entrance beam. The coarse alignment is now complete.

- Place a light pipe at the focus of the SPECAC parabolic mirror, and place the other end of the light pipe into a bolometer detector.

- Turn on the FIR laser, and begin scanning the SPECAC motor. You should observe a sinusoidal varying intensity. Tweak the SPECAC stationary flat mirror until the maximum %- change between peaks and valleys is observed.

4.4 Characterizing individual components

4.4.1 Rotator phase noise characterization

An independent characterization of the phase noise produced by the nonuniform angular velocity of the rotator is measured. The optical diagram of our set-up is shown in figure 4.3 and the electronic set-up is shown in figure 4.5. Our light source is a microscope lamp that has a flexible optical waveguide. The end of the waveguide is placed against an iris aperture at the focus of an off-axis parabolic mirror (M6). The light is focused by an off-axis parabolic mirror (M7) and passes through 3 dichroic sheet polarizers. The first sets the initial polarization, the second is mounted inside the rotator, and the last is parallel to the first. Another off-axis parabolic reflector (M8) collimates the beam. The light is then focused by a 4" diameter plano-convex lens onto a PIN-10D photoconductive silicon diode.[37]

The silicon photodiode detector is negatively biased with a 9V battery and the photo-generated voltage is fed into a 7265 lock-in amplifier (figure 4.5). A TTL pulse is emitted by the motor controller once every revolution. We use these TTL pulses as the reference frequency on our lock-in amplifier. The EG&G 7265 harmonically decomposes the second harmonic of the signal. Data from the X and Y channels are acquired through the GPIB bus via a computer running a homemade Labview program. The Labview program averages 20 data points per point recorded. The time per recorded point is approximately 1/2 second. The lock-in time constant is set to 1/2 second.

The noise associated with the 2ω phase signal (y-channel) is $\sim 5 \times 10^{-5}$ at an amplitude of .8V (x-channel) as seen in figure 4.4. From the figure, we see that

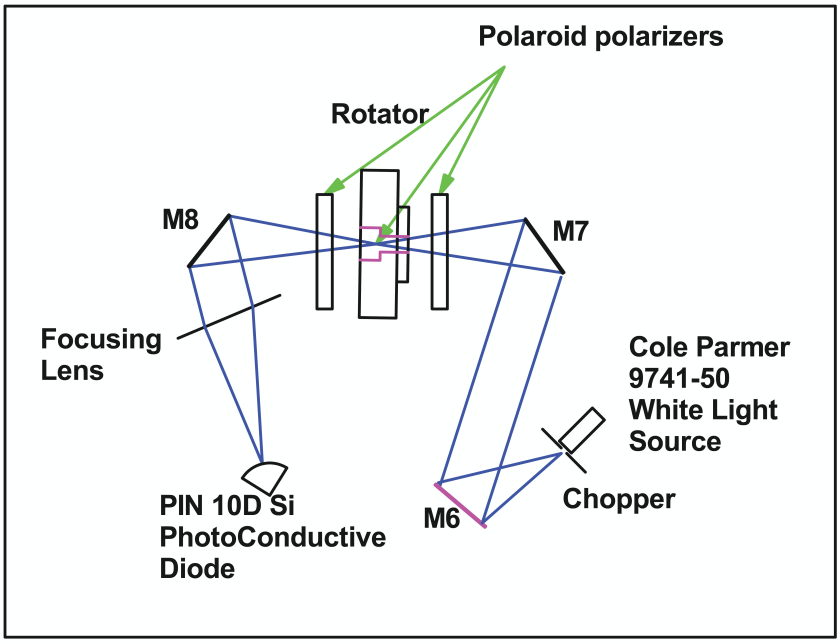

Figure 4.3: Optical layout for the rotator noise characterization. The light path is traced in blue.

the noise scales with the intensity of the light source implying the dominance of detector noise. We can calculate the predicted phase noise of the .8V magnitude signal associated with the detector noise measured at a .04V magnitude signal level (after marker number 4 in figure 4.4) as follows:

$$\begin{aligned}
\Delta\phi &= \text{the phase noise associated with .04V signal level} \\
&= \frac{\Delta Y}{X} \sim 5 \times 10^{-4} \\
&\quad \text{where } X = .04V \\
\Delta\phi' &= \text{the predicted phase noise associated with a .8V signal level} \\
&= \frac{\Delta Y}{X'} = \frac{\Delta\phi \times X}{X'} \sim 3 \times 10^{-5} \\
&\quad \text{where } X' = .8V
\end{aligned}$$

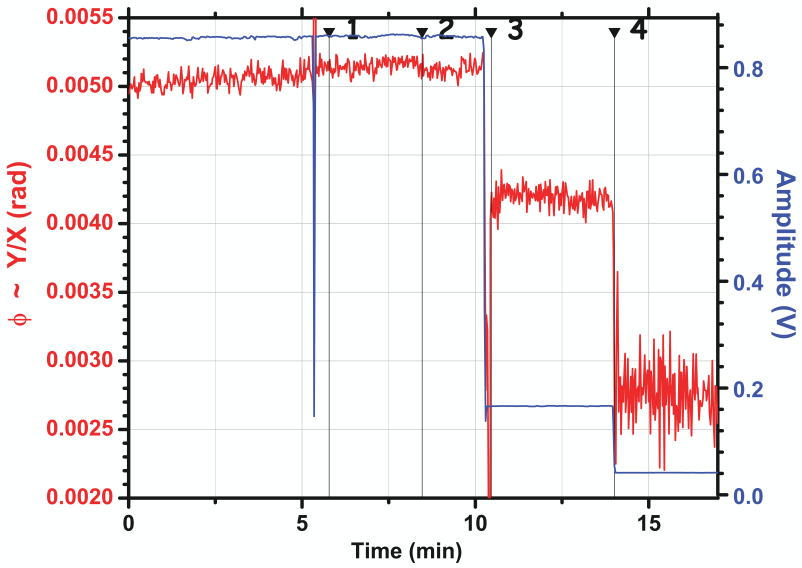

Figure 4.4: Rotator characterization: the magnitude of the lock-in signal is plotted in blue, and the ratio of the Y- to X- channel signals (the zero phase is arbitrary as long as Y$\ll$X) is plotted red. Between markers '2' and '3' characterizes the system at a signal magnitude of .8V. Between markers '4' and '5' characterizes the system at a signal magnitude of .04V.

This level of phase noise is observed at the .8V signal level, which means that the phase noise produced by the rotator is $\lesssim$ .03 mrad. However, it should be noted that the phase drift over 30 minutes is typically observed to be $\sim$.1 mrad.

4.4.2 Bolometer frequency characterization

There is a trade-off between sensitivity and the response time of a bolometer detector. The time constant is chosen to optimize averaging time without too severe a loss in responsivity (for a detailed explanation of the principles of operation, see reference 24). Experimentally, measuring the detector frequency roll-off is a straight

forward matter.

I used two methods. The first is to chop the input radiation at a low frequency ($\lesssim$ 30Hz) *and* chop at a frequency which sweeps from 30Hz to 1 kHz. Two lock-in amplifiers were used to measure the magnitude of the signal at the two separate frequencies. The ratio of the signals characterizes the detector frequency roll-off. Note that the phase response of the bolometer is also significantly effected.

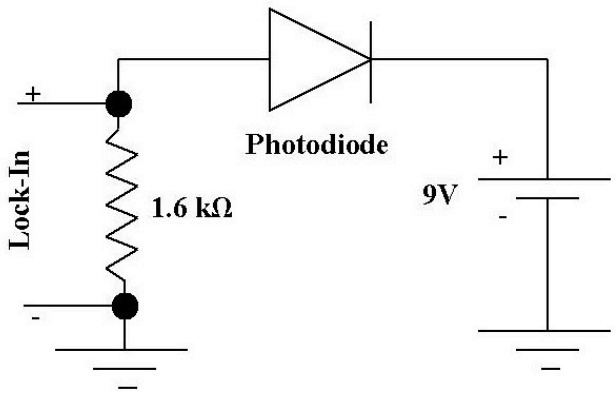

Figure 4.5: PIN-10D silicon photodiode circuit schematic

The noise spikes observed in figure 4.6(a) is a manifestation of the mixing of the higher harmonics of the reference signal (square-wave) with the frequencies of interest. There are also other frequencies (such as 30, 60, and 120Hz) present which cause apparent noise in certain parts of the spectrum. Other noise spikes are caused from the lock-in amplifier poorly tracking the sweeping frequency.

The second method uses two bolometers as in figure 2.3. A chopper which is allowed to discretely change frequency is inserted at the location of the rotator. The normalization of the magnitude of the signal measured by the transmission bolometer with respect to the reference bolometer gives the desired result.

The sensitivity of the bolometer is measured by a method described in section D.7.1. Results for the three bolometers used in this experiment are given in appendix C.

4.4.3 Mylar wire polarizers

The FIR polarizers are evaporated wire polarizers on a mylar substrate with 4 μm pitch and 2 μm width. The ratio of the transmitted signal from two crossed polarizers to the signal from two parallel polarizers measures the extinction coefficient of the polarizers. This was done at 84 cm^{-1} and found to be $1 : 10^{-5}$.

The extinction ratio gives a direct upper bound on the errors introduced into both the real and imaginary part of the Faraday angle. That is, the error is less than .01 mrad.

In practice, the errors introduced in measuring the Faraday angle due to polarizer imperfections are directly observed to be negligible at all pertinent FIR wavelengths (see the calibration plots in figure 5.6 and 5.8).

4.4.4 Waveplate preparation and characterization

In order to analyze the raw data acquired in the Faraday experiment, it is essential that the differential phase shift ($\Delta\beta$) and absorption ($\Delta\Gamma$) of the waveplates be known. Two characterization methods are used to find the waveplate parameters.

By inserting a waveplate at some angle θ between two parallel polarizers, the

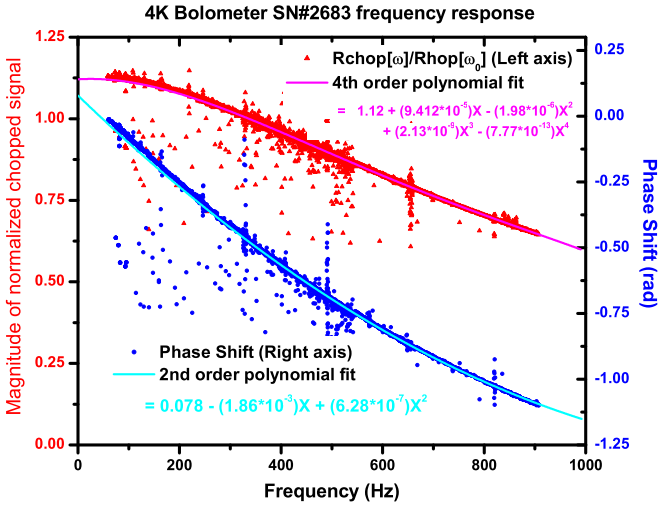

(a) 4 K bolometer (SN#2683) frequency response

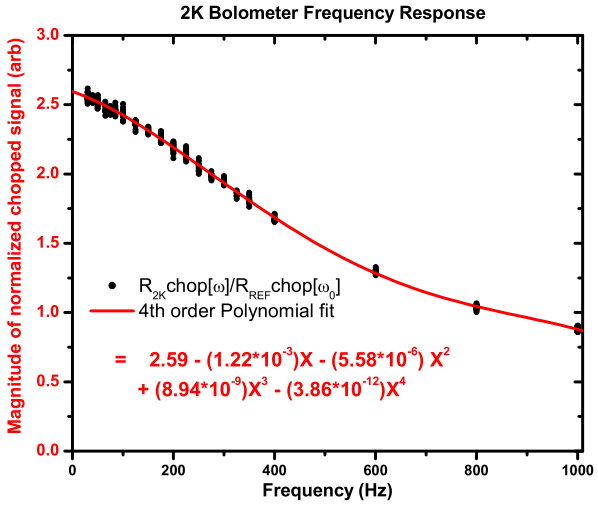

(b) 2 K bolometer (SN#2187) frequency response

Figure 4.6: Characterization of the bolometer frequency dependence. **(a)** The 4 K bolometer frequency response, amplitude and phase, is measured. The red curve (left axis) is the ratio of the magnitudes of bolometer signals at 2 distinct frequencies, a sweeping chopper frequency (ω) and a fixed chopper frequency (ω_0). The blue curve (right axis) is a measure of the differential phase. **(b)** An FIR beam is split by a thin mylar beam splitter. The first beam is modulated by a chopper that sweeps frequency (ω) and measured by the 2 K bolometer. The second beam is modulated by a fixed frequency chopper (ω_0) and measured by a 4 K reference bolometer. The left axis is the ratio of the two signals.

intensity relative to the input intensity is given by the following:

$$I(\theta) = \cos^2(\theta)\, e^{-2\gamma_1} + \sin^2(\theta)\, e^{-2\,\gamma_2} + 2\sin^2(\theta)\ \cos^2(\theta)\ \cos(\Delta\beta)\, e^{-(\gamma_1+\gamma_2)}$$

where

I is intensity (4.2)

$\gamma_1,\ \gamma_2$ is the absorption along the e- and o- axis of the waveplate

$\Delta\beta$ is the differential phase shift between the e- and o- axis

Taking specific ratios yield:

$$R_1 = \frac{I(\pi/4)}{I(\pi/2)} = \frac{1}{4}(1 + e^{-2\Delta\Gamma} + 2e^{-\Delta\Gamma}\cos(\Delta\beta)) \quad (4.3)$$

$$R_2 = \frac{I(\pi/4)}{I(0)} = \frac{1}{4}(1 + e^{2\Delta\Gamma} + 2e^{\Delta\Gamma}\cos(\Delta\beta)) \quad (4.4)$$

$$R_3 = \frac{I(0)}{I(\pi/2)} = e^{-2\Delta\Gamma} \quad (4.5)$$

$$R_{add} = R_1 + R_2 = \cosh(\Delta\Gamma)(\cos(\Delta\beta) + \cosh(\Delta\Gamma)) \quad (4.6)$$

Data was taken using a FT-FIR spectrometer with a waveplate set at angles 0, $\pi/4$, and $\pi/2$ radians. We can use two of the above equations in order to obtain $\Delta\Gamma$ and $\Delta\beta$ as a function of frequency.

The simultaneous solutions of R1 and R2 are given in figures 4.7(a) and (b). The separate solution found from R3 is plotted in figure 4.7(b) as well. Ideally the differential phase shift should obey equation 2.10. This is indeed the case; however, inverse functions were used to calculate the graph presented in figure 4.7. $\Delta\beta$ is the inverse cosine of a function resulting in a range that is constrained to the interval $\{0,\pi\}$. Figure 4.7 is indeed constrained by this interval but never reaches the value of

π. This is a result of the transmission of the waveplate never quite reaching zero, but instead obtains a minimum of 3% at approximately 135 cm^{-1}. This is due to errors in aligning the waveplate optical axis with respect to the polarizers.

Quartz has a phonon absorption feature at approximately 130 cm^{-1} which manifests itself clearly in the data of figure 4.7 as a spike in $\Delta\Gamma$.

The preferred method for calibrating waveplates involves *in situ* measurements in the Faraday system. Inserting a polarizer in place of the sample and inserting the unknown waveplate into the rotator, the effective $\Delta\beta$ and $\Delta\Gamma$ are measured. This will be covered in more detail in section 5.2.3.

4.4.5 Lasers

Each laser line is spectrally analyzed with a SPECAC step scan FT-FIR spectrometer to ensure the presence of only one frequency. Figure 4.8 represents a set of discrete single frequency lines for various FIR laser configurations. The resolution is 1 cm^{-1}, and the measured frequency range is from 1 cm^{-1} to 250 cm^{-1}, the cut-off frequency of quartz. The power spectrum plotted in figure 4.8 is the absolute value of the discrete complex Fourier transform of the interferogram. The symmetric side lobes associated with the individual peaks are a result of rectification of the side lobes which are generally present in all finite-sized interval complex Fourier transforms performed with little or no apodization. The peak values are all scaled to 1.

The absolute power of various FIR laser lines are given in table 4.1. Note that the power is two orders of magnitude lower than commonly published values.

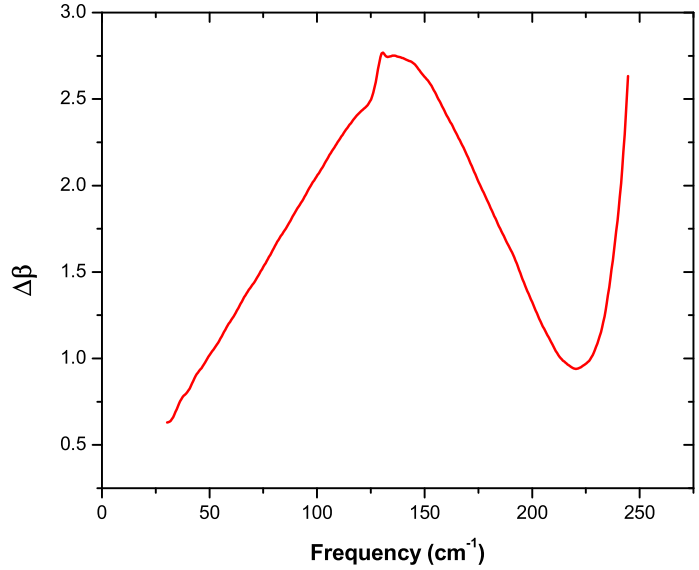

(a) Bomem $\Delta\beta$ measurement

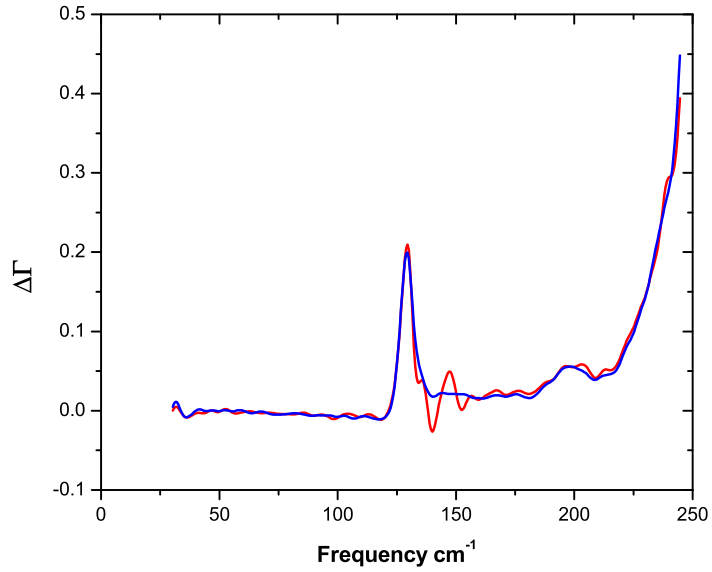

(b) Bomem $\Delta\Gamma$ measurement

Figure 4.7: (a) $\Delta\beta$ and $\Delta\Gamma$ found from the simultaneous solutions of R_1 and R_2 of equation 4.3 for a .7mm thick x-cut quartz waveplate. The blue trace in figure **(b)** is the solution to R_3, and the red is the simultaneous solution to R_1 and R_2 of equation 4.3

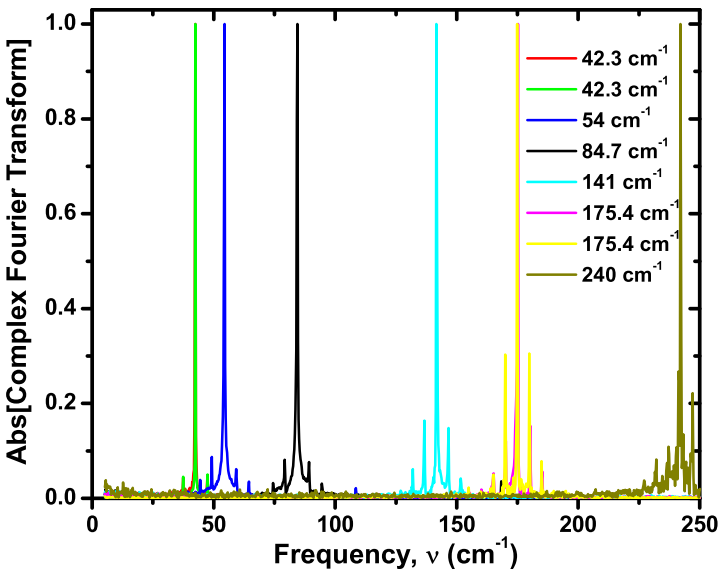

Figure 4.8: Power spectrum of individual FIR laser lines normalized to 1 measured with a SPECAC step-scan Fourier transform spectrometer.

Discussion of FIR laser power issues

The CO_2 laser has an axial mode spacing of $\Delta\nu_{ax} = c/(2L) \sim 75$ MHz where c is the speed of light and L is the length of the cavity ($\sim 2m$). Thus, the order of the mode is $q = 2L/\lambda \sim 10^5$. Inhomogeneous Doppler broadening is given by $\Delta\nu_d = \sqrt{\frac{8kT\ln 2}{Mc^2}}\nu_0 \sim 30$ MHz where k is the Boltzmann constant, T is the temperature of the gas (~ 300 K), M is the total mass of the CO_2 molecule (44 amu), and c is the velocity of light. Homogeneous pressure broadening at $10\mu m$ is ~ 5.5MHz/torr $\times$ 15torr $= 80$ MHz.[31] Spacing between the the CO_2 lines of the P branch is ~ 50 GHz.

The FIR laser has a dielectric waveguide with two flat molybdenum mirrors at either end incorporating conical apertures in the centers. A CO_2 beam coaxially optically pumps the FIR gas into an excited vibrational-rotational state, and the

molecules relaxes back to the original vibrational-rotational state. The lasing FIR energy is the difference between rotational states that occurs during the relaxation process. The axial mode spacing is $\Delta\nu_{ax} = c/(2L) \sim 150$ MHz, the doppler broadening is ~ 5 MHz for methanol, and pressure broadening is typically ~ 40MHz/torr ≈ 4 MHz under the operating pressure of 100 mTorr.

Both the CO_2 laser and FIR laser have the same approximate FWHM of the half-power points associated with the resonator's Lorentzian response curve:[38]

$$\Delta\nu_{1/2} = \frac{\nu}{Q} = \frac{c}{2\pi n}(\alpha - \frac{1}{L} ln\sqrt{R1R2})$$

where Q is the resonator quality factor,

c is the speed of light,

L is the length of the waveguide,

n is the index of refraction of the gas ≈ 1

α is the loss per unit length in the resonator

neglecting losses due to the mirrors

R1 (R2) is the reflectivity of mirror 1 (2)

Assuming that the loss contribution of the mirrors is the dominant factor (α small), $R1 \approx .85$, and $R2 \approx 1$ yields $\Delta\nu_{1/2} \sim 4$ MHz for the CO_2 laser cavity and ~ 8 MHz for the FIR laser cavity.

The dielectric waveguide resonator strongly favors one mode. Diffraction losses through the waveguide strongly attenuate higher order modes.[39] Lower order modes are only slightly attenuated due to the grazing incidence with the waveguide.[40] Diffraction loss in a cylindrical dielectric waveguide in the lowest order mode is negligible if

the following condition is met:

$$a > \left(\frac{\lambda^2 L}{.05}\right)^{1/3}$$

$$\Rightarrow a > 5.8mm \text{ at } 118\text{um}$$

Under the above (large radius waveguide) condition, the waveguide defines the spacial dimensions of the approximately Gaussian beam profile in the cavity.[29]

Reported values using similar dielectric waveguide dimensions and pump power are in the vicinity of 1-10 mW.[32,41,42] Typical input coupling aperture diameters range from a couple of millimeters to 5 millimeters, output coupling aperture diameters range from a few millimeters to 5 millimeters. Wire meshes have yielded a factor of 2 to 3 increase in power.[42] Wood *et al* reported $\sim$ 400 mW at 118 μm using large CO_2 pump powers $\sim$ 100W, a wire mesh output coupler, and a 2m long laser cavity. Correcting for these enhancements, we would expect to obtain an output power in the vicinity of 10 mW with the current FIR laser configuration. It is worthwhile to note that Edinburgh Instruments manufactures an FIR laser that guarantees 150 mW power output at 118 μm using the PL-5 CO_2 laser.[43]

The fractional loss due to a finite separation (d) between the end of a dielectric waveguide (of radius a) and a flat mirror (assuming $\lambda \ll a$) is given by:[29]

$$\approx 6\left(\frac{d}{ka^2}\right)^{3/2} \approx 4 \times 10^{-5}$$

$$\text{for } d = 5mm,\ a = 15mm,\ \lambda = .1mm,\ \text{k} = 2\pi/\lambda$$

It appears that the current existing gap between the molybdenum mirrors and the Vycor tube is negligible.

Performance trade-offs exist between the Q (quality factor) of the CO_2/FIR cavity and line-widths due to the nature of off-resonant optical pumping. Experimentally, it is a straight forward matter to explore the parameter space involved in changing the Q of the cavities, the line-widths, and the (slight) de-tuning of the pump frequency. In so doing, I have performed a range of tasks to explore the appropriate parameters as well as other possible sources of deficiencies:

- Various output couplers ranging from 3mm to 6mm apertures were used with no appreciable change of signal.

- Three Vycor insert tubes of 2.2, 3.0, and 4.5 cm diameters (appendix A) were used to define the cavity with no significant difference in total output power. A polished 1 cm diameter brass insert tube roughly doubled the total output power. However, the brass waveguide presumably supports higher order spacial modes which is undesirable.

- Replacement and realignment of the CO_2 output coupler altered the CO_2 beam spatial mode but caused no apparent change in total signal.

- Leak testing of the entire FIR gas handling system, as well as the entire CO_2 laser system, revealed no diffusion of ambient contaminates into the system.

- The total CO_2 power level transmitted through the front flange and diamond window of the FIR laser was measured at $\sim$ 20W.

- The purity of the methanol was changed from research grade 99.99% methanol to an ultra pure grade 99.999% methanol with no increase in total power.

- Three different bolometer detectors were characterized (load curves recorded) and used to measure the power output. All measurements agreed. No corrections were made in assuming the quantum efficiency of detection or attenuation by cold windows. Corrections would increase the quoted values in table 4.1 by roughly a factor of 2 or 3.

- Copper mirrors were used instead of molybdenum mirrors with no apparent change in output power.

- Methyl fluoride, deuterated methanol, and double- deuterated methanol yielded similarly low power at other FIR laser lines.

- The FIR laser was dismantled and thoroughly cleaned to eliminate the possibility of contaminates.

- Suppression of possible higher order modes using an adjustable (absorbing) wire hoop inside the laser cavity showed no discernable change in power.

- Variation of the focal length of the CO_2 input coupling optics caused no discernable change in output power.

- Changing the temperature of the water-cooled CO_2 laser tube caused no discernable change in FIR laser output power.

- Cooling the methanol liquid reservoir did not change the output power.

- The spectral output of the FIR and CO_2 lasers were measured to be at the correct frequencies.

- Attenuation by water vapor in the air was not appreciable at 118 μm.

The following is a suggestive list of experiments and improvements in the pursuit of improved FIR laser performance:

- A wire mesh output coupler can yield a factor of 2 to 3 increase in power.[39]
- Incorporating a layered dielectric near-IR reflector would eliminate the need for a quartz filter.
- An enhancement of roughly 50% has been reported by using methane (CH3F) as an exchange gas for the 118 μm line increasing the thermalization collision rate of the methanol gas.[39]
- Cooling of the laser tube walls yields higher power, though the research group that reports these findings do not report the quantitative factor. However, they do report markedly improved amplitude and frequency stability.[44]
- Output power scales with the FIR laser tube length up to $\sim$ 3m yielding up to a factor of 3 increase in power.[41]
- Sand/diamond blasting the output coupling diamond window will scatter CO_2 radiation thus reducing the necessary thickness of the CO_2 quartz filter which will greatly improve the high frequency through-put.
- A calibrated calorimeter may expose a significant increase in power than that reported in table 4.1. However, bolometer elements are known to have a lower NEP. If the bolometer elements are absorbing a small fraction of radiation, remounting the elements to a more efficient FIR absorbing material may be warranted.

FIR Frequency	CO_2 Pump	FIR Medium	Output Power
24.6 cm^{-1}	10R12	CD_3OD	1 μW
42.3 cm^{-1}	9R06	CH_3F	1 μW
84.7 cm^{-1}	9P36	CH_3OH	5 μW
175.4 cm^{-1}	9R8	CH_3OD	.1 μW

Table 4.1: FIR laser output power through table optics with no sample (total factor of $\sim$ 10 attenuation)

4.5 Running the FIR Faraday system

The remaining sections discuss detailed operational aspects of the experiment: bolometer detector cooling, operation and tuning of both lasers, wiring and configuring electronics, Oxford magnet preparation and operation, and data acquisition software concept and instructions.

4.5.1 Detectors

The bolometer detectors require cooling to 4 K or 2 K, depending upon the detector. The vacuum jacket must be pumped down to a pressure of $\sim 10^{-7}$ Torr. Pre-cool the system by filling the liquid nitrogen (LN) and liquid helium (LHe) reservoir with LN. Turn on the power to the FET cold module as well as the pre-amplifier mounted to the bolometer dewar. Ensure that the two 9V batteries are >8V each. Wait approximately 1.5 hours to ensure that the entire system is pre-cooled.

Blow out the LN from the LHe reservoir and transfer LHe. The transfer should take between 15 and 20 minutes. The plume of frozen water vapor emanating from the reservoir will become visibly denser when the LHe reservoir is filled.

4.5.2 Lasers

CO2 laser

Turn on the external water source to the CO_2 chilling system, then turn on the chiller itself which will begin circulating the temperature regulated 50-50 mixture of 99.9% ethylene glycol/distilled water solution through the outer CO_2 laser tube.

Turn on the roughing pump to evacuate the CO_2 laser tube. Turn on the CO_2 laser gas mixture and throttle the flow with the needle valve mounted to the main control panel until the pressure inside the laser tube is 15 mBar.

Ensure the optical path of the output beam is blocked. Turn on the PS4P laser power supply with the current/voltage set on the highest value. Press the high-voltage button in order to begin the ionization process. Turn the pressure up to the recommended value for the chosen laser line by adjusting the throttling needle valve.

Turn on the optical chopper that is mounted inside the CO_2 lasing cavity near the cavity diffraction grating. Mount the pyro-electric detector in the optical path. Connect the output of the detector to an oscilloscope and unblock the CO_2 output. Scan the cavity by adjusting the front piezo-electric crystal via the knob on the CO_2 laser main control panel while concurrently adjusting the angle of the diffraction grating in order to maximize the power output.

Guide the CO_2 beam into the Optical Engineering, Inc. manufactured diffraction grating spectrometer. Adjust the CO_2 diffraction grating until the desired line is lasing as measured by the spectrometer. Maximize the power by adjusting the CO_2 laser current, pressure, as well as the cavity length (front piezo-electric voltage) and the diffraction grating.

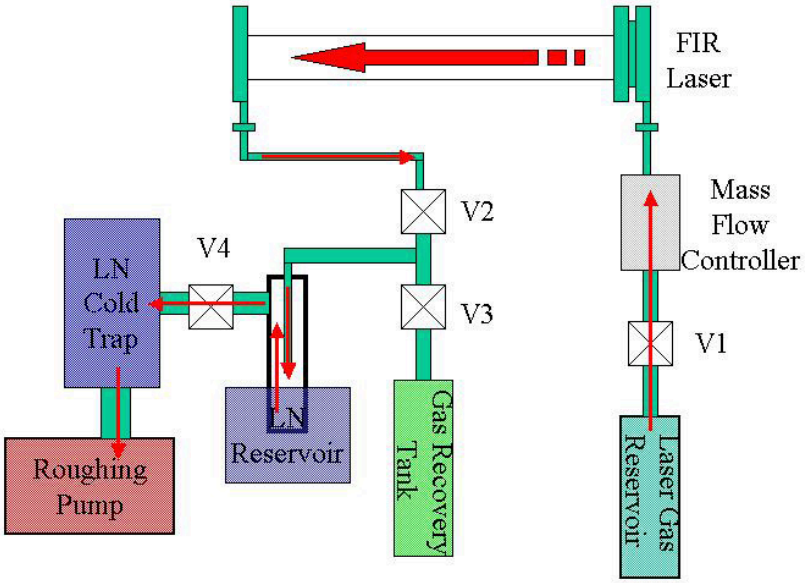

Figure 4.9: Gas handling system for the FIR laser. The letter "V" labels the valves

FIR laser cavity

Using figures 4.9 and 2.8 for reference, pump out the FIR laser system with the roughing pump. Make sure that valve 'V1' is open, and that the mass flow controller is in purge mode. Fill both cold traps. After the base pressure reaches $\lesssim$ 3 mTorr, activate the mass flow controller feedback loop (cease purge mode) and open the laser gas reservoir valve that precedes valve 'V1' (not shown in diagram). Flush the system for about 1/2 hour.

Align the CO_2 beam with the input coupling hole by using the method outlined in section 4.3.1. Note that this alignment is altered every time the CO_2 lasing line is changed.

Set the gas flow rate such that the pressure inside the FIR laser cavity is at the

desired level. Position a bolometer detector at the output of the FIR laser. Make sure the beam is modulated either by chopping inside the CO_2 cavity or by chopping the FIR output since the bolometer pre-amplifier is ac- coupled. It is imperative that the CO_2 beam is blocked with a quartz filter at or after the output coupler of the FIR laser. Attach the bolometer to an oscilloscope triggering on the chopper.

Begin searching for an FIR lasing signal by adjusting the CO_2 laser's piezo. Concurrently translate the output coupling mirror of the FIR. If the coarse alignment was done reasonably well, you should see the oscilloscope signal jump when passing through a resonance. Tune into a resonance and maximize the signal. Compare the power output to previously attained values. If the power is low, translate to a new mode. If all modes appear too low, then begin adjusting the tilt of the input and output coupling mirrors in order to search for the T00 mode.

Once the power output is maximized, perform a SPECAC scan on the laser line to ensure that one mode is lasing (see section 4.3.3).

Place the transmission bolometer on the optics table. Maximize the signal by finely tuning mirror M2 (see figure 2.3). Make sure that the spatially filtering aperture is set at a diameter of $\lesssim$2mm to ensure that the beam is accurately propagating through the sample location. Once aligned, make sure that the FIR beam is centered on all optical components. By partially blocking the beam and watching the oscilloscope signal, a good estimate of the center of the beam can be made.

To recapture the FIR laser gas after completing a data run, shut-off valves V1, V2, V3, and V4. Insert the gas recovery tank into a bath of LN. Open up the recovery tank valve as well as valve V3. Remove the LN bath cooling the pyrex tube cold trap and heat the tube. Cryopump all contents into the recovery tank and valve off the

tank. Heat the recovery tank to room temperature under supervision to ensure the tank does not become over-pressurized.

4.5.3 Electronics

Set up the electronics as shown in figures 2.5 and 2.6. Adjust the speed of rotation of the rotator and chopper to 311Hz and 32Hz, respectively.

The output of the transmission bolometer (either the pre-amp output or the cold stage FET at point "Vs", depending upon the magnitude of the signal) should be attached to the EG&G Instruments (Princeton Applied Research) model 5113 pre-amplifier. The 5113 should be set to dc- mode with band-pass filtering set to reasonable values (I use 6db/octave at 3Hz and 3kHz), high-dynamic range, and a gain between 1 and 750. The 5113 serial communication should be attached to the main control computer. The output of the 5113 should be attached to the oscilloscope as well as one EG&G lock-in amplifier configured such that it is run with an FET input setting (1kΩ input impedance), time constant of 500msec, single reference mode, rear panel TTL reference, sensitivity set to no more than 3 times the maximum voltage expected, a unique GPIB address, and first harmonic mode.

The reference bolometer pre-amplifier output should be connected to a separate EG&G lock-in amplifier in exactly the same way. The TTL output of the chopper controller should be connected to the rear panel reference input.

The output of the 5113 pre-amplifier should also be connected to a second lock-in amplifier. The rotator controller TTL output connects to the rear TTL reference input. The lock-in should be configured for dual-harmonic mode, FET input setting (1kΩ input impedance), time constants of 500msec, rear panel TTL trigger, the 2 sep-

arate sensitivity scales set to no more than 3 times the maximum voltages expected, a unique GPIB address, and the second and fourth harmonics selected.

Connect the GPIB I/O ports of the three EG&G lock-in amplifiers and the Lakeshore 340 temperature controller to the control computer.

The Lakeshore 340 temperature controller thermometer and heater inputs attach to the appropriate pins of the Oxford sample stick (see appendix E for wiring details). Configure the controller settings: the heater to 2.5W max, the PID constants to manual (100, 100, 3), a unique GPIB address, the units of the thermometers to Kelvin, thermometer A as the control thermometer for Loop 1 (the high powered 2.5W heater loop), disable loop 2, and the resistance of the heater to 400 Ω. Load the appropriate cernox calibration curves (thermometer serial numbers are given in appendix A) from the control computer. Adjust the set-point to a value slightly above the current temperature. Make sure the thermometers show the correct values with the heater on to ensure that the thermometer itself is not shorted to the copper sample mounts.

For the purposes of testing computer control and data acquisition, short the Oxford magnet controller output as well as the heater switch. Connect the main control computer serial cable to the Oxford PS120-10 power supply.

4.5.4 Oxford magnet

Cooling the magnet

The Oxford magnet dewar vacuum jacket should be pumped to a base pressure of 10^{-7} Torr before pre-cooling. This requires at least one full day of pumping with the small diffusion pump equipped mobile stations due to the out-gasing of charcoal

mounted to the outside of the LHe reservoir.

The day before beginning a data run, the magnet should be pre-cooled to LN temperatures. Turn on the blower for the vacuum windows. Pump (with a large roughing pump) and purge the LHe reservoir with dry N_2 gas 4 times. Throttle the vacuum pump to ensure that you do not overload the pump (subsequently burning up the motor) or blow out the lubricating oil. *Be absolutely certain that the magnet dewar vacuum jacket is always maintained at a lower pressure than the LHe reservoir so that the thin stainless steel reservoir does not implode! Make sure that the inner jacket is cooled completely before cooling the outer LN jacket to ensure that thermal contraction neither causes damage to the copper bore insert tubes nor the magnet itself.*

The LN transfer rate can be quite high without significantly raising the pressure of the LHe reservoir ($\lesssim$ 3 PSI when the LN dewar pressure is $\approx$ 20 PSI during the transfer). The transfer should take no less than three hours. When completed, ensure that no water condenses into the system by attaching a one-way valve capping the reservoir. I usually do this by attaching a homemade vacuum line manifold which incorporates a 1 PSI relief valve. This maintains a 1 PSI positive pressure of N_2 boil-off gas.

Fill the LN jacket with LN. The outer jacket should fill within an hour.

The system should pre-cool for at least 4 hours (this ensures that the system does not warm up too much overnight). Blow out the LN from the LHe jacket. To do this, use pressures $\lesssim$ 10 PSI on the reservoir.

Attach a He gas cylinder to the now empty LHe reservoir. With a relief valve in place, regulate the pressure of the He gas to be slightly less than that of the relief

valve. Note that I actually used the CVL (part# 120-BA Type 100LR) pressure regulator as the relief valve and regulator, and maintained a pressure of 2 PSI. Let the inner LHe reservoir warm above LN temperature by leaving the system in this configuration overnight. This ensures that *all* the LN will be eliminated from the reservoir to prevent ice (frozen N_2) from forming on the magnet when transferring LHe. About 1/4 of the gas in a full "A" cylinder will be lost overnight in this configuration.

The next day, check the thermometers with the Keithley 197 mounted in a home-made switch box (shown in figure 2.11). Choose the "LP" (lowest point in the magnet dewar) thermometer and make sure that the temperature is slightly above LN temperature (<177 Ω). Pump and purge the LHe reservoir with dry He gas 4 times.

Begin the transfer. Insert the transfer tube into the mobile LHe dewar and pressurize to 1.8 PSI. The transfer should take approximately 3 hours. The LP thermometer should very slowly increase towards 944 Ω, at which point the He will begin condensing. At this point, increase the pressure in the dewar to 2 PSI to increase the flow rate. Turn on the He level detector (Oxford model $ILM^2$10) to monitor the fill progress. When the 100% fill point is reached, the magnet is truly filled and the plume will quickly change to a visibly denser cloud.

The plume size is by far the most sensitive control parameter in maximizing the efficiency of the transfer. I was able to completely fill the magnet three times with one 100L dewar by maintaining a plume size of 1/3 to 1/2 meter during transfers. Finely tune the pressure to maintain this plume size.

Once the dewar is full, maintain a positive pressure of He gas to ensure that no water/N_2/O_2 is cryopumped into the bath.

Refilling the magnet is very similar. The only difference is that you do not want to blow out the existing LHe in the bath by blowing warm He gas into it. To avoid this, cool down the transfer line until a dense white cloud is emanating from the tip. Quickly stop the LHe flow by venting the LHe dewar, and immediately insert the transfer tube into the Oxford (you want to minimize icing of the transfer line tip). Re-pressurize the dewar and liquid helium will immediately begin transferring to the bath.

It is important to note that the magnet is nearly empty at a reading of 30% on the LHe level detector allowing no more than one complete magnet sweep (-8 to +8T) before warming above LHe temperatures.

To completely fill the magnet from 77 K should take about 40-45L of LHe. To refill the magnet at a reading of $\sim 30\%$ on the level detector should take about 25L.

Inserting the sample stick into the Oxford dewar

Refer to figure 4.10.

Make sure that the sample stick's stainless steel sheath is coated with a clean layer of vacuum grease. Also ensure that the o-rings in the two valves attached to the Oxford sample stick bore are clean and well lubricated as well as the three o-rings located in the bore itself. Slide the sample stick into the bore.

Open both valves directly attached to the bore. Attach a pump station as shown in figure 4.10 and pump the system down to $\approx 10^{-7}$ Torr. Open the Oxford vacuum jacket ball valve at the base of the Oxford sample stick bore tube and immediately close valve #1. Monitor the pressure on the pump station at all times! Begin sliding the sample stick into the magnet dewar. If the pressure rises above 10^{-5} Torr, stop

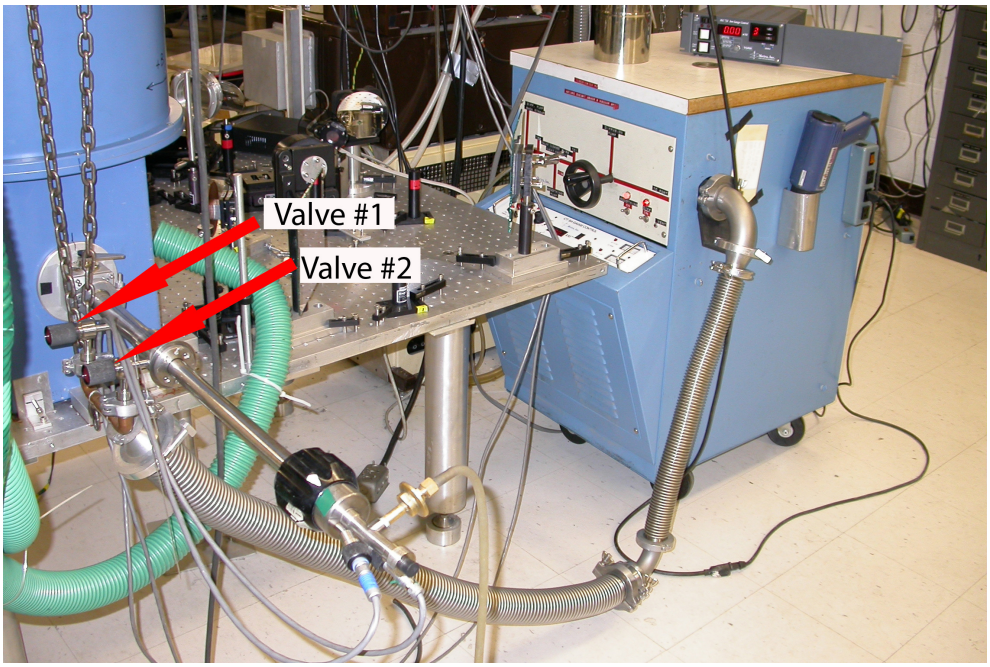

Figure 4.10: Inserting the sample stick into the Oxford dewar.

the motion of the sample stick and wait for the pressure to decrease. Note that this is not the pressure bleeding into the Oxford dewar vacuum jacket, but merely the pressure on the back side of an o-ring. Continue until the sample stick is completely inserted into the Oxford dewar.

Close valve #2. Detach the pump station vacuum lines. Vibrational noise from the pump station adversely effect the bolometers.

Note that once the sample stick is cooled, the o-rings become chilled. Moving the sample stick in and out of the Oxford sample stick bore tube should be done extremely slowly. Watch the pressure on the pump station.

Cooling the sample stick

The continuous LHe flow cooling of the sample stick is throttled with a built-in needle valve in the transfer line. I found that the best parameter for controlling the flow rate is the pressure in the dewar with the needle valve opened about 1/8 of a turn.

Note the transfer line is not long enough to accommodate a 100L LHe dewar.

Slowly lower the transfer line into the dewar with the needle valve fully closed. Use the temperature gradient of the vapors in the dewar to gradually cool the transfer line to minimize LHe boil-off. It should take about 1/2 hour to lower the transfer line completely.

Insert the transfer tube into the sample stick. Open the needle valve roughly 1/8 of a turn, and pressurize the dewar to 6 PSI.

To ensure that the sample stick does not change temperature significantly while heating the sample, a fair amount of cooling power is required. The sample stick should be at roughly 22 K (with the sample heater off and the end of the sample stick clamped).

Plan on using 10 to 15L of LHe per day (that is, per one Oxford magnet fill of LHe) for sample cooling.

4.5.5 Rotator

Inserting waveplates

Rubber cement was used to glue one side of the waveplates to o-rings of the same OD. This allows for easy insertion and extraction from the bore of the rotator with

tweezers.

The rotator bore itself is threaded. A ring whose outer threads match the bore threads is screwed into the bore. An o-ring is inserted and the waveplate (with an o-ring glued to it) is placed such that it is sandwiched between the two o-rings. Two more rings are screwed into place to lock the o-rings and waveplate into place. A fair amount of compression of the o-rings is required to ensure that the retaining rings do not unscrew during the experiment (manifesting as very peculiar phase noise).

4.5.6 Data acquisition/control software

The electronics should be connected as described in section 4.5.3. There should be a serial cable connecting a computer COM port to the Oxford magnet power supply, and a separate cable connecting a separate COM port to the EG&G 5113 pre-amplifier. A GPIB cable should be connecting the computer to all three EG&G lock-in amplifiers as well as the Lakeshore 340 temperature controller.

I wrote a Labview program to control equipment and acquire data. A screen-shot of two different areas of the desktop are shown in figures 4.11 and 4.12.

The program can be run in one of three modes: magnetic field scan, time scan, and x-parameter scan mode.

In summary, the program running in magnetic-field-scan mode initializes all pertinent electronics and begins a magnetic field sweep. The program acquires data from both channels of each lock-in amplifiers, temperature of the sample, magnetic field, and gain of the EG&G pre-amplifier. The program averages this data over some specified window and records the average as a data point. This averaged data is plotted in real time for each channel of each lock-in amplifier versus magnet field. Furthermore,

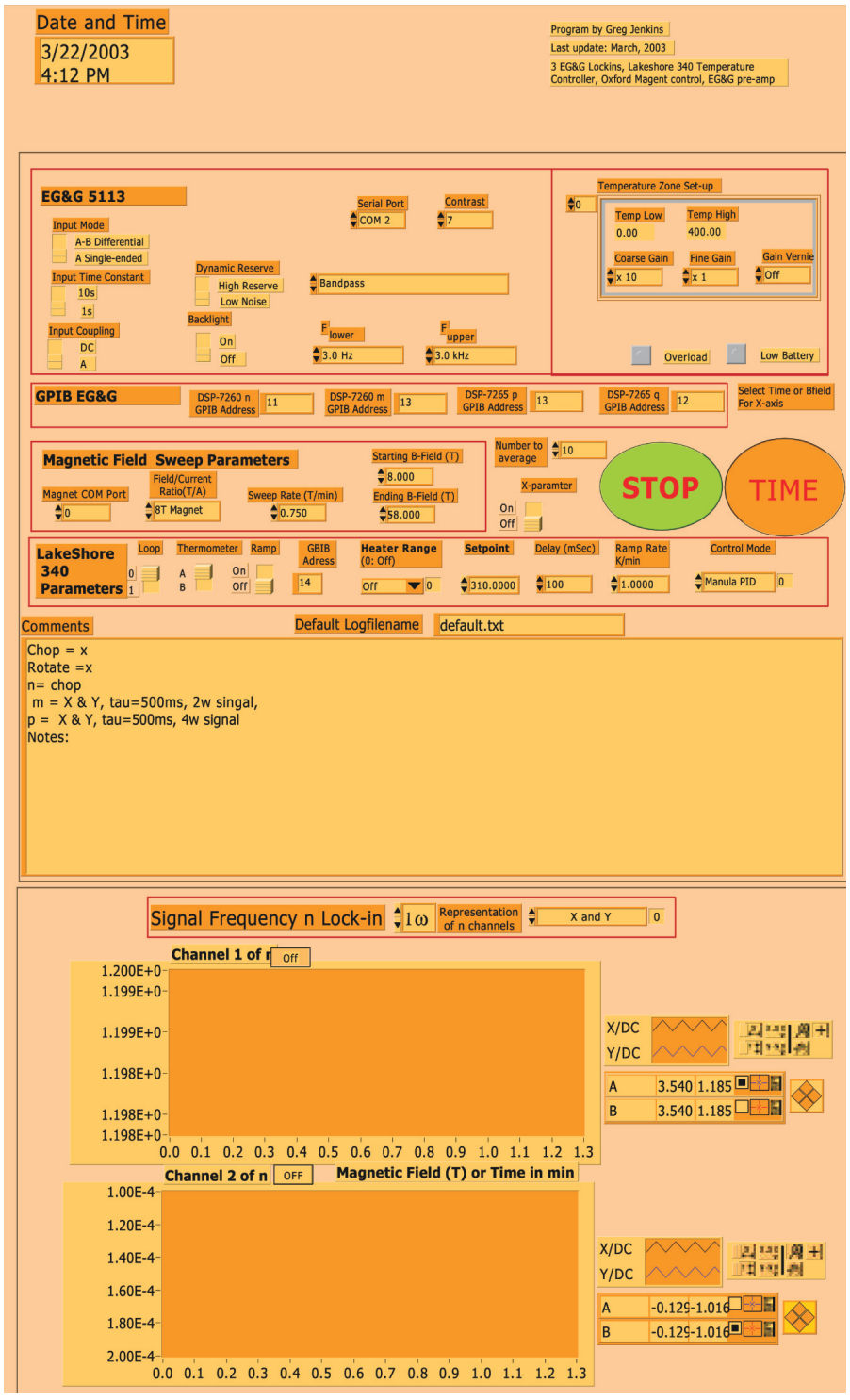

Figure 4.11: Top sections of the main computer control Labview data acquisition software

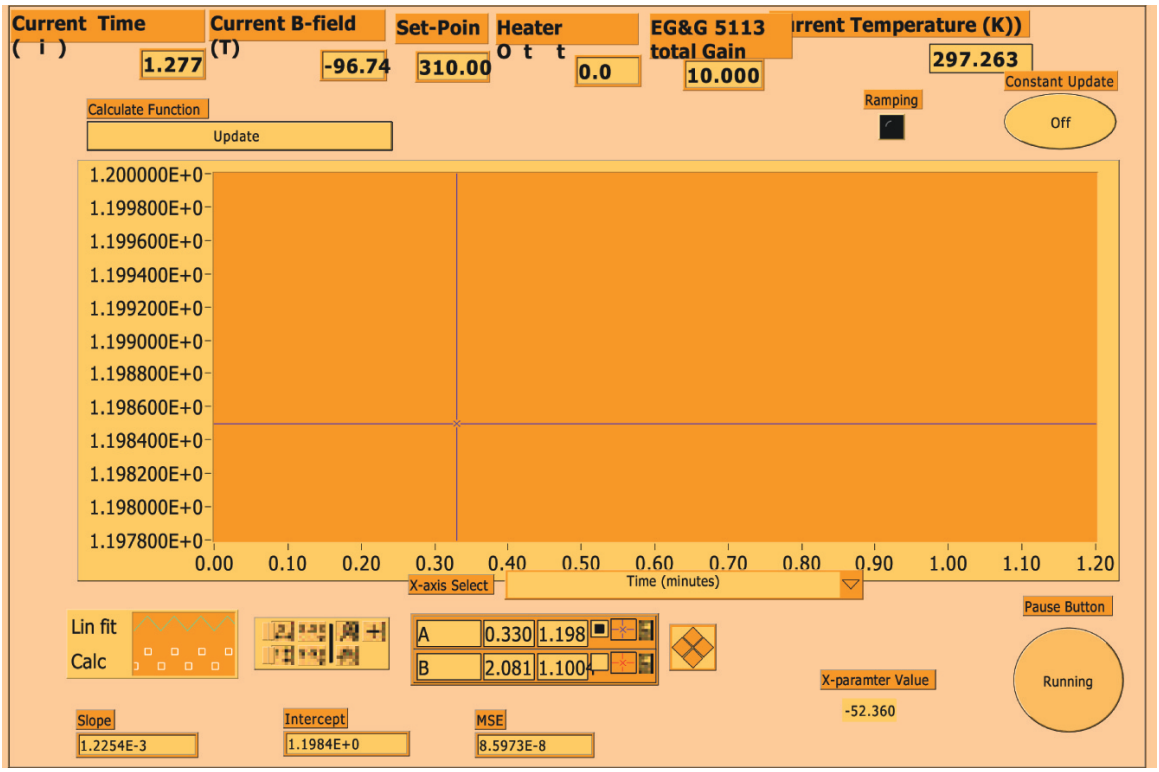

Figure 4.12: Bottom sections of the main computer Labview data acquisition software

as seen in figure 4.12, real-time calculations of equations selected from a pull down menu may be viewed on a graph in real-time.

During temperature-scan mode, the program controls the sweep rate of the sample temperature. Since the transmission signal through the sample changes by orders of magnitude as a function of sample temperature, the gain requires adjustments during the scan. Temperature zones may be defined with different gain settings to automate this process. This ensures that temperature scans are taken in a consistent manor.

The x-parameter mode is the same as time-sweep mode except that a user definable x-value may be inserted in real time by the user. Together with a pause button, this mode is useful when, for instance, you want to calibrate the real part of the Faraday

angle versus a sample polarizer angle. The x-parameter would then be the value of the angle of rotation of the sample polarizer.

The top two main sections of the program are shown in figure 4.11. The top left hand corner contains the initialization setting for the EG&G 5113 pre-amplifier.

The section in the top right corner are the programable gain setting and the corresponding temperature zones. Define a temperature region in the top row, and a gain setting in the bottom row. An unlimited number of zones may be set by stepping through the array. In the example, one temperature zone is set such that if the sample temperature is between 0 and 400 K, then the gain of the EG&G 5113 is set to (or remains) a gain of 10.

The section below the 5113 pre-amp section defines the GPIB addresses corresponding to lock-ins labelled n, m, p, and q. There are only three physical lock-in amplifiers, but one lock-in is set to dual-harmonic mode. For our experiment, this lock-in will measure $X_{2\omega}$, $Y_{2\omega}$, $X_{4\omega}$, and $Y_{4\omega}$. I have divided this one lock-in amplifier into two virtual lock-ins, in this case lock-in m and p (note that they both have the same physical GPIB address 13). I have historically used lock-in n as the transmitted chopped signal, and the q lock-in as the reference chopped signal.

The next section defines the magnetic field sweep parameters for the magnet power supply. The user defines the starting and ending B-field, the sweep rate, and the computer COM port controlling the magnet. The Field/Current ratio, which is a conversion factor for converting electric current to magnetic field, is always set to 8T for the Oxford 8T magnet.

The section below this is the Lakeshore 340 temperature controller initialization settings. The Loop number defines the control loop (see the Lakeshore 340 user

manual for details), the thermometer used to measure the temperature of the sample, a ramp switch which, when on, will ramp the set-point from the current temperature to the temperature defined in the box labelled 'set-point' at a rate defined by 'ramp rate.' The heater power is selectable in decades from 2.5W down to 2.5mW. 'Delay' is used for timing purposes during the initialization and should not be changed from the value of 100 msec for the current computer (appendix A).

The large green 'STOP' button is used to end the data acquisition loop. The data is not saved until this button is pressed. Just to the right is a large oval button which is actually a toggle switch between time scan mode and B-field scan mode. To the left is a toggle switch which selects between time scan mode (off) and x-parameter scan mode (on). The 'Number to Average' slot is the number of points to average for each data point recorded. The number '10' corresponds to ~ 1 second in the present configuration.

Below the initialization section of the software are four pairs of graphs representing the four lock-in amplifiers with their two channels of information. Figure 4.11 shows one pair of graphs for lock-in n. Here, lock-in n is configured to de-modulate the first harmonic and the channels are represented in terms of X and Y (as opposed to R and θ, or eq1 and eq2, etc.). The graphs will continuously update when the toggle buttons located above each graph are turned 'ON'. The toolbars to the right are standard Labview palette toolbars. There are similar pairs of graphs for lock-ins m, p, and q.

At the bottom of the program (figure 4.12) is a section that allows the user to select functions from a pull down menu (not shown, but is directly above the current window) which are calculated from the data and plotted in real-time. The top row

shows the current time, temperature, set-point, magnet current, EG&G 5113 gain setting, heater output in percent of full scale, and an LED type indicator which, when red, indicates that the set-point temperature is currently ramping. The 'constant update' button toggles between real-time update and the user having to press the 'update' button in order to display the results. Below the graph is a pause button and a slot for the user to input an x-parameter. A real-time linear fit of the calculated values are performed where the slope, intercept, and mean-squared-error are reported, and the fit is superimposed on the graph.

The data is recorded in a tab delimitated text format. Columns are separated by tabs, and the rows are terminated with a carriage return and new-line character. The first row contains the column labels. An 'EOF' string terminates the data, and footer strings are appended to the file which include configuration information and user notes.

4.5.7 Raw data analysis software

It is imperative to analyze the data while acquiring data. Trouble-shooting problems with the Faraday angle measurement requires the calculated Faraday angles! For this reason, I consider the analysis software as integral to the data acquisition software.

Mathematica (version 4.1) is used to analyze all data. I wrote an analysis package called "LVDataAnalysis" and a general purpose package called "GJDataAnalysis" which include many useful functions for manipulating data. The documentation is accessed within Mathematica by typing "?<command>" after loading the packages. I have written many programs to analyze my data that may serve as examples of how

AppendXYFiles	Convertnktos1e1	Convertnktos1s2	ExtractCols
Filmnk	LoadManyColFile	LoadXYFile	LoadXYZFile
MultiZapXY	OperateXYs	Rcomp	Rsubcomp
ScalerMultiplyXY	SmoothXY	SpliceXYs	StripXrepetition
Subnk	Tcomp	TruncateXY	Tsubcomp
WriteFNKFile	WriteManyColFile	WriteXYFile	ZapXY

Table 4.2: Command list of GJDataAnalysis

ExtractCols	LVAppendColumns	LVAvg	LVAvgXrepetition
LVDiff	LVJoinSmoothMC	LVLoadFile	LVOpCol
LVOpCols2files	LVPadXXX	LVSort	LVStripXrep
LVTruncate	LVWriteManyCol	LVWriteNotesFile	LVZapColumn

Table 4.3: Command list of LVDataAnalysis

to implement the functions.

The Labview analysis software requires input filenames of the form "XXT*.txt" where "XX" is a number from 01 to 99 and the letter "T" is a required flag. At the top of a typical Mathematica notebook is a section labelled "user input" where the user inserts a two digit file-number. The user is also required to enter the rotational frequencies of the rotator and chopper in order to correct for detector roll-off, $\Delta\beta$ and $\Delta\Gamma$ waveplate parameters for the particular waveplate in use, the current location of the data directory of the raw Labview text files, and basis-rotation angles for the second and fourth harmonic phases represented by $\alpha 2\omega$ and $\alpha 4\omega$ (see section 4.5.9 for their purpose). All the quantities listed in equations 3.10 are calculated. The values are appended as columns onto the raw data and saved in a directory named "MathematicaResults" one level down from the data directory.

4.5.8 Other data analysis software

There exist quite a few other data analysis programs which utilize the output from the raw analysis program. One program subtracts the Faraday angle temperature scans performed in positive and negative magnetic field and converts the results to the Hall angle. Another curve fits GaAs 2-DEG data. A different program shows the results of many different data runs on one graph.

The modularity of the analysis programs coupled with the data analysis packages provide great flexibility in performing analysis tasks. A complete record of the specific employed analysis method is stored with the raw data. A detailed account is recorded in convenient Mathematica front-end notebooks. This is quite powerful in an environment where the hardware and software associated with the experiment are in constant flux. The downside is that the user **must** be very proficient in using Mathematica in order to take advantage of the pre-existing modular programs.

4.5.9 Acquiring data

I always begin each data run by *in situ* calibration of the rotating waveplate with a sample polarizer (see section 5.6 for an exact procedure). This also provides a quick check of the entire system: the real part of the Faraday angle, $Re(\theta_F)_1$ as defined in equation 3.14 is independent of the waveplate parameters, so the polarizer rotation angle should be equal to the measured real part of the Faraday angle.

It is a good idea to perform two or three B-field scans of a GaAs 2-DEG in order to ensure that the real and imaginary part of the Faraday angle are consistent and no systematic drifts are occurring in the system (see secion 5.2.4 for details). *Always carefully check the optics table and surrounding area for loose magnetic materials*

before beginning a magnetic field scan!

If a 2-DEG is unavailable or the radiation frequency is too high (which is equivalent to the maximum achievable magnetic field being too low), it is recommended that a thin waveplate be used to ensure that the imaginary part of the Faraday angle is correctly measured (see section 5.2.3).

The sample aperture must be concentric with the spot. Ensure the sample stick is cold before aligning ($\lesssim 25K$). First, adjust the horizontal position of the sample stick. This is done by moving the sample aperture through the spot taking note of the two positions where the power is a factor of two less than the peak value. Set the position half-way between these two points. Clamp the sample stick in place using the homemade clamping mechanism located on the side of the magnet dewar opposite the sample stick. Note that this clamp is tightened via rotations in the *counter-clockwise* direction, opposite that of a normally threaded screw. The act of clamping will tend to systematically translate the entire sample stick. Adjust accordingly.

Vertical adjustment is accomplished in the same manor except the entire cryostat must be translated via $4 \times 1/4$-20 screws located on the underside of the optics table directly beneath the magnet dewar.

Once vertically aligned, tighten the PVC pipe brace (between the ceiling and the top of the dewar) via the homemade platform resting on top of the magnet. This will change the vertical alignment slightly. Adjust the 1/4-20 screws beneath the optics table to counter-act the extra downward pressure.

Make sure that all optical components are firmly clamped and that no loose magnetic material is near the magnet. Set the temperature of the sample to a reasonable value. Turn on the persistent mode switch at the magnet power supply. Zero all

lock-in amplifiers in zero field.

Using the data acquisition program, begin a magnetic field sweep. After acquiring the data, use the Mathematica analysis software to calculate the Faraday angle. The zero phase of the 2ω lock-in is found by rotating the phase in the Mathematica analysis software until the imaginary part of the Faraday angle response is maximized (this method is justified in section 5.3.4). Zero the 4ω lock-in phase by rotating the phase in the Mathematica analysis software until the real part of the Faraday angle has zero intercept.

Using the data acquisition software, begin a temperature sweep. Observe the signals on the lock-in amplifiers as the temperature of the sample changes. Write down the EG&G 5113 gain setting required to prevent clipping and the temperature at which a gain change is required. Define the temperature zones and the corresponding gain setting in the Labview data acquisition program.

Continue sweeping magnetic field and performing temperature scans at $\pm$8T. Subtract the real and imaginary part of the Faraday angle acquired at the two magnetic field extremes and convert to the Hall angle.

Chapter 5

Analysis

Before viably obtaining the Hall angle from the raw data, the sample must be characterized and the system calibrated. The first section characterizes the longitudinal conductivity of the BSCCO sample required to convert the Faraday angle to the Hall angle. The next section describes the various calibrations of the system. The last section explains the correction factors required to convert the raw data into the Faraday angle.

5.1 BSCCO sample characterization

5.1.1 Testing of etalon in epoxy

Multiple reflections inside the epoxy between the quartz substrate and BSCCO sample are a concern. It would be very difficult to analyze the Faraday angle data if the impedance mismatch between the quartz and the epoxy were large.

The index of refraction of quartz at room temperature and low frequency is 2.12,[30] and that of epoxy can be found from the published dielectric constant (appendix A),

$\epsilon = 4.1 \Rightarrow n_{epoxy} = \sqrt{\epsilon} = 2.02.$

Geoff Evans independently characterized the epoxy. He epoxied two silicon substrates together. The transmission was measured in the FIR and an etalon pattern was observed. The spacing of the etalon peaks in frequency is related to the index in the following way:

$$
\begin{aligned}
n =& (2d\Delta\nu)^{-1} \\
& \text{where} \\
& \text{n is the index of refraction of epoxy} \\
& \text{d is the epoxy thickness} \\
& \Delta\nu \text{ is the etalon period in the frequency domain.}
\end{aligned}
\tag{5.1}
$$

Cutting the sample with a diamond saw and measuring the thickness of the epoxy layer with an SEM yielded an epoxy thickness of $100 \pm 2\mu m$. The etalon spacing was found to be $24.25 \pm 0.35\ cm^{-1}$ at $100\ cm^{-1}$. This yields an index of refraction of $n \sim 2.01 \pm .09$ which is in agreement with the published value.

He used a second method to verify the first measurement. A very thick impenetrable (at $\sim$100 cm^{-1} where the attenuation is sufficiently large) layer of epoxy was placed on a quartz substrate. Reflection measurements in the FIR reveal an etalon pattern produced within the quartz substrate. The amplitude of the etalon pattern is directly related to the impedance mismatch between quartz and epoxy. Estimates of the index from the etalon amplitude are consistent with the first measurement.

Errors in the Faraday angle experiment associated with multiple reflections can be estimated. Considering only the first order reflection associated with the quartz-

epoxy interface and assuming that the Fresnel reflection coefficient is small at this interface and large at the epoxy-BSCCO interface, in the circular polarization basis we may write:

$$\theta_F = i\frac{t^+ - t^-}{t^+ + t^-}$$

$$t^+ \approx t_0^+(1 + r_{EQ}^+ r_{EB}^+ t_{EQ}^+)$$

$$t^- \approx t_0^-(1 + r_{EQ}^- r_{EB}^- t_{EQ}^-)$$

where the subscripts EQ and EB denote the epoxy-quartz interface and epoxy-BSCCO interface, respectively

r (t) is the Fresnel reflection (transmission) coefficient at a boundary

t_0 denotes a single pass through the entire sample

Let

$$t_{EQ}^{\pm} = t_{EQ} \approx 1 - \varepsilon'_{EQ}$$

$$r_{EQ}^{\pm} \approx \varepsilon_{EQ}$$

$$r_{EB}^{\pm} \approx 1 - \varepsilon_{EB}$$

Keeping only first order terms in epsilon yield:

$$\Rightarrow \theta_F = \theta_{F0}(1 + r_{EQ})$$

Inserting the index of refraction for quartz and epoxy into the reflection Fresnel

coefficient (see appendix F) yields:

$$\begin{aligned} r_{eq} &= \frac{n_1 - n_2}{n_1 + n_2} \\ &= \frac{2.12 - 2.01}{2.12 + 2.01} \\ &\approx .02 \end{aligned}$$

In our experiment, a 2% error in the Faraday angle is negligible compared to other errors in the system.

5.1.2 AC magnetic susceptibility measurement

The ac- magnetic response of the sample was measured using a small ac- driving coil (∼1.5 mm diameter coil driven at 250 kHz) on one side of the sample and a similar pick-up coil on the opposite side. See appendix B for the full details of the apparatus. The changes in magnetic flux through the sample was measured as a function of temperature.

When the sample enters the superconducting state upon cooling below T_c, there is a large phase shift between the pick-up coil and the driving coil due to the inductive nature of the superconducting state (the conductivity is mostly imaginary) compared to the normal state (the conductivity is mostly real). There is also an associated drop in magnitude due to strong shielding currents.[45]

The measured transition temperature of five different nominally optimally doped BSCCO samples are given in figure 5.1. The sample labelled 'BSCCO#3' is our primary sample. The sample labelled 'BSCCO#4' was peeled from the same crystal in exactly the same manor and displays a 3 K shift in T_c. The bulk single crystals

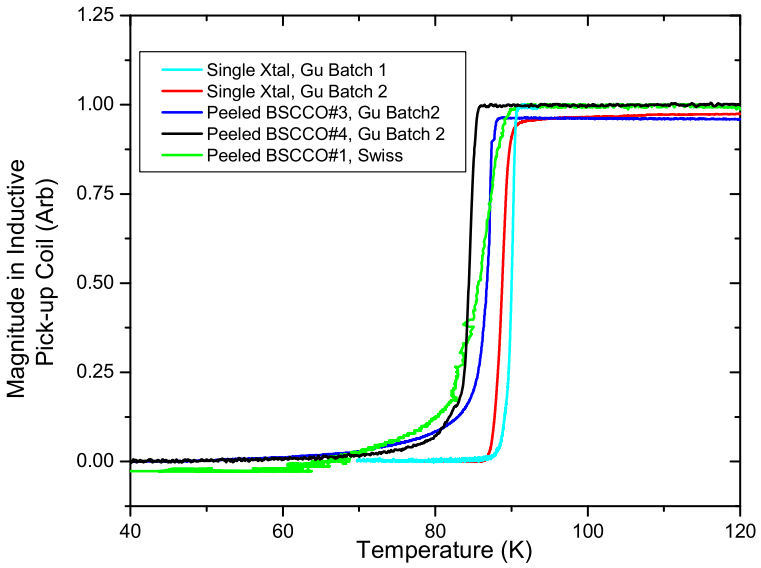

Figure 5.1: ac- magnetic susceptibility measurements of various (nominally) optimally doped single crystal BSCCO samples. BSCCO#3 (blue) is our main sample. BSCCO#4 (black) and both bulk single crystals (cyan and red) were diced from different parts of the same crystal.

consistently show sharper, higher transition temperatures. However, even the bulk crystals demonstrate some variation in T_c. A 5 K spread in T_c is, evidently, typical due to inhomogeneities present in the as-grown parent crystal.

The remainder of this section is focussed on the possible reasons the bulk crystals exhibit slightly higher transition temperatures.

The samples may be inherently inhomogeneous on each layer thus showing a sharper transition for the thicker bulk crystal due to averaging over many more layers.

The peeled samples which are epoxied to a quartz substrate experience thermal stresses which may reduce T_c. We can estimate the stress-induced shift in T_c given the difference in the thermal coefficient of contraction of BSCCO and epoxy, the hy-

drostatic pressure-induced coefficient of contraction, and the change in T_c associated with a change in hydrostatic pressure:

Thermal coefficients of contraction:

BSCCO: $\alpha_a = 7.5 \times 10^{-7}/K$ [46]

Epoxy: $\alpha_{Epoxy} = 5 \times 10^{-5}/K$ (appendix A)

Pressure coefficient of contraction:

BSCCO $\alpha_P = 2 \times 10^{-3}/GPa$ [47]

Pressure induced change in T_c:

$\Delta T_c = 3K/GPa$ [48]

The thermal stress induced by a temperature change from 300 to 100 K is equivalent to a hydrostatic pressure given by:

$$\Delta P = \frac{(\alpha_a - \alpha_{Epoxy})200K}{\alpha_P}$$

The change in T_c associated with a pressure of this magnitude is given by:

$$\begin{aligned} \Delta T_c &= 3K/GPa * \frac{\alpha_a - \alpha_{Epoxy}}{\alpha_P} \\ &\approx 15K \end{aligned} \tag{5.2}$$

This is substantially larger than the observed shift. However, the accuracy of the calculation is limited due to the unknown changes in α_{Epoxy} with temperature. It is likely that α_{Epoxy} significantly decreases with decreasing temperature as other typical polymers.[49] Furthermore, the coefficient of contraction of quartz is 7.1×10^{-6}/K.

There will exist stress between the epoxy and the quartz which will tend to decrease the effective value used in equation 5.2. If we substitute the value of quartz in equation 5.2 in place of α_{Epoxy}, we obtain a shift in T_c of 1.9 K. This is approaching the observed shift.

Note that the above analysis assumes that the a- and b- axis behave in the same manor, and that the c-axis contraction does not contribute to a shift in T_c. From reference 50 and 46, it is experimentally demonstrated that this is indeed the case.

The peeling process may damage the crystal in some way. It is known that depositing an AR coating onto the back of a quartz substrate with a mounted peeled BSCCO crystal causes no extra shift or widening of T_c, so the damage would necessarily be caused by the epoxy or the physical peeling of the sample. The electronic properties may be effected by the presence of other layers causing a higher, sharper T_c. However, pressure studies applied along the c-axis suggest that interaction between layers has little effect on T_c.[50]

It should be noted that thin films epitaxially grown on substrates (I have measured various YBCO and BSCCO samples on MGO, Si with a YSZ buffer, and LAO) universally show a similiar foot in the ac- susceptibility response, and typically show a wider transition temperature compared to large single crystals.

Recent STM experiments measure severe variations across the surface of BSCCO of the superconducting gap magnitude.[51,52] However, as Loram points out,[53] this is most likely due to anomalous effects associated with surface states. Heat capacity, NMR, and magnetic susceptibility experiments are able to probe the bulk properties revealing a much more homogeneous gap function. The universal increase in transition widths observed in thin films compared to bulk crystals may be a manifestation of

the much larger surface-to-volume ratio.

5.1.3 Obtaining $\sigma_{xx}d$

In order to convert from the Faraday angle to the Hall angle, the correction factor given in equation 3.39 requires the value of $\sigma_{xx}d$. It is possible to extract $\sigma_{xx}d$ directly from transmission data. The complex conductivity of BSCCO is known to approximately obey a simple Drude model in the FIR.[11] If the transmission as a function of frequency and temperature are known, it is possible to extract the Drude parameters (scattering rate and mass) directly from the transmission data.

The correction factor appearing in equation 3.39 is itself complex. This effectively mixes real and imaginary parts of the Faraday angle in the Hall angle conversion. It should be noted, however, that the correction is quite small, $\lesssim 15\%$ in the worst case scenario. Only gross errors in $\sigma_{xx}d$ will effect the final Hall angle results.

Ideally, the absolute transmission as a function of both temperature and frequency can be directly measured with a spectrometer. A substrate with known optical properties or an exact duplicate substrate for normalization is required. Unfortunately, in the case of our BSCCO-epoxy-quartz sample, there is no exact duplicate substrate (epoxy-quartz sample) nor are the exact optical properties of the epoxy known since the thickness is unknown. This severely complicates the analysis.

The transmission of a thin film on a substrate with respect to the substrate is given by (appendix F):

$$T = \frac{1}{|1 + Z\ \sigma_{xx}d|^2} \tag{5.3}$$

Within an extended Drude model,[54] the conductivity is given by:

$$\sigma_{xx} d = \frac{\Omega^*}{\gamma^* + i\,\omega}$$

where

$$\Omega^* = \frac{n\ e^2\ d}{m^*}$$

γ^* is the effective electronic scattering rate

m^* is the effective mass

ω is the frequency of radiation

n is the electron density

e is the charge of the carriers

(5.4)

Brief overview

The following analysis becomes quite tedious, so a brief overview of the procedure is in order. Before beginning, however, it should be noted that the same final Hall angle is obtained using σ_{xx} measured by Tu[10] on similar BSCCO crystals.

The transmission of the BSCCO-epoxy-quartz sample is measured in a spectrometer at 300 K relative to a quartz substrate, and the dc- extrapolation yields γ/Ω of the BSCCO crystal. A reasonable scattering rate is assumed ($\sim$ 350 cm^{-1}) and the complete transmission as a function of frequency at 300 K is constructed using a Drude model for a BSCCO-quartz sample. Since the epoxy alone was determined to be temperature independent, the transmission of the BSCCO-epoxy-quartz sample measured at 200 K and 100 K are divided by the 300 K transmission data, and then multiplied by the modelled transmission of a BSCCO-quartz sample. Fitting to a

Drude model yields γ and Ω at 200 and 100 K as a function of frequency.

The transmission of the BSCCO-epoxy-AR quartz as a function of temperature at a discrete set of frequencies measured in the Faraday experiment is normalized to the 300 K spectroscopic transmission. Furthermore, the transmission data is corrected due to the significant temperature dependence of quartz. Once the absolute transmission of BSCCO as a function of temperature is determined, the zero temperature extrapolation yields Ω_S, the superconducting spectroscopic weight $n_S e^2/m^*_S$. Ω_N, ne^2/m^* in the normal state, is set equal to Ω_S.[11] Fitting the transmission as a function of temperature yields γ as a function of temperature. With Ω_N, Ω_S, and γ determined, $\sigma_{xx}d$ is calculated as a function of temperature at the relevant set of frequencies.

Transmission as a function of frequency at 300, 200 and 100 K

A Bomem DA.3 was used with a 12 μm mylar beam splitter, a 2 K bolometer detector, a continuous flow Janos cryostat with mylar vacuum windows, and a mercury vapor lamp as a broad-band FIR light source. Transmission data of the BSCCO-Epoxy-AR coated quartz sample was taken at 100, 200, and 300 K using an AR coated quartz substrate as a reference.

Unfortunately, the transmission of the epoxy is significantly frequency dependent in the FIR. The epoxy is slightly temperature dependent. In order to properly characterize the transmission of BSCCO, the temperature and frequency dependence of the epoxy was determined separately. Three separate samples were mounted in an Infrared Laboratories dewar that allows concurrent temperature regulation of up to 4 samples. The transmission of a free standing epoxy film, an AR-coated quartz sub-

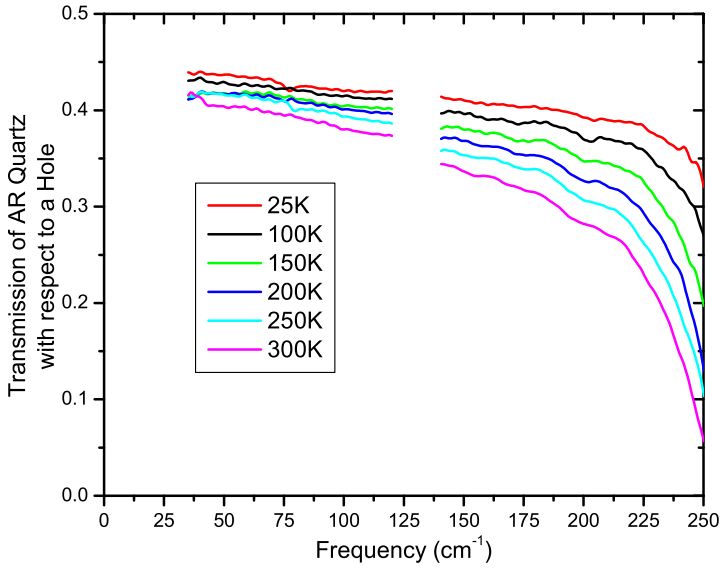

Figure 5.2: Temperature dependent transmission of a .02" thick z-cut quartz substrate. The obvious gap at 130 cm^{-1} is a manifestation of a phonon absorption feature.

strate, and a sample made from epoxy sandwiched between two .5mm thick wafers of high resistivity ($\gtrsim$ 10 M$\Omega/\square$) silicon, were all measured with respect to an open hole at 300, 250, 200, 150, 100, and 25 K. The results are displayed in figures 5.2 through 5.3.

The transmission is necessarily an even function of frequency. We expect the zero frequency extrapolation of the Si-Epoxy-Si sample to approach the transmission of bare silicon at zero frequency, $T_{BareSi} = .539$ for $n_{Si} = 3.12$.[30] Fitting the 300 K curve to a fourth degree even polynomial yields, at zero frequency, a transmission extrapolated value of .538 (see figure 5.3).

Fitting the transmission of the BSCCO-epoxy-quartz sample in precisely the same manor, we expect the zero frequency extrapolation to be the bare transmission of a

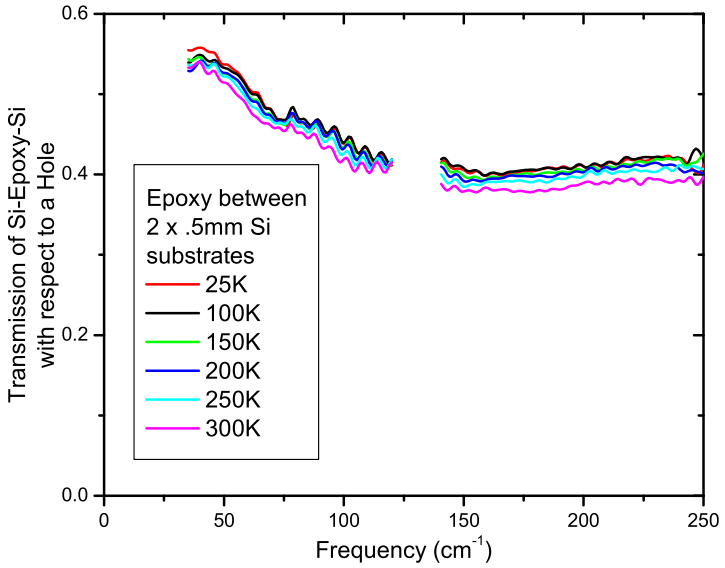

Figure 5.3: Temperature dependent transmission of an epoxy film of unknown thickness between two .5 mm thick silicon substrates.

(hypothetical) BSCCO-quartz sample.

Taking our value of the zero frequency extrapolation of the transmission for the BSCCO sample, we now know the 300 K value of Ω/γ at zero frequency. Assuming a reasonable scattering rate value at room temperature, γ_{300K}, and inserting our dc-value of Ω and γ into a Drude model, the transmission of a BSSCO-AR coated quartz sample can be calculated.

The ratios of the 100 and 200 K transmission data to the 300 K transmission data multiplied by the modelled 300 K BSSCO-AR coated quartz sample transmission yields the transmission of a BSSCO-AR coated quartz sample at 100 and 200 K. Curve fitting with a Drude model gives Ω and γ at 100 and 200 K. The conductivity can be calculated at 100 and 200 K over the frequency range of 20 to 240 cm^{-1}.

The entire described analysis can be written in mathematical form as the following:

$$\begin{aligned}\frac{T_{BSCCO}|_t}{T_{ARQ}|_t} &\approx \frac{T_{BSCCO}|_t}{T_{EBQ}|_t} \times \frac{T_{EBQ}|_t}{T_{EBQ}|_{300K}} \\ &\times \frac{T_{EBQ}|_{300K}}{T_{BSSCO}|_{300K}} \times \frac{T_{BSCCO}|_{300K}}{T_{BQ}|_{300K}} \times \frac{T_{BQ}|_{300K}}{T_{ARQ}|_{300K}} \\ &= \frac{(T_{BSCCO}/T_{EBQ})|_t}{(T_{BSCCO}/T_{EBQ})|_{300K}} \times \frac{T_E|_t}{T_E|_{300K}} \\ &\times \frac{T_{ARQ}|_{100K}}{T_{ARQ}|_{300K}} \times \frac{T_{BSCCO}}{T_{BQ}}|_{300K} \times \frac{T_{BQ}|_{300K}}{T_{ARQ}|_{300K}}\end{aligned} \tag{5.5}$$

where

T denotes Transmission

t denotes either 100 K or 200 K

ARQ denotes AR-coated Quartz (5.6)

BQ denotes Bare Quartz

E denotes Epoxy

EBQ denotes Epoxy and Bare Quartz

The first factor is the ratio of the measured transmission of our BSCCO-epoxy-quartz sample taken at two different temperatures. The next factor is the ratio of the transmission of the free-standing epoxy film taken at two different temperatures. The third factor is the ratio of transmission of AR-coated quartz taken at two different temperatures. The fourth factor is the Drude modelled 300 K transmission based upon the zero frequency extrapolated transmission value. The last factor is a scaling factor due to the AR-coating directly calculated using the published value of the index of quartz (2.12), and the known sheet resistance of the AR-coating (338 $\Omega/\Box$).

Temperature	Ω_N	γ	γ/Ω_N
300 K	1550 $\Omega^{-1}cm^{-1}$	350 cm^{-1}	.23 Ω
200 K	1414 $\Omega^{-1}cm^{-1}$	232 cm^{-1}	.16 Ω
100 K	1434 $\Omega^{-1}cm^{-1}$	115 cm^{-1}	.08 Ω

Table 5.1: Bomem measurements where $\gamma|_{300K} \equiv 350\ cm^{-1}$

The main assumption made in the above analysis was in choosing the 300 K scattering rate. The transmission at the frequencies of interest are not significantly perturbed by errors in the chosen scattering rate since the highest frequency of interest (175 cm^{-1}) is much smaller than the scattering rate at 300 K ($\sim 300\ cm^{-1}$) :

$$\frac{T_{BSCCO}(\omega)|_{300K}}{T_{BSCCO}(\omega \to 0)|_{300K}} \approx 1 + \left(\frac{\omega}{\gamma}\right)^2$$

Transmission as a function of temperature at 24, 42, 84, and 175 cm^{-1}

The transmission as a function of temperature of our BSCCO-epoxy-AR coated quartz sample is measured directly in the Faraday experiment. The data is acquired concurrently with the Hall angle measured in $\pm 8T$. The chopped transmitted bolometer signal is normalized to the chopped reference bolometer signal. Note that the transmission, and consequently $\sigma_{xx}d$, is effected by magnetic fields at low frequency and temperature.[24]

Unfortunately, as shown in figures 5.2 and 5.3, the quartz substrate and the epoxy contribute to the temperature dependent transmission measurement. Since the quartz is AR-coated and the index of epoxy matches that of quartz, the transmitted beam makes a single pass through the sample. Therefore, the temperature dependence of the quartz and epoxy measured separately can be used to cancel out their contribution

to the transmission. The data is then normalized to the 300 K Bomem transmission measurement. The final absolute transmission of BSCCO (normalized to an idealized AR-coated quartz substrate at 300 K) as a function of temperature at one particular frequency is given by the following:

$$\frac{T_{BSCCO}(t)}{T_{ARQ}|_{300K}} \approx \frac{T'_{BSCCO}(t)/T'_{EARQ}(t)}{T'_{BSCCO}(300K)/T'_{EARQ}(300K)} \times \frac{T_{BSCCO}|_{300K}}{T_{ARQ}|_{300K}} \times \frac{T_E(t)}{T_E(300K)} \times \frac{T_{ARQ}(t)}{T_{ARQ}(300K)} \tag{5.7}$$

where

T denotes transmission

T' denotes transmission data from the Faraday experiment

t denotes temperature as a continuous variable

ARQ denotes AR-coated Quartz

BQ denotes Bare Quartz

E denotes Epoxy

EARQ denotes Epoxy and AR-coated Quartz

The first and second factor are the measured transmission from the Faraday experiment as a function of temperature scaled to the 300 K value found in the previous section, 5.1.3. The third factor is the temperature dependent transmission of the epoxy. The data shown in figure 5.3 has been interpolated so as to construct a continuous function of temperature at a specific frequency. The temperature dependence of quartz represented by the fourth factor is found in a similar manor (results are shown in figure 5.2).

Frequency	Transmission	$\Omega_N \equiv \Omega_S$	$\gamma\|_{300K}$
24 cm^{-1}	3.2 $\times 10^{-4}$	1375 $\Omega^{-1}cm^{-1}$	320 cm^{-1}
42 cm^{-1}	6.7 $\times 10^{-4}$	1630 $\Omega^{-1}cm^{-1}$	370 cm^{-1}
84 cm^{-1}	17.5 $\times 10^{-4}$	2020 $\Omega^{-1}cm^{-1}$	466 cm^{-1}
175 cm^{-1}	75.7 $\times 10^{-4}$	2007 $\Omega^{-1}cm^{-1}$	475 cm^{-1}

Table 5.2: Parameters from the zero temperature extrapolation of the transmission

Calculation of $\sigma_{xx}d$ at 24, 42, 84, and 175 cm^{-1}

The absolute transmission of BSCCO (with respect to a temperature independent substrate) as a function of temperature at our desired frequencies has been obtained as discussed in the previous two sections. Equation 5.3 is inverted to give $\sigma_{xx}d$ in terms of the transmission. Using the Drude parameterization given in equation 5.4, we can solve for Ω as a function of γ and the transmission:

$$\Omega(t) = \gamma(t) + \sqrt{\frac{\gamma(t)^2 + \omega^2}{T(t)} - \omega^2}$$

where

T is the transmission relative to a substrate

t is temperature (5.8)

At zero temperature, we expect the FIR scattering rate to approach zero.

$$\Omega_S \equiv \Omega(t \to 0) = \omega \left(\frac{1}{\sqrt{T(0K)}} - 1 \right) \tag{5.9}$$

The amount of spectroscopic weight in the normal state that condenses into the

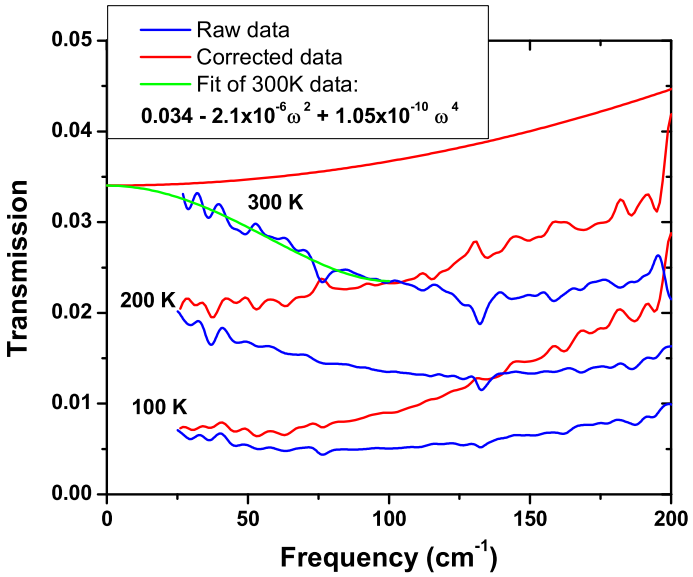

Figure 5.4: The raw transmission curves of the BSCCO-epoxy-AR quartz sample with respect to an AR-coated quartz substrate at (from top to bottom) 300, 200, and 100 K are plotted in blue. The green curve is the zero frequency extrapolation of the 300 K transmission curve via an even 4th order polynomial fit. The top red curve is the modelled Drude transmission based upon the DC extrapolated value of Ω/γ and an assumed scattering rate of 350 cm^{-1}. The remaining two red curves are the 100 and 200 K data normalized to the 300 K model.

superconducting state has been measured,[11] and to a good approximation $\Omega_S = \Omega_N$ (the normal state Drude plasma frequency at 100 K found using a 2-fluid analysis equals the 20 K superfluid plasma frequency). In section 5.1.3, values of Ω_N were found at temperatures 300, 200, and 100 K and show very little temperature dependence. The values of Ω_N are also approximately equal to the values found for Ω_S (see tables 5.1 and 5.2).

Knowing Ω_N at the relevant set of frequencies, we can calculate γ as a function

of temperature.

$$\gamma(t) = \frac{T(t)\Omega_N + \sqrt{{\Omega_N}^2 T(t) - \omega^2(1-T(t))^2}}{1-T(t)} \tag{5.10}$$

The values of γ as a function of frequency in table 5.2 agree well with other published values.[10]

Inserting the parameters $\gamma(t)$ and Ω found at each frequency into equation 5.4 yields the desired result:

$$\sigma_{xx} d(t) = \frac{\Omega_N}{\gamma(t) - i\omega} \tag{5.11}$$

The final result of the complex conductivity as a function of temperature for 24.6, 42.3, 84.7, and 175.4 cm^{-1} is plotted in figure 5.5. The figure shows, as stated earlier (see equation 5.1.3), that the initial chosen γ_0 at 300 K (in the range of 300 to 500 cm^{-1}) has virtually no effect on $\sigma_{xx}d$ for the lowest three frequencies, 24.6, 42.3, and 84.7 cm^{-1}.

It is possible to estimate the error introduced into the Faraday to Hall angle conversion from errors in $\sigma_{xx}d$. As a worst case scenario, the 175.4 cm^{-1} at room temperature shows a 15% spread for the imaginary part of $\sigma_{xx}d$, and a 10% spread

for the real part of $\sigma_{xx}d$ caused by choosing γ_{300K} in the interval 300 to 500 cm^{-1}.

$$\begin{aligned}
&\theta_H = (\frac{1}{Z\ \sigma_{xx}d} + 1)\theta_F \\
&\Rightarrow Re(\theta_H) = \left(\frac{Re(Z\ \sigma_{xx}d)}{|Z\ \sigma_{xx}d|^2} + 1\right) Re\,(\theta_F) + \frac{Im(Z\ \sigma_{xx}d)}{|Z\ \sigma_{xx}d|^2} Im(\theta_F) \\
&\Rightarrow Im(\theta_H) = \left(\frac{Re\,(Z\ \sigma_{xx}d)}{|Z\ \sigma_{xx}d|^2} + 1\right) Im(\theta_F) + \frac{Im(Z\ \sigma_{xx}d)}{|Z\ \sigma_{xx}d|^2} Im(\theta_F) \\
&\qquad \text{For } 175\ cm^{-1} \text{ at } 300 \text{ K} \\
&\qquad\quad Im(Z\ \sigma_{xx}d) \sim 1.5 \pm .1 \\
&\qquad\quad Re\,(Z\ \sigma_{xx}d) \sim 5 \pm .25
\end{aligned} \tag{5.12}$$

$$\begin{aligned}
Re(\theta_H) &\approx (1.18 \pm .01) Re(\theta_F) + (.04 \pm .01) Im(\theta_H) \\
Im(\theta_H) &\approx (1.18 \pm .01) Im(\theta_F) + (.04 \pm .01) Re(\theta_H)
\end{aligned}$$

The errors introduced in the Hall angle from errors in $\sigma_{xx}d$ are well within the noise of the experiment.

Using published room temperature dc- conductivity values, the thickness of our sample can be estimated:

$$\begin{aligned}
&\sigma_{xx}|_{300K} \approx 3900\ \Omega^{-1} cm^{-1} \qquad \text{published value}^{27} \\
&\sigma_{xx}d(300K)|_{24cm^{-1}} \approx 3.6 \times 10^{-3}\ \Omega^{-1} \\
&\Rightarrow d = 95\ nm
\end{aligned} \tag{5.13}$$

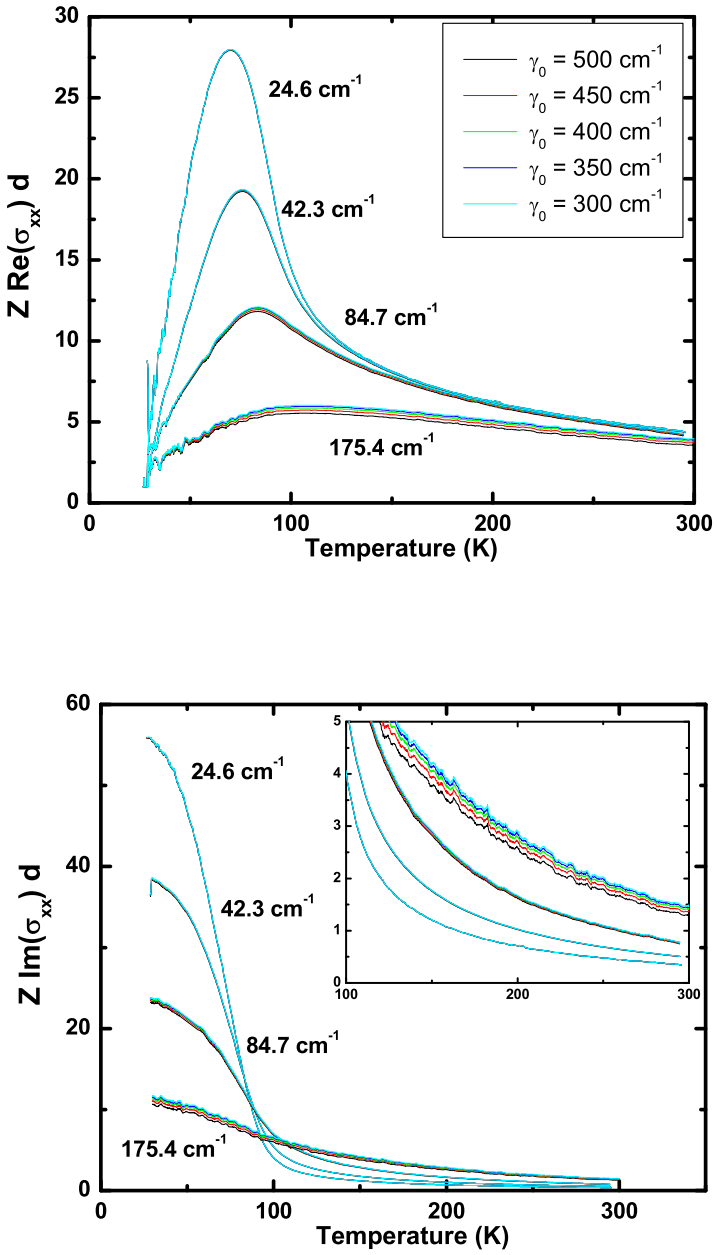

Figure 5.5: The correction factor $Z\sigma_{xx}d$ for various values of an assumed γ_0 at 300 K (ranging from 300 to 500 cm^{-1} in 50 cm^{-1} increments) and $\Omega_N \equiv \Omega_S$. Z is 377 Ω / (n+1) and n is the index of quartz (≈ 2.12)

5.1.4 BSCCO leakage light signal

A separate test was performed to determine the leakage light signal which may contribute to the transmission in the Faraday experiment. The sample was removed and replaced with a piece of copper tape of similar size and shape and mounted to a quartz substrate. The leakage signal observed with respect to an open hole was 6×10^{-6}. The lowest transmission value was measured at 24 cm^{-1} and $\sim$ 30 K, which is $\sim 10^{-4}$. Leakage light appears not to be a problem.

The decrease in the values of Ω_S in table 5.2 as the frequency is reduced suggests either a physical transmission enhancement or a leakage signal consistent with diffraction effects increasing the spot size. At low frequency and temperature, we know that the transmission is ideally proportional to ω^2. From reference 24, the high-frequency transmission values should not exhibit significant magnetic field dependence.

The plot of the transmission as a function of ω^2 is shown in figure 5.7 as well as the expected zero-field transmission based upon the high frequency values. The transmission enhancement at lower frequencies is immediately obvious. The transmission enhancement can be calculated as follows:

$$T|_{42.4} \; / \; \left(\frac{75.7}{175.4^2} \, \omega^2 \right) \Big|_{42.4} = 1.5$$
$$T|_{24.6} \; / \; \left(\frac{75.7}{175.4^2} \, \omega^2 \right) \Big|_{24.6} = 2.1$$

S. Wu[24] found transmission enhancements of $\sim$ 1.0 and $\sim$ 1.5 for optimally doped YBCO at 42.4 and 24.6 cm^{-1}, respectively. This suggests that the resonance observed by S. Wu (which he assigned to a vortex core resonance) is shifted higher in

frequency, or is much broader, for single crystal BSCCO. In Chapter 6, I model the Hall angle where a higher frequency resonance than that measured by S. Wu is required to qualitatively describe the data. STM measurements by Pan *et al.*[55] report an observed FIR resonance that is significantly higher in BSCCO (7meV) than in YBCO (5.5meV).

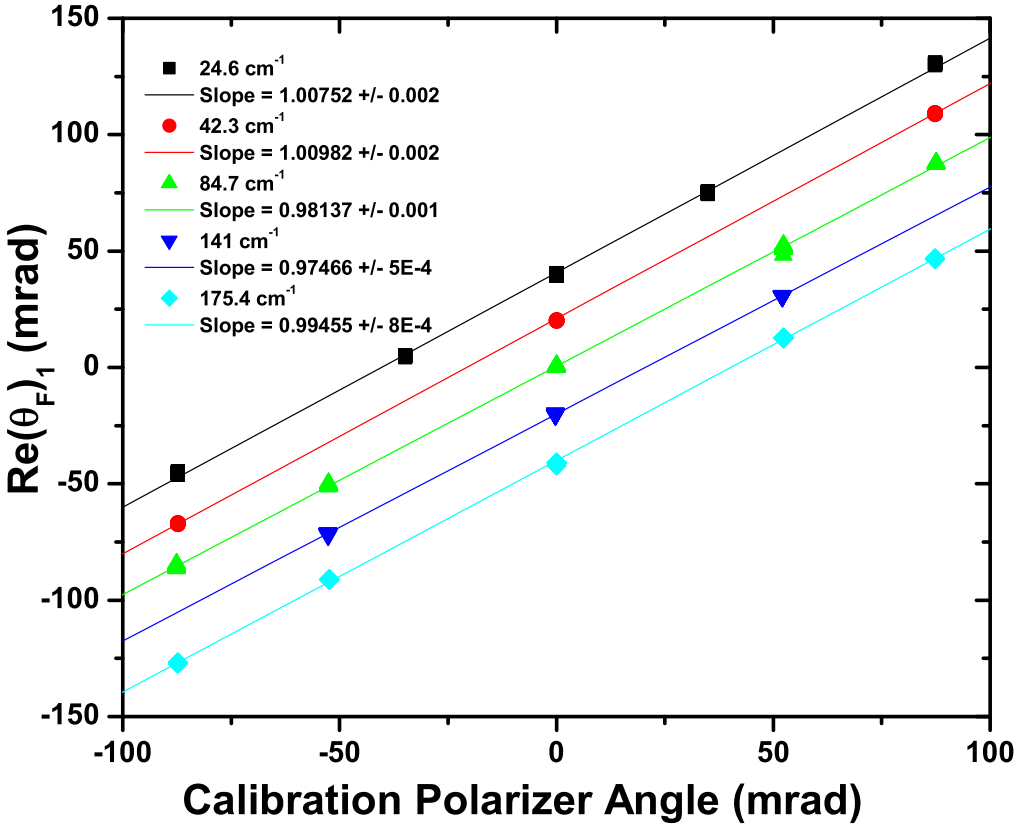

Figure 5.6: The real part of the Faraday angle measured when a polarizer is manually rotated to discreet angles. The different plots represent the laser frequencies 24.6, 42.3, 84.7, 141, and 175.4 cm^{-1}. The vertical cascade is for visual clarity only.

5.2 Calibration

5.2.1 Epoxy and quartz

The main sample under investigation is a thin crystal of BSCCO epoxied to an AR coated quartz substrate. An AR-coated quartz substrate as well as a free-standing epoxy sample ($\sim$ 150 μm thick) were independently inserted into the Faraday system. Both samples were mounted on separate graphite apertures and displayed no observable B-field dependent optical activity.

5.2.2 Sample polarizer calibration

A polarizer mounted on a rotation stage was inserted directly in front of the analyzing polarizer. The angle of the polarizer was set so that the measured Re(θ_F) was unchanged upon insertion into the optical path. The physical angle of rotation was measured via tick marks on the rotation stage, and the Re(θ_F) recorded. The results are shown in figure 5.6. The deviations in slope away from the value of 1 are within the errors produced by physically reading the rotation stage angle.

5.2.3 Sample waveplate calibration of Im(θ_F)

A waveplate mounted on a rotation stage was inserted directly in front of the analyzing polarizer. The angle of the waveplate was set so that the measured Re(θ_F) was unchanged upon insertion into the optical path. The Re(θ_F) and Im(θ_F) was measured as a function of the waveplate angle measured via tick marks on the rotation stage. Using equation 3.19, it is possible to calibrate the imaginary part of the Faraday angle with respect to the real part. The waveplate parameters, $\Delta\beta$ and $\Delta\Gamma$,

are obtained by fitting the real part of the Faraday angle. The fit parameters are then used to calculate the imaginary part, and overlayed on the imaginary Faraday angle data.

Results for the 84.7 cm^{-1} data using a .3 mm thick waveplate and 175.4 cm^{-1} data using a .7 mm thick waveplate are shown in figure 5.8. The fit parameters from the .7 mm thick waveplate (top graph) may be compared directly to figure 5.6. The .3 mm thick waveplate parameters (bottom graph) can be compared to figure 5.6 by using the fact that $\Delta\beta$ is a linear function of thickness (for $\Delta\Gamma \lll 1$):

$$\Delta\beta|_{.3mm,\ 85cm^{-1}} = \Delta\beta|_{.7mm,\ 85cm^{-1}} \times \frac{.3}{.7} \approx 1.78 \times \frac{.3}{.7} = .76$$

5.2.4 GaAs 2-DEG heterostructure preparation and low frequency calibration

A GaAs 2-DEG heterostructure was provided by Matt Grayson from the Walter Shottky Institut. An AR-coating was deposited on the substrate, and a 25 $\Omega/\Box$ layer of NiCr was deposited on the sample side in order to approximate the transmission level that a typical BSCCO sample allows at 100 K ($\sim 1\%$). The calibration sample was mounted on an exact duplicate aperture as that used with the BSCCO sample.

A GaAs 2-DEG resonance is well described using a simple free-electron model (see equation 3.36). In this model, the mobility and the density of electrons are used as parameters. A simple Drude model is used to model the electronic response of the NiCr layer (the AR-coating is negligible) using the scattering rate as an unknown parameter and the known sheet resistance.

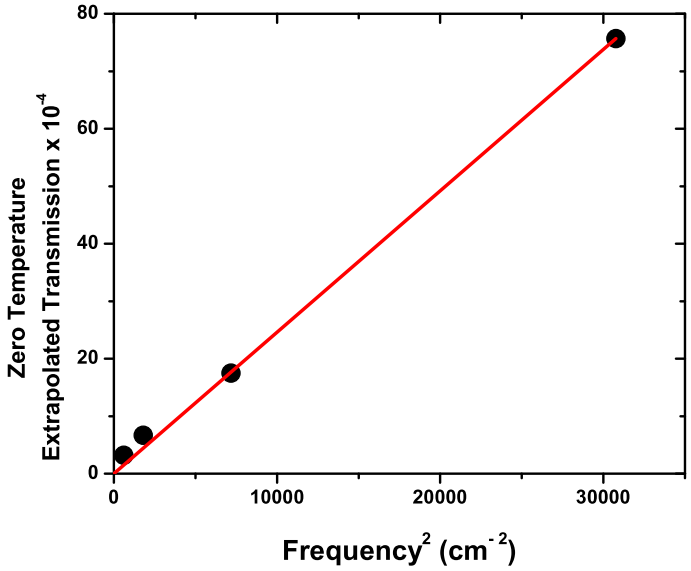

Figure 5.7: Plot of the zero temperature extrapolated transmission. The red line, $T = \frac{75.7\times10^{-4}}{175.4^2}\omega^2$, represents the ideal Drude-like zero temperature ω^2 behavior that is observed at higher frequencies in magnetic field.[24]

This sample was used to check the imaginary part of the Faraday angle with respect to the real part at three separate frequencies: 24.6, 42.3, and 84.7 cm^{-1}. The real part was fit, and the imaginary part was then calculated using the fit parameters from the real part. The results are shown in figure 5.9.

The same electron density and NiCr scattering rate were used for all three frequencies, namely $1.78 \times 10^{15} m^{-2}$ and $5100 cm^{-1}$. Strangely, the mobility is a function of frequency and found to be 14, 12, and 8.4 $m^2/Vsec$ at 24.6, 42.3, and 84.7 cm^{-1}, respectively. The temperature was held at 80 K for all data. Furthermore, the 84 cm^{-1} data was repeated four times over the course of one year and found not to change significantly. Since the mobility is inversely proportional to the effective mass as well as the scattering rate, the data suggest that either the mass or the hall scat-

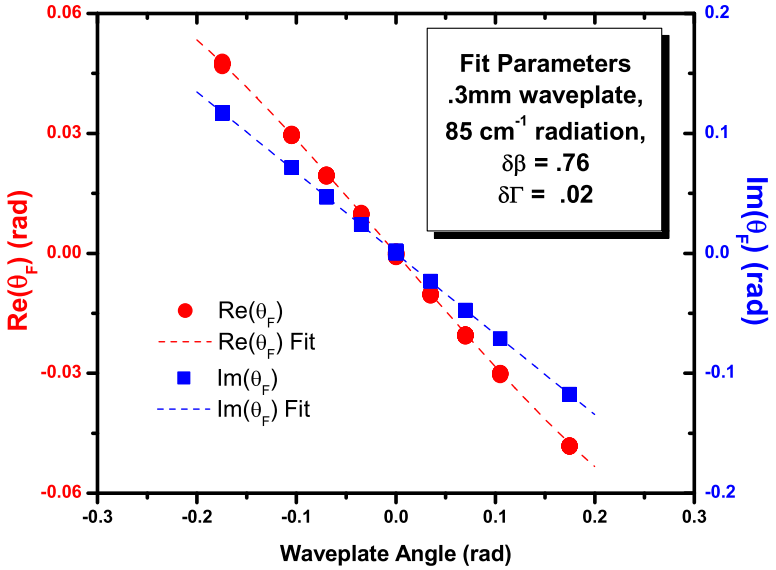

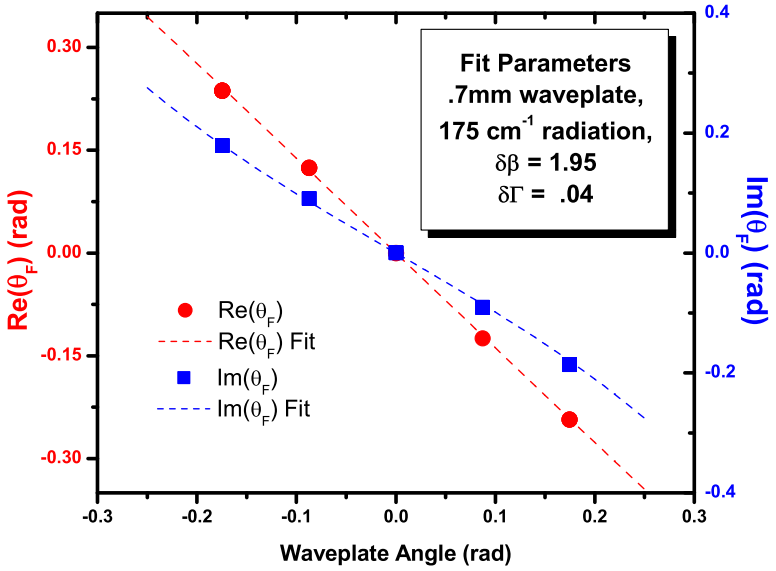

Figure 5.8: The real and imaginary part of the Faraday angle is measured as a function of angle for a quartz waveplate and fit using the waveplate parameters $\Delta\beta$ and $\Delta\Gamma$. The imaginary part is calculated using the fit parameters and overlayed on top of the data.

tering rate is enhanced as the frequency is increased. Since the resonant frequency is not significantly shifted away from the calculated cyclotron frequency ($\propto 1/m$), it would appear that the frequency dependence is associated with the scattering rate.

All of the data show some asymmetry about the resonance in the imaginary part of the Faraday angle. It is not a result of magnetic field directional averaging since the same asymmetry is present upon up and down magnetic field sweeps. This is most likely due to some mixing of the real part with the imaginary part of the Faraday angle. Inspection of equations 3.10, 3.23, and 3.27 show that it is possible for the real and imaginary part of the Faraday angle to mix, although the precise reason remains unclear since these mixing terms should be negligibly small.

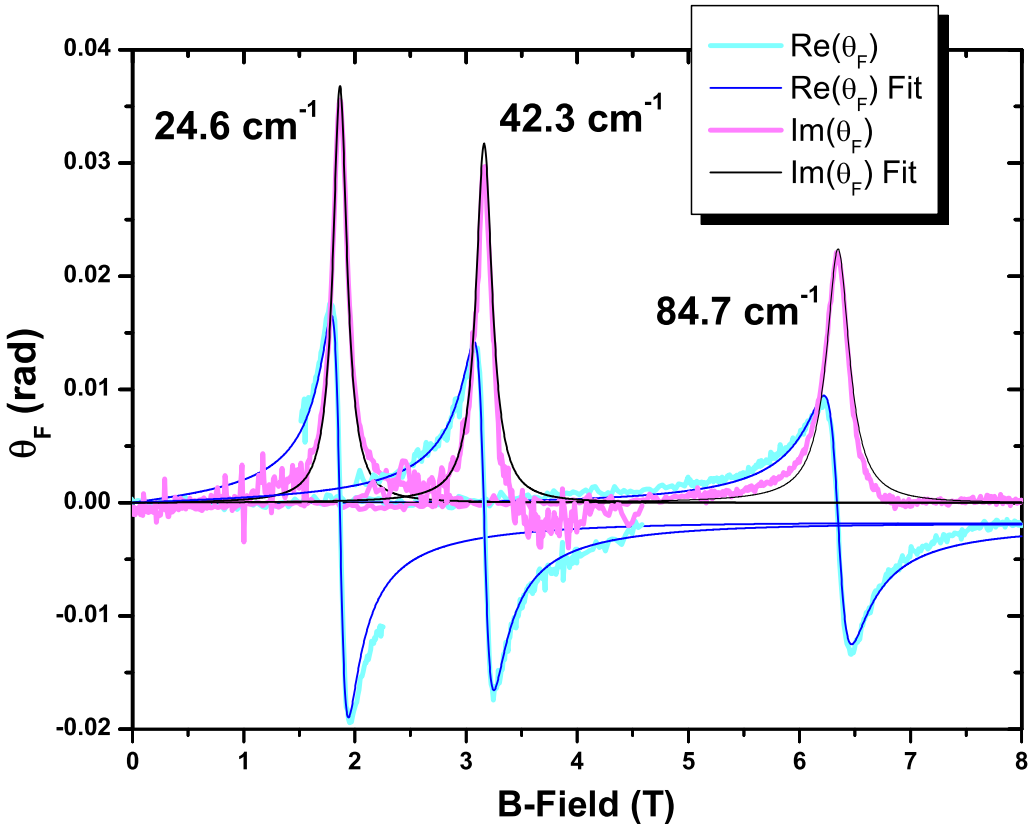

Figure 5.9: The Faraday angle measured at 3 frequencies as a function of magnetic field for an AR-coated GaAs 2-DEG heterostructure with a 25 $\Omega/\square$ layer of NiCr at 80 K. The real part of the Faraday angle is fit using the mobility (μ), electron density (n), and NiCr electron scattering rate (γ_{NiCr}) as parameters. For all frequencies, $n = 1.78 \times 10^{15} m^{-2}$ and $\gamma_{NiCr} = 5100\ cm^{-1}$. The mobility was found to be 14, 12, and 8.4 $m^2/Vsec$ for 24.6, 42.6, and 84.7 cm^{-1}, respectively. The GaAs electron mass was taken to be $0.07 \times m_e$.

5.3 Obtaining the Faraday angle: corrections to the raw data

5.3.1 *In situ* waveplate calibration

In section 4.4.4, waveplates used in the Faraday experiment were characterized in a Bomem DA.3 spectrometer. We can also characterize the waveplates *In situ* using the Faraday experiment. A polarizer on a rotation stage is inserted into the system in front of the analyzing polarizer. The waveplate with unknown parameters is inserted into the rotator. This is the more desirable way to calibrate since errors from imperfections associated with the waveplate are effectively eliminated from the system (see section 3.5.1 and 5.3.4). Taking measurements of the complex Faraday angle at various angles of the polarizer and using equations 3.10 and 3.14 give:

$$Re(\theta_F)_1 = Re(\theta_F)_2 = -\tan(2\alpha). \tag{5.14}$$

Equations 3.10 show that $Re(\theta_F)_2$ is a function of $\Delta\beta$ and $\Delta\Gamma$ while $Re(\theta_F)_1$ is not. In practice, measurements of $Constant_1$ and $Constant_2$ yield $\Delta\Gamma \sim 0$ so that we can effectively solve for $\Delta\beta$ from equation 5.14.

The plot of $Re(\theta_F)_1$ as a function of $\tan\alpha \approx \alpha$ has a slope of 1 (see figure 2.4). If we plot $\sin(4\omega)/DC$ as a function of α, the slope may be used to find $\Delta\beta$ in the

following way:

$$
\begin{aligned}
Re(\theta_F)_2 &= \frac{1}{2}\frac{\cos(\Delta\beta)+3\cosh(\Delta\Gamma)}{\cos(\Delta\beta)-\cosh(\Delta\Gamma)}\,\frac{\sin(4\omega t)}{DC} \\
&\Rightarrow \frac{\sin(4\,\omega t)}{DC}\Big|_{\text{slope}} \times \frac{1}{2}\frac{\cos(\Delta\beta)+3\cosh(\Delta\Gamma)}{\cos(\Delta\beta)-\cosh(\Delta\Gamma)} = 1 \\
&\Rightarrow \Delta\beta = \cos^{-1}\left(\frac{3\,m+2}{2-m}\right) \\
&\text{where } m \equiv \frac{\sin(4\omega t)}{DC})\Big|_{\text{slope}}
\end{aligned}
\tag{5.15}
$$

5.3.2 Lock in amplifiers and harmonic analysis

The complete detector signal can be written as:

$$I_D = DC + A_1 \sin 2\omega + A_2 \cos 2\omega + A_3 \sin 4\omega + A_4 \cos 4\omega$$

The EG&G lock-in amplifiers measure the RMS-amplitude of all signals. The amplitude of the first harmonic of a square wave with a peak-to-peak value of 1 is .63662.

The measured DC value needs to be multiplied by a factor of 2 since the actual DC level is the peak-to-peak value of the square waveform.

$$DC \Rightarrow DC_{measured} \times 2/.63662$$

$$A_i \Rightarrow A_{imeasured}$$

The chopped signal is not perfectly square due to a finite spot size. However, if the spot size is much less than the chopper blade slot width, the chopped signal will

be approximately square. I constructed a model such that the shape of a square wave became trapezoidal. A considerable amount of distortion was required before the first Fourier component began to change significantly. The shape of the waveform that I observed on the oscilloscope did not approach a severe distortion. The chopped signals were sufficiently square to not warrant any further corrections.

5.3.3 Frequency dependence of bolometers

There are three frequencies involved in the Faraday experiment: the chopper frequency, and the second and fourth harmonics of the rotating waveplate. Since the sensitivity of the bolometers are frequency dependent, all amplitudes were normalized according to the fits shown on graph 4.6.

5.3.4 Setting the 2ω phase

All of the formalism leading to equation 3.9 assumes zero phase occurs when θ_F is physically zero, namely that $y_{2\omega}$ and $y_{4\omega}$ are zero in zero magnetic field. The $x_{2\omega}$ channel is proportional to $\sinh \Delta\Gamma$ which is $\lesssim .01$ for lower frequencies (see section 4.4.4). The $y_{2\omega}$ channel is ideally zero in zero field. However, inspection of equations 3.24 and 3.28 show that errors from an imperfect waveplate or arbitrary scattering after the waveplate can become substantial when the true signals in the $x_{2\omega}$ and $y_{2\omega}$ channels both approach zero. It should be noted that in zero field the $x_{4\omega}$ channel, which is proportional to $|t_{xx}|^2(\cos \Delta\beta - \cosh \Delta\Gamma) \sim |t_{xx}|^2$, is much greater than $y_{4\omega}$ which is itself proportional to $\mathrm{Re}(\theta_F)$. This means that the fourth harmonic phase can easily be accurately set in zero field.

It is critical that the 2ω phase be set correctly since the only channel that contains the $\mathrm{Im}(\theta_F)$ factor is the $y_{2\omega}$ channel. In practice, the phase of the lock-in was set to zero in zero field. After the data was collected, the phase could then be adjusted in the analysis so as to maximize the $\mathrm{Im}(\theta_F)$ response. For the GaAs 2-DEG samples, this means adjusting the 2ω phase to maximize the $\mathrm{Im}(\theta_F)$ resonant peaks. For the BSCCO sample, the 2ω phase was adjusted to maximize the slope of the $\mathrm{Im}(\theta_F)$ as a function of B-field. Here we will analyze this procedure in depth, and calculate an approximate expression for the errors that may result from this procedure.

Ignoring any direct scaling of our signal in the y-channels due to scattering, we can write a general expression for errors induced by an imperfect waveplate or arbitrary scattering between the sample and the rotating waveplate (see equations 3.28 and 3.24):

$$\begin{aligned} \bar{y_2} &= y_2 + \epsilon_y \\ \bar{x_2} &= x_2 + \epsilon_x(B) \\ \bar{y_4} &= y_4 + C \\ \bar{x_4} &= x_4 + D(B) \end{aligned} \tag{5.16}$$

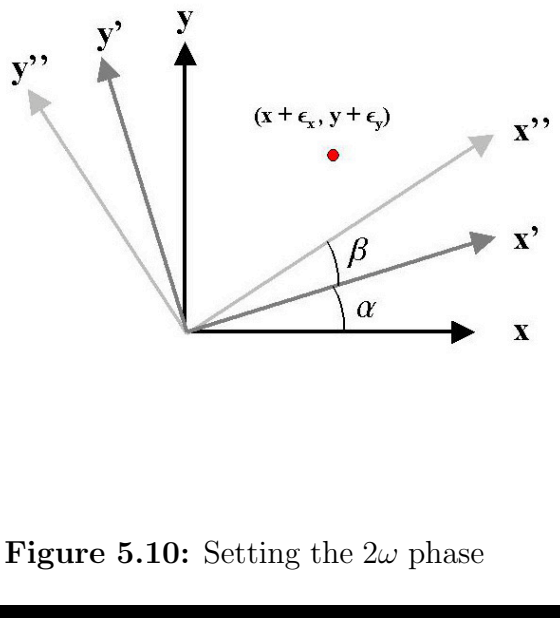

Figure 5.10: Setting the 2ω phase

Notice that:

$$\begin{aligned} &y_2 \propto Re(\theta_F) \\ &x_2 \sim constant \\ &y_4 \text{ is linear in both } Re(\theta_F) \text{ and } Im(\theta_F) \\ &x_4 \sim constant \gg D(B) \\ &\epsilon_y \text{ and C are both constant} \end{aligned} \tag{5.17}$$

and in zero field:

$$\begin{aligned} y_2 &\to 0 \\ y_4 &\to 0 \end{aligned} \tag{5.18}$$

If we zero the 2ω lock-in in zero field, the angle that results compared to the error-free ideal basis (refer to figure 5.10) is:

$$\tan\alpha \equiv \frac{\epsilon_y}{x_2 + \epsilon_x(B)} \tag{5.19}$$

We are interested in finding the slope as a function of magnetic field in this new basis and comparing it to the ideal slope, $m \equiv \frac{\delta y_2}{\delta B}$:

$$\begin{aligned} y_2' &= \bar{y_2}\cos\alpha - \bar{x_2}\sin\alpha \\ x_2' &= \bar{x_2}\cos\alpha + \bar{y_2}\sin\alpha \\ \Rightarrow \frac{\delta y_2'}{\delta B} &= m\cos\alpha - \frac{\delta\epsilon_x'}{\delta B}\sin\alpha \\ \frac{\delta x_2'}{\delta B} &= m\sin\alpha + \frac{\delta\epsilon_x'}{\delta B}\cos\alpha \end{aligned} \tag{5.20}$$

Recall that I adjust the basis (angle β in figure 5.10) until the slope is maximized. This is written Mathematically as:

$$\begin{aligned} y_2'' &= y_2' \cos\beta - x_2' \sin\beta \\ \Rightarrow \frac{\delta}{\delta\beta}\frac{\delta y_2''}{\delta B} &= 0 \text{ occurs when the observed slope is maximized} \\ &= \frac{\delta}{\delta\beta}\left(\frac{\delta y_2'}{\delta B}\cos\beta - \frac{\delta x_2'}{\delta B}\sin\beta\right) \\ &= -\frac{\delta y_2'}{\delta B}\sin\beta - \frac{\delta x_2'}{\delta B}\cos\beta \\ \Rightarrow \tan\beta_0 &\equiv -\tan\alpha \frac{1 + \frac{1}{m}\frac{\delta\epsilon_x}{\delta B}}{1 - \frac{1}{m}\frac{\delta\epsilon_x}{\delta B}\tan\alpha} \end{aligned} \tag{5.21}$$

The angle, β_0, is the angle of the basis in which the slope has been maximized. If we assume $\epsilon_x \to 0$, the result shows that the maximum slope occurs when we rotate to the ideal (unprimed) basis. It also shows that errors in this method increase when the slope decreases.

We can estimate the errors in the measured slope, m'', compared to the ideal slope, m:

$$\begin{aligned} m'' &= \left.\frac{\delta y_2''}{\delta B}\right|_{\beta=\beta_0} \\ &= \frac{\delta y_2'}{\delta B}\cos\beta_0 - \frac{\delta x_2'}{\delta B}\sin\beta_0 \\ &= \left(m\cos\alpha - \frac{\delta\epsilon_x}{\delta B}\right)\cos\beta_0 - \left(m\sin\alpha\sin\beta_0 + \frac{\delta\epsilon_x}{\delta B}\cos\alpha\sin\beta_0\right) \\ &= m\cos(\alpha+\beta_0) - \frac{\delta\epsilon_x}{\delta B}\sin(\alpha+\beta_0) \\ &= m\cos\delta - \frac{\delta\epsilon_x}{\delta B}\sin\delta \end{aligned} \tag{5.22}$$

where $\delta \equiv \alpha + \beta_0$

The error in obtaining the maximum peak height of the GaAs 2-DEG sample, Δy_{max}, can be found from equation 5.22 as follows:

$$\begin{aligned} m'' &\rightarrow \frac{\Delta y''_{max}}{B_0} \\ m &\rightarrow \frac{\Delta y_{max}}{B_0} \end{aligned} \tag{5.23}$$

where B_0 is the B-field where the maximum peak occurs

$$\Rightarrow \Delta y''_{max} = \Delta y_{max} \cos\delta - \epsilon_x(B_0) \sin\delta$$

Chapter 6

Results and discussion

6.1 Faraday angle

In this chapter, I describe my measured Faraday angle results of optimally doped single crystal BSCCO at frequencies 24.6, 42.3, 84.7, and 175.4 cm^{-1} in the temperature range from ∼25 K to 300 K.

I also measured the Faraday angle as a function of magnetic field at 100 K. This temperature is chosen so as to maximize the slope of the imaginary part of the Faraday angle in order to minimize systematic errors in setting the 2ω lock-in phase (discussed in section 5.3.4) while, at the same time, allowing an appreciable absolute transmission signal.

The Faraday angle temperature dependence is performed at +8T and -8T. Taking half of the difference of the two functions yields the desired Faraday angle as a continuous function of temperature.

6.1.1 B-field sweeps

Figure 6.1 shows the Faraday angle of BSCCO at 100 K as a function of magnetic field for two frequencies, 42.3 and 84.7 cm^{-1}. Inspection of equation 3.35 shows $\theta_F \propto \omega_c \propto B$ if $\gamma \gg \omega_c$ or $\omega \gg \omega_c$. Since the cyclotron frequency at 8T is $\sim 3\, cm^{-1}$, this condition is satisfied. Therefore, the Faraday angle as a function of magnetic field is expected to be a straight line passing through zero. A complete compilation of slopes of both the real and imaginary part of the Faraday angle for all frequencies are given in table 6.1.

Although the data is predominantly linear, the random noise from the detector is observable in all four graphs of figure 6.1. In addition, systematic oscillations, most easily observed in the 42.3 cm^{-1} data, is a common occurrence at all measured frequencies. The amplitude of the oscillations is sensitive to anything affecting the relative alignment of the sample and the beam, and can vary anywhere between zero to $\pm$ 2.5 mrad.

The oscillations are an even function of magnetic field with a period behaving as $1/B^2$. Two possible causes may be ruled out. A magnetic force exerted by a constantly sweeping magnetic field on a permanent magnetic dipole is linear in the applied field. For uniform applied magnetic fields, torques on induced eddy currents are proportional to the product of the magnetic field and the time derivative of the field (a constant in our case), while any net forces average to zero. A linear media with an average magnetization induced by the B-field results in a force between the applied B-field and the induced magnetic moment which obeys a B^2 law.

The oscillations are not observable with the sample removed from the system nor with a bare aperture in place of the sample. The sensitivity of the sample alignment

suggests that an etalon is formed between the sample and another optical component. By inserting an attenuator between various optical components, one would expect the etalon amplitude to scale with attenuation. This was not observed, suggesting that an etalon is occurring within the cryostat.

From figures 6.1 (b) and (c), 5 full etalons are observed. The optical path length change associated with a resonant cavity is found by multiplying the wavelength of the radiation ($\sim 240\mu m$) times the number of etalons (~ 5) and dividing by 2 which results in $\approx 3/4mm$ of movement! In order to directly observe such large motion, I attached a small mirror to various optical components in the system. A small HeNe laser beam was deflected from this small mirror and projected onto a screen ten meters away. Using this large lever-arm magnifying any possible movement of the optical component, the magnetic field was swept from -8 to +8 T. No significant motion of the cryostat nor any optical components were observed. Though perplexing, it should be noted that no clear frequency dependence of the oscillation period is observed.

Because of the manor in which the sample stick is clamped inside the cryostat, it is hard to imagine the sample moving such a large distance with respect to the vacuum jacket. However, the LN cold shield can easily move such a large amount. Copper tubes are mounted to the LN cold shield which introduce reflective surfaces roughly parallel to the sample. To minimize scattering problems within the cryostat, I glued FIR absorbing foam to these surfaces. In addition, I tilt the sample away from normal incidence as much as possible without clipping the beam or causing light leakage. Tilting the sample has a strong effect on the oscillation amplitude, but most of the time can not be fully eliminated. It is not possible to tilt the sample more than 5-10 degrees without causing significant light leakage around the sample which

is a smaller angle than the acceptance cone angle associated with the f-number of the system. Some fraction of the beam is inevitably scattered from the sample back into the system.

The oscillations seem to have little effect on the slope of the magnetic field sweeps. There are ∼5 oscillations with a 2.5 mrad amplitude, which, in a worst case scenario, translates into systematic noise in the slope of $\lesssim \pm 2.5\ mrad/\sqrt{5} \approx 1\ mrad$ over 16T. The slope is effected by less than $\pm 1 mrad/16T = \pm .06\ mrad/T$. This is reduced if we visually inspect the oscillations and truncate the magnetic field scans such that the end points do not occur at an extremum before performing a linear fit. Secondly, the oscillation spacing and amplitude is altered by subtle changes in laser or sample alignment. Averaging multiple curves reduces slope uncertainty even further. Thirdly, these oscillations are largely symmetrically even. Since we are fitting the data to a symmetrically odd linear function, any superimposed error signals that may be symmetrically even about the origin do not effect the slope values. The slopes at all measured frequencies for both the real and imaginary part of the Faraday angle are given in table 6.1.

Slopes of B-field sweeps (mrad/T)							
24.6 cm^{-1}		**42.3** cm^{-1}		**84.7** cm^{-1}		**175.4** cm^{-1}	
Re(θ_F)	**Im**(θ_F)	**Re**(θ_F)	**Im**(θ_F)	**Re**(θ_F)	**Im**(θ_F)	**Re**(θ_F)	**Im**(θ_F)
2.031	0.374	1.992	0.457	1.865	1.081	0.854	1.853
1.937	0.409	2.074	0.450	1.886	1.105	0.865	1.829
2.057	0.394	1.992	0.457	1.957	1.067	0.872	1.547
1.982	0.373	2.035	0.446	1.911	1.097	-.—	-.—
-.—	-.—	2.051	0.443	-.—	-.—	-.—	-.—
2.002	0.388	2.029	0.451	1.905	1.088	0.864	1.743

**last row is the column average*

Table 6.1: BSCCO results: Faraday angle magnetic field sweep slopes (mrad/T) at 100 K

6.1.2 84 cm^{-1} Hall angle data as a function of temperature

The temperature dependence of the Faraday angle was measured at ± 8T. Results are shown in figures 6.2 (a) and (b) for the 84 cm^{-1} data. As stated in the previous section, most B-field scans are performed at 100 K. For all reported data, the temperature sweeps are from 100 to 300 K and from 300 to 25 K. The sweep rate is ∼25 K/min. Temperature lag is about 2.5 K at this sweep rate, which translates into a thermal time constant of ∼5 seconds between the temperature of the sample and the temperature of the thermometer.

There is a substantial temperature dependent background signal that is of the same order of magnitude as the Faraday angle. This background is associated with the sample mechanically moving as a function of temperature. Since the difference of the temperature sweeps taken in positive and negative magnetic field is the quantity of interest, it is imperative that the temperature sweeps be performed in precisely the same manor. Otherwise, the sample may move a bit differently causing relatively

severe errors.

Even though these errors are relatively small at 100 K, at room temperature the real and imaginary part of the Faraday angle is much smaller, in some cases well below $\sim 1/2$ mrad (see figure 6.6 for a clear illustration). Drift errors that are $\sim 1/5$ mrad are common, which translates into huge relative errors at room temperature. This is the primary limitation of the system in analyzing the low frequency BSCCO data.

The precise cause of the background is not clear. Precautions have been taken to minimize the motion of the sample resulting from thermal expansion and contraction. The sample is mounted to a copper plane with an attached heater that is weakly coupled to the sample stick. The copper plane rests on three 2mm thick plastic stand-offs. Plastics generally have a relatively large coefficient of thermal expansion/contraction, but for a 2mm thick piece of plastic, a typical thermal expansion coefficient (10^{-2} from 300 K to 0 K) yields a negligible amount of movement, 20 $\mu m \ll 3/4mm$. The entire sample stick is maintained in the temperature range of 25 to 35 K during all temperature sweeps.

The sample is somewhat inhomogeneous when viewed by the naked eye. However, the same Hall angle results when the sample is coarsely realigned and a different part of the sample is measured. In the thin film limit, the Hall angle reduces to a surface effect (the thickness of the film drops out of the Hall angle expression). Drift in the measured Faraday angle due to sample inhomogeneity or variations in spatial alignment of the sample with respect to the beam does not explain the observed background signal.

The small time dependent drift of the background signal is a separate issue, but

of primary concern. Since the precise cause of the background signal itself is unclear, any time dependence of the background signal is even further obfuscated.

To insure the best reproducibility, the temperature sweeps are automated. The gain changes at pre-programmed temperatures are automated (section 4.5.6). The sweeps up in temperature are controlled by a Lakeshore 340 temperature controller with constant PID-loop settings. By switching off the heater, the thermal link between the sample and bath reproducibly controls the downward temperature sweep rate. The flow of LHe used in cooling the sample stick is controlled using a fixed needle valve and a precise pressure regulator set at a relatively large pressure ($\sim$5 PSI) to pressurize the transfer dewar.

The automated gain changes during the temperature sweeps cause the EG&G 5113 pre-amplifier to temporarily overload. About five seconds is required for the EG&G 5113 pre-amplifier to recover from a gain change. This causes spikes to appear in the data in the temperature range corresponding with the gain change. In the 84 cm^{-1} data, the gain is changed at $\sim$105 K. The data has been deleted in a temperature range corresponding to the spikes.

Due to thermal lag, all increasing temperature sweeps were shifted by +2.5 K, while the decreasing temperature sweeps were shifted by -2.5 K. All Faraday angle results for the 84 cm^{-1} data are presented in figures 6.2 through 6.5.

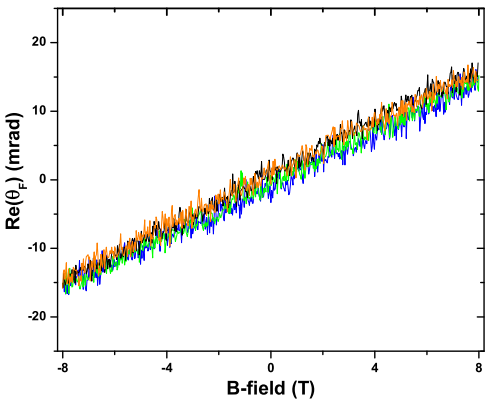

(a) Re(θ_F) at 84.7 cm^{-1}

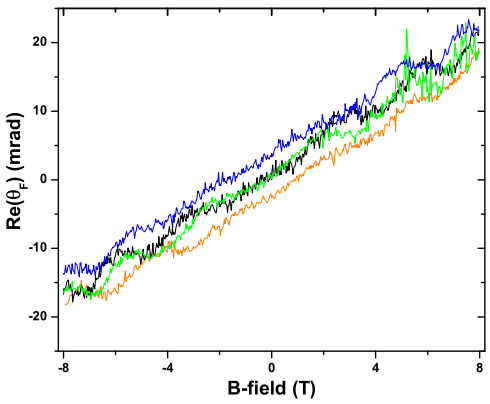

(b) Re(θ_F) at 42.3 cm^{-1}

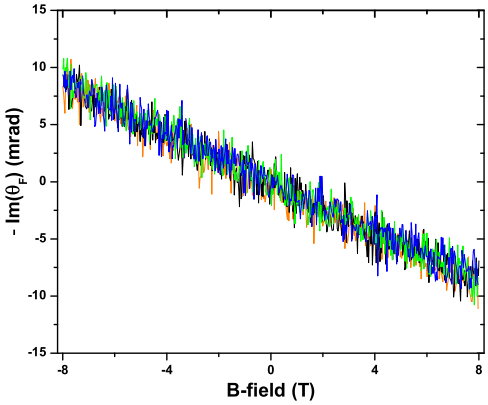

(c) Im(θ_F) at 84.7 cm^{-1}

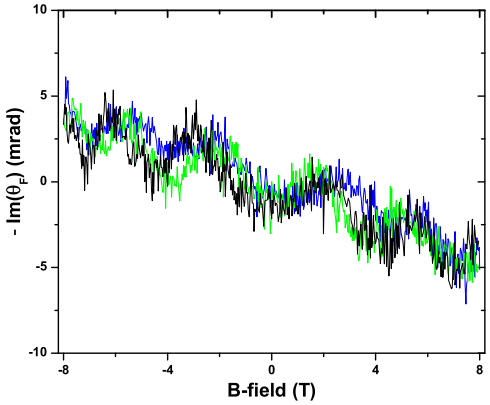

(d) Im(θ_F) at 42.3 cm^{-1}

Figure 6.1: The Faraday angle is measured as a function of magnetic field for single crystal BSCCO. Each color represents a separate scan. Two typical data sets are shown for the frequencies 42.3 and 84.7 cm^{-1}.

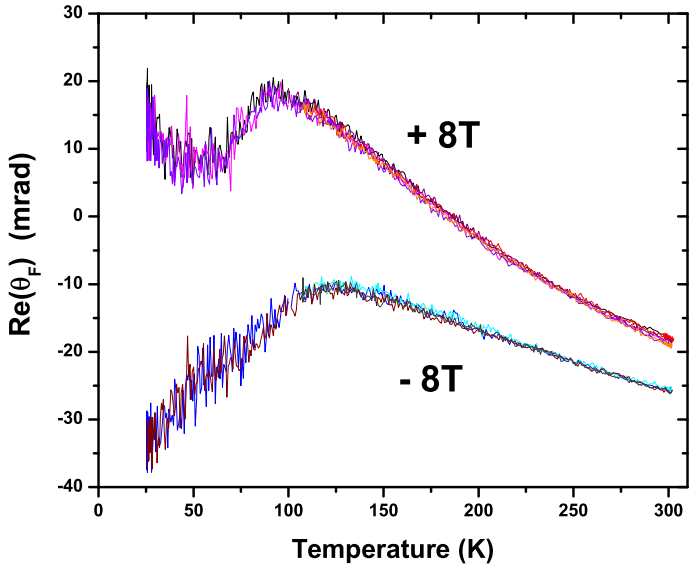

(a) Re(θ_F) measured in mrad at 84.7 cm^{-1}

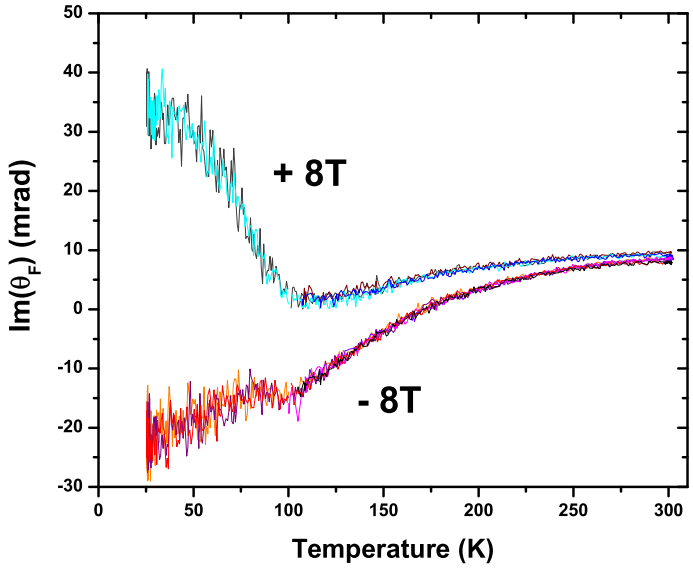

(b) Im(θ_F) measured in mrad at 84.7 cm^{-1}

Figure 6.2: The Faraday angle is measured as a function of temperature for single crystal BSCCO at 84 cm^{-1} in $\pm$ 8 T. Each color represents a separate scan.

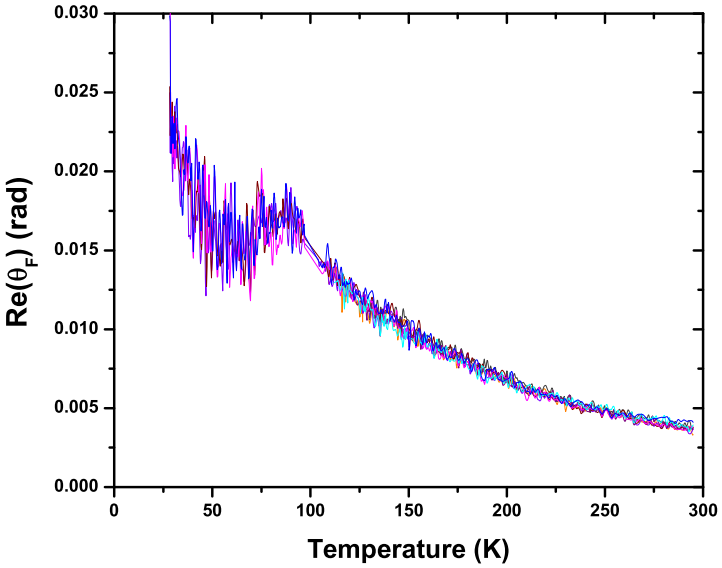

(a) Re(θ_F) at 84.7 cm^{-1} and 8 T

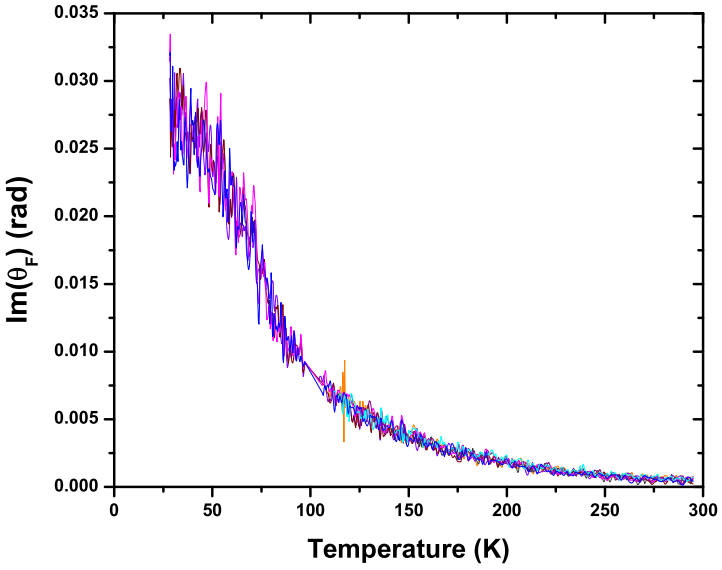

(b) Im(θ_F) at 84.7 cm^{-1} and 8T

Figure 6.3: BSCCO Faraday angle response in 8T acquired via subtracting the positive and negative magnetic field curves in figure 6.2 and dividing by two. Each color represents a separate scan.

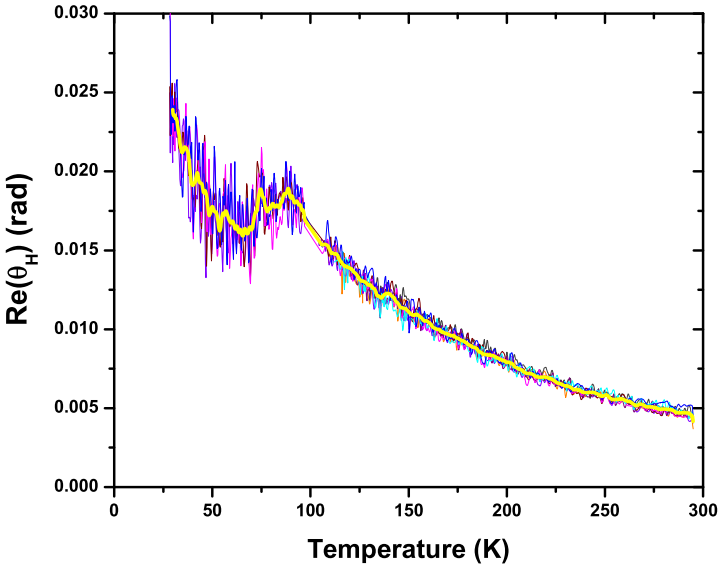

(a) Re(θ_H) at 84.7 cm^{-1} and 8 T

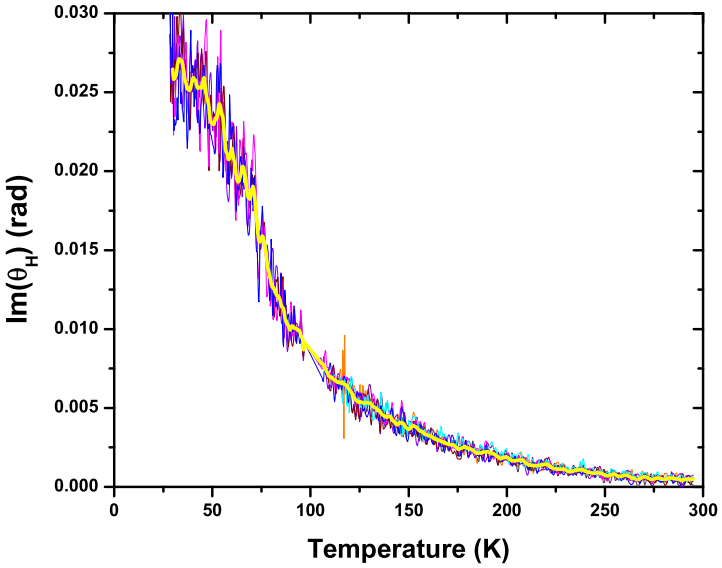

(b) Im(θ_H) at 84.7 cm^{-1} and 8 T

Figure 6.4: BSCCO Hall angle response in 8 T. The thick yellow line is the average of all curves and a 3 K moving average. Each color represents a separate scan.

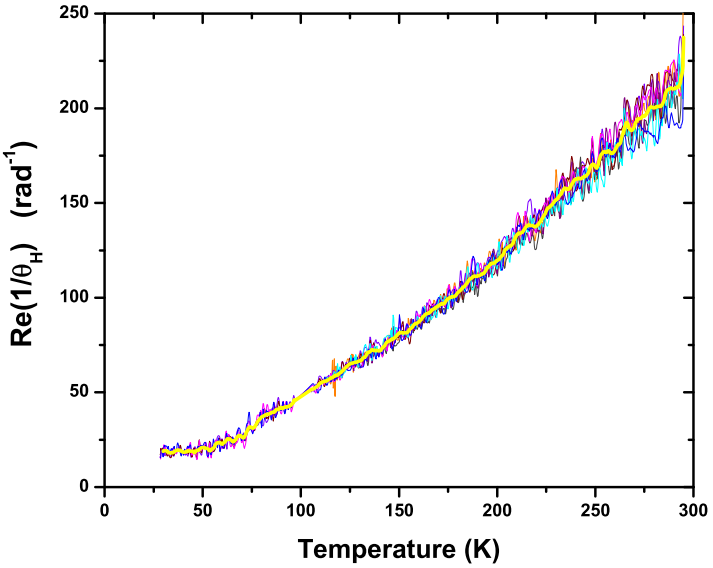

(a) Re$(1/\theta_H)$ at 84.7 cm^{-1} and 8 T

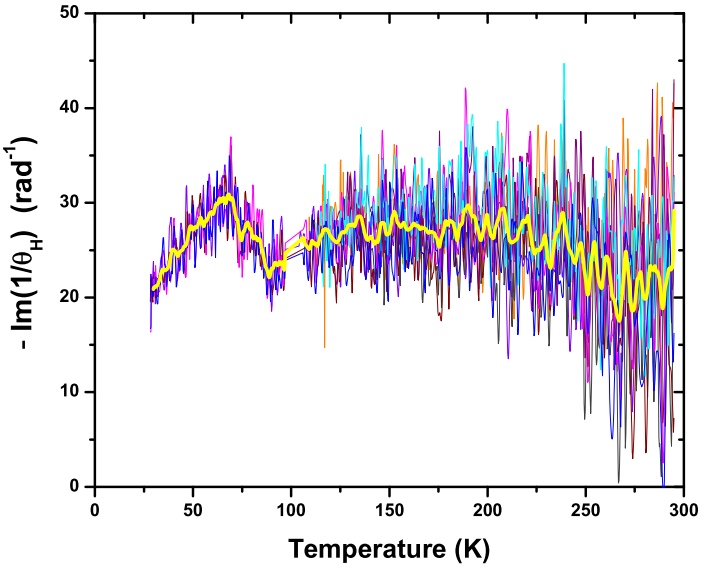

(b) Im$(1/\theta_H)$ at 84.7 cm^{-1} and 8 T

Figure 6.5: BSCCO Hall angle response in 8 T. Each color represents a separate scan. The thick yellow line is the average of all curves in addition to averaging over a 3 K moving average.

6.2 Average Hall angle as a function of temperature at all measured frequencies

In the 24 and 42 cm^{-1} cases, it was necessary to slightly offset the averaged Faraday angle temperature sweeps to be consistent with the average 100 K Faraday angle magnetic field scan slopes. The shift in the data was $\sim$1/6 mrad for the 42 cm^{-1} data and less than $\sim$1/10 mrad for the 24 cm^{-1} data.

The data at all four measured frequencies is averaged and smoothed in precisely the same manor as illustrated in the previous section for the 84 cm^{-1} data. The resulting Faraday and Hall angle data is presented in figures 6.6 through 6.11.

Due to the lack of source intensity, the signal-to-noise of the 175 cm^{-1} data was a factor of 15 smaller than the 84 cm^{-1} data. In order to increase the signal-to-noise by a factor of two, the chopper was removed from the system. Due to excessive noise, I could not observe the signal drift in real time. Smoothing each individual trace revealed a severe drift problem in the imaginary part of the Faraday angle on the order of 1.5 mrad. In short, the imaginary part of the Hall angle at 175 cm^{-1} is problematic and will be omitted in the analysis where appropriate. However, within the resulting averaged noise, the real part of the Faraday angle was reproducible.

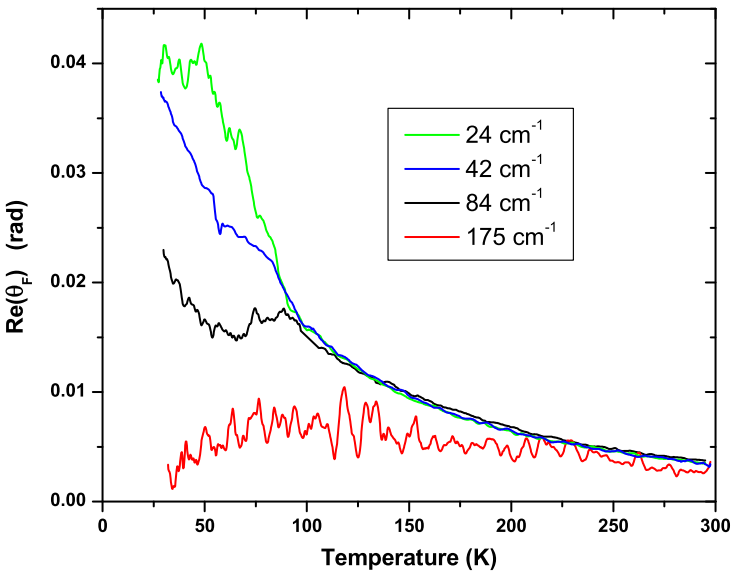

(a) Averaged Re(θ_F) at all measured frequencies in 8T

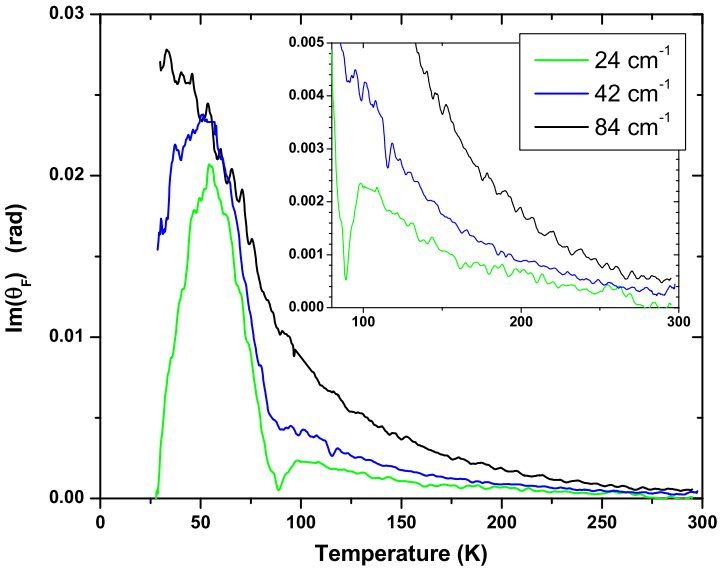

(b) Averaged Im(θ_F) at all measured frequencies in 8T

Figure 6.6: The Faraday angle is measured as a function of temperature for single crystal BSCCO at 24.6, 42.3, 84.7, and 175.4 cm^{-1} in 8T.

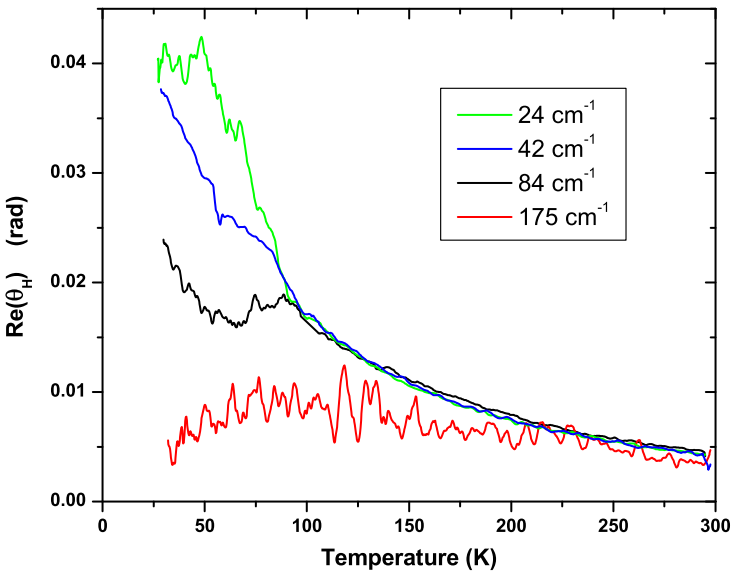

(a) Averaged Re(θ_H) at all measured frequencies in 8T

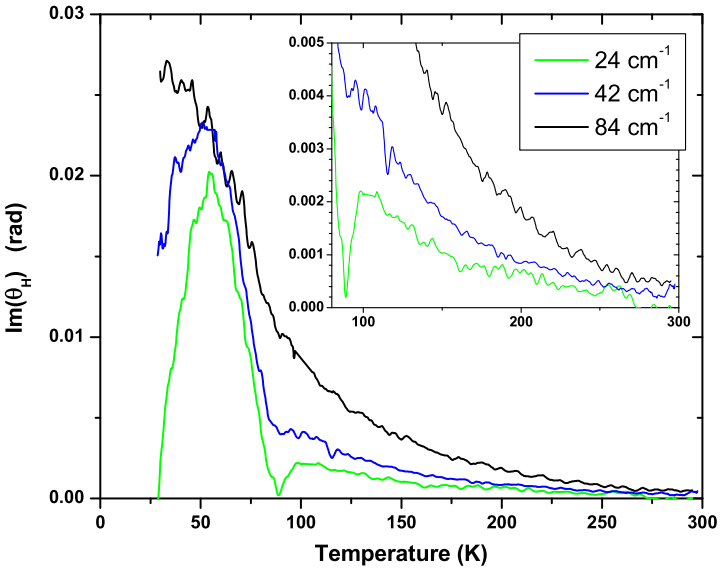

(b) Averaged Im(θ_H) at all measured frequencies in 8T

Figure 6.7: The Hall angle as a function of temperature for single crystal BSCCO at 24.6, 42.3, 84.7, and 175.4 cm^{-1} in 8T.

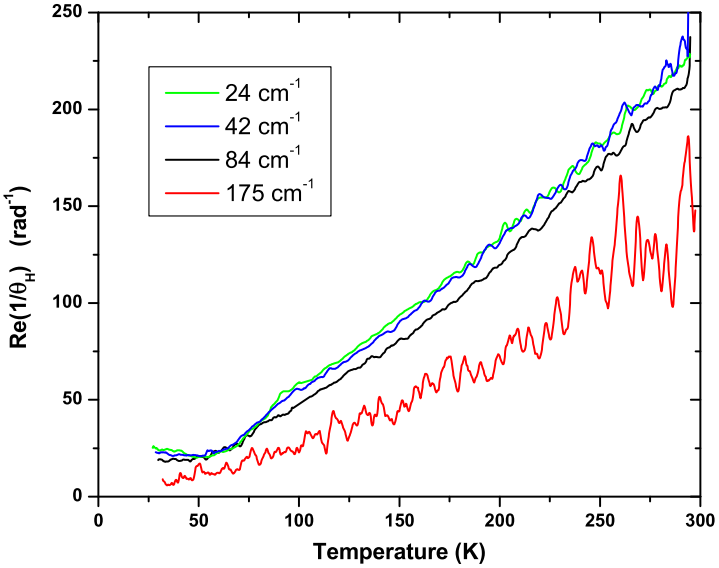

(a) Averaged Re$(1/\theta_H)$ at all measured frequencies in 8T

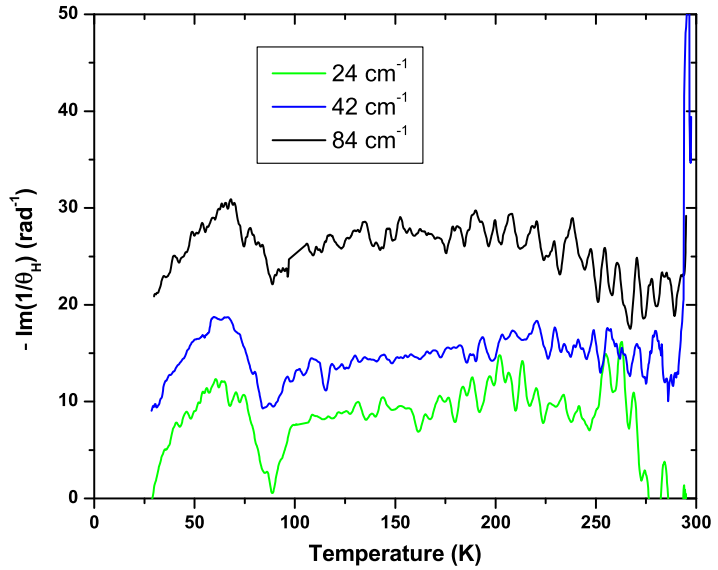

(b) Averaged Im$(1/\theta_H)$ at all measured frequencies in 8T

Figure 6.8: The inverse Hall angle as a function of temperature for single crystal BSCCO at 24.6, 42.3, 84.7, and 175.4 cm^{-1} in 8T.

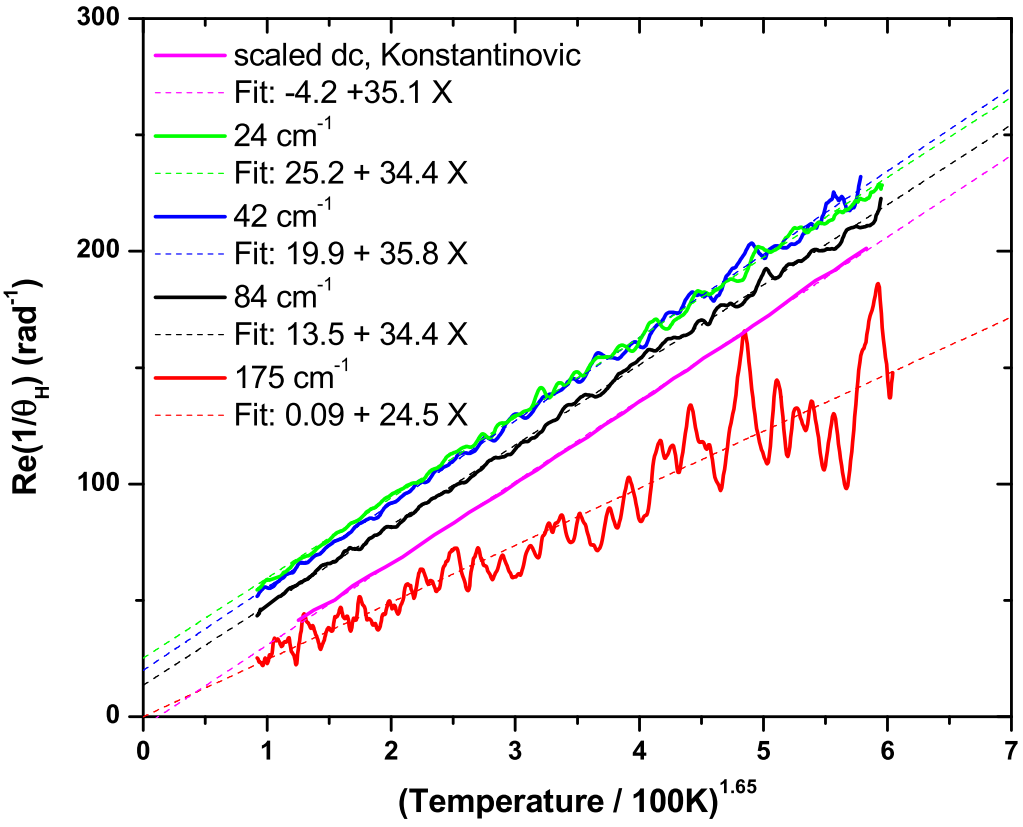

Figure 6.9: The real part of the inverse Hall angle as a function of a temperature power law, $T^{1.65}$, for single crystal BSCCO at 24.6, 42.3, 84.7, and 175.4 cm^{-1} in 8 T. Scaled dc- data from reference [12] is plotted for comparison (actual value is $\approx$ 400 mrad in 8T at 300 K). Linear fit parameters are given in the caption where $X = (T/100)^{1.65}$.

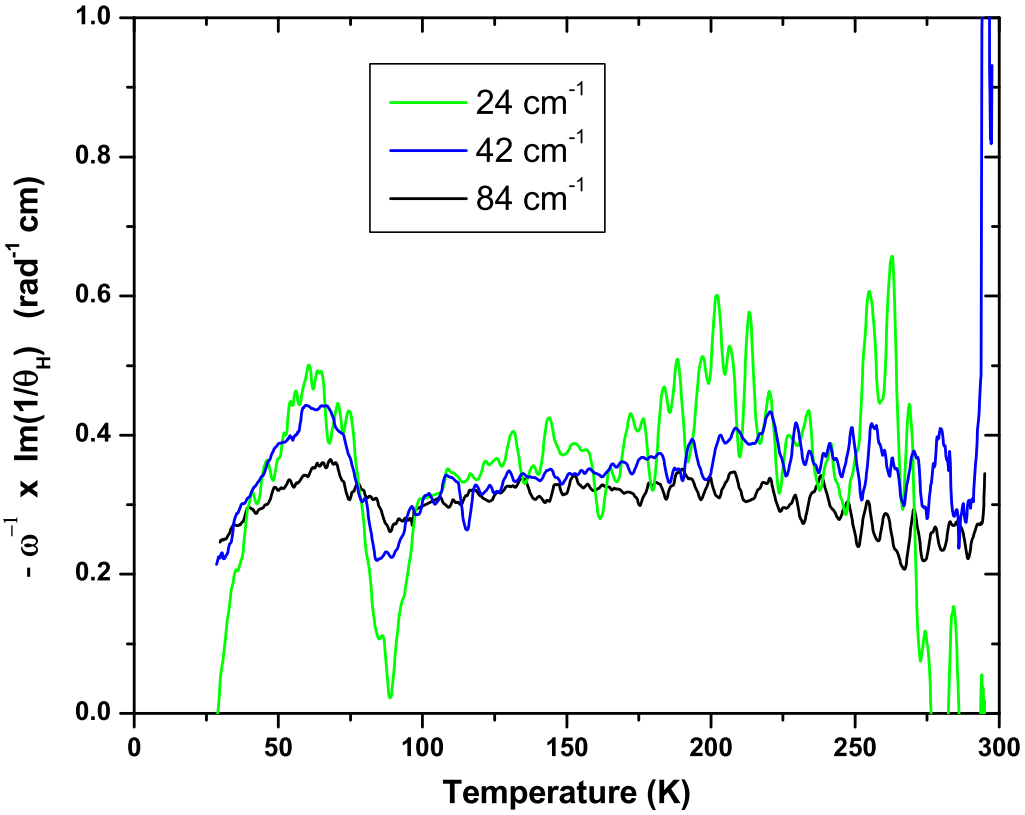

Figure 6.10: The imaginary part of the inverse Hall angle divided by frequency demonstrating a clear precursive behavior to the superconducting state above T_c.

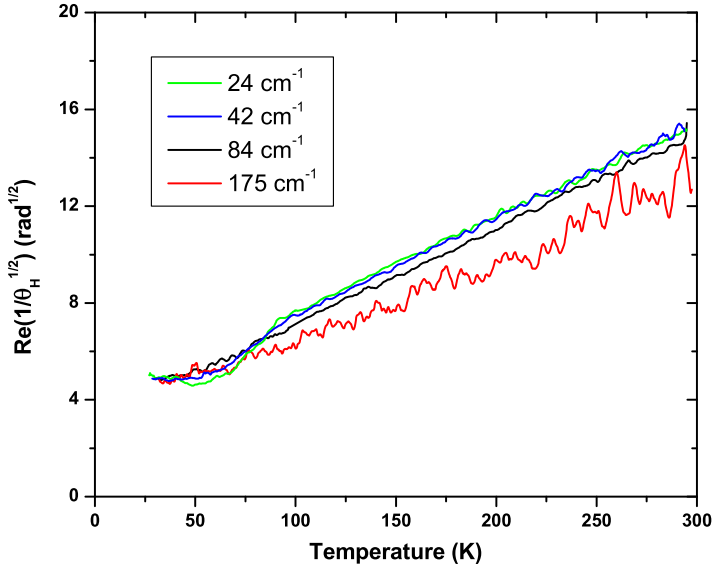

(a) Averaged Re($\sqrt{1/\theta_H}$) at all measured frequencies in 8T

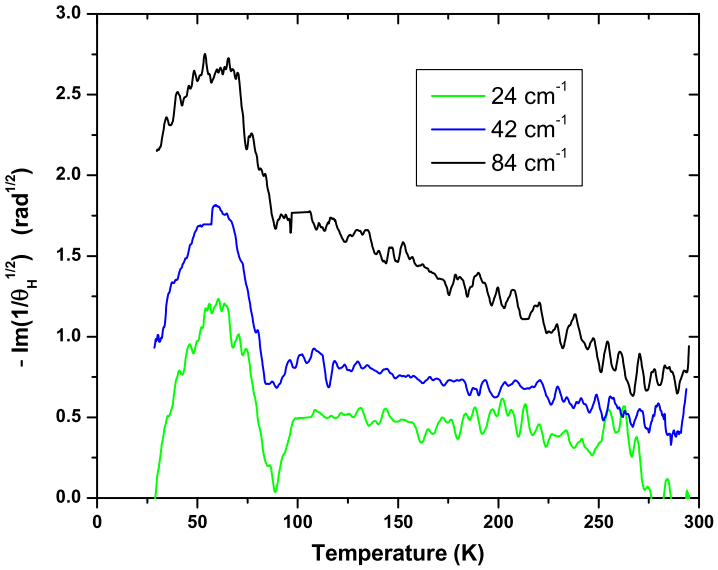

(b) Averaged Im($\sqrt{1/\theta_H}$) at all measured frequencies in 8T

Figure 6.11: The square-root inverse Hall angle as a function of temperature for single crystal BSCCO at 24.6, 42.3, 84.7, and 175.4 cm^{-1} in 8T.

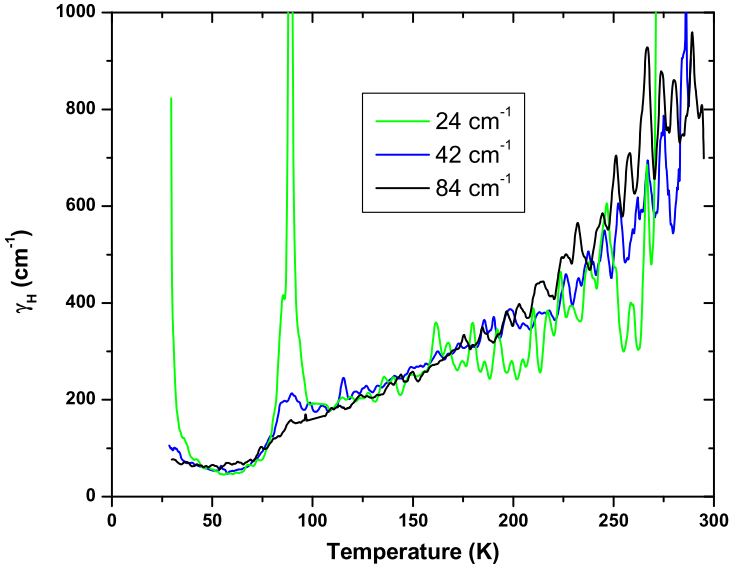

(a) γ_H at all measured frequencies in 8T

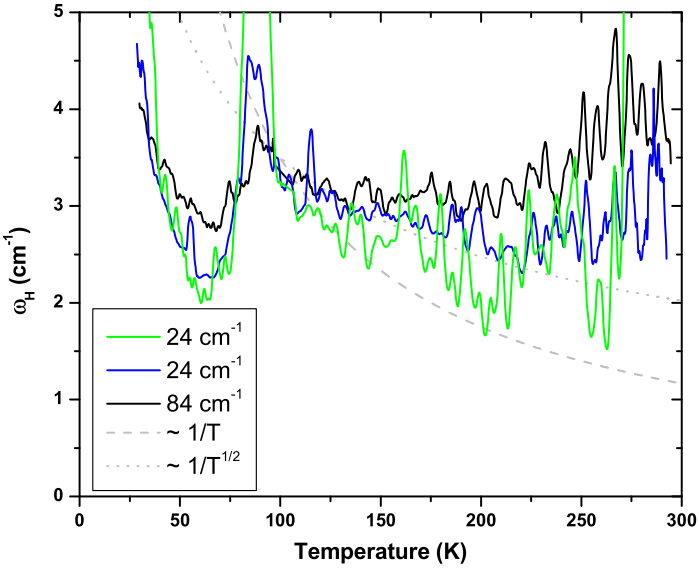

(b) ω_H at all measured frequencies in 8T. Represented in grey are curves of a 1/T and $\sqrt{1/T}$ power laws for comparison.

Figure 6.12: BSCCO response modelled with a Drude Hall scattering rate, γ_H, and a Hall frequency, ω_H, for 24.6, 42.3, and 84.7 cm^{-1} in 8T

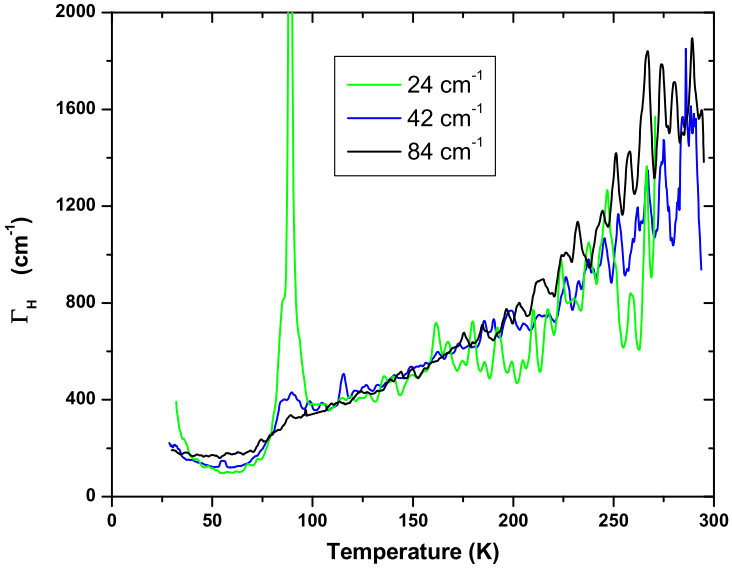

(a) Γ_H at all measured frequencies in 8T

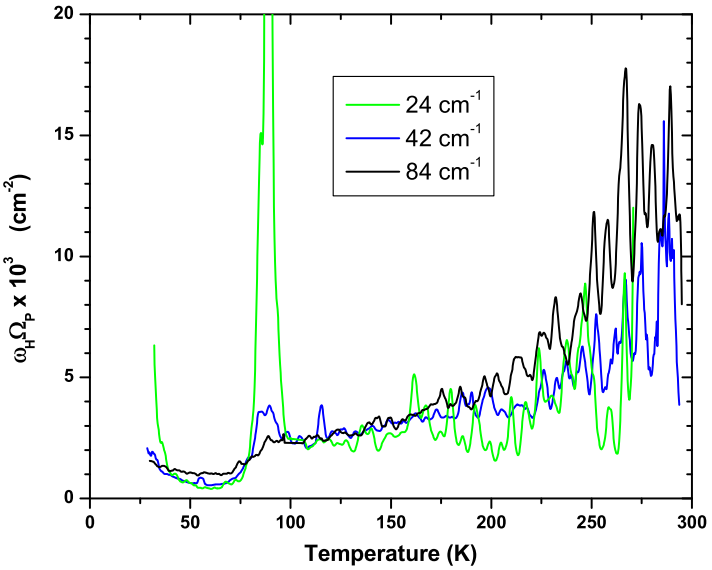

(b) $\Omega_H\Omega_P$ at all measured frequencies in 8T

Figure 6.13: BSCCO response modelled with a square- Lorentzian scattering rate, Γ_H, and a characteristic frequency parameter, $\omega_H\Omega_P$, for 24.6, 42.3, and 84.7 cm^{-1} in 8T

6.3 Normal-state discussion

The positive sign of the real part of the Hall angle as shown in figure 6.7 is consistent with hole-like charge carriers. ARPES[4] and previous FIR-[14] and dc-[12] Hall angle measurements confirm this result.

Drude model

To begin analyzing the normal state Hall data, we use a simple Drude model. This model assumes a particularly simple form for the ac- Hall angle:

$$\begin{aligned} \cot\theta_H \approx 1/\theta_H &= \frac{\gamma_H}{\omega_H} - i\frac{\omega}{\omega_H} \\ &\text{where } \gamma_H \text{ is the scattering rate,} \\ &\omega_H = (qB)/(m^*c) \text{ is the scattering rate,} \\ &m^* \text{ is the effective Hall mass,} \\ &\text{and } \omega \text{ is the frequency of radiation} \end{aligned} \tag{6.1}$$

The real and imaginary part of the inverse Hall angle as a function of temperature at four frequencies are shown in figure 6.8. The resulting extracted Drude parameters, γ_H and ω_H, are given in figure 6.12.

In figure 6.8, notice the noise in both the real and imaginary part of the inverse Hall angle which increases with temperature. The Hall angle is approaching zero with increasing temperature. The resulting relative signal-to-noise decreases with temperature. Therefore, drift errors associated with the system become more significant at high temperatures. For the 24 and 42 cm^{-1} data, the signal-to-noise of the $Im(1/\theta_H)$ degrades quite rapidly resulting in severe errors above $\approx$ 220 K.

The $Re(1/\theta_H)$ data shown in figure 6.8 demostrates a definitive concavity suggestive of a temperature power law whose coefficient is greater than one. The $Im(1/\theta_H)$ displays very little temperature dependence.

The results of parameterizing the Hall data in terms of a Drude model is shown in figure 6.12. The scattering rate shows a clear super-linear temperature dependence. The Hall frequency shows little to no temperature dependence. The best signal-to-noise is given by the 84 cm^{-1} data. For this particular frequency, the Hall frequency shows virtually no temperature dependence. As the frequency is decreased, the system drift problems become increasingly more severe. However, even the 24 and 42 cm^{-1} Hall frequency data show very slight temperature dependencies. For comparison, a plot of 1/T and $\sqrt{1/T}$ is displayed on the same figure.

Konstantinovic[12] measured the dc- $\cot\theta_H$ and found a temperature power law with an exponent of 1.78. I digitized his data and found a power law of $1.75 \pm .05$ from T_c to room temperature by plotting the data as a function of T^α for various values of alpha. Significant deviations from linearity define the error bars. Performing the same analysis on the ac- data yields a power law of 1.65 ± 0.1 for the 24.6, 42.3, and 84.7 cm^{-1} data. The ac- and scaled dc- data versus $T^{1.65}$ in conjunction with the corresponding linear fits are given in figure 6.9. Comparison of the ac- and dc-temperature power law appear remarkably similar.

Therefore, a temperature independent Hall frequency and a Hall scattering rate which obeys the same temperature power law as the measured dc- cotangent Hall angle well describes the ac- Hall angle data. However, the Hall scattering rate exhibits a decrease with increasing frequency demonstrating a clear deviation from a simple Drude model.

Square-Lorentzian model

A similar decrease in the Hall scattering rate with frequency was observed by Grayson *et al*[14] in the ac- FIR Hall angle response of optimally doped YBCO. However, they observed a strong 1/T dependence of the Hall frequency. By ascribing a square- Lorentzian Hall angle response, their observed frequency and temperature dependencies collapsed into a frequency and temperature independent re-normalized Hall frequency and a scattering rate linear in temperature:

$$\begin{aligned} \cot\theta_H \approx 1/\theta_H &= \frac{(\Gamma_H - i\omega)^2}{\omega_H \Omega_P} \\ \Rightarrow \sqrt{\frac{1}{\theta_H}} &= \frac{\Gamma_H - i\omega}{\sqrt{\omega_H \Omega_P}} \end{aligned} \tag{6.2}$$

where Γ_H is a renormalized square-scattering rate,

ω_H is the Hall frequency,

Ω_P is a characteristic frequency,

and ω is the frequency of radiation

Grayson found Γ_H to be linear in temperature (with zero intercept for the dc-extrapolation) and slightly increasing with frequency. The parameter $\omega_H \Omega_P$ was found to be temperature and frequency independent within an error of about 30%. The dc- extrapolation shows a T^2 cotangent Hall angle power law.

The real and imaginary part of $\sqrt{1/\theta_H}$ is plotted in figure 6.11. To be consistent with the square-Lorentzian model, we would expect the real part of $\sqrt{1/\theta_H}$ to be linear in temperature with a possible slight increase with frequency. Although no discernable frequency dependence exists which is consistent with his data below 85

cm^{-1}, a strong deviation away from linearity is observed. The data measured by Grayson was found to be linear in a small temperature range from 95 to 190 K. Within this range, the present data appears to be approximately linear which is in agreement with his observations.

Within the same model, we would expect the imaginary part of $\sqrt{1/\theta_H}$ to be constant in temperature and linear in frequency. Although the linearity in frequency is observed, a strong temperature dependence is observed in the 84 cm^{-1} data. The temperature dependence tends towards a constant as the frequency is decreased.

The actual parameters of the square-Lorentzian model are plotted as a function of temperature in figure 6.13. Γ_H is frequency independent and approximately linear in temperature in the range 95 to 190 K with a strong deviation from linearity above 200 K. $\omega_H \Omega_P$ shows a definitive increase with temperature becoming less temperature dependent with decreasing frequency.

Within the relatively large errors of the experiment performed by Grayson, the current data is consistent with his observations over the temperature range 95 to 190 K. Clear deviations from his model are observed becoming more pronounced at temperatures above 200 K. Namely, the square-scattering rate is super-linear in temperature, and the re-normalized Hall frequency is temperature dependent.

It is interesting to consider the full ramifications of the current data in terms of new power laws within the square-Lorentzian model. The $\mathrm{Re}(\sqrt{1/\theta_H})$ and Γ_H at 84.7 cm^{-1} as a function of temperature reveal the following power laws (found in the same

manor as the Re($1/\theta_H$) power law coefficient illustrated in figure 6.9):

$$
\begin{aligned}
Re(\sqrt{1/\theta_H}) &= 3.3 + 3.9\ t^{1.0\pm.1} \approx 4(1+t) \quad \sqrt{rad^{-1}} \\
\Gamma_H &= 293.3 + 60.3\ t^{3.0\pm.2} \approx 60(5+t^3)\ \ cm^{-1} \\
&\text{where t= T/100 K}
\end{aligned}
\tag{6.3}
$$

Results in the following:

$$
\begin{aligned}
\Rightarrow \omega_H\Omega_P &= \frac{\Gamma_H^2}{Re(\sqrt{1/\theta_H})^2} = \Big(\frac{60}{4}\frac{1+t}{5+t^3}\Big)^2 \\
\text{and } \Rightarrow \frac{1}{\omega} Im(1/\theta_H) &= 2\frac{\Gamma_H}{\omega_H\Omega_P} = 2\ \frac{16}{60}\frac{(1+t)^2}{5+t^3} \\
\text{and } \Rightarrow Re(1/\theta_H) &= \frac{\Gamma_H^2-\omega^2}{\omega_H\Omega_P} \approx \frac{\Gamma_H^2}{\omega_H\Omega_P} = 16(1+2t+t^3)
\end{aligned}
$$

Γ_H obeys a T^3 power law instead of the linear-T dependence observed by Grayson, and the Re($\sqrt{1/\theta_H}$) obeys a linear-T power law. Consequently, $\omega_H\Omega_P$ produces the correct temperature dependent curve shown in figure 6.13(b). The resulting Im($1/\theta_H$) reproduces the dome-shaped curve shown in figure 6.8(b). The Re($1/\theta_H$) produces a *linear curve* when plotted against $T^{1.65}$. This particular model comprehensively fits the data. However, this is not all that surprising since the frequency dependent term in the Re($\sqrt{1/\theta_H}$) is slight between the 24 and 84 cm^{-1} data at all temperatures. Since it is possible to assign virtually any temperature dependence to the two parameters (γ_H and ω_H in the Drude model, and Γ_H and $\omega_H\Omega_P$ in the square-Lorentzian model), the key to clearly discerning the correct parameterization is only accomplished by analyzing the divergence of the two models at sufficiently high frequencies, $\omega \gtrsim \Gamma_H \,||\, \gamma$.

To summarize, the current data is consistent with that observed by Grayson *et*

al. However, in comparison, the substantial increase in signal-to-noise of my data over a wider temperature range show clear deviations of the temperature power laws inferred by Grayson *et al.* Namely, the square-Lorentzian model does not describe my data (unless very different and peculiar temperature dependencies are assigned to the parameters). Furthermore, clear non-Drude behavior is demonstrated in the frequency dependence of the real part of the inverse Hall angle.

Effective Hall mass comparisons within a Drude model

It is interesting to compare the mass enhancement in the FIR ac-Hall angle measurements to that found in other experiments. Calculating the free electron cyclotron frequency gives $\omega_H = .93\ cm^{-1}/T$. The measured FIR ac- Hall frequency within a Drude model is given by:

$$\omega_H = \frac{e\ B}{c\ m_H} = \frac{3.0 \pm .25\ cm^{-1}}{8T} = .375 \pm .03\ cm^{-1}/T \tag{6.4}$$

Inverting equation 6.4 and comparing to the bare cyclotron frequency gives a mass enhancement of $m_H = (2.5 \pm .21)m_e$. Tu[10] measured the longitudinal ac- conductivity, σ_{xx}, and found a mass enhancement of approximately $(3.0 \pm .4)m_e$.

ARPES measures the angular momentum dependent dispersion at the Fermi level[4] on optimally doped BSCCO at 100 K. The Hall angle heavily weights the higher curvature sections of the Fermi surface.[56] ARPES measurements show the high curvature sections are along the $\{\pi, \pi\}$ direction where $k_f = .446\ \mathring{A}^{-1}$. Converting to a hole-like Fermi surface using the fact that the Brillouin zone diagonal is $2\pi/5.5\ \mathring{A}^{-1}$ gives $k_f \approx 2\pi/5.5 - .446 \approx .69\ \mathring{A}^{-1}$. The Fermi velocity along this direction is measured

to be 1.8 $eV\mathring{A}$. The effective mass is given by:

$$m_{ARPES} = \frac{\hbar k_f}{v} = \hbar k_f \Big(\hbar k_f \frac{\delta E}{\delta k_f}\Big)^{-1} = 2.9\ m_e \tag{6.5}$$

Near-IR ac- Hall angle measurements on optimally doped BSCCO made by D. Schmadel[13] find a strikingly similar $m_H = 2.8\ m_e$ at $950cm^{-1}$ and 100 K, with a 20% linear decrease with an increase in temperature from 100 K to room temperature.

The current FIR ac- Hall angle, ARPES, Near-IR ac- Hall angle, and FIR spectroscopy measurements show approximately the same mass enhancement.

Hall scattering rate comparisons within a Drude model

Direct comparison between the longitudinal and Hall scattering rates are theoretically problematic. The off- diagonal conductivity heavily weights the scattering rate at high curvature regions of the Fermi surface.[56] The longitudinal conductivity averages the scattering rate uniformly around the Fermi surface (with the exception of a $\cos^2(\theta)$ factor favoring the electric field direction). Anisotropic momentum dependent scattering, for example, can cause deviations between the longitudinal and Hall effective scattering rates.

Theory aside, it is interesting to directly compare other experimental scattering rates. Drew *et al.*[57] calculated the longitudinal scattering rate of optimally doped BSCCO applying the relation $\gamma_S \equiv \frac{1}{\omega}\frac{Re(\sigma_{xx})}{Im(\sigma_{xx})}$ using the conductivity from spectroscopic measurements.[11] The longitudinal scattering rate acquired from transmission measurements in table 5.1 and the Hall scattering rates presented in figure 6.12 are compiled in table 6.2 for comparison. The Hall scattering rates are within ∼30% of

Temperature	γ_S	γ_B	γ_H
100 K	168 cm^{-1}	115 cm^{-1}	170 $\pm$ 10 cm^{-1}
200 K	504 cm^{-1}	232 cm^{-1}	380 $\pm$ 10 cm^{-1}
300 K	672 cm^{-1}	350 cm^{-1}	800 $\pm$ 100 cm^{-1}

Table 6.2: γ_S, γ_B, and γ_H are the scattering rates from reference 57, transmission measurements, and FIR ac-Hall measurements, respectively.

the scattering rates reported by Drew *et al.*

Normal state synopsis

When analyzed within a Drude model, the Hall frequency is found to be temperature and frequency independent. The extracted effective Hall mass of $(2.5 \pm .21)\ m_e$ is in agreement with values found in FIR optical measurements $(3.0 \pm .4)$, ARPES $(2.9\ m_e)$, and near-IR ac- Hall measurements $(2.8\ m_e)$. The temperature dependence of the real part of the inverse Hall angle matches that found from dc- cotangent Hall angle measurements. A decrease in the real part of the inverse Hall angle with increasing frequency demonstrates non-Drude like behavior. The present data is consistent with that reported by Grayson *et al* over a narrow temperature range. However, due to the substantial increase in signal-to-noise, the present data demonstrates clear deviation of the previously inferred temperature power laws of the Hall scattering rate and Hall frequency in both the Drude and Lorentzian models. The present data is well described by the square Lorentzian model. However, the inferred temperature dependencies of the model parameters are rather peculiar.

6.4 Superconducting-state discussion

A model of the low temperature superconducting conductivity developed by Drew *et al.* is detailed in section 3.8.2. The conductivity (equation 3.42) consists of the sum of four Lorentzian oscillators: three associated with the vortices and superfluid, and one with the thermally excited nodal quasi-particles.

The dichroic magneto-optical response was measured by H. S. Lihn[22] and S. Wu[24] in optimally doped YBCO. The parameters in the model were found by fitting data measured at low temperatures (< 20 K). The best fit parameters revealed an electron-like low frequency oscillator at $\sim -3\ cm^{-1}$ of width $10\ cm^{-1}$ with a weight of .14, a hole-like high frequency oscillator at $\sim 24\ cm^{-1}$ of width $\sim 17\ cm^{-1}$ with a weight of .11, a superfluid oscillator strength of .36, and a quasi-particle cyclotron frequency of $\sim 3\ cm^{-1}$ of width $\sim 4\ cm^{-1}$.

Weaker resonant-like features were observed at 72 (width 8), 90 (width 16), 116 (width 3.5), and 158 (width 8) cm^{-1}.

Pan *et al.*[55] probed the vortex core states via STM measurements. They measured the first excited state core level at an energy of ~ 7 meV ($55\ cm^{-1}$) above the Fermi energy for optimally doped Bi-2212, and ~ 5.5 meV ($44\ cm^{-1}$) for YBCO.

The present data covers a wide range of temperature. Many parameters can not realistically be assumed temperature independent. For example, the size of the vortex cores increase with temperature[58] which decrease the core level spacing. The pinning frequency depends strongly upon temperature (for example, it is *a priori* known that pinning force vanishes above the vortex glass melting temperature, ~ 70 K). The high frequency resonances ($> 100\ cm^{-1}$) observed by S. Lihn demonstrated quite strange temperature dependencies.

Application of the Drew *et al.* phenomenological model

It remains instructive to extrapolate this low temperature model to high temperatures. The temperature dependence of the nodal quasi-particle fraction and scattering rate have been measured in microwave experiments.[59] The functional form is incorporated into the model (see equation 6.6).

The salient features of the FIR ac- Hall data are described by the following minimum number of terms: a zero frequency superfluid resonance (London term), a cyclotron resonance associated with the nodal quasi-particles, and a finite frequency oscillator:

$$\sigma_{\pm} = \Big(\frac{f_L}{-i\omega} + \frac{f_p}{-i(\omega \pm \omega_p) + \Gamma_p(t)}\Big)(1 - f_n(t)) + \frac{f_n(t)}{-i(\omega \pm \omega_n) + \Gamma_n}$$

where $t = T/T_c$, the normalized temperature

$$f_n(t) = \begin{cases} 1 & : \quad t > 1 \\ t^2 & : \quad t < 1 \end{cases} \approx (t^{-2*40} + 1)^{-40}$$

$$\Gamma_n(t) = \begin{cases} 130\ cm^{-1}\ \ t^{1.65} & : \quad t > 1 \\ 130\ cm^{-1}\ \ t^4 & : \quad t < 1 \end{cases} \approx 130\ cm^{-1}\ (t^{-4*40} + t^{-1.65*40})^{-40} \tag{6.6}$$

$\omega_n = 3.0\ cm^{-1}$

$f_p = .04$

$\Gamma_p = 20\ cm^{-1}$

$\omega_p = 35\ cm^{-1}$

$f_L = .45$

$T_c = 90K$

The model is plotted in figures 6.15 (a)-(f). Figure 6.15(a)/(b) is a plot of only the quasi-particle term ($f_L = 0$ and $f_p = 0$). Figure 6.15(c)/(d) incorporates the London term ($f_p = 0$). Figure 6.15(e)/(f) shows the full model.

The 175 cm^{-1} data is well described by the quasi-particle cyclotron resonance independent of other possible resonant terms. This is consistent with the observations made by Karrai *et al.*[25]

The London term alone in the conductivity causes no Hall effect ($\theta_H \propto \sigma_+ - \sigma_- = 0$). With the Addition of the quasi-particle term, the coarse structure observed in the real part of the Hall angle data can not be produced. The low frequency data is not well described without the presence of a finite frequency oscillator.

Most of the salient features observed in the data are represented by the full model of equation 6.6. The real part of the Hall angle (6.15(e)) at 84 cm^{-1} demonstrates a broadly peaked feature with an upturn with decreasing temperature. The 24 and 42 cm^{-1} traces show a sharp increase below T_c. A measured narrow peak-dip feature corresponds with the broad peak-dip feature of the model. The 24 cm^{-1} trace in the model, though decreasing at 60 K, shows a maximum as eluded to by the levelling-off of the data. The 24 and 42 cm^{-1} traces cross at low temperature as represented by the data.

The imaginary part of the Hall angle (6.15(f)) at 84 cm^{-1} demonstrates the inflection point behavior in the vicinity of T_c and levels-off below 70 K in agreement with the data. The 24 cm^{-1} model shows an initial decrease in the vicinity of T_c together with a dome feature. The 42 cm^{-1} model shows a sharp increase below T_c, and a partial dome feature.

There are obvious deviations from the model suggesting either the presumed tem-

perature dependencies are not correct or more resonances are required. The absolute values of the real and imaginary part of the Hall angle do not quite agree with the data. Some of the features, such as the 42 cm^{-1} broad shallow peak, are either grossly exaggerated or under represented. The precise location in temperature of the features are not the same as in the data. A deviation of particular interest is the narrow dip feature beginning above T_c in the imaginary part of the Hall angle, which the model completely ignores.

Transition region above T_c

A dip feature in the superconducting state has an onset temperature well above T_c observable in the $Im(1/\theta_H)$ in figure 6.10 at 24, 42, and 84 cm^{-1}, but is most pronounced at 24 cm^{-1}. This appears to be precursive superconducting behavior well above the transition temperature. No discernable deviant features are observable above T_c in the $Re(1/\theta_H)$ (figure 6.8(a)).

Corson and Orenstein observed a similar phenomenon above T_c in both under-[60] and optimally-[61] doped BSCCO in the longitudinal conductivity, $\tilde{\sigma}_{xx}$, using a terahertz spectroscopy technique. For the underdoped material, the imaginary part of $\tilde{\sigma}_{xx}$ exhibits a relatively strong increase beginning 25 K above T_c and increases with decreasing temperature. They suggest that a Kosterlitz-Thouless transition,[62] whose vortex- anti-vortex recombination time defines a cross-over frequency (ω_{KT}) in the low far-infrared frequency regime, is responsible. If the probe frequency is below ω_{KT}, phase fluctuations in the order parameter caused by the relatively rapid creation and annihilation of vortices kill superconductivity resulting in a putative normal state. For frequencies above ω_{KT}, the phase in the order parameter is not observed

to fluctuate on the time scale of the measurement. At frequencies above ω_{KT} and at temperatures above T_c (but below the temperature in which the order parameter *magnitude* vanishes), superconductivity phenomena, or 'superconducting remnants', may be observable.

The maximum dephasing rate is given by the frequency[2] $\sim k_B T_c/\hbar = 60cm^{-1}$ for $T_c = 90$ K. Within this model and slightly above T_c, the normal state is indistinguishable from the superconducting state when probed with frequencies above the maximum dephasing rate.

Various experiments have exhibited precursive superconducting behavior in the normal state in the high-Tc cuprates: microwave cavity measurements in optimally doped YBCO[63] with an onset 10 K above T_c, various terahertz spectrocopy measurements in optimally and under doped BSCCO and YBCO,[60,61,64] Nernst effect measurements with onset temperatures of 50 to 100 K above T_c at various doping levels in $La_{2-x}Sr_xCuO_4$ and $Bi_2Sr_{2-y}La_2CuO_6$,[65] specific heat measurements in optimally doped BSCCO,[66] infra-red reflectivity experiments in under- and optimally doped BSCCO,[67] dc- Hall angle measurements in slightly underdoped $GdBa_2Cu_3O_{7-\delta}$[68] and $YBa_2Cu_4O_8$[69] and under- and optimally- doped $YBa_2Cu_3O_{7-\delta}$,[70] tunnelling experiments in slightly underdoped BSSCO,[71] and ARPES measurements in underdoped BSCCO.[72] Heat capacity measurements and terahertz measurements suggest the existance of a pseudogap regime in optimally doped BSCCO.

To analyze the dip feature, it is instructive to recast the Hall angle into the

following form:

$$\begin{aligned} \theta_H \equiv \frac{\sigma_{xx}}{\sigma_{xy}} &= \frac{\sigma_{xx}\sigma_{xy}^*}{\sigma_{xy}\sigma_{xy}^*} \\ \Rightarrow -\frac{Im(1/\theta_H)}{Re(1/\theta_H)} &= \frac{Im(\sigma_{xy})Re(\sigma_{xx}) - Re(\sigma_{xy})Im(\sigma_{xx})}{Re(\sigma_{xy})Re(\sigma_{xx}) + Im(\sigma_{xy})Im(\sigma_{xx})} \end{aligned} \tag{6.7}$$

Representing the complex conductivities and Hall angle in polar coordinates yield:

$$\theta_H \equiv \theta_{H0} e^{i\,\phi_H}$$

$$\sigma_{xx} \equiv \sigma_{xx0} e^{i\,\phi_{xx}}$$

$$\sigma_{xy} \equiv \sigma_{xy_0} e^{i\,\phi_{xy}}$$

substitution gives:

$$\tan\phi_H = \tan\left(\phi_{xy} - \phi_{xx}\right) \tag{6.8}$$

where

$$\begin{aligned} \tan\phi_{xy} &= \frac{Im(\sigma_{xy})}{Re(\sigma_{xy})} \\ \tan\phi_{xx} &= \frac{Im(\sigma_{xx})}{Re(\sigma_{xx})} \end{aligned} \tag{6.9}$$

Within a Drude model, the quantities may be written as the following (see equations

3.30) in the approximation $\omega_c \ll \omega \ll \gamma$:

$$\begin{aligned} \tan\phi_{xy} &= \frac{Im(\sigma_{xy})}{Re(\sigma_{xy})} \approx \frac{2\omega}{\gamma} \\ \tan\phi_{xx} &= \frac{Im(\sigma_{xx})}{Re(\sigma_{xx})} \approx \frac{\omega}{\gamma} \\ \Rightarrow \tan(\phi_H) &\approx \frac{2\omega}{\gamma} - \frac{\omega}{\gamma} = \frac{\omega}{\gamma} \end{aligned} \tag{6.10}$$

The 24 cm^{-1} data in figure 6.10 deviates from the high temperature behavior at $\sim$ 100 K, and $\tan(\phi_H)$ reduces to ~ 0 at T_c. This is equivalent to stating that $\phi_{xx} \approx \phi_{xy}$ at T_c. This requires a deviation away from that predicted by a simple Drude model from 100 K to T_c: either ϕ_{xx} increases by a factor of 2, or ϕ_{xy} decrease by a factor of 2, or some combination of an increase in ϕ_{xx} and decrease in ϕ_{xy} such that the difference vanishes at T_c. The remaining discussion focuses on discerning these 3 possibilities.

In section 5.1.3, the real and imaginary part of the longitudinal conductivity was extracted from the transmission using a Drude model analysis. The complex conductivity is sufficient for the purpose of converting the Faraday angle to the Hall angle. However, in the transition region, the analysis is inadequate. From terahertz measurements,[60] the conductivity behavior is distinctly non-Drude exposing the analysis as suspect. Since the real part of the conductivity dominates the transmission in this region, the method is inherently insensitive to the relative changes between the real and imaginary parts of the conductivity. There is no plausible method to extract ϕ_{xx} from the transmission data without the capability of modelling.

Four unknown quantities exist as a function of temperature, the real and imaginary parts of the transverse and longitudinal conductivities. Only three quantities are

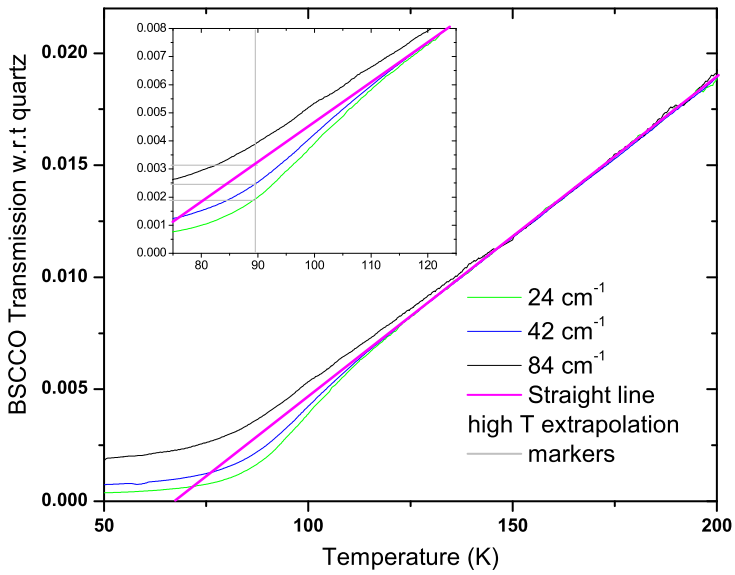

Figure 6.14: The transmission of BSCCO on a quartz substrate normalized to a quartz substrate at 24, 42, and 84 cm^{-1}. The straight magenta colored line is a high-temperature extrapolation of the transmission. The inset contains guides for the eye in aiding the extraction of transmission values at 90 K.

measured: the transmission and the real and imaginary part of the Hall angle. The relationship between these quantities is given by the following:

$$\begin{aligned} Tr &= \frac{1}{|1 + Z' d\sigma_{xx}|^2} \\ Im(\theta_H) &= \frac{1}{|\sigma_{xx}|^2}(Im(\sigma_{xy})Re(\sigma_{xx}) - Re(\sigma_{xy})Im(\sigma_{xx})) \\ Re(\theta_H) &= \frac{1}{|\sigma_{xx}|^2}(Re(\sigma_{xy})Re(\sigma_{xx}) + Im(\sigma_{xy})Im(\sigma_{xx})) \end{aligned} \tag{6.11}$$

where $Z' = 377\Omega/(n+1)$, $n = 2.12$, and Tr is the transmission. Unfortunately, no derivable relation exists which cast the ratio of any two of the unknown quantities as a function of known quantities.

In figure 6.14, a deviation of the transmission from the high-temperature Drude-like extrapolation (represented by the magenta line) is evident in both the 24 and 42 cm^{-1} data. The enhancement of σ_{xx} above that expected from the Drude contribution may be estimated at 90 K:

$$Tr^D = 31 \times 10^{-3} \qquad Tr_{42} = 25 \times 10^{-3} \qquad Tr_{24} = 19 \times 10^{-3}$$
$$\frac{|\sigma_{xx}|}{|\sigma_{xx}^D|} \approx \sqrt{\frac{Tr^D}{Tr}} = \begin{cases} 1.1 \text{ for } 42cm^{-1} \\ 1.3 \text{ for } 24\ cm^{-1} \end{cases} \tag{6.12}$$

where Tr^D is the expected transmission based upon the high temperature measurements, Tr_{42} is the measured transmission at 42 cm^{-1}, and Tr_{24} is the measured transmission at 24 cm^{-1}. The downturn in the transmission measured at 24 cm^{-1} and 90 K is a result of an enhancement of the longitudinal conductivity magnitude of approximately 30% above that expected from a simple Drude model.

In a 1999 Nature publication,[61] Orenstein and Corson report the real and imaginary part of σ_{xx} of underdoped BSCCO (T_c=75 K) as a function of temperature at 100GHz $\sim$ $3.3cm^{-1}$. The ratio of ϕ_{xx} at T_c to ϕ_{xx} at 100 K is $\gtrsim 4$ indicating the imaginary part of σ_{xx} increases more rapidly than the real part of σ_{xx}. In a 2000 PRL publication,[60] they report only the real part of σ_{xx} as a function of temperature on optimally doped BSCCO but show deviations away from the Drude (quasi-particle) contribution at .2, .6, and .8 THz. The conductivity enhancement above the Drude contribution is a factor of 2, 1.2, and 1.13, respectively. The enhancement that I measure in the *magnitude* of the conductivity at 24 cm^{-1} $\sim$ .7 THz is 1.3. The enhancement of the magnitude of the conductivity is expected to be larger than the enhancement of the real part of the conductivity due to the onset of a substantial

imaginary part.

Whether the dip feature is primarily due to ϕ_{xx} or ϕ_{xy} remains illusive. However, the reported values of the conductivity, at least at 100GHz,[61] show the imaginary part of σ_{xx} increasing faster than the real part of σ_{xx} by at least a factor of 4 as the temperature decreases from 100 K to T_c. For the 24 cm^{-1} data, a similar hypothetical enhancement of ϕ_{xx} by a factor of 2 in the current ac- Hall data would be both qualitatively consistent with the terahertz measurements as well as explain the dip feature in figure 6.10.

To clearly discern the cause of the dip feature, another measurement is necessary. Measuring, for instance, the transmission and reflection of the BSCCO sample, the complex conductivity could be extracted. However, as was painfully obvious in section 5.1.3, the epoxy severely complicates the analysis. A possible alternative exploits a technique that Jeff Simpson[73] and Dennis Drew have recently developed. The transmission through a thin film mounted (or grown) on a substrate is spectrally measured with a resolution much better than the spectral spacing of the etalon produced inside the substrate. By measuring the etalon peak locations and absolute transmission as a function of temperature and frequency, the complex conductivity may be extracted. This technique may prove especially useful considering the characteristics of the present sample. In the transition region, the imaginary part of the conductivity is expected to substantially increase as T_c is approached from the normal state. The shift in the spectral etalon pattern is particularly sensitive to the inductive response of the conductivity. This is demonstrated by considering the phase of the reflection

Fresnel coefficient at the superconducting-substrate boundary inside the substrate:

$$
\begin{aligned}
r &= \frac{n-1-Z_0\sigma_{xx}d}{n+1+Z_0\sigma_{xx}d} = -\frac{1-(n-1)/(Z_0\sigma_{xx}d)}{(n+1)/(Z_0\sigma_{xx}d)+1} \\
&\approx -(1-(n-1)/(Z_0\sigma_{xx}d))(1-(n+1)/(Z_0\sigma_{xx}d)) \approx -(1-\frac{2n}{Z_0\sigma_{xx}d}) \text{ for } Z_0\sigma_{xx}d \gg n \\
&\approx -e^{-\frac{2n}{Z_0\sigma_{xx}d}} \\
&= -e^{-\frac{2n}{Z_0 d}Re(1/\sigma_{xx})}e^{-i\frac{2n}{Z_0 d}Im(1/\sigma_{xx})} \\
&\equiv r_0 e^{-i\beta}
\end{aligned}
$$

where $r_0 = -e^{-\frac{2n}{Z_0 d}Re(1/\sigma_{xx})}$, $\beta = \frac{2n}{Z_0 d}Im(1/\sigma_{xx})$, and $Z_0 = 377\Omega/\Box$.

Superconducting state synopsis

The superconducting state is qualitatively described by a phenomenological model of the conductivity which contains a quasi-particle cyclotron resonance, a zero frequency superfluid resonance, and one finite frequency chiral oscillator at $\sim 35\ cm^{-1}$. The 175 cm^{-1} real part of the Hall angle data is consistent with one collective mode cyclotron resonance consistent with the measurements made by Karai *et al.*[25]

Precursive superconducting behavior in the normal state 10 K above T_c is observed in the imaginary part of the inverse Hall angle at 24 and 42 cm^{-1}. Whether σ_{xy} exhibits precursive behavior is undetermined, though $|\sigma_{xx}|$ demonstrates an anomalous enhancement as measured by transmission.

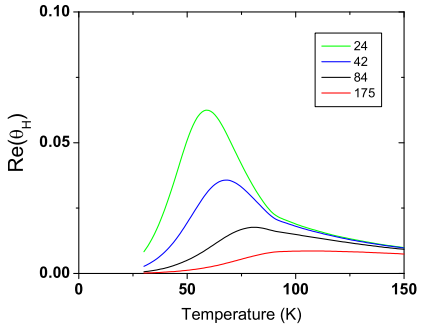

(a) $Re(\theta_H)$: Quasi-particle only

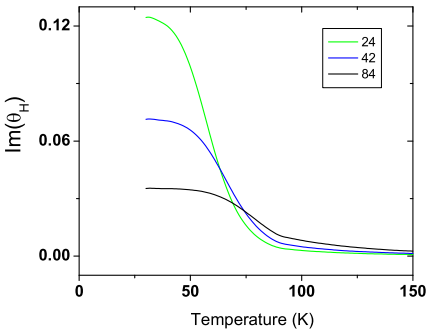

(b) $Im(\theta_H)$: Quasi-particle only

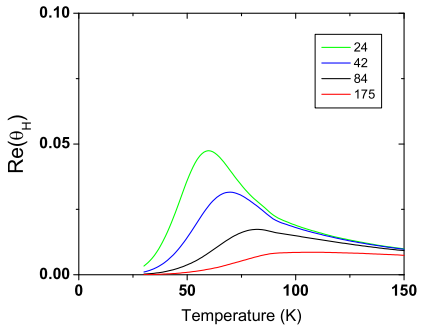

(c) $Re(\theta_H)$: Quasi-particle and London

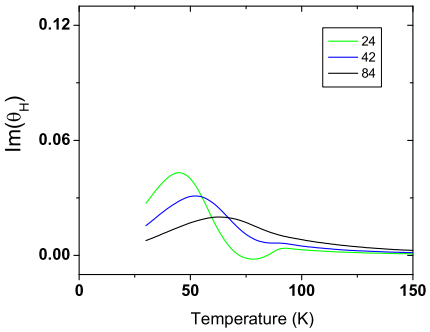

(d) $Im(\theta_H)$: Quasi-particle and London

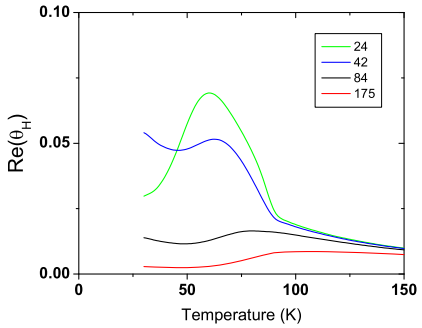

(e) $Re(\theta_H)$: Quasi-particle, London, and 35 cm^{-1} oscillator

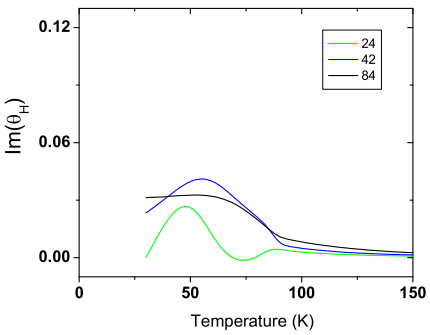

(f) $Im(\theta_H)$: Quasi-particle, London, and 35 cm^{-1} oscillator

Figure 6.15: Superconducting state models of BSCCO at 24.6, 42.3, 84.7, and 175.4 cm^{-1}. All angles measured in radians.

6.5 Conclusion

Summary of results

The complex ac- Hall angle was measured in the far-infrared in optimally doped single crystal $Bi_2Sr_2CaCu_2O_{8+x}$ as a continuous function of temperature. The temperature was varied from 25 to 300 K at four frequencies: 24.6, 42.3, 84.7, and 175.4 cm^{-1}.

The important findings are summarized with details to follow:

- The BSCCO FIR Hall measurements are neither well described by a square-Lorentzian model nor a Drude mode.

- The BSCCO FIR Hall measurements are consistent with previous measurements on YBCO.[14]

- The cotangent of the Hall angle in the FIR obeys the same temperature power law as that found from dc- Hall angle measurements. The temperature dependence is fully attributed to the Hall scattering rate, which leaves the discrepancy between longitudinal (dc[12] and IR spectroscopic[11]) and ARPES measured linearly temperature dependent scattering rates and the dc- Hall scattering rate[12] ($\propto T^{1.78}$) unresolved.

- NIR ac- Hall angle measurements[13,19] reveal a temperature and frequency independent mass enhancement which is within 20% of that found in the FIR, and a scattering rate (though linear) which is within 15% of that found in the FIR from T_c to room temperature.

- Precursive superconducting behavior is observed over 10 K above T_c which is consistent with the longitudinal conductivity enhancements measured by Corson and Orenstein.[60,61]

- A finite frequency chiral Lorentzian oscillator ($\sim$35 cm^{-1}) was required to qualitatively describe the superconducting behavior within the Drew-Lihn-Wu phenomenological model.

- The data measured at 175.4 cm^{-1} is described by one chiral collective mode resonance, consistent with the measurements performed by Karai *et al.*[25]

The real part of the inverse Hall angle obeys a temperature power law, T^{α}, where α is $1.65 \pm .1$ which is consistent with the dc- value of $1.75 \pm .05$. The values decrease with increasing frequency clearly displaying non-Drude behavior. The Hall frequency is 0.38 ± 0.03 cm^{-1}/T, approximately constant in temperature and frequency for the lowest 3 frequencies. The resulting effective mass is $(2.5 \pm .21)$ m_e which is in reasonable agreement with the values found in FIR optical measurements $(3.0 \pm .4)$, ARPES dispersion results along the (π, π) nodal direction (2.9 m_e), and near-IR ac-Hall measurements (2.8 m_e).

The current results agree with those found by Matt Grayson *et al.*[14] over the narrow temperature range 95 to 190 K considering his relatively large noise level. However, with the significantly improved signal-to-noise of the current experiment, large discrepancies are revealed in the temperature dependencies inferred by Grayson. Within the square Lorentzian model, Grayson well described his data with a slight frequency dependent renormalized scattering rate with a linear temperature dependence, and a renormalized Hall frequency which is inversely proportional to temperature and

frequency independent. I find a severely superlinear temperature dependence of the renormalized scattering rate, and a definitive temperature dependent renormalized mass.

Abandoning the power laws observed by Grayson *et al* and assigning rather peculiar temperature dependencies to the renormalized Hall frequency and scattering rate, the data is described by the square Lorentzian model. However, this is not surprising considering that, at the frequencies measured, the scattering rate is much larger than the measured frequency resulting in a two parameter model whose parameters may be assigned any arbitrary temperature dependence to describe the two measured parameters, the real and the imaginary part of the Hall angle.

A temperature dependent feature in the imaginary part of the inverse Hall angle is observed above T_c that suggests a precursor to the superconducting state. The onset is clearly observed in both the 24 cm^{-1} data and 42 cm^{-1} data at ∼100 K. It is undetermined whether the onset is due to σ_{xy}, σ_{xx}, or a combination of both. However, the onset temperature is quantitatively similar to the onset observed by Corson and Orenstein,[60] and the enhancement of σ_{xx} above T_c extracted from my transmission measurements is qualitatively consistent. That is, the absolute value of σ_{xx} demonstrates precursive behavior as measured by transmission, but its roll in relation to σ_{xy} in the precursive behavior of the Hall angle is undetermined.

The salient features of the superconducting state are qualitatively consistent with a simple model of the conductivity which contains a quasi-particle cyclotron resonance, a zero frequency superfluid resonance, and one finite frequency chiral oscillator at $\sim 35\ cm^{-1}$. The real part of the Hall angle data at 175 cm^{-1} is consistent with one collective mode cyclotron resonance consistent with the measurements made by Karai

et al. Though no firm conclusions are drawn from the analysis, the necessity of a high frequency oscillator is suggestive of a vortex core resonance measured by S. Wu[24] and Sonier.[74]

Experimental proposals

By improving the signal at frequencies above 84 cm^{-1}, the divergence between the square Lorentzian model and the Drude model at high frequencies may be more adequately discerned independent of the temperature dependencies of the scattering rate and Hall frequency. Also, since the imaginary part of the Hall angle at high frequency is substantially larger at room temperature (> 1 mrad), the measurements are insensitive to the relatively small drifts associated with the current instrument. The existing system with an increase in FIR laser output power at high frequencies is capable of precise measurements of the temperature power laws associated with the Hall angle.

FIR magneto-optical transmission measurements by S. Lihn[22] and S. Wu[24] at low temperature in optimally doped YBCO reveal a spectrally resolved resonant feature that is interpreted as a vortex core resonance at $\sim$24 cm^{-1}. Measurements at many frequencies in the current experiment may allow the spectral resolution of distinct Lorentzians.

The temperature dependence of resonant features could prove interesting. Muon-spin-rotation spectroscopy measurements reveal the vortex core size increases with temperature and decreases with magnetic field.[58] The core size increases sharply as the temperature approaches T_c. A change in core size would manifest as a shift in the core resonant frequency. Furthermore, Lihn and Wu measured resonant-like features

at approximately integral multiples of the fundamental core resonance. Some of these features exhibit peculiar temperature dependencies which urge further exploration.

Many theories have been developed in an effort to explain the many different behaviors associated with vortex dynamics: low temperature vortex dynamics, vortex lattice melting, vortex glass melting, vortex bundle dynamics, and vortex fluctuations in the vicinity of T_c. By measuring the temperature dependence of the vortex dynamics across all of the various regimes at many FIR frequencies where the energy scales associated with vortex pinning, cyclotron resonances, and vortex core excitations occur, various proposed models may be explored (see reference 75 for a comprehensive review).

The pseudogap regime in high-T_c materials is typically characterized by an onset temperature, T^*. The FIR ac- Hall effect may prove to be a sensitive measurement for defining the onset temperature. It would be interesting to map T^* as a function of doping in single crystal BSCCO. The phase stiffness energy $\sim k_B T_c/\hbar$ would theoretically vary as a function of doping causing a change in the cross-over frequency, ω_{KT}. Testing of the relation $\omega_{KT} \propto T_c$ would be of significant importance.

The normal state electronic response as a function of doping is of substantial interest as well. Rigal *et al.*[19] report an increase of the Hall frequency and decrease of the plasma frequency with decreasing doping in $YBa_2Cu_3O_7$. The results indicate an enhancement of the effective mass and a decrease in the charge density with decreased doping. These results seem to be qualitatively consistent with photoemission experiments which exhibit the development of Fermi surface pockets. The FIR ac-Hall effect may manifest similar behavior, or, as interesting, may not.

Instrument improvements

The system is capable of measuring the real and imaginary part of the Hall angle to an accuracy of $\sim \pm.1$ mrad over a temperature range of 20 to 320 K, and a frequency range of 20 cm^{-1} to 240 cm^{-1}. The transmission is concurrently measured and normalized to a reference bolometer.

The main deficiency in the current BSCCO measurements is lack of data at higher frequencies which is a direct result of insufficient power output from the FIR laser. As outlined in section 4.4.5, various improvements are suggested. Other than the direct improvements in signal-to-noise and obvious applicability to higher frequency measurements, attenuation of drift problems associated with the system may be possible. Narrowing the spacial filter iris aperture influences drift and peak-to-peak B-field oscillations. Also, attenuation of the beam within the cryostat may reduce possible etalon effects that may occur within the cryostat. A reduction in the number of necessary waveplates (the modulation depth no longer requiring precise optimization) would reduce the characterizations necessary to acquire data at various frequencies.

As mentioned in section 6.4, an independent measurement of σ_{xx}, such as the method developed by J. Simpson,[73] is required to discern the cause of the precursive behavior in the imaginary part of the Hall angle. However, it would be useful to acquire the transmission in- and out- of field. The magneto-enhanced transmission could accurately be measured as a function of temperature with minimal effort. No change in the existing system is necessary.

Separation of the cryostat from the optics table may prove beneficial. Reduction in the peak-to-peak oscillations in the magnetic field- sweep data was observed as a result of clamping the cryostat between the ceiling and floor. The oscillations may

be a result of the optics table flexing caused by magnetic forces between the magnet and ferrous materials located in the floor, walls, and ceiling. Also, the change in the cryogen level during the course of an 8 hour experiment gradually alters the weight on the table. The Oxford cryostat dewar has a total liquid helium capacity of 20L ($\sim$ 6lbs) and a total liquid nitrogen capacity of 24L ($\sim$ 8lbs). If, during the course of an experiment, all the liquid helium and half of the liquid nitrogen evaporates, the total weight change of the cryostat is $\sim$8lbs. A 10lb weight can cause a 2 mrad shift which corresponds to an approximate .2 mrad per hour drift signal. It may be necessary to reinforce the optics table or completely separate the magnet cryostat from the optics table to improve system performance.

The stability of the rotator as measured in section 4.4.1 demonstrated significant circuitous phase drift on the order of .1 mrad over half an hour. This amount of drift is approximately the current level observed in the system. Significantly improving the stability of the rotator is necessary to substantially reduce the phase drift of the system.

The EG&G 5113 pre-amplifier overloads during an automated gain change initiated by the control computer over the serial bus. No overload occurs when manually changing the gain from the front panel. Since this feature was recently implemented, a simple solution is likely, either by a firmware upgrade or by using different commands.

Setting the 2ω lock-in phase may be more easily accomplished than the method outlined in section 5.3.4. Since both the 4ω and 2ω phases are physically measured on the same EG&G lock-in configured for 'single reference/dual harmonic' mode, it may be possible to set the phase of the 2ω channel equal to the phase necessary to zero the 4ω channel. The frequency dependent phase shift associated with the bolometer

detector would necessarily need to be taken into account (see graph 4.6).

Appendix A

List of equipment

1. CO_2 **laser** Edinburgh Instruments Ltd., Research Park, Riccarton Currie, Edinburgh EH14 4AP, England laser model PL5 CO_2 laser, output over 50W on strongest lines, tunable over 9-11um, 7.5mm $1/e^2$ beam diameter at output coupler, beam divergence of ca. 3.5 mRads, discharge length = 130 cm, cavity length = 183 cm, 6m ROC output coupler, dual cylinder piezo, gas pressures typically 20 mBarr (15 torr)

   cooling Affinity Industries Inc, Affinity R-series chiller with FUJI 1/16 DIN temperature controller ($\sim \pm$, 1/2 degree regulation) at 70C, 99.9% ethylene glycol (part # 3190K246 from McMaster-Carr) in 50-50 mixture

   power supply Type PS4P, 0-30mA Cts, 0-33kV

   spectrometer Optical Engineering Inc diffraction grating CO_2 spectrometer

   roughing pump Leybold Trivac model D2A

   misc optics 2 x 1" dia. Au coated mirrors to steer beam into the FIR laser cavity + 1 AR coated, ZnSe beam splitter,ZnSe Brewster windows Laser

Research Optics part# L59261012-10, Output Coupler: 6mRCC, 1" diameter, 1/8" thick, AR coated and 70% reflectance at 10.6 μm, Laser Research Optics

detectors unknown pyroelectric detector (calibrated with thermometer detector Optical Engineering, Inc model 25A)

laser Gas 7% CO_2, 17% N2 with He balance from MESA and Air Gas

2. **FIR laser** homemade

piezos Thorlabs 3 channel piezo driver,

roughing pump model MDT690 Leybold Trivac model D4A roughing pump

flow controller Sierra Instruments, Inc mass flow controller model 810C-DR-13, flow range 0-100 sccm

input optics 1" diameter, AR coated at 10.6 μm ZnSe plano convex lens, 8" FL

input/output couplers all 2" diameter, SPAWR Industries, Inc

Flat	3mm	molybdenum
Flat	5mm	molybdenum
Flat	6.5mm	molybdenum
Flat	1.5mm	molybdenum
RC10m	1.5mm	Copper
RC3m	1.0mm	Copper
Flat	2mm	Copper
Flat	4mm	Copper
RC10mt	3mm	Copper

windows

ZnSe 1" dia., AR coated at 10.6 μm

diamond 8mm x .25mm thick CVD Polycrystalline Diamond, Harris Diamond Corp

quartz 1" dia x .5mm thick, Z-cut, Boston Piezo

lasing gases CD3OD, CH3OH HPLC Grade (Fisher Scientific, part A452-1), Dimethyl Flouride

dielectric waveguides Vycor Tubing, VWR Scientific

22mm	OD	(#32835-180)
25mm	OD	(#32835-205)
30mm	OD	(#32835-249)
38mm	OD	(#23835-260)
45mm	OD	(#32835-307)

Borosilicate heavy wall tubing 1.75"x5/32"x4', Sundance, index of refraction = 1.46, Coefficient of thermal expansion = 7.5×10^{-7}

3. **optical table components**

off-axis parabolic mirrors 2 types of mirrors

3.5" dia. electroformed Cu substrate from ORC Electroformed Products, ORC model PB108 with .0003 inch flash of nickel on optical surface, Al-MgF2 coating

4" dia. Al machined substrate from Janos Technology, Inc, optical polish, Al-MgF2 coating

M#/fig 2.3	EFL (mm)	Angle (deg)	Part	coating/substrate
M1	76.2	90	A8037-405	Protected Al/Al
M5	152.4	45	A8037-610	Protected Al/Al
M6	152.4	45	A8037-610	Protected Al/Al
M7	271.78	72.5	PB108	Al/Cu
M8	271.78	72.5	PB108	Al/Cu
M9	271.78	72.5	PB108	Al/Cu
M10	271.78	72.5	PB108	Al/Cu
M11	326.69	30	A8037-413	Protected Al/Al

waveplates X-cut quartz, Boston Piezo, Homemade NiCr AR-coating with sheet resistance of 338 $\frac{\Omega}{\square}$

optimum frequency(cm^{-1})	thick (mm)
3	15.3
10	5.1
21	2.5
26	2.0
35	1.5
55	1.0
81	.7
110	.5
135	.4
172	.3
240	.16

polarizers ScienceTek mylar polarizers, Unmounted GP-2, FIR grid Polarizer, 4 um pitch, 2 um linewidth, 6um thick mylar substrate

beam splitter Dupont Films, mylar LB polyester film for packaging, 48 guauge = .00048 in. thickness

bolometer detectors Infrared Laboratires, Inc.,

2K 2 K pre-amp model #HD-3, bolo S/N 2187, quartz 4 K filter, white poly vacuum window, unknown 77K filter, MKS type 626 pressure sensor and MKS PDR-C-2C controller

4k S/N 2683 pre-amp model#HD-3, quartz 4 K, white poly vacuum window and 77K filter

4K S/N 1835 pre-amp model#HD-3, AR coated quartz vacuum window, quartz 4 K and 77 K filters, FET cold module DC/CM LN-6C

rotator AC100V Motor Controller with a MelServo MR-C10A10L motor, encoder = 4000 pulses/ revolution

chopper Thorlabs model MC100 optical chopper controller with/10 slot blade (MFC1F10)and 2 x optical head assemblies (MC1000-Assy2)

alignement light source Cole Parmer 9741-50 Low Noise Illuminator

4. **Main electronics rack**

sample temperature controller Lakeshore model 340, heater 2A/2.5W max, Manual PID of (100, 100, 3), Switchcraft 12CL5M 5-pin DIN connector w/30 degree lock, Allied Electronics, PN 932-0166

frequency generator Wavetek model 184 5 MHz sweep generator

oscilloscope Tektronix 2215A 60MHz dual trace oscilloscope with external trigger

spectrum analyzer Hewlett Packard 35665A Dynamic Signal Analyzer

lock-in amplifiers PerkinElmer (EG&G) 1 x model 7265 and 2 x model 7260 DSP lock-in amplifiers, dual harmonic mode, 500 msec time constants, 5nV//$sqrtHz$ at 1kHz with FET input (10 $M\Omega$ input impedance), external reference phase noise $<$ .01 deg rms at 1kHz, drift $<$ .01 deg/C below 1kHz

pre-amplifier EG&G Instruments (Princeton Applied Research) model 5113 Pre-amplifier, drift 10uV/C, noise 4nV/$\sqrt{Hz}$ at 1 kHz, gain from 1 to 750 for high dynamic reserve

5. **Magnet and peripherals**

magnet 8T split coil magnet with persistent switch, current at full field = 96.706 A, .1% homogeneity over 1mm spherical volume, magnet bore diameter = 54mm

dewar type MD20, LHe volume 20L, LN volume 24L

helium level detector Oxford model $ILM^2$10

magnet power supply Oxford PS120-10, 120A 10V, remote operation through RS-232

measuring Oxford He reservoir thermometers Keithely 197 DVM + homemade switch box

vacuum windows Kapton, 1 mil thick

cold shield bore inserts home made LN shield Cu bore insert cylinders with light absorbing material

fine pressure regulator CVL,Inc part# 120-BA Type 100LR Pressure regulator, fine tuning of LHe dewar pressure

6. **Data Aquisition Computer**

   Computer Processor AMD Duron(tm) processor 900 MHz

   Math Support Present

   BIOS Award Modular BIOS v6.00PG, 09/06/01

   Bus Type PCI, ISA, USB

   Ports 1 Parallel, 2 Serial

   Memory 256 MB

   Disks Floppy Disks: 1.44 MB Hard Disks: 76.69 GB, CD-ROM

   Video 1280 x 1024 in True Color, SiS 5598/6326 Ver. 4.11

   GPIB National Instruments PCI GPIB card

   Software Labview 5.1.1 program written by Greg Jenkins to acquire all data and control select instruments (4.5.6)

7. **SPECAC spectrometer** IR fourier transform step-scan polarizing spectrometer, Part Number 40.00, Analytical Accessories, limited resolution = .1 cm^{-1}, 48mm effective travel

   step motor Compumotor 057051-1-8-021-010, Compumotor stepping motor drive SD2

polarizers 25 μm mylar wire polarizers

computer NI-6032 Multi I/O data acquisition card with homemade scsi break out box, 200MHz PC, motor controller card

control software Homemade SPECAC data acquisition software written by Geoff Evans

8. **Bomem DA3.02 Spectrometer** DA3.02 continuous scan Fourier transform spectrometer

   configuration for BSCCO transmission measurements

   beam splitter 25 and 12 μm mylar B/S

   light source Hg lamp source

   detector 2 K bolometer detector

   sample cryostat Janos continuous LHe flow cryostat, 1" Mylar vacuum windows, no cold windows

9. **sample and Oxford sample-stick**

   thermometers sample stick, 3 x cernox thermometers held in place with Emerson and Coming, Inc, Eccobond Solder 59C siver epoxy using toluene as a solvent

   Top S/N 22340, Lakeshore, Model CX-1070-SD-4L (see figure 2.9)

   Bottom S/N 14031, Lakeshore, Model CX-1070-SD-4L

   Cu block, unknown canister cernox thermometer

wiring Ph Bronze (5%), .005" diameter, California Fine Wire Company

sample grown by Genda Gu, Brookhaven National Laboratories, floating zone method, peeled and mounted with epoxy to substrate by Don Schmadel

sample substrate 3/8" dia x .02" thick z-cut quartz, Boston Piezo, AR coated with 338 $\Omega/\square$ NiCr

epoxy epo-tek 301, 2 part epoxy, coef of thermal expansion $50x10^{-6}$ in/in/C, optical index in the visible = 1.539, dc- $\epsilon = 4.1$, Epoxy Technology, Inc 14 Fortune Drive Billerica, MA, 01821-3972

sample heater 400Ω, 1/4W resistors, held in place with stycast 2850FT using Catalyst # 9

Appendix B

AC/DC/Temperature-calibration measurement station

B.1 Probe description

This multi-purpose low temperature probe allows for ac- magnetic susceptibility measurements, dc- resistivity measurements, and thermometer calibration as a function of temperature.

The probe is made of a stainless steel tube, 18 - pin hermetic military style connectors (used on the side of ICBMs in the erroneously named 'defense' complex[76]), 10 - pin Oxford connector, and a heater. The wiring of the pins is shown in figure B.1.

The double vertical lines group twisted pairs of wire. The wires in the probe are $\sim$.005" dia. phospher-bronze wire with polyimed insulation (with the exception of 2 wires that connect to the heater which are $\sim$ .0105" dia. copper). All wires were manually twisted into tight pairs to minimize pick-up noise. Silver-tin soft solder was used for the connector-wire joints.

The heater wire is made of 32 AWG constantin wire ($\sim$ 10.7 Ω/ft) that is approximately 6 feet long resulting in a 60Ω heater. Since this type of wire is difficult to

AC/DC Probe Wiring

18-pin Miltary connector at Probe Top		10 - pin Connector at Probe Bottom	Temp Calibrator: 10-pin	AC Susceptability: 10-pin	DC 4 Probe: 10-pin
A		A - unused			
B		B - unused			
C		C	V+	V+	V+
D		D	V-	V-	V-
E		E	I+	I+	I+
F		F	I-	I-	I-
G		H	V+	Driving	sample V+
H		J	V-	Coil	sample V-
J		L	I-	Pickup	sample I-
K		K	I+	Coil	sample I+
L	Thermometer wires at 60 Ohm Heater. Note that each twisted pair is continuous (loop) as of 10-25-00				
M					
N					
P					
S	Heater: 60 Ohms				
R					

Note: Double line denotes twisted pairs of wires

Figure B.1: AC-DC-Temperature calibration probe wiring chart

solder, I tightly wrapped copper wire around the 2 bare ends of the heater wire, wetted the copper/constantin with silver-tin solder, and soldered the ends to the .0105" dia. copper lead wire resulting in an effective crimp type connection.

The pick-up coils and heater are run the length of the probe in their own separate heat shrink tubbing. All other wires are run in a nylon tube. The reason for doing this is to maximize the separation between the pick-up and driving coil wires in order to minimize capacitive as well as inductive coupling. It should be stated that the separation between the pick-up and driving coil pins on both the oxford and military connector were also maximized in order to minimize coupling.

All metal joints on the probe were hard soldered into place using silver-tin high temperature solder.

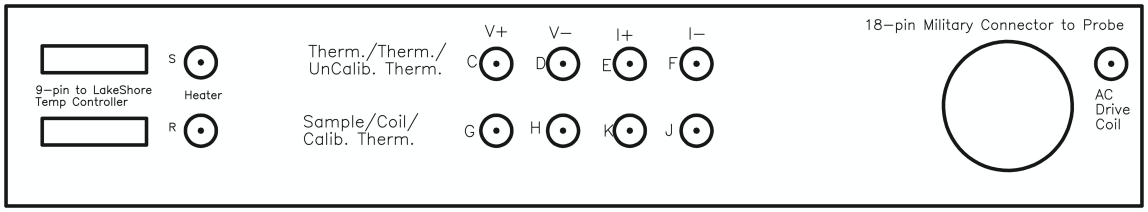

Figure B.2: AC-DC-Temperature break-out box

The diameter of the probe was designed to fit narrow-mouth dewars from Air Products, but unfortunately some narrow-mouth dewars are smaller than others. I did not know this, so the probe fits into some narrow-mouth dewars, and not others. A flange converter was welded together to attach to the liquid helium dewars on one end and a KF-50 flange on the other end. The probe is equiped with a KF-50 flange that has a quick-connect o-ring seal along the stainless steel tube. Note that due to the long tube in the narrow mouth dewars that extend about 1/3 of the way down from the mouth, the probe may be over constrained. That is, the KF-50 flange of the probe together with the head of the probe extending down into the tube of the dewar can cause binding if the tube is not quite perpendicular with the mouth. For this reason, I use a small flexible billows between the two KF-50 flanges to allow the probe to be constrained only by the tube allowing the probe to easily move in and out of the narrow mouthed dewars.

The cable used to go from the probe to a break-out box has 22 wires, each pair is twisted and has its own shielding (this is 4 too many, but I found the nice wire bundle in the lab). The cable is connected to a break-out box which is shown in figure B.2

The connectors are labelled by letter corresponding to the 18-pin military connector. Additionally, a description is given in the picture above to aid in cross referencing to the different head attachments of the probe. All BNC connectors use the center

pin to connect to the military connector. Additionally, the bottom row connectors are internally wired as twisted pairs (V+ and V-, and I+ and I-) of copper wire with a shield that connects to the outer connector of the BNC cable of V+ and I+, respectively. These shields are additionally attached to the chassis of the box. This configuration of twisted pairs of wires is essential for driving the AC probe attachment head at high frequencies ($\sim$ 250 kHz). This is desirable since, as a result of Faraday's law, the signal in the pick-up coil is proportional to the driving frequency.

B.2 The different head attachments

There are several attachments that may be attached to the end of the probe. All head attachments have a 10-pin female Oxford connector. All wires are thermally anchored with 5 turns around the copper rails between the Oxford connector and the 4-pin connectors. I initially made a "copper can" that was placed over the head attachment which was drilled with many holes, 'swiss-cheesed' if you like, to allow exchange gas to flow freely to the sample and thermometers. However, this led to unstable temperature readings. It seems that the holes are undesirable. The exchange gas in the canister is able to come into equilibrium with the copper (which effectively averages over the temperature gradient in the He dewar) as opposed to moving ballistically from the sample or thermometer to the outside He dewar volume.

B.2.1 Temperature calibration head attachment

The idea is that an uncalibrated thermometer can be purchased and calibrated with respect to a more expensive calibrated thermometer.

There are two 4-pin connectors mounted on either side of the attachment. There is a hole where an uncalibrated thermometer may be placed and GE varnished directly to the calibrated thermometer. The wiring of the thermometers are always in the following configuration:

To 4 pin connector

Male connector: ! ! ! !

I- V- I+ V+

Thermometer

B.2.2 AC head attachment

The purpose of this ac- head attachment is to measure the magnetic susceptibility of samples. We are not measuring an absolute number of the magnetic permeability of the material. Instead, we are looking at the temperature dependence of the magnetic permeability in a more qualitative way. That is to say, the geometry of the coils is not accurately defined so that one can calculate exactly the magnetic permeability based on the data (I have never tried this and am guessing that the coil geometry together with the exact sample dimensions would be too difficult to accurately crank through Maxwell's equations).

The ac- probe consists of 2 coils of wire ($\sim$10 turns each), one driving coil and one pick-up coil (see figure B.3). The design of this attachment makes it very simple to make different coils and place them on the probe. Currently, the coils are made of phospher-bronze since copper exhibits a broad resistivity feature around 40 K.

The coils are easily plugged into the 4-pin connector that is GE varnished down to the brass head attachment. The reason this attachment is made of brass is that I thought initially that the broad resistivity feature was due to eddy currents in copper

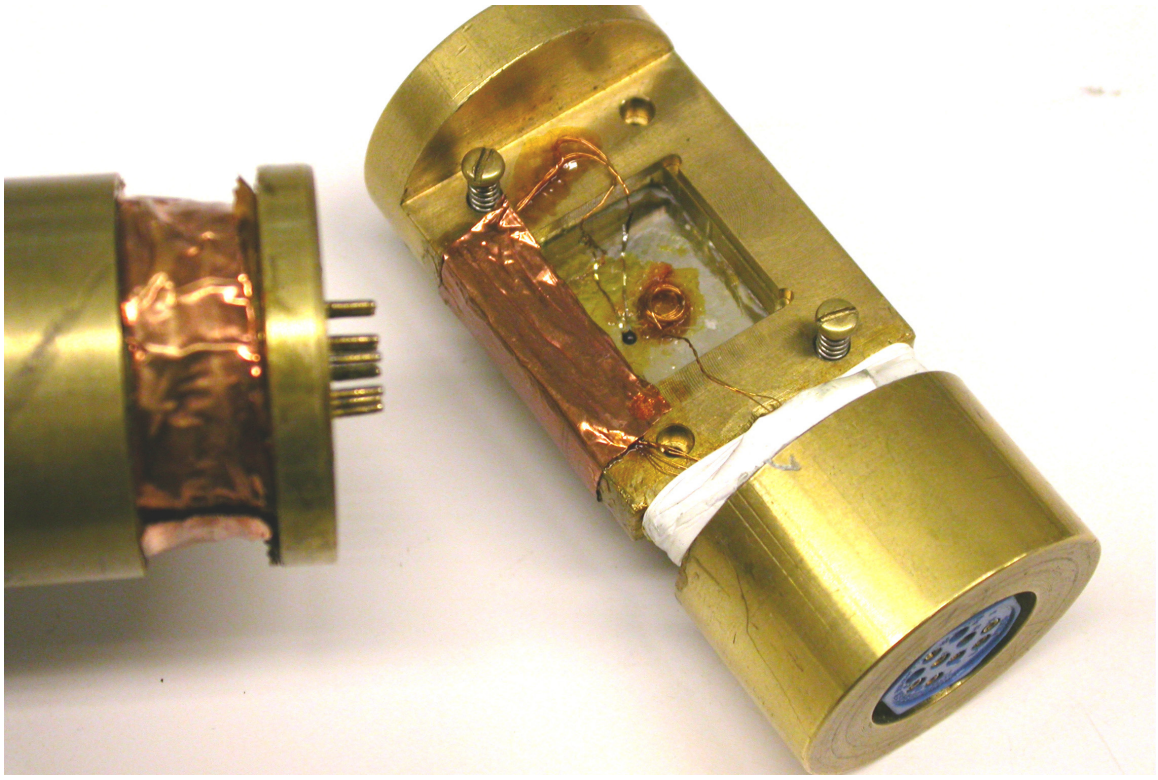

Figure B.3: AC head and bottom-end of probe

driven by the coil. I now think this is not the case, so there is no real reason to make it of brass. However, there is not really a good reason to make it of copper either. The other head attachments are made of copper because of the excellent thermal conductance of copper which transfers directly to the samples. This helps maintain a reasonably large thermal time constant.

B.2.3 DC head attachment

This is similar to the temperature calibration head attachment, except one side has a male connector. This is the side for the 4-probe measurement of the sample. The wiring of the connector is as follows:

To 4 pin connector

Male connector: ! ! ! !

V- I- V+ I+

Thermometer

The sample may be mounted to the copper attachment using vacuum grease or double-backed tape. Wires can be soldered to the pins of the 4-pin connector using indium solder. It is important to use indium since a) you could otherwise unsolder the wires leading to the connector if you used silver-tin solder, and b) these plastic connectors are very easy to melt. Make certain that you use low heat so that you do not melt the connector! The Si diode thermometer S/N D39594 is currently mounted.

B.3 National Instrument data acquisition break out box

The National Instrument data acquisition PCI card comes with a SCSI connector. I used a third party break-out terminal block for a SCSI connector purchased for $100, about a tenth of the price that National Instruments wanted for theirs. I wired all connections using coaxial cable. The wiring of the box is shown in figure B.4.

The card is very well documented in PDF format. Look on the data acquisition computer (McDonalds) for the full documentation, or the National Instruments web site: search for the 6034E/6035E User's Manual. One important page that I use as a reference is page 4-10 of the 6034E/6035E User's Manual. It shows the meaning of the three types of inputs: differential, single-ended ground referenced (RSE), and single-ended non-referenced (NRSE). The resistors seen on this diagram can be inserted on channels 0 through 7 by inserting a resistor between the inner and outer leads of the

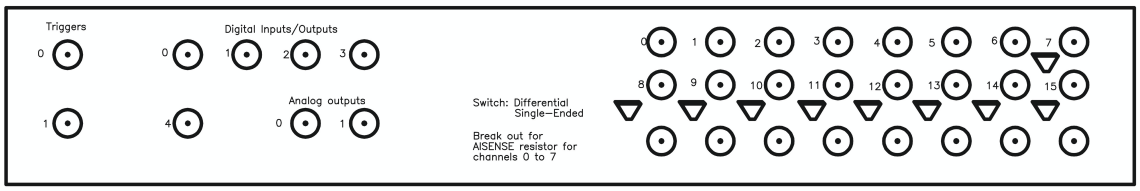

Figure B.4: *NI-DAQ card break-out box*

3^{rd} row of BNC connectors.

When the toggle switch is in the up position, then the differential mode may be used. In differential mode, there are only 8 channels (0 through 7). For instance, channel 0 in differential mode would be the inner connector of the BNC of channel labelled '0' as V+ and the inner connector of the BNC of channel labelled '8' as V-. In both single ended modes (RSE and NRSE), there are 16 channels (as labelled 0 through 15) where V+ is the inner of a BNC and V- as the outer of a BNC.

Two analog outputs can be used simultaneously and are labelled. There are many digital I/O's. All of them are software configurable to be either an input or an output. Not all of them are connected to BNC connectors. I have only connected the 5 labelled above. If more are required, more connectors may be attached to the box. I wired 2 trigger inputs. There are also many counters. I chose not to dedicate any front panel space for them.

It should be noted that the terminal block inside the break-out box is easily rewired. All the wires are clamped into place on the terminal block by a screwing mechanism. Therefore, if you need to have counters wired, simply wire up one of the BNC connectors to the appropriate connector on the terminal block. The wiring of the SCSI connector showing the pin-out can be found in the user's manual.

B.4 Wiring up the experiments

B.4.1 Heater

A power supply capable of producing about one quarter of an amp across 60 Ω is necessary. Currently I am using an HP6294A power supply. I have limited the current to 1/2 A, although I have run the heater up to .6 amps in the past. I would not recommend running the heater this high. The head attachments can become extremely hot if the heater is left on for too long. At 1/4 amps, I have not had trouble though I am paranoid enough not to leave the heater on for prolonged periods of time.

Currently, the power supply is wired as in diagram 3-5 of the power supply's user manual except that I wired an extra resistor in parallel to the voltage source/Rx combination. The values I chose for the resistors are Rx = 10 $k\Omega$ and the series resistor is 500 Ω. I crowbar the voltage such that no more than a 1/2 ampere can flow through the 60 Ω heater.

I have written a couple of Labview heater programs that allow the user to warm up the probe. This is a simple program that reads the temperature of the probe head. If this temperature is below 290 K, then a voltage is applied via the analog output of the NI-DAQ card to the HP power supply. When the temperature reaches 290 K, the heater is turned off by setting the voltage output to zero on the NI-DAQ card. This little program will save you lots of time —- pull the probe out, run the program, and walk away. There is no need to manually monitor the heater to make sure that the probe does not overheat.

To wire up the heater, wire the + and - from the rear panel connector of the

power supply to the probe break-out box BNC labelled "heater" (polarity does not matter). Wire the separate (completely independent from the + and - described in the last sentence!!!!) reference voltage input from the rear panel of the power supply to the analog output of the NI-DAQ card.

B.4.2 AC susceptability

To drive the coils, I use a Wavetek model 184. The TTL output of the Wavetek is connected to an EG&G 7260 lock-in amplifier rear panel input "Ref TTL". The 50 Ω output of the Wavetek is connected to the driving coil BNC connector. The pick-up coils are connected to the differential input of the 7260. The coils are driven at the highest possible frequency limited by the 7260 at 250 kHz (reason was described earlier). BEWARE: Do not drive at a frequency even slightly larger than 250 KHz since the 7260 will begin doing strange things (signal will suddenly jump in amplitude and phase) intermittently due to aliasing problems.

Use the Lakeshore 102 current source to drive the Si diode thermometers at 10 uA. Connect the + and - of the current source to I+ and I- of the break out box (1st row). The V+ and V- across the diode is read using the NI data acquisition card. Use differential mode.

Run the Labview package "AC.vi." Set the GPIB address of the lock-in to the appropriate value. Choose "R and Phase" for the measurement of the lock-in. The device number of the data acquisition board is always equal to 1. Choose the NI-DAQ channel number where you have the V+ and V- connection for the thermometer. "Scans per second" is the sample rate, and "number of samples to average" is the number of data points to average before recording a data point.

For instance, if you want a data point every half second, and the sample rate is set to 10,000, then the "number of samples to average" should be set to 5,000. The "Input limits" should be set to ensure that the A/D conversion has the highest possible resolution (that is, the minimum possible full-scale voltage divided up into 2^{16} steps; note that these full-scale values are a discrete set specified in the 6035E User's Manual). For a Si diode thermometer, the maximum is about 2V and the minimum is about 1/2 volt.

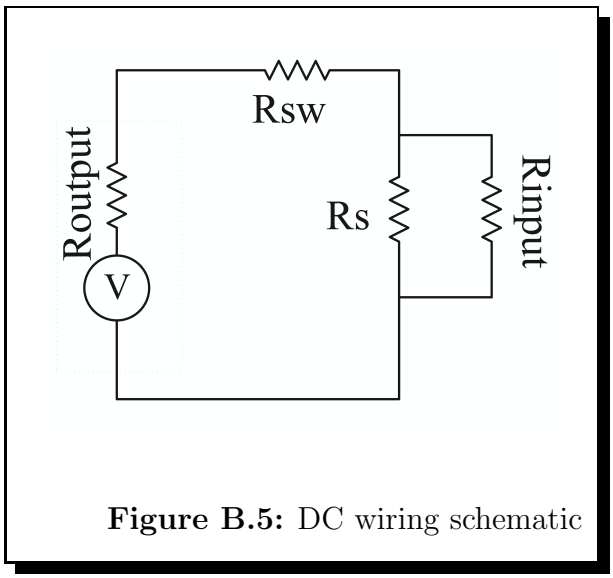

Figure B.5: DC wiring schematic

Select the "Input Config" as differential, and the coupling as dc. The big red light will blink on and off at the rate data points are being taken (in the example above, every 1/2 second). The displays under the big red light show the voltage read on the data acquisition board, the resulting temperature conversion, and the lock-in value obtained through the GBIB bus. The toggle switch turns on and off the graph. Updating and plotting the full data array uses alot of computer resources so if you update every single point with a fairly high sample rate, then the timing can become delayed. An error will appear saying that the buffer has become overrun with data (this is the buffer used by the NI-DAQ low level routines to acquire data). To avoid this, toggle the on/off switch only when you want to see the latest update.

Now you are ready to take some data. Make sure that you do not sweep too fast

in temperature. The rate that seems to work is about 1 K/5 seconds through a sharp feature. After acquiring a data run, make sure you hit the big green "Stop" button in order to save your data. Otherwise, all the data will be lost.

Note that another version of this software was written to incorporate the Lakeshore 330 temperature controller in conjunction with a LakeShore calibrated Si diode thermometer (see figure B.6 for a screenshot).

B.4.3 DC resistance 4-probe measurement

The thermometry is wired exactly the same as in the ac- susceptibility measurement. The thermometer that is mounted in the dc- head attachment is currently S/N D39594.

The wiring into channels "A" and "B" of the 7260 should be wired to V+ and V- of the 2nd row of the probe break out box. The oscillator of the 7260 should be wired into a resistor box whose selectable resistances (Rsw) are as follows: 1 $k\Omega$, 10 $k\Omega$, 100 $k\Omega$, 1 $M\Omega$, 10 $M\Omega$, and 100 $M\Omega$. This resistor is in series with the current leads going to the sample. The purpose of the resistor is to effectively convert the output of the lock-in from a voltage source to a current source. The input impedance of the lock-in is 10 $M\Omega$ (Rinput) on the FET setting. The circuit is shown in figure B.5.

B.4.4 Temperature calibration

Mount the thermometer to be calibrated to a 4-pin connector. Use GE varnish to glue the un-calibrated thermometer to the calibrated Si diode. Make sure that the lead wires are in good thermal contact with the head attachment.

To 4 pin connector

Male connector: ! ! ! !

I- V- I+ V+

Thermometer

Use the Lakeshore 102 current source to drive the un-calibrated Si diode thermometers at 10 μA. Connect the + and - of the current source to I+ and I- of the break out box (1st row). The V+ and V- across the diode is read using the NI data acquisition card. Use differential mode. Connect the 9-pin connector (2nd row) to the LakeShore model 330 temperature controller. Curve 14 currently has the data for the calibrated Si diode Model DT-450-SR-13 SN D08722.

The Labview program "CalibrateThermometer.VI" will acquire the temperature from the calibrated thermometer through the GPIB bus from the LakeShore model 330. The voltage will be acquired through a differential measurement via the NI-DAQ card. The resulting X-Y data file is imported into a Mathematica program to curve fit the data using a 15th order Chebychev polynomials in 4 piecewise continuous regions. The curve fit parameters can then be cut and pasted into your own custom-made Labview submodule. The submodule converts a voltage reading (using the curve fit parameters that you have input along with the respective valid voltage ranges) to temperature.

The module "VoltageToTemperature.VI" has several inputs. The top voltage ranges define the crossover to begin using different Chebychev polynomials depending upon the voltage read by the NI-DAQ card. The bottom voltage ranges define the VH (high) and VL (low) used to calculate the Chebychev function. These are the values that are inserted into Mathematica to curve fit a certain region. The other

array displayed holds the 15 Chebychev fit parameters. Note that the indexing of all three arrays coincide with each other. That is, index number one in the voltage ranges corresponds to index number one in the Chebechev fit parameters. It should be stated that it is easy to cut and paste the values produced by the Mathematica curve fitting program into this Labview module. I would not even think about typing all of these in by hand.

Note that a good rule of thumb for the rate at which to sweep temperature is to take about 3 hours to go from room temperature down to 4 K.

Once you have programmed your submodule, you can test it by using the Labview program "CalibrationTestDT.VI". It plots the difference in the thermometer temperature readings versus temperature read by the calibrated thermometer. Make sure that you modify this program by inserting your own submodule icon for your specific thermometer. By using this test program, I have found that the curve fit is the limitation on the temperature reading. That means that the curves found in the Mathematica curve fitting routine shows the error in temperature reading. The thermometer can be unmounted and the attached 4-pin connector can be directly connected to another head attachment. Currently, both the ac and dc pin configuration are the same as the thermometer calibration head attachment.

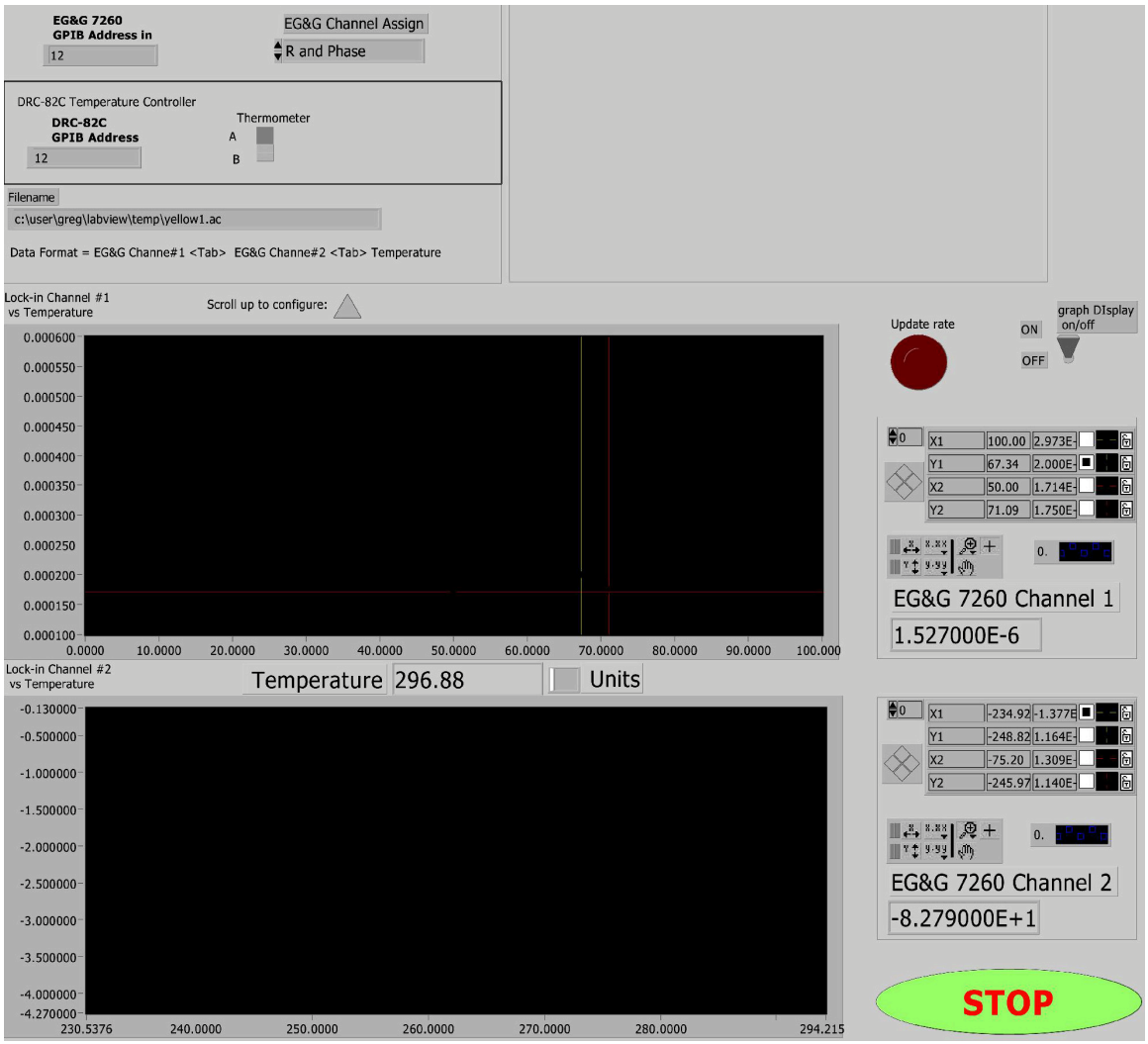

Figure B.6: *Screen-shot of the latest version of AC.VI Labview program*

Appendix C

Bolometer load-curve data

C.1 Bolometer load curves

Load curve data measures the detector sensitivity as a function of dissipative power of a bolometer element. It does not, however, give any information regarding the efficiency in which radiant power is absorbed, nor the inherent noise level of the device.

Details on the method used to acquire load curve data is given in section D.7.1.

A current is applied to the bolometer element whose resistance is measured using an FET cold module (see the IR-Laboratory user manual for details, or reference[24]). The resistance as a function of dissipated electrical power can then be used to directly calculate the responsivity of the bolometer elements.

The noise level is measured at a certain set frequency with an EG&G 5260 lock-in amplifier and converted to the noise-equivalent power at that frequency.

2K Bolo #1515 2.5mTorr He Vapor Pressure

V	Vs	Eb	Rbolo(Ohms)	Ibolo(amps)	PowerBolo(Watts)	Responsivity (V/W)	1/R (uW/V)
0	1.188	0		0.00E+00	0.00E+00		
0.492	1.4	0.212	7.57E+06	2.80E-08	5.94E-09	3.57E+07	2.80E-02
1.028	1.599	0.411	5.91E+06	6.17E-08	2.54E-08	1.02E+07	9.76E-02
2.116	1.92	0.732	4.19E+06	1.38E-07	1.01E-07	4.23E+06	2.37E-01
4.26	2.349	1.161	2.50E+06	3.10E-07	3.60E-07	1.66E+06	6.03E-01
6.112	2.611	1.423	1.65E+06	4.69E-07	6.67E-07	8.52E+05	1.17E+00
8.28	2.841	1.653	1.19E+06	6.63E-07	1.10E-06	5.37E+05	1.86E+00
10.19	3	1.812	9.08E+05	8.38E-07	1.52E-06	3.76E+05	2.66E+00
12.26	3.138	1.95	7.14E+05	1.03E-06	2.01E-06	2.80E+05	3.57E+00
14.478	3.268	2.08	6.23E+05	1.24E-06	2.58E-06	2.29E+05	4.37E+00
16.437	3.355	2.167	4.65E+05	1.43E-06	3.09E-06	1.69E+05	5.90E+00
18.316	3.429	2.241	4.10E+05	1.61E-06	3.60E-06	1.45E+05	6.89E+00
20.276	3.495	2.307	3.48E+05	1.80E-06	4.15E-06	1.22E+05	8.23E+00
24.824	3.611	2.423	2.62E+05	2.24E-06	5.43E-06	9.05E+04	1.11E+01
30.434	3.713	2.525	1.85E+05	2.79E-06	7.05E-06	6.30E+04	1.59E+01
34.898	3.774	2.586	1.39E+05	3.23E-06	8.36E-06	4.66E+04	2.15E+01

Actual Operating Bias

14.478	3.268	2.08

Ro =R at zero bias ~ 7.571428571 Mohms

Rload = 10 Mohms

Noise (V/rootHz)

100Hz

4.2E-08

NEP@100Hz

1.8362E-13

Figure C.1: 2 K bolometer load curve data

4K Bolo #2868 *AR coated Quartz vacuum window, White Poly 77K filter, quartz 4.2K filter, Bolo # 2868*

V	Vs	Eb	Rbolo(Ohms)	Ibolo(amps)	PowerBolo(Watts)	Responsivity (V/W)	1/R (uW/V)
0	1.0051	0		0.00E+00	0.00E+00		
1.0197	1.2	0.1949	2.36E+06	8.25E-08	1.61E-08	1.21E+07	8.25E-02
2.2659	1.396	0.3909	1.87E+06	1.88E-07	7.33E-08	3.43E+06	2.92E-01
3.2491	1.546	0.5409	1.80E+06	2.71E-07	1.46E-07	2.05E+06	4.88E-01
4.59	1.746	0.7409	1.75E+06	3.85E-07	2.85E-07	1.44E+06	6.93E-01
5.2107	1.835	0.8299	1.67E+06	4.38E-07	3.64E-07	1.14E+06	8.81E-01
6.9785	2.079	1.0739	1.60E+06	5.90E-07	6.34E-07	9.02E+05	1.11E+00
8.1197	2.228	1.2229	1.50E+06	6.90E-07	8.43E-07	7.12E+05	1.40E+00
10.1143	2.473	1.4679	1.40E+06	8.65E-07	1.27E-06	5.75E+05	1.74E+00
12.2507	2.716	1.7109	1.28E+06	1.05E-06	1.80E-06	4.55E+05	2.20E+00
15.6403	3.062	2.0569	1.14E+06	1.36E-06	2.79E-06	3.49E+05	2.86E+00
17.5207	3.235	2.2299	1.01E+06	1.53E-06	3.41E-06	2.81E+05	3.56E+00
20.2013	3.463	2.4579	9.30E+05	1.77E-06	4.36E-06	2.40E+05	4.17E+00
22.789	3.664	2.6589	8.42E+05	2.01E-06	5.35E-06	2.03E+05	4.93E+00
25.499	3.856	2.8509	7.63E+05	2.26E-06	6.46E-06	1.74E+05	5.75E+00
30.265	4.15	3.1449	6.57E+05	2.71E-06	8.53E-06	1.42E+05	7.05E+00

Actual Operating Bias

15.6403	3.062	2.0569

Ro =R at zero bias ~ 2.36299709 Mohms

Rload = 10 Mohms

Noise (V/rootHz)
100Hz
7.50E-08

NEP@100Hz
1.6483E-13

Figure C.2: 4k bolometer SN#1835 load curve data

Bolo # 2683 ***White poly vacuum window, White Poly 77K, Quartz 4K***

V	Vs	Eb	Rbolo(Ohms)	Ibolo(amps)	PowerBolo(Watts)	Responsivity (V/W)	ısitivyt (uW/V)
0	1.01	0		0.00E+00	0.00E+00		
1.019	1.326	0.316	4.50E+06	7.03E-08	2.22E-08	1.42E+07	7.03E-02
2.088	1.645	0.635	4.25E+06	1.45E-07	9.23E-08	4.55E+06	2.20E-01
3.08	1.933	0.923	4.09E+06	2.16E-07	1.99E-07	2.70E+06	3.71E-01
3.96	2.184	1.174	3.99E+06	2.79E-07	3.27E-07	1.96E+06	5.10E-01
5.029	2.458	1.448	3.45E+06	3.58E-07	5.19E-07	1.43E+06	6.99E-01
6.278	2.75	1.74	3.05E+06	4.54E-07	7.90E-07	1.08E+06	9.28E-01
6.94	2.9	1.89	2.93E+06	5.05E-07	9.54E-07	9.10E+05	1.10E+00
8.239	3.167	2.157	2.59E+06	6.08E-07	1.31E-06	7.47E+05	1.34E+00
8.953	3.308	2.298	2.46E+06	6.66E-07	1.53E-06	6.48E+05	1.54E+00
10.112	3.527	2.517	2.33E+06	7.60E-07	1.91E-06	5.73E+05	1.75E+00
11.009	3.682	2.672	2.09E+06	8.34E-07	2.23E-06	4.91E+05	2.04E+00
11.984	3.844	2.834	1.99E+06	9.15E-07	2.59E-06	4.43E+05	2.26E+00
14.584	4.22	3.21	1.69E+06	1.14E-06	3.65E-06	3.55E+05	2.81E+00
16.27	4.4	3.39	1.20E+06	1.29E-06	4.37E-06	2.52E+05	3.97E+00
18.5	4.71	3.7	1.61E+06	1.48E-06	5.48E-06	2.79E+05	3.58E+00
19.963	4.86	3.85	1.14E+06	1.61E-06	6.20E-06	2.06E+05	4.85E+00
24.923	5.32	4.31	1.02E+06	2.06E-06	8.88E-06	1.72E+05	5.83E+00
30.02	5.71	4.7	8.29E+05	2.53E-06	1.19E-05	1.29E+05	7.73E+00
34.901	6	4.99	6.32E+05	2.99E-06	1.49E-05	9.59E+04	1.04E+01

Actual Operating Bias

16.27	4.4	3.39

Ro =R at zero bias ~ 4.495021337 Mohms

Rload = 10 Mohms

Noise (V/rootHz)
100Hz
5.00E-08

NEP@100Hz
1.99E-13

Figure C.3: 4k bolometer SN#2683 load curve data

Appendix D

He3 bolometer system: a user's manual

This manual is intended to be used in conjuction with the manual provided by IR-Laboratories.

D.1 Overview

In order for the He3 bolometer to function, it must be cooled to 320 mK. This is achieved in a dewar that has a nitrogen cold sheild, a He4 reservoir, and a He3 reservoir. By pumping on the He4 reservoir, a base temperature of roughly 1.7 K can be achieved. At this temperature, most of the 5 liters of He3 gas (at STP) is condensed into a liquid. Charcoal that is thermally isolated from the He3 reservoir acts as a sorption pump when the charcoal is cooled to the He4 bath temperature. By pumping on the He3 bath in this way, a base temperature of 320 mK can be achieved. The bolometer element rests on a stage that is in thermal contact with the He3 bath.

D.2 Electronics

There is a germanium thermometer mounted on the He3 cold stage, a carbon thermistor mounted on the charcoal pump, a charcoal heater, a mechanical heat switch/clamp that thermally shorts the He3 stage to the He4 bath when closed (He3 heat switch), and a mechanical heat switch/clamp that thermally shorts the charcoal pump to the He4 stage when closed. The heat switches are nothing more than vice-like mechanical clamps that cause a thermal short when closed. These clamps are actuated by rotating two protruding knobs located at the bottom of the bolometer dewar. "Open" and "Closed" directions are labelled on the bolometer dewar itself. Note that the two heat switches are actuated in *opposite* rotational directions.

In order to conveniently measure the temperature and apply a current to the charcoal heater, I have constructed a small box located underneath the external He3 reservoir tank (see figures D.3 and D.4). The labelling on the side of the box should be fairly self- explanatory. A four probe resistance measurement is needed to monitor the germanium thermometer. Two BNC connectors are provided for this purpose. It is recommended that the 200 kΩ scale (corresponding to 40 μA) of the Keithley 197A DMM be used as the ohm-meter. Self-heating caused by the current used to measure the resistance causes inaccuracies in the reading (the larger the current, the hotter the thermometer, the lower its resistance). However, since all of the thermometry was shipped un-calibrated, the accuracy is not the issue. By consistently using the same current, the resistance may be correlated to a temperature.

The charcoal heater resistance is monitored in a two-probe configuration. It is recommended that the Keithley 196 be used on the 300 kΩ scale. This scale corresponds to an applied current of 50 μA. The same self-heating arguments need to

be heeded, although experimentally it can easily be determined that self heating is negligible on the two highest resistance scales.

The charcoal heater circuit is merely an ac- transformer with a potentiometer whose knob protrudes the top of the box. A BNC connector allows a voltmeter to monitor the applied ac- voltage. *I have never applied a voltage larger than 6 volts to the charcoal heater*, although the employees at IR Laboratories state that a maximum of around 40 volts may be applied to the heater without melting the wires. I would not trust this number.

IR Laboratories mounted a gold box on the side of the dewar that contains BNC connectors, bias batteries, and a pre-amplifier. I have corrected many mistakes regarding their schematic, so please beware of any mistakes that I have not corrected. On the schematic, you will see the "Bias Test" BNC connector and the bias battery. The bias battery applies 1.5 volts across the 20 MΩ load resistor (physically, the load resistor is mounted very close to the bolometer element and is thermally sunk to the He3 bath in order to reduce Johnson noise) that is in series with the bolometer. A gate from a JFET (physically mounted to the He4 stage) senses the voltage at the point between the load resistor and the bolometer element, basically making the bolometer element part of a voltage divider. As the resistance of the bolometer changes, the voltage at the JFET gate will change. The JFET acts as a gain one voltage follower, converting the high impedance of the bolometer to something that can be read by a run-of-the-mill voltmeter at the BNC connector, pin-out "Vs." This point is dc- coupled to the bolometer. Also, any kind of voltage offset introduced from the JFET will register as an offset voltage at this point. A capacitor separates "Vs" from the cascaded op-amp pre-amplifier. The BNC connector labelled "Input"

is merely the ac- coupled version of pin-out "Vs." This is the signal that is amplified. The "Output" BNC connectors is the signal at the "Input" amplifed by a gain of either 1000 or 200, depending on the position of the gain switch. Note that the bias, power, and input switches all have to be "ON" for a signal to occur at the "Output." Also note that the 9 volt batteries should be replaced when the voltage falls to around 7.5 volts. This occurs very frequently and should be checked often.

A signal can be applied to the "Input" BNC connector, and the "Output" viewed on a voltmeter or oscilloscope in order to test the gain of the amplifier. I would highly recommend turning the "power" switch off in order to turn off the voltage to the cold module JFET, and short the "Vs" BNC connector to ensure that nothing can possibly happen to the cold module JFET (this would be very hard to physically replace). The frequency response of these op-amps are used as audio microphone pre-amplifiers, so should have good frequency characteristics up to at least 15kHz.

An important note: While using the bolometer, always disconnect the thermometry and rear power chord, and ground connectors by connecting BNC cables from Ge V+ to Charcoal heater, and Ge V- to Charcoal thermometer.

D.3 He3 charging

D.3.1 Cleaning the He3 gas

A predecessor graduate student built a He3 gas exchange system. I most certainly do *not* want to take credit for this monstrosity. The purpose of the gas exchange system is to charge an external system with He3, and to reclaim the gas when finished. It contains many valves, two 8 Liter He3 tanks, a vacuum gauge used to measure the

pressure inside the tanks, and a diaphragm roughing pump.

I built a simple gas cleaner shown in figure D.4. The basic idea is to allow the He3 gas to flow into a cold vessel held at 4 K. Any impurities (besides He4 impurities) will be cryo-pumped to the side of the cold vessel. The clean He3 can then be pumped back into the 8 liter tanks.

The first step is to pump out the gas cleaner at room temperature and close off the valve. Insert the gas cleaner into a He4 dewar. A vacuum "T" should be inserted between the gas cleaner and the gas exchange system so that a separate pump station may be connected in order to evacuate the gas exchange system up to the He3 storage tank valves. Pumping these lines took a very long time ($\sim$8 hours) due to persistent outgassing. Make sure that you turn on the roughing pump periodically to release trapped air inside the pump. The cause of this large amount of outgassing is most likely the copper fibers used in the oil trap in conjunction with remnant solder flux. I found it necessary to apply heat via heater tape to the oil trap in order to pump down the system. Make certain that there are no vacuum leaks.

Once the system is pumped down and leak tight, open up all the appropriate valves to allow the He3 to flow into the 4 K vessel. The impurities should be cryopumped to the 4 K vessel. Allow the system to stay in this configuration for around 10 minutes. Pump all the He3 back into the storage tanks and check the pressure. The pressure reading should be about the same or *slightly* lower. Repeat the procedure in this paragraph about 3 or 4 times. The He3 gas should be sufficiently clean.

D.3.2 He3 charging

I need to emphasize that I built the external blue He3 tank mounted on the outside of the He3 bolometer dewar. It differs from the IR Laboratories design. If you call them, keep this in mind. The design criteria for the size of the bottle was based on information I was able to extract from IR Laboratories. The only firm number I was able to decipher was that the external blue tank plus the internal reservoir is 5 liters at STP. I was able to deduce that the volume of the reservoir and tubes inside the dewar was around 1/2 a liter. In any case, the pressure at room temperature of the He3 gas should be 30 PSI for the present system which corresponds to 5 liters of gas at STP.

The idea is to cool down the He3 bolometer dewar and allow the low temperature gradient to cryopump the He3 into the He3 reservoir inside the bolometer dewar. Make sure that a good vacuum $\sim 10^{-}7$ Torr is present in the He3 bolometer dewar before cooling. Transfer liquid nitrogen (LN) into the LN and He4 reservoirs. Make sure the He3 stage heat switch is closed. Allow the system to pre-cool for about 2 hours. Blow out the liquid nitrogen from the He4 reservoir and transfer liquid helium into the He4 reservoir.

To charge the system, connect up a "T" between the gas exchange system and the He3 charge port that is connected to the blue bottle mounted on the side of the He3 bolometer dewar. Connect a pump station to the "T" in order to evacuate the entire system including everything in the gas exchange system except the 8 liter tanks and the blue bottle. Again, allow everything to outgas and pump down, and make sure there are no leaks.

Once the gas exchange system and the He3 system are evacuated and cooled to 2

K, check the pressure in the 8 liter bottles. Using the gas law, calculate how much you expect the pressure to drop in those tanks if you subtract 5 liters at STP:

$$
\begin{aligned}
P_1 &= \text{initial tank pressure} \\
V &= \text{volume of tank} \\
P_2 &= \text{final pressure in tank after transfer} \\
N_1 &= \text{initial number of moles} \\
N_2 &= \text{final number of moles after transfer} \\
R &= \text{gas constant} \\
T &= \text{Room temperature} \\
P_1V &= N_1RT, P_2V = N_2RT \\
&\rightarrow (N_1 - N_2)RT = (P_1 - P_2)V = 5L \times 1atm \\
&\rightarrow P_2 = P_1 - (1atm) \times 5L/V
\end{aligned}
$$

Crack open the valves in the gas exchange system in order to throttle the flow of gas into the He3 bolometer reservoir until the pressure drops to the calculated pressure, P_2. Once the pressure reaches this value, close the throttling valve and valve off the He3 blue tank. Turn on the diaphragm roughing pump to recover the

remnant He3. Valve off the He3 tanks.

Closely monitor the He3 bolometer dewar as it warms up. To warm the bolometer quickly, I spoil the vacuum slowly with nitrogen, and use heater tape and a heat gun to keep the dewar from frosting (be careful not to build up any pressure inside the dewar when the exchange gas warms!). **Make sure that the pressure does not exceed 38 PSI in the He3 reservoir!!!** I don't know what kind of pressures this system can endure. I know that IR Laboratories runs their system at 38 PSI. If you charged the system to this pressure, too much He3 was used since the bottle I attached is larger than the one used by IR Laboratories. The pressure should read 30 PSI at room temperature.

D.4 Cooling the system

Pump out the He3 bolometer dewar. A good base pressure is 5×10^{-7} mBar. Pre-cool the dewar by filling both the liquid nitrogen jacket and the He4 reservoir with liquid nitrogen. Make sure that the charcoal and He3 stage heat switches are closed and that the copper blank is chosen on the filter slide. Let the system pre-cool for at least 2 hours. At 77 K, the charcoal should read approximately 2.7 kΩ, the germanium approximately 25 Ω, and the He3 gas pressure should drop to around 24 PSI.

Blow out the liquid nitrogen in the He4 reservoir, open the charcoal heat switch, and begin transferring liquid helium into the He4 reservoir. The plume during the transfer should be about 3 feet high. When the reservoir is full, the plume will drastically change to a much more dense 'cloud' of frozen water vapor. The transfer

will take approximately 20 minutes (this depends upon how long the system was pre-cooled as well as the transfer rate).

Begin pumping on the He4 reservoir. Attach the MKS vacuum gauge and vacuum line to the top of the He4 reservoir via a "T". Throttle the pumping rate so that the pressure changes approximately .1 mmHg/sec. Concurrently, begin heating the charcoal pump (I begin with an rms voltage of ∼5V, and decrease to ∼2.5V while cooling to 1.5 K). The idea is to warm up the charcoal pump to approximately 1.9 kΩ by the time the He4 pressure reaches 10 mmHg. Once the lowest pressure is reached, back off of the heater voltage to keep the charcoal temperature at 1.9 kΩ. Stay at this state for about half an hour. This is the point when all the He3 condenses. You want to make sure that most condenses into a liquid.

Temperature	Charcoal Thermomter	Ge Thermometer
.35 K	12.5 kΩ	1.580 kΩ
2 K	–.-	000.500 kΩ
4 K	–.-	000.101 kΩ
77 K	2.7 kΩ	000.025 kΩ
RmT	1.1 kΩ	000.001 kΩ

Table D.1: Charcoal thermometer measured by Keithley 196 on a 300 kΩ scale, Ge thermometer measured by Keithley 197A on a 200 kΩ scale

By the way, you can tell you are condensing He3 by the rate the charcoal temperature increases for the same applied power to the charcoal heater voltage. As the He3 condenses, there is less exchange gas to transfer the heat from the charcoal to the He3 bath. Therefore, less power is required to keep the charcoal temperature at 1.9 kΩ.

There is a coarse pressure gauge that also indicates that condensation is taking place. The pressure on the gauge should increase to $\sim$ .4 inches of Hg vacuum at the highest value of this process. The pressure should drop close to zero (absolute) as the He3 condenses.

At the lowest He4 pressure (9 mmHG $\sim$ 1.6 K), the germanium thermometer should read about 530 Ω.

Open the He3 stage heat switch, turn off the charcoal heater, close the charcoal pump heat switch, and stop pumping on the He4. You are now pumping on the condensed He3. The germanium temperature sensor and charcoal thermistor should both increase in resistance quickly.

After about 15 minutes, purge the vacuum line with He4 until the pressure of the He4 bath is at atmosphere. Remove the MKS gauge and pump line and re-transfer liquid helium into the He4 reservoir.

Turn on the "power," "bias," and "input" switches. Wait for the JFET to warm up and the electronics to stabilize ($\sim$1/2 hour).

Depending upon the heat load to the bolometer (i.e. the incident power flux onto the bolometer element plus electrical power), the length of time the bolometer remains cold will vary. Make sure that the liquid nitrogen jacket and He4 reservoir are never empty. Measure the He4 level periodically and retransfer as necessary.

Switch the scale of the Keithley 197A to the highest resistance scale. The resistance of the germanium thermometer should increase to around 15 or 16 kΩ, and the charcoal temperature should increase to about 20 to 24 kΩ (depending on how long you wait).

I achieved a He3 run time of 35 hours with the copper blank, but I had to retransfer He4 at around 20 hours. I also refilled the nitrogen jacket periodically. I achieved a hold time of around 23 hours when the bolometer filter was set to fluorogold and was illuminated by a 200W Hg vapor lamp run through the SPECAC and focused down into the bolometer.

Time (sec)	Temp (K)	He3 (PSI)	Ge, kOhm	Charcoal, kOhm	Procedure and notes
0	300	+25	.001	1.0700	Close Charcoal clamp and He3 clamp, Cu Blank Filter, base vacuum pressure at 2x10^-7 Torr
220			.001		Begin LN Transfer
4361	77K	+20	.001	1.5900	Blow Out LN
4541	77K	+20	.001		Begin He4 Transfer
4766			.001		Disconnect Diff pump from Bolometer
5168					He4 begins condensing
5873	4K		.120	17.500	Begin pumping on He4
6071			.120		Unclamp charcoal, turn on charcoal heater (7V initially)
8190	2K		.480	1.8500	He4 pressure at 3.6Torr (lowest will be 2.5)
9800			.480		Turn off charcoal heater, close charcoal clamp, open He3 clamp, stop pumping on He4
9970					Purge He4 chamber with He4 gas and remove pressure gauge
10225					Begin second He4 transfer
10594	~350mK	-26	1.580	13.000	End second He4 transfer

Figure D.1: Typical He3 bolometer cooling time-line

D.6 Re-cooling: running out of He3

Make sure there is plenty of He4 in the reservoir. Open the charcoal heater switch and close the He3 stage heater switch. Begin pumping on the He4 reservoir, and follow section D.4 beginning with the paragraph that begins "Begin pumping on the He4 reservoir."

D.7 Load curves

A load curve gives the bolometer responsivity as a function of dissipative power. The bolometer element is inherently nonlinear. The resistance of the bolometer depends upon the power put into it and the rate of dissipation to the cold bath.

It would at first appear that the more sensitive a detector, the better. The sensitivity is defined as the change in measured voltage, or voltage across the bolometer element, divided by the change in radiant power. Since the current through the bolometer is roughly constant, a high sensitivity requires a large voltage change. This is equivalent to the bolometer element having a large dynamical resistance. This is great! Make the bolometer approach infinite resistance and the detector will have infinite sensitivity.

The problem is that Johnson noise, or shot noise, is directly related to resistance: the higher the resistance, the higher the shot noise. In fact, the entire reason the bolometer element is cold is to reduce the shot noise as much as possible. There is an optimum resistance that maximizes not the sensitivity, but the signal-to-noise. The noise-equivalent power (NEP) is the relevant parameter, the noise voltage in a 1 Hz band divided by the detector sensitivity.

Position	Material	Freq. cut-off
#1	Quartz + Garnet powder	100 μm
#2	Quartz + Diamond powder	170 μm
#3	Fluorogold	280 μm
#4	thick copper blank	0 μm

Table D.2: Cold filter summary

Since the bolometer element itself is a nonlinear device, the heat load will change the NEP of the detector. The thermal conductance to the heat bath is specifically chosen to minimize the NEP under presumed operating conditions. Excessive thermal loading of the bolometer will decrease the sensitivity slightly increasing the NEP away from the optimal condition. Different filter settings change the sensitivity of the bolometer due to radiant thermal loading.

D.7.1 Measuring the load curve

Apply a voltage at the "BIAS" port. Make sure that the "BIAS" switch is open! Also turn on the power to the cold module JFET ("power" switch) and open the "Input test" switch. I used a Fluke meter and a Wavetek generator to measure and apply a dc- voltage. Do not exceed 2.0 Volts! Too much current through the bolometer can damage it (that is, doping impurities could migrate due to intense electric fields causing the characteristics of the bolometer to change). Measure the voltage at the "Vs" port when 0 volts (V) is applied. This voltage will be called V_{offset}. Next, apply a voltage V and measure the voltage at V_s. The voltage across the bolometer is given

by $V_b = V_s - V_{offset}$. The current through the bolometer is then given by:

$$I_d = (V - V_b)/R_{load}$$

where R_{load} is 20 MΩ. The resistance of the bolometer is given by:

$$R_b = \frac{\delta V_b}{\delta I_d}$$

R_b will change as a function of V_b due to self heating of the bolometer element.

The sensitivity is calculated as follows:

$$S = \frac{\delta V_b}{\delta(I_d \times V_b)}$$

The inherent noise of the bolometer can be found by using either a spectrum analyzer or a lock-in amplifier. I used the EG&G 7260 lock-in amplifier with the internal oscillator set to the frequency of interest and directly measured the rms voltage noise per $\sqrt{Hz}$.

All the load curve data is given in figure D.2.

He3 Bolometer **Rload =** 20 Mohms

Filter	V (Volts)	Vs (Volts)	Vb (Volts)	Rbolo(Ohms)	Ibolo(amps)	PowerBolo(Watts)	Responsivity (V/W)	Sensitivyt (uW/V)	Rbolo (Mohm
#4	0	0.7225	0		0.00E+00	0.00E+00			
	0.10024	0.7966	0.0741	5.67E+07	1.31E-09	9.68E-11	7.65E+08	1.31E-03	5.67E+01
	0.20518	0.841	0.1185	1.47E+07	4.33E-09	5.14E-10	1.07E+08	9.39E-03	1.47E+01
	0.3078	0.8703	0.1478	7.99E+06	8.00E-09	1.18E-09	4.38E+07	2.28E-02	7.99E+00
	0.4014	0.891	0.1685	5.68E+06	1.16E-08	1.96E-09	2.65E+07	3.77E-02	5.68E+00
	0.5032	0.909	0.1865	4.30E+06	1.58E-08	2.95E-09	1.82E+07	5.51E-02	4.30E+00
	1.4945	0.9919	0.2694	1.83E+06	6.13E-08	1.65E-08	6.12E+06	1.63E-01	1.83E+00
#3	0	0.7289	0		0.00E+00	0.00E+00			0.00E+00
	0.1005	0.7764	0.0475	1.79E+07	2.65E-09	1.26E-10	3.77E+08	2.65E-03	1.79E+01
	0.2052	0.7986	0.0697	5.38E+06	6.78E-09	4.72E-10	6.41E+07	1.56E-02	5.38E+00
	0.3052	0.8129	0.084	3.34E+06	1.11E-08	9.29E-10	3.13E+07	3.19E-02	3.34E+00
	0.4051	0.8239	0.095	2.47E+06	1.55E-08	1.47E-09	2.02E+07	4.94E-02	2.47E+00
	0.5143	0.8336	0.1047	1.95E+06	2.05E-08	2.14E-09	1.44E+07	6.92E-02	1.95E+00
	1.5475	0.8906	0.1617	1.17E+06	6.93E-08	1.12E-08	6.29E+06	1.59E-01	1.17E+00
#2	0	0.7347	0		0.00E+00	0.00E+00			0.00E+00
	0.10284	0.7589	0.0242	6.15E+06	3.93E-09	9.52E-11	2.54E+08	3.93E-03	6.15E+00
	0.2018	0.7705	0.0358	2.66E+06	8.30E-09	2.97E-10	5.74E+07	1.74E-02	2.66E+00
	0.3119	0.7799	0.0452	1.87E+06	1.33E-08	6.03E-10	3.08E+07	3.25E-02	1.87E+00
	0.4065	0.7868	0.0521	1.57E+06	1.77E-08	9.23E-10	2.15E+07	4.64E-02	1.57E+00
	0.5058	0.7932	0.0585	1.38E+06	2.24E-08	1.31E-09	1.66E+07	6.02E-02	1.38E+00
	1.555	0.8313	0.0966	7.54E+05	7.29E-08	7.04E-09	6.64E+06	1.51E-01	7.54E-01
#1	0	0.7428	0		0.00E+00	0.00E+00			0.00E+00
	0.1076	0.7468	0.004	7.72E+05	5.18E-09	2.07E-11	1.93E+08	5.18E-03	7.72E-01
	0.2052	0.7502	0.0074	7.22E+05	9.89E-09	7.32E-11	6.48E+07	1.54E-02	7.22E-01
	0.3048	0.7532	0.0104	6.21E+05	1.47E-08	1.53E-10	3.75E+07	2.66E-02	6.21E-01
	0.4072	0.756	0.0132	5.62E+05	1.97E-08	2.60E-10	2.62E+07	3.82E-02	5.62E-01
	0.5068	0.7585	0.0157	5.15E+05	2.46E-08	3.86E-10	1.99E+07	5.02E-02	5.15E-01
	1.531	0.7734	0.0306	2.95E+05	7.50E-08	2.30E-09	7.80E+06	1.28E-01	2.95E-01

Figure D.2: Electronic load curve of the He_3 bolometer exposed to room temperature radiation with different filter settings

Figure D.3: He3 bolometer side-mounted gas system and electronics

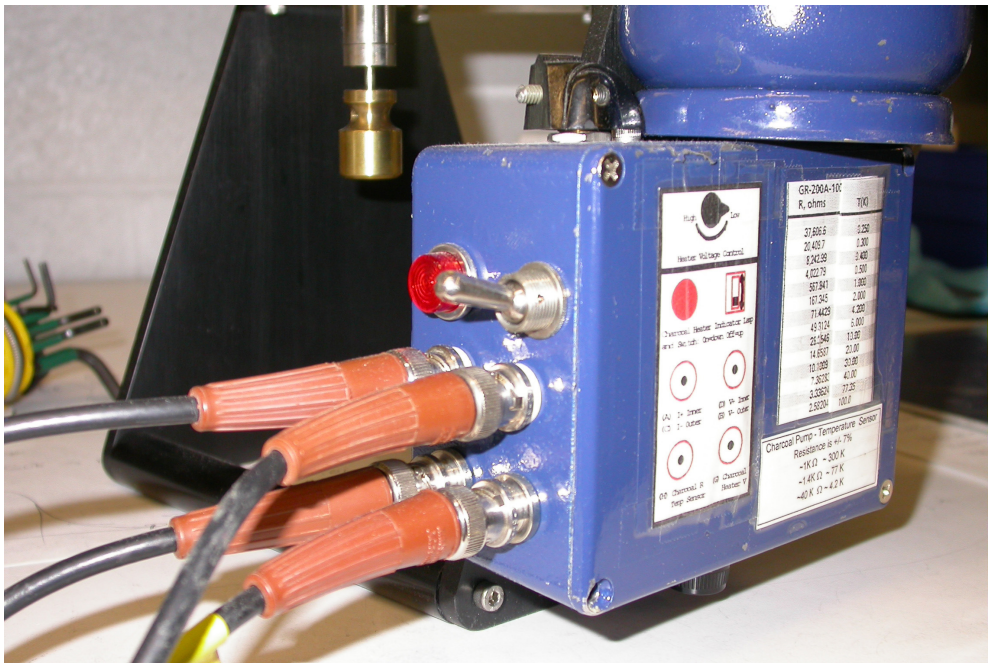

(a) Close-up view of the electronics box showing the heater thermometer and heater voltage break-out BNC connectors

(b) He3 gas cleaner: A copper reservoir that is inserted into a He4 dewar.

Figure D.4: He3 electronics and gas cleaner.

Appendix E

Oxford sample stick wiring chart

20 Pin Kapton Connector	Oxford 10-pin connector	Wire Color	Description	
1	Blue Connector	Black	Cu Block 75Ohm Heater	
2	Blue Connector	White		
3	Blue Connector	Blue	Cu Block Thermometer +	Use Cernox SN-X22073 (NOT THE CORRECT ONE, BUT CLOSE ENOUGH)
4	Blue Connector	Brown		
5	Blue Connector	Orange	Cu Block Thermometer -	
6	Blue Connector	Yellow		
7	Blue Connector	Purple	Top Sample 400Ohm Heater	
8	Blue Connector	Grey		
9	Blue Connector	Red	Bottom Sample 400Ohm Heater	
10	Blue Connector	Green		
11	Green Connector	Orange	Top Sample Thermometer -	Cernox SN-X22340
12	Green Connector	Green		
13	Green Connector	Purple	Top Sample Thermometer +	
14	Green Connector	White		
15	Green Connector	Black	Bottom Sample Thermometer -	Cernox SN-14031
16	Green Connector	Grey		
17	Green Connector	Yellow	Bottom Sample Thermometer +	
18	Green Connector	Blue		
19	Green Connector	Brown	Nothing	
20	Green Connector	Red		

Figure E.1: Oxford sample stick wiring chart

Appendix F

Transmission and reflection: thin films on dielectrics

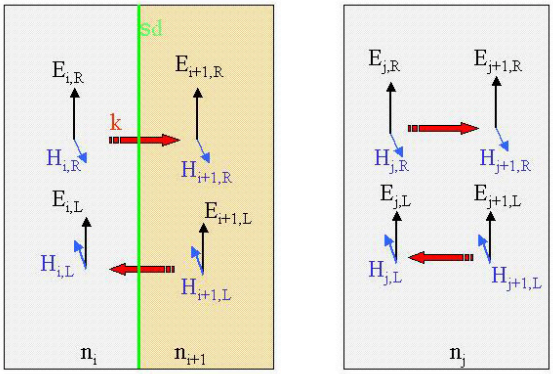

Figure F.1: Electromagnetic plane waves in dielectrics

The complex transmission and reflection Fresnel coefficients are derived using the appropriate Maxwell equations, applying boundary conditions, and solving for the amplitude of the transmitted and reflected electric field normalized to the initial incoming electric field amplitude. We will develop a general form for the transfer functions across boundaries with thin conductive films and through dielectrics in order to calculate the reflected and transmitted fields from a multi-layered system when the initial field is at normal incidence and all boundaries are parallel.

Consider the left-hand picture shown in figure F.1. We begin with Maxwell's equations in linear media:[77]

$$\vec{\nabla} \times \vec{H} = \frac{4\pi}{c}\vec{J} + \frac{1}{c}\frac{\delta\vec{D}}{\delta t} \qquad \vec{\nabla} \times \vec{E} = -\frac{1}{c}\frac{\delta\vec{B}}{\delta t}$$

$$\vec{\nabla} \cdot \vec{B} = 0 \qquad \vec{\nabla} \cdot \vec{D} = 4\,\pi\,\rho = 0$$

$$\vec{J} = \tilde{\sigma}\vec{E}$$

It should be noted that all indices of refraction are assumed to be complex. Integrating along a contour chosen as a rectangle straddling the interface, and taking

the limit as the width (area) of the contour goes to zero gives:

$$\begin{aligned}\int \vec{\nabla}\times\vec{H}\cdot d\vec{A} &= \oint \vec{H}\cdot d\vec{L} = L(H_{i,R} - H_{i,L} + H_{i+1,L} - H_{i+1,R}) \\ &= \frac{4\,\pi}{c}\int \tilde{\sigma}\vec{E}\cdot d\vec{A} \;=\; \frac{4\,\pi}{c}\int_{\substack{l\mapsto L \\ W\mapsto d\sim 0}} \tilde{\sigma}\vec{E}\; dW\; dL \\ &= \frac{4\,\pi}{c}\; L\;\tilde{\sigma d}\;(E_{i+1,R} + E_{i+1,L}) \end{aligned} \tag{F.1}$$

where

the subscript i denotes the interface number,

L and R denote left and right travelling waves,

and

$$\int \vec{\nabla}\times\vec{E}\cdot d\vec{A} \;= \oint \vec{E}\cdot d\vec{L} = (E_{i,R} - E_{i+1,R} + E_{i,L} - E_{i+1,L}) = 0 \tag{F.2}$$

and

$$\begin{aligned}\vec{\nabla}\times\vec{E} \qquad &= -\frac{1}{c}\,\frac{\delta\vec{B}}{\delta t}, \text{ and assuming a solution form of } E, B = e^{i(\vec{k}\cdot\vec{x}-\omega t)} \\ &\Rightarrow i\;kE = i\;\frac{\omega}{c}B \\ \text{where} \qquad &B = \mu H,\;\; n = \frac{c}{v},\;\; v = \frac{\omega}{k} \\ &\Rightarrow \text{magnitude of amplitudes obey: } E = \frac{\mu}{n}\,H \end{aligned} \tag{F.3}$$

Combing equations F.1-F.3 and letting $Z \equiv 4\pi/c \approx 377\Omega/\square$, and casting the results into vector form yield:

$$\begin{pmatrix} E_{i+1,R} \\ E_{i+1,L} \end{pmatrix} = \underbrace{\frac{1}{n_{i+1}}\begin{pmatrix} n_i + n_{i+1} - Z\;\sigma d & n_{i+1} - n_i - Z\;\sigma d \\ n_{i+1} - n_i + Z\;\sigma d & n_i + n_{i+1} + Z\;\sigma d \end{pmatrix}}_{\equiv M_i} \begin{pmatrix} E_{i,R} \\ E_{i,L} \end{pmatrix} \tag{F.4}$$

The transfer function that represents the wave propagation from one boundary to another within one dielectric is given by (see the right figure in F.1):

$$\begin{pmatrix} E_{j+1,R} \\ E_{j+1,L} \end{pmatrix} = \underbrace{\begin{pmatrix} e^{i\,2\pi\,n_j\,d\,\nu} & 0 \\ 0 & e^{-i\,2\pi\,n_j\,d\,\nu} \end{pmatrix}}_{\equiv K_j} \begin{pmatrix} E_{j,R} \\ E_{j,L} \end{pmatrix} \tag{F.5}$$

where ν is the frequency of radiation, (wavelength)$^{-1}$

For 'n' number of multi-layers with some initial incident radiation moving to the right (R), we have:

$$\begin{pmatrix} E_{transmitted,R} \\ 0 \end{pmatrix} = \left(M_{n+1} \prod_{i}^{n} K_i M_i \right) \begin{pmatrix} E_{initial,R} \\ E_{reflected,L} \end{pmatrix} \tag{F.6}$$

The complex Fresnel transmission and reflection coefficient are defined as:

$$t \equiv \frac{E_{transmitted,R}}{E_{initial,R}} \qquad\qquad r \equiv \frac{E_{reflected,L}}{E_{initial,R}} \tag{F.7}$$

The transmission and reflection is defined as:

$$T \equiv |t|^2 \qquad\qquad R \equiv |r|^2 \tag{F.8}$$

For a thin-film between two semi-infinite substrates:

$$t = \frac{2n_1}{n_1 + n_2 + Z\,\sigma d} \qquad\qquad r = \frac{n_1 - n_2 - Z\,\sigma d}{n_1 + n_2 + Z\,\sigma d} \tag{F.9}$$

$$T = \left| \frac{2n_1}{n_1 + n_2 + Z\,\sigma d} \right|^2 \qquad\qquad R = \left| \frac{n_1 - n_2 - Z\,\sigma d}{n_1 + n_2 + Z\,\sigma d} \right|^2 \tag{F.10}$$

BIBLIOGRAPHY

[1] J. G. Bednorz and K. A. Muller, Z. Phys. B **64**, 189 (1986).

[2] J. Orenstein and A. J. Millis, Science **288**, 468 (2000).

[3] Phillip Anderson and Robert Schrieffer, Physics Today **June** (1991).

[4] T. Valla *et al.*, Phys. Rev. Lett. **85**, 2581 (2000).

[5] D. Orgad, S. A. Kivelson, E. W. Carlson, V. J. Emery, X. J. Zhou, and Z.-X. Shen, Phys. Rev. Lett. **86**, 4362 (2001).

[6] C.C. Tsuei and J.R. Kirtley, Physica C **4**, 282–287 (1997).

[7] C. M. Varma, P. B. Littlewood, S. Schmitt-Rink, E. Abrahams, and A. E. Ruckenstein, Phys. Rev. Lett. **63**, 1989 (1996).

[8] T. R. Chien, Z. Z. Wang, and N. P. Ong, Phys. Rev. Lett. **67**, 2088 (1991).

[9] J. M. Harris, Y. F. Yan, and N. P. Ong, Phys. Rev. B **46**, 14293 (1992).

[10] J. J. Tu, C. C. Homes, G. D. Gu, D. N. Basov, and M. Strongin, Phys. Rev. B **66**, 144514 (2002).

[11] M. A. Quijada, D. B. Tanner, R. J. Kelley, M. Onellion, H. Berger, and G. Margaritondo, Phys. Rev. B **60**, 14 917 (1999).

[12] Z. Konstantinovic, Z. Z. Li, and H. Raffy, Phys. Rev. B **62**, R11 989 (1989).

[13] Donal Cronin Schmadel. *The ac- Hall Effect in Single Crystal* $Bi_2Sr_2CaCu_2O_{8+\delta}$. PhD thesis, University of Maryland, College Park (2002).

[14] M. Grayson, L.B. Rigal, D. C. Schmadel, H. D. Drew, and P.-J. Kung, Phys. Rev. Lett. **89**, 37003 (2002).

[15] C. M. Varma and Elihu Abrahams, Phys. Rev. Lett. **86**, 4652 (2001).

[16] C. M. Varma and Elihu Abrahams, Phys. Rev. B **68**, 094502 (2003).

[17] Hlubina, Phys. Rev. B **89**, 037003–1 (2002).

[18] J. Cerné *et al.*, Phys. Rev. Lett. **84**, 3418 (2000).

[19] L. B. Rigal, D. C. Schmadel, H. D. Drew, B. Maiorov, E. Osquigil, J. S. Preston, R. Hughes, and G.D. Gu, arXiv:cond-mat/0309108, 2003.

[20] J. Bardeen, L. N. Cooper, and J. R. Schrieffer, Phys. Rev. **108**, 1175 (1957).

[21] W. N. Hardy *et al.*, Phys. Rev. Lett. **70**, 3999 (1993).

[22] Horng-Twu Steve Lihn. *Far-Infrared Magneto-Optics of Superconducting $YBa_2Cu_3O_{7-\delta}$ Thin Films and the Theory of Vortex Dynamics*. PhD thesis, University of Maryland, College Park (1996).

[23] S. G. Kaplan, S. Wu, H.-T. S. Lihn, and H. D. Drew, Phys. Rev. Lett. **76**, 696 (1996).

[24] Shanlu Wu. *Far-Infrared Magneto-optical Study of the ac- Hall Effect in $YBa_2Cu_3O_{7-\delta}$ Thin Films*. PhD thesis, University of Maryland, College Park (1997).

[25] K. Karrai, E. Choi, F. Dunmore, S. Liu, X. Ying, Qi Li, T. Venkatesan, and H. D. Drew, Phys. Rev. Lett. **69**, 355 (1992).

[26] T. C. Hsu, Physica C **213**, 305 (1993).

[27] G. D. Gu *et al.*, Physica C **263**, 180 (1996).

[28] Dean T. Hodges, Infrared Physics **18**, 375 (1978).

[29] John J. Dugnan, Appl. Phys. **33**, 1 (1976).

[30] E. D. Palik, *Handbook of Optical Constants of Solids II* (Academic Press, San Diego, 1991).

[31] Stellan Jacobsson, Infrared Physics **29**, 853–874 (1989).

[32] M. Rosenbluh, R. J. Temkin, and K. J. Button, Applied Optics **15**, 2635 (1976).

[33] Neil W. Ashcroft and N. David Mermin, *Solid State Physics* (Saunders College Publishing, Orlando, 1976).

[34] J. I. Gittleman and B. Rosenblum, Phys. Rev. Lett. **16**, 734 (1966).

[35] S. W. McKnight, K. P. Stewart, H. D. Drew, and K. Moorjani, Infrared Physics **27**, 327 (1987).

[36] Danilo Romero, Private communications, 2000.

[37] Inc. UDT Sensors, http://www.udt.com/, PIN-10D Planar Diffused Silicon Photodiode.

[38] Amnon Yariv, *Quantum Electronics Third Edition* (John Wiley and Sons, NYC, 1989).

[39] T. Sawatari and N. S. Kapany, Journal of the Optical Society of America **66**, 362 (1976).

[40] P. Schwaller, H. Steffen, J. F. Moser, and F. K. Kneubuhl, Applied Optics **6**, 827 (1967).

[41] D. T. Hodges and T. S. Hartwick, Appl. Phys. Lett. **23**, 252 (1973).

[42] R. A. Wood, N. Brignall, C. R. Pidgeon, and F. Al-Berkdar, Infrared Physics **16**, 201–205 (1976).

[43] Edinburgh Instruments website, http://www.edinst.com/fir.htm, FIR laser specifications.

[44] A. Tanaka, A. Tanimoto, N. Murata, M. Yamanaka, and H. Yoshinaga, Japan. J. Appl. Phys **13**, 1491 (1974).

[45] Charles P. Poole, Jr., Horacio A. Farach, and Richard J. Creswick, *Superconductivity* (Academic Press, Inc, San Diego, 1995).

[46] T. Asahi, H. Suzuki, M. Nakamura, H. Takano, and J. Kobayashi, Phys. Rev. B **48**, 10 (1993).

[47] T. S. Olsen, S. Steenstrup, L. Gerward, and B. Sundqvist, J. Phys. Scr. **44**, 211 (1991).

[48] T. Huang, M. Itoh, J. Yu, Y. Inaguma, and T. Nakamura, Phys. Rev. B **14**, 55 (1997).

[49] Guy Kendall White, *Experimental Techniques in Low-Temperature Physics, second edition* (Oxford Unversity Press, London, 1968).

[50] T. S. Olsen, S. Steenstrup, L. Gerward, and B. Sundqvist, Phys. Rev. B **82**, 15 (1999).

[51] S. H. Pan *et al*, Nature **413**, 282 (2001).

[52] K. M. Lang *et al*, Nature **415**, 412 (2002).

[53] J.W. Loram, J.L. Tallon, and W.Y. Liang, arXive:cond-matt/0212461 v1, 2001.

[54] A. V. Puchkov, D. N. Basov, and T. Timusk, J. Physics. Condensed Mater. **8**, 10049–10082 (1996).

[55] S. H. Pan, E.W. Hudson, A. K. Gupta, K.-W. Ng, H. Eisaki, S. Uchida, and J. C. Davis, Phys. Rev. Lett. **85**, 1536 (2000).

[56] N. P. Ong, Phys. Rev. B **43**, 193 (1991).

[57] A. J. Mills and H. D. Drew, Phys. Rev. B **68**, 149901(E) (2003).

[58] J. E. Sonier, R. F. Kiefl, J. H. Brewer, D. A. Bonn, S. R. Dunsiger, W. N. Hardy, R. Liang, and R. I. Miller, Phys. Rev. B **59**, 729 (1999).

[59] D. A. Bonn, Ruixing Lian, T. M. Riseman, D. J. Baar, D. C. Morgan, Kuan Zhang, P. Dosanjh, T. L. Duty, A. MacFarlana, G. D. Morris, J. H. Brewer, and W. N. Hardy, Phys. Rev. B **47**, 11314 (1993).

[60] J. Corson, J. Orenstein, S. Oh, J. O'Donnell, and J. N. Eckstein, Phys. Rev. Lett **85**, 2569 (2000).

[61] J. Corson, R. Mallozzi, J. Orenstein, J. N. Eckstein, and I. Bozovic, Nature **398**, 221 (1999).

[62] J. M. Kosterlitz and D. J. Thouless, J. Phys. C **6**, 1181 (1973).

[63] S. Kamal, Ruixing Liang, A. Hosseini, D.A. Bonn, , and W.N. Hardy, arXiv:cond-mat/9803292 v1, 1998.

[64] B. Parks, S. Spielman, J. Orenstein, D. T. Nemeth, F. Ludwig, J. Clark, P. Merchant, and D. Lew, Phys. Rev. Lett. **74** (1995).

[65] Yayu Wang, Z. A. Xu1, T. Kakeshita, S. Uchida, S. Ono, Yoichi Ando, and N. P. Ong, arXiv:cond-mat/0108242 v1, 2001.

[66] J. W. Loram, j. L. Luo, J. R. Cooper, W. Y. Liang, and J. L. Tallon, Physica C **341-348**, 831–834 (2000).

[67] H. J. A. Molegraaf, C. Presura, D. van der Marel, P. H. Kes, and M. Li, Science **295**, 2239 (2002).

[68] D. Matthey, S. Gariglio, B. Giovannini, and J.-M. Triscone, Phys. Rev. B **64**, 24513 (2001).

[69] B. Bucher, P. Steiner, J. Karpinski, E. Kaldis, and P. Wachter, Phys. Rev. Lett. **70**, 2012 (1993).

[70] J. Jin and H. R. Ott, Phys. Rev. B **57**, 13872 (1998).

[71] Ch. Renner, B. Revaz, J.-Y. Genoud, K. Kadowaki, and . Fischer, Phys. Rev. Lett. **80**, 149 (1998).

[72] M. R. Norman, M. Randeria, H. Ding, and J. C. Campuzano, Phys. Rev. B **75**, R11093 (1998).

[73] J. Simpson, PhD thesis to be published in 2004, University of Maryland, College Park.

[74] Yoshishige Tsuchiya *et al.*, Phys. Rev. B **63**, 184517 (1996).

[75] G. Blatter, M. V. Feigle'man, V. B. Geshkenbein, A. I. Larkin, and V. M. Vinokur, Rev. Mod. Phys. **66**, 1125 (1994).

[76] Noam Chomsky, *Understanding Power* (The New York Press, NYC, 2002).

[77] J. D. Jackson, *Classical Electrodynamics, second edition* (John Wiley and Sons, Inc., USA, 1975).